Heinrich Heine Universität Düsseldorf

JÜLICH Forschungszentrum

Indole *C*-methyltransferases – creating an efficient platform for the enantioselective methylation of bioactive compounds

Diana-Alexandra Amariei

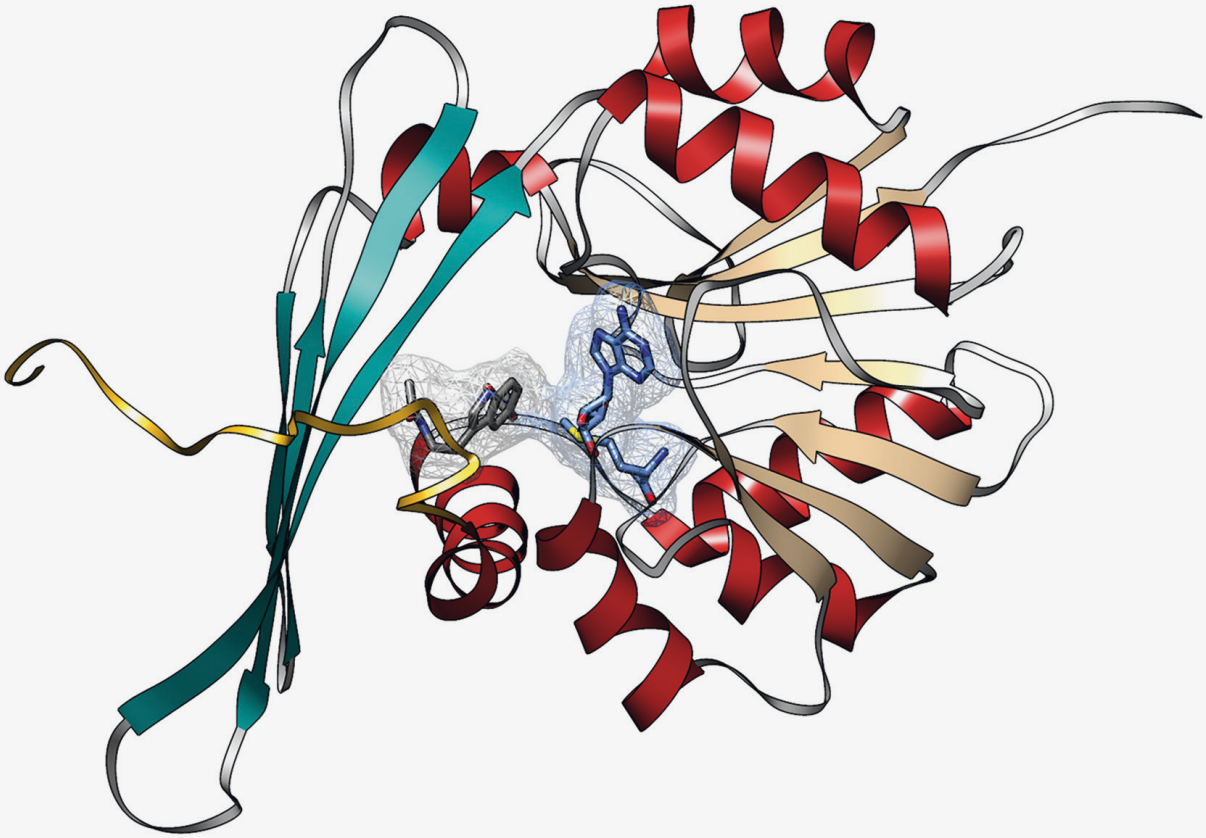

Bioorganische Chemie an der Heinrich-Heine-Universität
im Forschungszentrum Jülich

Indole *C*-methyltransferases – creating an efficient platform for the enantioselective methylation of bioactive compounds

Inaugural dissertation

for the attainment of the title of doctor
in the Faculty of Mathematics and Natural Sciences
at the Heinrich Heine University Düsseldorf

presented by

Diana-Alexandra Amariei
from Gheorgheni, Romania

Düsseldorf, October 2025

from the institute for Bioorganic Chemistry
at the Heinrich Heine University Düsseldorf

Published by permission of the
Faculty of Mathematics and Natural Sciences at
Heinrich Heine University Düsseldorf

Supervisor: Prof. Dr. Jörg Pietruszka
Co-supervisor: Prof. Dr. Holger Gohlke

Date of the oral examination: 31.10.2025

Heinrich Heine
Universität
Düsseldorf

Indole *C*-methyltransferases – creating an efficient platform for the enantioselective methylation of bioactive compounds

Inaugural-Dissertation

zur Erlangung des Doktorgrades
der Mathematisch-Naturwissenschaftlichen Fakultät
der Heinrich-Heine-Universität Düsseldorf

vorgelegt von

Diana-Alexandra Amariei
aus Gheorgheni (Rumänien)

Düsseldorf, Oktober 2025

Bibliografische Information der Deutschen Nationalbibliothek.
Die Deutsche Nationalbibliothek verzeichnet diese Publikation in der
Deutschen Nationalbibliografie; detaillierte Bibliografische Daten
sind im Internet über http://dnb.d-nb.de abrufbar.

Gedruckt mit der Genehmigung der
Mathematisch-Naturwissenschaftlichen Fakultät
der Heinrich-Heine-Universität Düsseldorf

Referent:	Prof. Dr. Jörg Pietruszka
Korreferent:	Prof. Dr. Holger Gohlke
Tag der mdl. Prüfung:	31.10.2025
Herausgeber:	Prof. Jörg Pietruszka
Umschlaggestaltung:	Grafische Medien, Forschungszentrum Jülich GmbH
Druck:	Grafische Medien, Forschungszentrum Jülich GmbH
Copyright:	Forschungszentrum Jülich 2026

Bioorganische Chemie an der Heinrich-Heine-Universität Düsseldorf
im Forschungszentrum Jülich, Band 54

D 61 (Diss. Düsseldorf, Univ., 2025)

ISSN 3054-2197
ISBN 978-3-95806-881-0

Vollständig frei verfügbar über das Publikationsportal des Forschungszentrums Jülich (JuSER)
unter www.fz-juelich.de/zb/openaccess.

Publications

Parts of this work have been published in scientific journals or presented at scientific conferences. Some of the figures and experimental descriptions in this work also appear in the publications mentioned bellow, and are used here with the agreement of the respective journals:

Publications in scientific journals during the doctoral studies

1. Amariei, D. A., Pozhydaieva, N., David, B., Schneider, P., Classen, T., Gohlke, H., Weiergräber O. H. & Pietruszka, J. (**2022**). Enzymatic C3-Methylation of Indoles Using Methyltransferase PsmD─ Crystal Structure, Catalytic Mechanism, and Preparative Applications. *ACS Catal.*, *12*(22), 14130-14139.[1]

Contribution: conceptualization, methodology, analysis, investigation, writing (original draft, review & editing), visualization, project administration.

2. Amariei, D. A.*, Haase, M.,* Klischan, M. K. T., Wäscher, M., & Pietruszka, J. (**2024**). High-Throughput Colorimetric Detection and Quantification of Indoles and Pyrroloindoles for Enzymatic Activity Determination. *ChemCatChem*, e202400052.[2]

* Shared first authorship

Contribution: conceptualization, methodology, analysis, investigation, writing (original draft, review & editing), visualization.

3. Amariei, D. A., Tenhaef, J., Classen, T., David, B., Rosch, T. M., Gohlke, H., Noack, S. & Pietruszka, J. (**2024**). Directed evolution of C-methyltransferase PsmD for enantioselective pyrroloindole derivative production. *Catal. Sci. & Technol.*, *14*, 6298-6306.[3]

Contribution: conceptualization, methodology, analysis, investigation, writing (original draft, review & editing), visualization.

Conference presentations

- Global Biobased Businessplan Competition (G-BiB), CLIB International Conference (02/2022), Düsseldorf, Germany, Mona Haase, Marcel Schatton, Benjamin Chapple, Diana A. Amariei, Pascal Schneider, J. Pietruszka, "*Methylation (im)-possible – a useful tool for tailoring drug products"* - **Pitch competition, 2nd place**

- BASF Summer school (08/2022), Ludwigshafen, Germany; Diana A. Amariei, Nadiia Pozhydaeva, Oliver Weiergräber, Benoit David, Pascal Schneider, Thomas Classen, Holger Gohlke, Jörg Pietruszka, "*Enzymatic C-methylation of indoles: a biocatalytic path towards new AchE inhibitors."* - **Poster and pitch presentation**

- **Biocat (08/2022)**, Hamburg, Germany; Diana A. Amariei, Nadiia Pozhydaieva, Oliver Weiergräber, Benoit David, Pascal Schneider, Holger Gohlke, Jörg Pietruszka, "*New insights into the enzymatic C-methylation of indoles."* - **Poster and pitch presentation**

- **PhD Workshop Topic 7: Towards a Sustainable Bioeconomy – Resources, Utilization, Engineering and AgroEcosystems (11/2022),** Leipzig, Germany, Diana A. Amariei, Nadiia Pozhydaieva, Oliver Weiergräber, Benoit David, Pascal Schneider, Holger Gohlke, Jörg Pietruszka, "*New Insights into the C-methylation of Indoles"* - **Poster**

- **ACS publications symposium: Biological and medicinal chemistry (02/2023),** Bonn, Germany; Diana A. Amariei, Nadiia Pozhydaeva, Benoit David, Pascal Schneider, Julia Tenhaef, Stephan Noack, Thomas Classen, Holger Gohlke, Oliver Weiergräber, Jörg Pietruszka, "*Structural diversification of bioactive indole-based alkaloids using enzymatic methylation."* **– Poster**

- **BioökonomieRevier Jahrestagung (2023)**, M. Bott, S. Noack, J. Marienhagen, W. Wiechert, K.-E. Jaeger, J. Pietruszka, J. Tenhaef, S. Matamouros, A. Loeschke, D. A. Amariei, T. Stoltmann, T. Rosch, *Innovationslabor AutoBioTech: Automatisierung der Biotechnologie für die Bioökonomie* - **Poster**

- **Biotrans (07/2023)**, La Rochelle, France; Diana A. Amariei, Julia Tenhaef, Tobias Rosch, Pascal Schneider, Stephan Noack, Jörg Pietruszka, "*Enzyme engineering approaches on a stereospecific C3-indole methyltransferase – challenges, new functions and solutions for practical applications."* - **Poster and pitch presentation**

- Jülich Innovation and Entrepreneurship Certificate program (09/2023), Forschungszentrum Jülich, Germany, Diana A. Amariei, Lisa M. Böhmer, Benjamin Chapple,

Mona Haase, "*Methylution: selective methylation of drug candidates.*"- **Pitch competition, 2nd place**

- **NordBio II (06/2024),** Stockholm, Sweden; Diana Amariei, Julia Tenhaef, Thomas Classen, Benoit David, Holger Gohlke, Stephan Noack, Oliver Weiergräber, Jörg Pietruszka "*Secondary metabolite diversification through the engineering of an indole C-methyltransferase"* **– Presentation**

- Dechema Forum (09/2024), Friedrichshafen Germany, Diana Amariei, Julia Tenhaef, Thomas Classen, Benoit David, Holger Gohlke, Stephan Noack, Oliver Weiergräber, Jörg Pietruszka, "*Stereospecific enzymatic C-methylation of indoles for the production of new AChE inhibitors"* - **Poster and pitch presentation**

- Towards a Sustainable Bioeconomy – Resources, Utilization, Engineering and AgroEcosystems - Fall meeting Topic 7 (11/2024), Forschungszentrum Jülich, Germany, Diana Amariei, Julia Tenhaef, Thomas Classen, Benoit David, Holger Gohlke, Stephan Noack, Oliver Weiergräber, Jörg Pietruszka, "*Stereospecific enzymatic C-methylation of indoles for the production of new AChE inhibitors"* - **Poster**

Theses

The current work contains results from the following theses:

- **M. Sc. Nadiia Pozhydaieva** (Heinrich-Heine-University Düsseldorf, master thesis), 2020: "*C-methyltransferases as a powerful tool for organic synthesis – characterisation, optimization and application for the stereoselective formation of indole alkaloids"*

The master project of Ms. Pozhydaieva was completed before the start of the doctoral project described in this work. Some of the early PsmD_*Sa* characterization data was produced during this master thesis project and used in this work for completeness. The data produced during Ms. Pozhydaieva's master project is marked as such and was included in the publication [1] along with the corresponding authorship.

- **B. Sc. Lisa Guo** (Heinrich-Heine-University Düsseldorf, bachelor thesis), 2022: *"Towards the Gram Scale Enzymatic Synthesis of a Physostigmine Precursor"*

The thesis was conducted under the author's supervision and the corresponding data presented in this work is specifically indicated.

Table of contents

Preface

In my view, the primary goal of scientific research is to improve people's lives. In the face of challenges like drug resistance and the depletion of natural resources, it is important to adapt technologies for more sustainable industrial practices and to develop alternatives for producing new molecules. Biocatalysis has seen important advancements in recent years, but further research is essential to make this technology widely accessible. At the start of this project, methyltransferases were a relatively “exotic” type of enzyme for biocatalytic applications. While the research in this study is centered around one enzyme, I aimed to tackle some of the general challenges related to methyltransferase biocatalysis. The core question guiding my research throughout this project has always been, "how can this be used?". As reflected in the title, the main objective of this work was to develop tools that can support the use of methyltransferases and be adaptable for other enzymatic methylations.

Biocatalysis operates at the intersection of multiple scientific fields. Nowadays, its successful application relies on integrating biology, process engineering, computer science, and chemistry. This frequently requires collaboration among teams with a range of expertise, and the willingness to adopt a generalist approach. The interdisciplinary approach to biocatalysis will be apparent in this work, as collaborations within multiple fields were crucial for understanding and using the targeted enzymes to their full potential. The relevance of the results obtained in this project within the local economy and the community has been assessed and (re)evaluated by participating in scientific conferences, innovation courses, and industry meetings. This had an important influence on the type of scientific questions I pursued, as I tried to align my research goals with the needs and context of the present time.

This work contains information and examples of methyltransferase applications from different perspectives: mechanistic, structural, biological and chemical. The importance of methyltransferase catalysis will be explored in the context of natural product diversification. I hope the data, techniques, and conclusions shared here can help establish a foundation for the broader use of methyltransferases as catalysts.

List of abbreviations

5′-CIDA – 5′-chloro-5′-deoxyadenosine
5-HT – 5-hydroxytryptamine
Abs – absorbance
AChE – acetylcholinesterase
ADP – adenosine diphosphate
AMP – adenosine monophosphate
Amp – ampicillin
API – active pharmaceutical ingredient
APP – amyloid β precursor protein
APS – ammonium persulfate
ATP – adenosine triphosphate
BChE – butyrylcholinesterase
BGC – biosynthetic gene cluster
BLAST – Basic Local Alignment Search Tool
BSA – bovine serum albumin
CC – creative commons
CDI – 1,1'-carbonyldiimidazole
CoA – coenzyme A
COMT – catechol *O*-methyltransferase
DBU – 1,8-diazabicyclo[5.4.0]undec-7-ene
DFT – density functional theory
DLS – dynamic light scattering
DMAB – dimethylaminobenzaldehyde
DMAP – 4-dimethylaminopyridine
DMAPP – dimethylallyl pyrophosphate
DMSO – dimethyl sulfoxide
DNA – deoxyribonucleic acid
dNTP – deoxyribonucleoside triphosphate
DTT – dithiothreitol
EDTA – ethylenediaminetetraacetic acid
Equiv. – equivalents
EtOAc – ethyl acetate
EV – empty vector
EZH2 – enhancer of zeste homolog 2
FACS – fluorescence-activated cell sorting
FAD – flavin adenine dinucleotide
FDA – U.S. Food and Drug Administration
FMN – flavin mononucleotide
HDAC6/8 – histone deacetylase 6/8
HIV – human immunodeficiency virus
HLM – human liver microsome
HMT – halide methyltransferase
HMT – halide methyltransferase
HPLC – high-performance liquid chromatography
HRMS – high-resolution mass spectrometry
HSMT – homocysteine S-methyltransferase
IBS – irritable bowel syndrome
IC_{50} – half-maximal inhibitory concentration
IGP - indole-3-glycerol phosphate
IPTG – isopropyl-β-D-thiogalactopyranosid
IR – infrared spectroscopy
ISM – iterative saturation mutagenesis
kDa – kilodalton
KIE – kinetic isotope effect
KP_i – potassium phosphate buffer
LB – lysogeny broth
LC – liquid chromatography
LLM – large language model
LogP – octanol-water partition coefficient
MAT – methionine adenosyltransferase
MD – molecular dynamics
MS – mass spectrometry
MTA - 5'-desoxy-5'-(methylthio)adenosine
NAD – nicotinamide adenine dinucleotide
NADP – nicotinamide adenine dinucleotide phosphate
NMR – nuclear magnetic resonance
NNMT – nicotinamide N-methyltransferase
NTA – nitriloacetic acid
OD – optical density
PAGE – polyacrylamide gel electrophoresis
PCR – polymerase chain reaction
PDB – protein data bank
PET – polyethylene terephthalate
PI3Kδ – phosphoinositide 3-kinase-δ
PIFA – phenyliodine bis(trifluoroacetate)
PiNPs - pyrroloindole-containing natural products
PKMT – protein-lysine methyltransferase
PLA – polylactic acid
PLP – pyridoxal phosphate
PPi – pyrophosphate
PRMT – protein-arginine methyltransferase
PRPP – phosphoribosyl pyrophosphate
PTFE – polytetrafluoroethylene
rcf – relative centrifugal force
RiPPs – ribosomally synthesized and post-translationally modified peptides
RNA – ribonucleic acid
rpm – revolutions per minute
rRNA – ribosomal ribonucleic acid
RT – room temperature
SAE – S-adenosylethionine
SAH – S-adenosylhomocysteine
SAM – S-adenosylmethionine
SAR – structure-activity relationship
SDS – sodium dodecyl sulfate
SOC – super optimal broth with catabolite repression
T4 – T4 *E. coli* phage virus
T_{50} – the temperature at which 50% enzymatic activity is lost
T7 – T7 bacteriophage
TB – terrific broth
TEA – triethylamine
TEMED – *N,N,N′,N′*-tetramethylethylenediamine
TFA – trifluoroacetic acid
TFAA – trifluoroacetic acid anhydride
THF – tetrahydrofolate

TLC – thin layer chromatography
TMS – tetramethylsilane
TRIS – tris(hydroxymethyl)aminomethane

Abstract

The biosynthesis of the acetylcholinesterase (AChE) inhibitor physostigmine was described for the producing organism *Streptomyces griseofuscus*, and it was found to include a stereoselective methylation step catalyzed by the SAM-dependent methyltransferase PsmD, which determines the configuration of the final compound and triggers the formation of the specific pyrroloindole ring. Several PsmD product analogs have already demonstrated AChE inhibition, making the structural diversification of PsmD products an intriguing prospect, as it provides potential for identifying new drug candidates to treat related neurological disorders. A new PsmD-like indole *C*-methyltransferase was identified, originating from *Streptomyces albulus (noursei)* (PsmD_*Sa*). The enzyme was expressed and analyzed regarding structure, mechanism and biochemical properties. The biochemical analysis revealed a higher stability, compared to its previously characterized homolog from *Streptomyces griseofuscus* (PsmD_*Sg*), while maintaining the stereoselectivity of the methylation reaction. The crystal structure of PsmD_*Sg* was determined experimentally using X-ray spectroscopy in collaboration with Prof. Dr. Oliver Weiergräber (IBI-7: Structural biochemistry, Forschungszentrum Jülich) and used as a template for the precise *in silico* modeling of the PsmD_*Sa* structure. Site-directed mutagenesis was used to map the catalytic site and elucidate the mechanism of PsmD_*Sa*. The results were corroborated with molecular docking and molecular dynamic simulations performed by Dr. Benoit David (IBG-4: Bioinformatics, Forschungszentrum Jülich), offering an overview of the PsmD catalysis. A mobile N-terminal "lid" was identified, playing a crucial role in triggering the catalytic process after the binding of the substrate and the cofactor. A Glu-His-Tyr catalytic triad was found to activate the substrate through a proton shuttling action.

The semi-rational engineering of PsmD_*Sa* led to the improvement of its activity towards bulky non-natural indole-containing substrates. Five positions in the catalytic site were targeted in a sequential manner through site saturation mutagenesis, producing focused mutant libraries. To generate and screen the resulting mutant libraries, the AutoBioTech integrated laboratory platform was utilized in collaboration with Dr. Julia Tenhaef (IBG-1: Biotechnology, Forschungszentrum Jülich). A modular approach was designed to automate the enzyme expression, enzymatic reactions and activity screening in 96-well microtiter plates. A new high-throughput colorimetric assay for indole detection was developed for the efficient screening of the resulting mutant libraries. The assay allows the detection of the PsmD substrate concentration in the presence of the isolated enzyme, as well as using whole-cell biocatalysts. The engineering and screening of the PsmD_*Sa* variants led to the identification of new

mutants with significantly improved activity for the tested substrates, and the key position 166 was found to play an important role in the productive binding of bulky substrate derivatives.

The site-directed mutagenesis of PsmD_*Sa* aimed to expand its alkylation capacity using an ethylated SAM cofactor derivative (SAE). Two enzymatic SAE supply systems were used in cascade with PsmD_*Sa* and the new mutants. The coupled PsmD_SAE supply systems were optimized, leading to a 7-fold improvement of PsmD-catalyzed conversion to the ethylated product using the wild-type enzyme. Two mutants, A125G and F126L performed better than the wild type in the reactions using several SAM cofactor derivatives.

Finally, the preparative enzymatic methylation catalyzed by PsmD_*Sa* was achieved using different enzyme formulations: lysates, whole cells and immobilized enzymes. The reactions were carried out in combination with a cofactor recycling system and the stereoselective methylation was successfully achieved using various substrates and enzyme variants, in scales up to hundreds of milligrams. Overall, this study aimed to provide new insights into the practical aspects of methyltransferase biocatalysis and showcase the potential of PsmD_*Sa* as a useful tool for the stereoselective *C*-methylation of indole derivatives.

Kurzzusammenfassung

Die Biosynthese des Acetylcholinesterase (AChE)-Hemmers Physostigmin wurde für den produzierenden Organismus *Streptomyces Griesofuscus* beschrieben, und es wurde festgestellt, dass sie einen stereoselektiven Methylierungsschritt umfasst, der durch die SAM-abhängige Methyltransferase PsmD katalysiert wird, die die Konfiguration der Endverbindung bestimmt und die Bildung des spezifischen Pyrroloindolrings auslöst. Mehrere Analoga von PsmD-Produkten haben bereits eine Hemmung von AChE gezeigt, was die strukturelle Diversifizierung von PsmD-Produkten zu einer interessanten Perspektive macht, da sie das Potenzial zur Identifizierung neuer Arzneimittelkandidaten zur Behandlung verwandter neurologischer Erkrankungen bietet. Es wurde eine neue PsmD-ähnliche Indol-*C*-Methyltransferase identifiziert, die aus *Streptomyces albulus* (*noursei*) stammt (PsmD_*Sa*). Das Enzym wurde exprimiert und auf Struktur, Mechanismus und biochemische Eigenschaften hin analysiert. Die biochemische Analyse ergab eine höhere Stabilität im Vergleich zu seinem zuvor charakterisierten Homologen aus *Streptomyces griseofuscus* (PsmD_*Sg*), wobei die Stereoselektivität der Methylierungsreaktion erhalten blieb. Die Kristallstruktur von PsmD_*Sg* wurde in Zusammenarbeit mit Prof. Dr. Oliver Weiergräber (IBI-7: Strukturelle Biochemie, Forschungszentrum Jülich) experimentell mittels Röntgenspektroskopie bestimmt und als Vorlage für die präzise in silico Modellierung der PsmD_*Sa* Struktur verwendet. Mittels ortsgerichteter Mutagenese wurde die katalytische Stelle kartiert und der Mechanismus von PsmD_Sa aufgeklärt. Die Ergebnisse wurden durch molekulares Docking und molekulardynamische Simulationen von Dr. Benoit David (IBG-4: Bioinformatik, Forschungszentrum Jülich) untermauert, die einen Überblick über die PsmD-Katalyse bieten. Es wurde ein beweglicher N-terminaler „Deckel“ identifiziert, der eine entscheidende Rolle bei der Auslösung des katalytischen Prozesses nach der Bindung des Substrats und des Cofaktors spielt. Es wurde festgestellt, dass eine katalytische Glu-His-Tyr-Triade das Substrat durch eine Protonen-Shuttle-Aktion aktiviert.

Das semi-rationale Engineering von PsmD_*Sa* führte zur Verbesserung seiner Aktivität gegenüber sperrigen, nicht-natürlichen indolhaltigen Substraten. Fünf Positionen in der katalytischen Stelle wurden nacheinander durch Sättigungsmutagenese angepeilt, wodurch gezielte Mutantenbibliotheken entstanden. Zur Generierung und zum Screening der resultierenden Mutantenbibliotheken wurde die integrierte Laborplattform AutoBioTech in Zusammenarbeit mit Dr. Julia Tenhaef (IBG-1: Biotechnologie, Forschungszentrum Jülich) eingesetzt. Ein modularer Ansatz wurde entwickelt, um die Enzymexpression, enzymatische Reaktionen und das Aktivitätsscreening in 96-Well-Mikrotiterplatten zu automatisieren. Für das effiziente Screening der resultierenden Mutantenbibliotheken wurde ein neuer kolorimetrischer

Hochdurchsatz-Assay zum Indol-Nachweis entwickelt. Der Assay ermöglicht den Nachweis der PsmD-Substratkonzentration in Gegenwart des isolierten Enzyms sowie unter Verwendung von Ganzzell-Biokatalysatoren. Das Engineering und Screening der PsmD_*Sa*-Varianten führte zur Identifizierung neuer Mutanten mit deutlich verbesserter Aktivität für die getesteten Substrate, und es wurde festgestellt, dass die Schlüsselposition 166 eine wichtige Rolle bei der produktiven Bindung sperriger Substratderivate spielt.

Die ortsgerichtete Mutagenese von PsmD_Sa zielte darauf ab, seine Alkylierungskapazität unter Verwendung eines ethylierten SAM-Cofaktor-Derivats (SAE) zu erweitern. Zwei enzymatische SAE-Versorgungssysteme wurden in Kaskade mit PsmD_*Sa* und den neuen Mutanten verwendet. Die gekoppelten PsmD_SAE-Versorgungssysteme wurden optimiert, was zu einer 7-fachen Verbesserung der PsmD-katalysierten Umwandlung zum ethylierten Produkt unter Verwendung des Wildtyp-Enzyms führte. Zwei Mutanten, A125G und F126L, schnitten bei den Reaktionen mit verschiedenen SAM-Cofaktor-Derivaten besser ab als der Wildtype.

Schließlich wurde die von PsmD_*Sa* katalysierte präparative enzymatische Methylierung mit verschiedenen Enzymformulierungen durchgeführt: Lysate, ganze Zellen und immobilisierte Enzyme. Die Reaktionen wurden in Kombination mit einem Cofaktor-Recycling-System durchgeführt, und die stereoselektive Methylierung wurde erfolgreich mit verschiedenen Substraten und Enzymvarianten in Größenordnungen bis zu Hunderten von Milligramm erreicht. Insgesamt sollte diese Studie neue Erkenntnisse über die praktischen Aspekte der Methyltransferase-Biokatalyse liefern und das Potenzial von PsmD_*Sa* als nützliches Werkzeug für die stereoselektive *C*-Methylierung von Indolderivaten aufzeigen.

1. Introduction

1.1 The role of biocatalysis

In 2015, the United Nations adopted the 2030 Agenda for sustainable development, containing seventeen goals, as a plan of action for addressing the most pressing challenges of humanity, with the target to improve people's lives at a global level.[4] Climate and sustainability are the underlying themes of six of the seventeen targets, with a holistic approach recognized as necessary for solving one of the biggest challenges that humanity is currently facing. This implies that scientific and technological innovations are a critical necessity and that they must be combined with societal and political actions. The current realities require that new technologies are developed with sustainability as a key parameter.

The chemical industry needs to be part of the transformation. According to a 2023 study, the 12 largest chemical parks in Germany produced around 23 Mt CO_2 in 2022, which corresponds to 14% of the emission from the entire industrial sector, and 3% of the overall national CO_2 emission.[5] The majority of emissions originate from energy production and can be lowered by shifting to sustainable energy sources. However, the impact of modifying the chemical processes themselves should not be understated, particularly in the production of bulk chemicals and building blocks, as they often rely on fossil-based raw materials and demand substantial energy in the first place. Chemical synthesis routes are continuously evolving, and the advent of green chemistry has produced important developments. Including biocatalysis in organic synthesis pathways holds significant potential for the development of a wider range of green chemistry solutions.

The idea of using biological entities for the production of chemicals has been around for thousands of years, since humans discovered fermentation as a means of food production. The scientific study and use of enzymes as catalysts started in the 19th century and took off once the understanding of DNA structure and function was achieved in the 1950s.

Table 1. The UN 17 sustainable development goals. The goals related to the environment and sustainability are highlighted.

1. No poverty	10. Reduced inequalities
2. Zero hunger	11. Sustainable cities and communities
3. Good health and well-being	12. Responsible consumption and production
4. Quality education	13. Climate action
5. Gender equality	14. Life below water
6. Clean water and sanitation	15. Life on land
7. Affordable and clean energy	16. Peace, justice and strong institutions
8. Decent work and economic growth	17. Partnerships for the goals
9. Industry, innovation and infrastructure	

The development of genetic engineering tools and recombinant DNA technology in the 1970s had a great impact on the field of biocatalysis, and companies started to use enzymes as part of their processes.[6] Currently, biocatalysis has become an effective solution for enabling selective and sustainable chemical transformations and has applications in industries such as pharmaceutical, agriculture, medicine, food chemistry or plastic production. Recent trends in the field involve the expansion of the biodiversity of known enzymes, the improvement through protein engineering and the integration of artificial intelligence for streamlining the discovery and modification of enzymes. Although the implementation of enzymes as catalysts has an almost two-century-long history, its large-scale application is still often side-lined, in favor of traditional synthetic routes. Enzymes offer excellent selectivity for synthesizing complex molecules. However, challenges such as low stability, high production costs, and long development times have limited the widespread use of biocatalysis. A notable issue that cannot be overlooked is also the reluctance to change already established processes. Nevertheless, the research and optimization of enzymatic processes hold great potential. The inherent milder functioning conditions of enzymes could offer an environmentally friendly alternative for many chemical processes. Besides their utility as selective catalysts for the production of valuable chemicals, enzyme technologies are being developed as potential solutions for other societal issues. Applications such as plastic recycling, carbon capture, or the development of new medicines are promising directions of this technology.

Furthermore, biocatalysis can play an important role in drug development. As medical advancements continue to broaden the range of available treatments for various diseases, the demand for new therapeutics remains a constant focus of research. The elucidation of new disease mechanisms, combined with the development of drug resistance, drives a continuous need for new drugs. Diseases are evolving, and pharmaceutical and medical science needs to keep up. Enzymes play an important role in the development of new drugs from two different perspectives: as targets or as catalysts for the production of new biologically active molecules.

The pharmaceutical industry has been the leading adopter of biocatalysis in the research and production of new therapeutics.[6, 7] This is largely due to the industry's requirement for producing complex molecules, which greatly benefits from the high selectivity of enzymatic reactions. Additionally, many small-molecule drugs are derived from natural products. The use of nature's own methods for producing them can be a powerful strategy.[8] The role of natural products and biocatalysis in drug discovery will be explored in detail in Chapter 2.

1.2 Topic introduction and objectives

Methylation is an important synthetic tool in medicinal chemistry, due to the ability of the methyl group to modulate the pharmacological properties of small molecule drugs.[9] Late-stage methylation is difficult to achieve chemically in a selective fashion. This led to the recent emergence of enzymatic methylation options, offering an attractive alternative.[10] SAM-dependent small molecule methyltransferases are involved in the biosynthesis of a plethora of secondary metabolites, displaying a wide range of target molecular scaffolds and superior chemo-, regio- and stereoselectivities. The use of methyltransferases as catalysts for natural product and drug production is currently limited by the low number of studied enzymes and the practical challenges of their implementation and scaling.[11, 12]

The general objective of this project was the development and implementation of an enzymatic methylation toolbox that can address the structural diversification of the AChE inhibitor physostigmine, using the *C*-methyltransferase PsmD from *Streptomyces albulus* (Figure 1). The following topics were addressed:

- Structural and mechanistic study

As more methyltransferase structures are uncovered, shared properties become apparent. The discovery of common mechanistic features not only enhances our understanding of enzymatic methylation but also influences the practical use of these enzymes as catalysts. The elucidation of new structures and their connection to a diversity of functions is necessary for the broader application of this enzyme class.

- Use of the structural knowledge for enzyme engineering

Enzyme engineering is a powerful method for the optimization of biocatalysts. New techniques in molecular biology are still emerging, and the prerequisite for resource-efficient engineering is the understanding of the target biocatalyst and the characteristics of different mutagenesis approaches.

- Establishment of a time and cost-efficient process for the screening of mutant libraries

The screening of large mutant libraries is a crucial part of enzyme engineering through directed evolution. Significant effort and optimization are usually necessary for an efficient screening process. Recent advancements in lab automation, analytical techniques and process design are useful for identifying and producing improved biocatalysts.

- Expansion of the catalysis scope

The high selectivity of enzymes is their greatest strength, but can also be an obstacle in the the way of many target transformations. Expanding the catalysis scope is one of the main targets of enzyme and reaction engineering efforts. For methyltransferases, this can mean either the expansion of the substrate scope or the modification of the transferred group by producing and incorporating cofactor analogs.

- Optimization of the preparative enzymatic reaction

The scalability of enzymatic processes is a prerequisite for their use as catalysts for the production of chemicals. There are specific challenges associated with the scaling of enzymatic reactions, such as the stability, substrate loading, and efficiency. Addressing these challenges often requires extensive optimization, tailored to each specific process type.

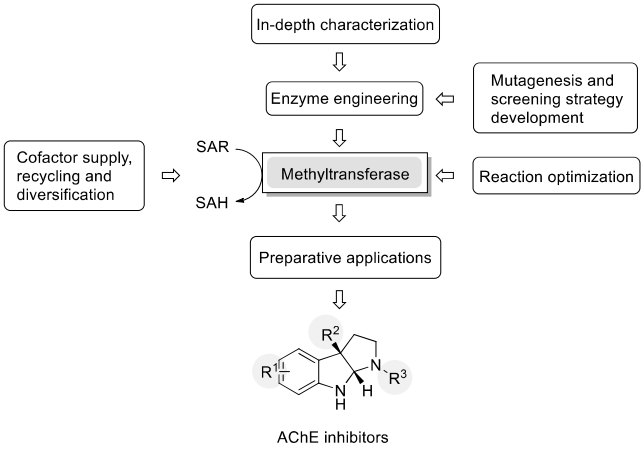

Figure 1. Overview of the topics covered in this project and their interconnection.

2. State of the art

2.1 Natural products and their role in drug discovery

Natural products are molecules produced by living organisms, and include a large part of known bioactive compounds. Harnessing natural products for medical treatment is as old as human society. The first medical attempts in history involve the use of medicinal plants and their extract for the treatment of wounds or infectious diseases. The use of the willow plant (*Salix* sp.), containing salicylic acid, for its analgesic properties was documented in ancient Egypt.[13, 14] Some other early examples of natural products used as medicines include morphine (poppy juice, analgesic), penicillin (bread and cheese moulds, antibiotic), curcumin (turmeric, anti inflamatory) and tetracyclines (*Steptomyces* sp. growing on grains, antibiotic).[15-19]

Natural products often contain privileged structural motifs, which evolved to preferentially interact with various protein targets. In modern times, their diversity in structure and therapeutic effects make them an important source of inspiration for the design and optimization of pharmaceuticals.[20-23] Natural products and their derivatives correspond to approx. 31% of all the FDA (U.S. Food and Drug Administration) approved small molecule drugs between 1981 and 2019, while another 35% are synthetic drugs, which mimic natural products or include a natural product pharmacophore (Figure 2). They are represented across all therapeutic groups, with the most significant occurence in antibacterial drugs, where they correspond to 68% of FDA approved drugs up to 2019.[8]

2.1.1 Secondary metabolites identification

The search for natural products as drug candidates is challenging due to the complexity of the biological mixtures. After a peak in the 1990's, they have lost popularity as inspiration for drug development, with the advent of combinatorial chemistry and the creation of "synthetically friendly" compound libraries for high-throughput screening.[24] Other reasons for this decline include the decreasing emphasis on the treatment of infectious diseases in the pharmaceutical industry, which was the main stronghold for natural products, and the difficulties in collecting biological samples, in the context of the international agreements for the movement of biomaterials.[25, 26] However, the blind screening of extensive combinatorial chemistry libraries did not yield the expected number of viable drug candidates, rekindling the interest in natural

products as scaffolds in recent years.[8, 24, 27] The need for new natural product scaffolds was met by the discovery and characterization of new biosynthetic gene clusters and the use of enzymes for their synthesis and diversification.[28, 29]

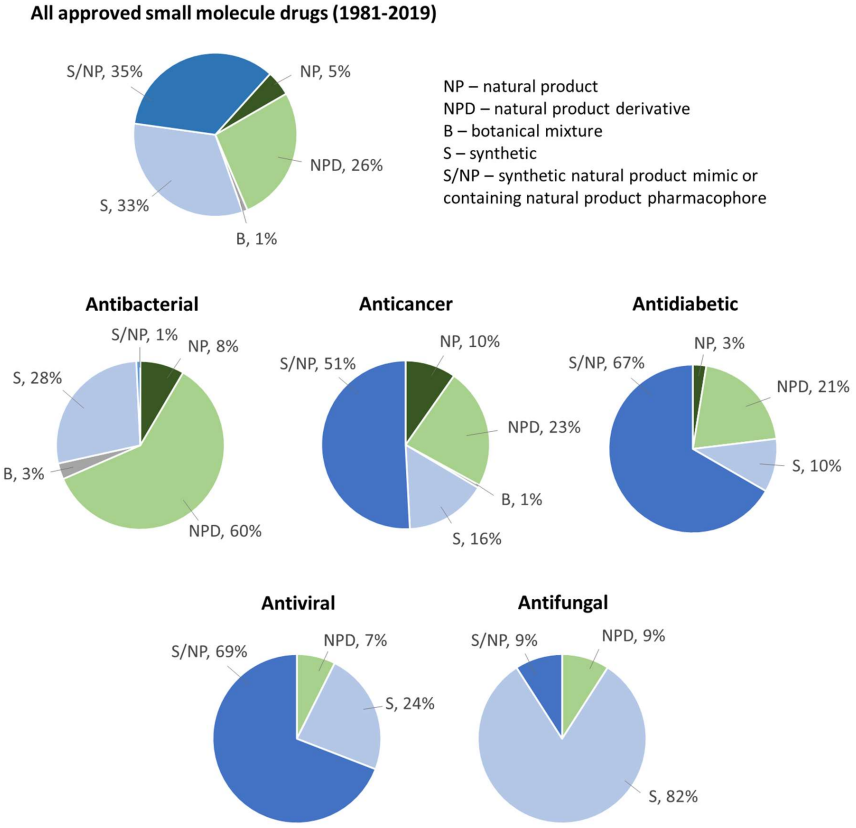

Figure 2. Sources of small molecule drugs approved by the FDA between 1981 and 2019 and their distribution among several different therapeutic classes. The data was compiled from a 2020 review.[8] The percentages were calculated and depicted only for the small molecule drugs. Other drug classes such as vaccines and biological macromolecules are not shown.

The large-scale isolation and synthesis of natural products and their derivatives is experimentally challenging due to their frequently complex structures. Computational tools can help reduce the experimental demands, while the development of machine learning and natural language processing tools help predicting the bioactivity of natural products, as well as their potential targets.[30, 31] Such tools are used for metabolome mining and the identification

of new biosynthetic routes (e.g. AntiSMASH,[32] PRISM,[33] ClusterFinder,[34] DeepBCG[35] and GECCO[36]), the elucidation of natural product structures out of analytical data from complex mixtures (e.g. SMART 2.0,[37] SMART-Miner[38] and COLMAR[39]) and for bioactivity prediction (e.g. SPiDER,[40] and RESFinder[41]). In some cases, these approaches also helped clarify the mechanism of action of bioactive natural products.[42] These tools can also help recognize molecular patterns and their role in biological interactions, streamlining the design of new derivatives inspired by natural products.[43-45]

2.1.2 Privileged scaffolds

Fragment-based drug discovery relies on the identification of small molecular frameworks, which can bind to target proteins and can then be optimized and combined for the development of new, more effective therapeutics. This strategy helped expanding the chemical space available in high-throughput compound screening, while reducing the synthetic efforts. It also helped circumvent some of the issues associated with traditional drug discovery from natural products, such as the high toxicity and low production efficiency.[46, 47] In order to reduce the size of screening libraries, structural and physico-chemical criteria such as Lipinski's "rule of five" or the "rule of three" were proposed, refering to the role of the lipophilicity, size, flexibility and functional groups of potential drug molecules on their bioavailablility and efficacy.[48-50] Although they are widely used in drug discovery and development, natural products with beneficial biological activities were also identified outside this space. For example, some antibiotics, antifungals, vitamins and cardiac glycosides tend to violate the rule of five.[51-53]

The scaffolds present in natural products are often considered privileged for the construction of compound libraries for fragment discovery. One point of interest is that fragments of natural products are often rich in stereogenic centers, providing access to a structural diversity that synthetic molecules typically do not provide.[54] The "privileged scaffold" term was introduced after observing that certain structural fragments appeared independently in hits of distinct drug discovery projects.[55-57] It is important to note that beyond biological activity, hits can also be attributed to phenomena such as unspecific activity, caused by reactive functional groups, the presence of multi-target promiscuous binders (such as tetrahydrofuran, pyrrolidine or benzene), or pan-assay interference leading to false positives.[28, 58-60] However, promiscuous ligands that can effectively bind to multiple macromolecular targets exist, and they occur frequently enough to earn special consideration as frameworks for compound library development. As such, they can serve as starting points for the design of new therapeutics and help streamline the drug development process. Heterocyclic scaffolds are common among

known privileged structures in drugs and natural products, with examples including quinoline, indole, purine, benzofuran, coumarin or benzothiophene. Other ring systems such as steroids or biphenyls are also common motifs in approved drugs. [61]

Natural products can serve as an excellent inspiration for new privileged scaffolds due to their structural diversity and complexity.[28, 61] Biologically active natural products generally contain more sp^3-hybridized atoms and stereogenic centers, compared to synthetic drugs, with fewer nitrogen but more oxygen atoms and a propensity for aliphatic rings, instead of aromatic.[62] A computational study from 2017 analyzed millions of bioactive compounds in order to assess the prevalence of certain structural trends and found that heterocyclic sp^3-rich molecular scaffolds are particularly well suited for drug candidate library design.[55] As the importance of the three-dimensionality of ligands on biological activity became more apparent for lead library design, inspiration can be drawn from the variety of multi-ring systems found in natural products. [28, 63-66]

2.1.3 Indoles as privileged scaffolds

The indole ring is documented as a privileged structural building block in medicinal chemistry.[67] Many biologically active natural products contain indole as the main pharmacophore. Its accessible structural modifications and the variety of available side chains and functionalities make it adaptable for a diverse range of therapeutic targets. Due to the high π-electron density and delocalization, it readily undergoes electrophilic substitution. In particular, the 3-position has the highest electron density and the highest tendency for electrophilic substitutions.[68] The structure-activity relationship (SAR) of drugs containing indoles was thoroughly documented in the treatment of malaria, Alzheimer's disease, diabetes, Parkinson's, hypertension, arrhytmia, migraine, tuberculosis, HIV infection and different types of cancer.[68, 69]

The indole ring is a fundamental part of important biological building blocks and signal molecules, such as tryptophan, serotonin and melatonin. The biosynthesis of most natural indole alkaloids is based on the functionalization of L-tryptophan.[70, 71] In plants and microorganisms, tryptophan biosynthesis usually uses anthranilate (**1**) as a precursor. An anthranilate-phosphoribosyl transferase forms the *N*-(5-phosphoribosyl)-anthranilate (**2**), and an isomerase catalyzes the formation of 1-(2-carboxyphenylamino)-1-deoxy-D-ribulose-5-phosphate (**3**). The indole ring is formed through the decarboxylation and intramolecular cyclization of **3** in a reaction catalyzed by indole-3-glycerol phosphate (IGP) synthase. The tryptophane synthase α subunit cleaves the 3-phosphoglyceraldehyde rest, forming simple

indole (**5**). Finally, a substitution of the 3-position with serine is catalyzed by the tryptophane synthase subunit β, forming L-tryptophan (**6**) (Scheme 1).[72] The industrial production of tryptophan from indole is often fermentative, using the biosynthetic pathways of production organisms such as *Escherichia coli* and *Corynebacterium glutamicum*.[73, 74]

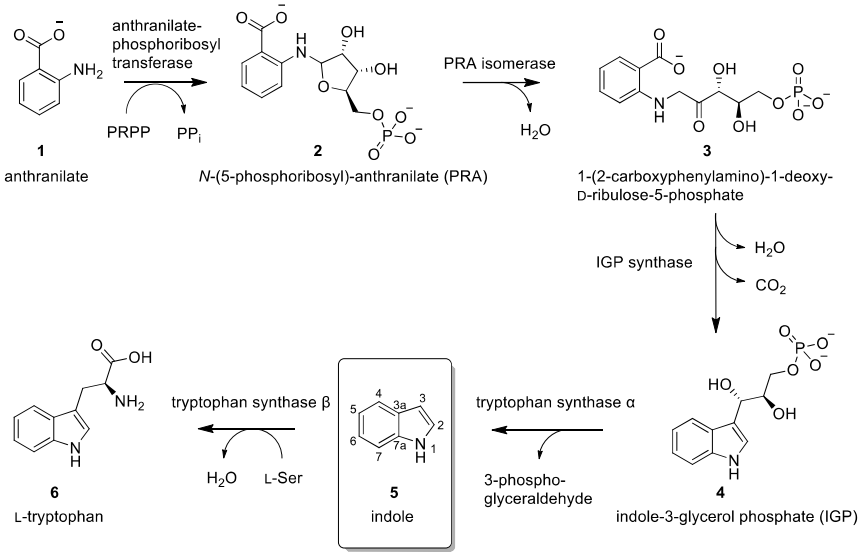

Scheme 1. Indole formation as part of the tryptophan biosynthesis.

The indole ring is traditionally synthesized using the Fischer indole synthesis from aryl hydrazones, at high temperatures, in the presence of Brønsted or Lewis acids (Scheme 2).[75-77] Newer methods for the synthesis of substituted indoles include the electrochemical intramolecular amination of 2-vinyl anilines,[78] the oxidative cyclization of 2-alkenyl anilines in the presence of phenyliodine bis(trifluoroacetate) PIFA,[79] the Pd-catalysed indole synthesis from cyclohexanones in the presence of ethylene and ammonium acetate,[80] and the Pd-catalyzed annulation of anilines with bromoalkynes.[81]

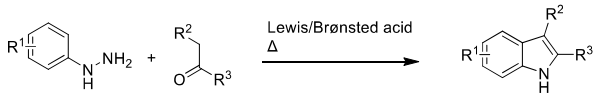

Scheme 2. Indole formation using the Fischer indole synthesis.

Alkaloids are heterocyclic secondary metabolites, containing one or more nitrogen atoms and are usually derived from amino acids. An analysis of the “Dictionary of natural products” from 2019 determined that alkaloids are one of the most represented classes of known natural products and are distributed across all kingdoms of life. They are about 20% of natural products of bacterial origin and approx. 15% of plant-derived natural products.[82] Within this structural family, indole alkaloids are a prominent class of biologically active natural products, displaying a wide range of bioactivity and structural diversity. New indole alkaloids are still identified and isolated from various species, displaying bioactivities such as antimicrobial, antioxidant, antimalarial, anti-inflammatory and antifungal.[83]

5-HT receptor inhibitors

A particularly interesting function of indole alkaloids is their involvement in neurological regulation. Serotonin is an indole-containing neurotransmitter, involved in regulating multiple biological processes such as sleep, mood, appetite, learning, sexual function, memory and anxiety. Serotonin receptors have been associated with neurological conditions such as psychosis, anxiety, schizophrenia, or depression, making them important targets for the development of new therapeutics.[84] In recent years, they were also proposed as therapeutic targets for autism,[85] epilepsy[86] and Alzheimer’s disease.[87] Many of the active serotonin receptor agonists and antagonists are serotonin derivatives. This showcases the value of further exploring the available structural diversity of these compounds, as potential new drug candidates.[88] An important class of serotonin-derived drugs are triptans, used mainly for the treatment of migraines (Figure 3).[89, 90] Other indole-containing approved drugs targeting the serotonin (5-HT) receptors display a variety of therapeutic actions, and include vilazodonefor for the treatment of depression,[91] pindolol for hypertension,[92] lisuride for the treatment of Parkinson’s disease,[93] alosetron - treating irritable bowel syndrome (IBS),[94] ondansetron against nausea induced by chemotherapy[95] and the antipsychotic sertindole (Figure 3).[96] In general, the effects of serotonin receptors and their interactions on the human organism are still not fully understood. Their structures and mechanisms of action, as well as the inhibitory mechanisms of 5-HT targeting drugs and drug candidates are currently an important subject of research and discovery, illustrated by the abundance of studies in recent years. Even within already approved drugs, overlapping biological effects are still occurring, mostly as side effects, but sometimes providing alternative therapeutic actions.[97] As serotonin plays a role in the modulation of many biological functions, the diversification of its molecular scaffold holds promise for the discovery of new bioactive compounds.

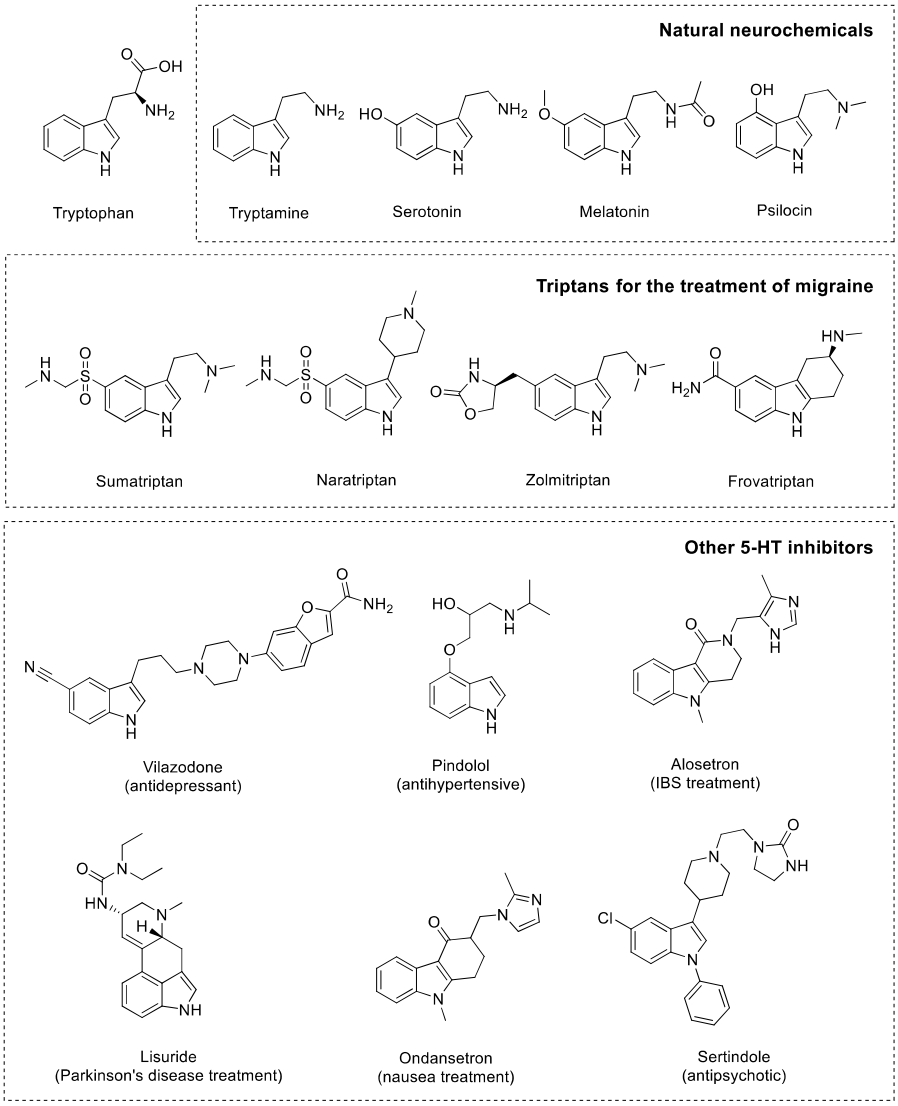

Figure 3. Structures of indole containing natural neurochemicals and examples of approved 5-HT receptor inhibitor drugs with their therapeutic uses.

2.1.4 Pyrroloindoles

Pyrroloindoles are a special class of indole derivatives containing the hexahydropyrrolo[2,3-b]indole motif (Figure 4), and are present in a variety of biologically active natural products, including antibiotics, antitumor agents, or cholinesterase inhibitors.[98] They are usually biosynthesized starting from the amino acid tryptophan, in sequences including cleavage, oxidation and cyclization reactions, leading to a variety of pyrroloindoline analogs. Within these sequences, a key recurring step is an enzymatically catalyzed group transfer on the C3-indole position of tryptamine derivatives, which triggers the intramolecular cyclization driven by the nucleophilic attack of the amine side chain on the C2 of the indole.[99] Multiple enzyme classes are known to produce pyrroloindoles from indole substrates, including monooxygenases,[100-103] cytochromes P450,[104] methyltransferases[105, 106] and prenyltransferases.[107-109]

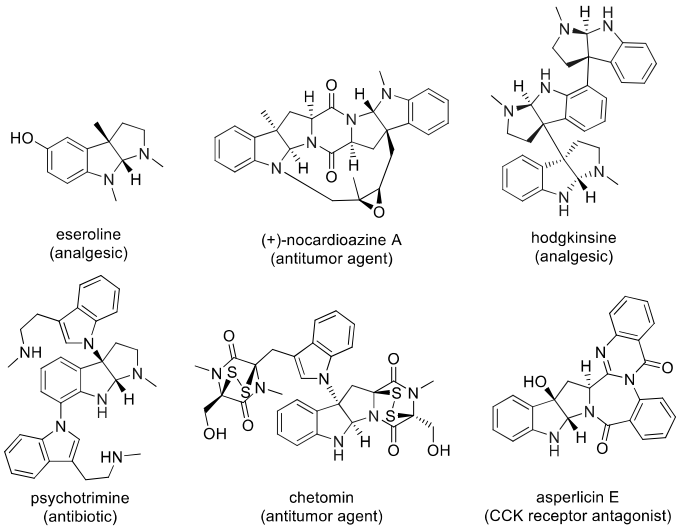

Figure 4. Examples of compounds containing the pyrroloindole structural motif and their biological activity

Based on the substituents on the C3 position, pyrroloindole-containing natural products (PiNPs) have been classified into five categories (Figure 5): type A (no substituent), type B (hydroxyl), type C (alkyl), type D (aryl) and type E (another pyrroloindole unit).[99] Type A PiNPs are relatively rare, compared to the other types. The representatives of this class belong to the newly explored class of ribosomally synthesized and post-translationally modified peptides (RiPPs). Although their intriguing structures have prompted the development of several total

synthesis routes, the scope of their biological activities remains largely unknown.[110] The biosynthetic pathway of crocagin A was identified, and it was proposed that the protonation in the C3-position occurs after or in parallel with the oxidation by the dioxygenase CgnC.[111, 112] Ultimately, at the time of this work it is still unclear what kind of enzymes are responsible for the pyrroloindole scaffold formation in the case of type A PiNPs. Consequently, uncovering the biosynthetic mechanism for pyrroloindole formation in this case is an exciting prospect for future research.

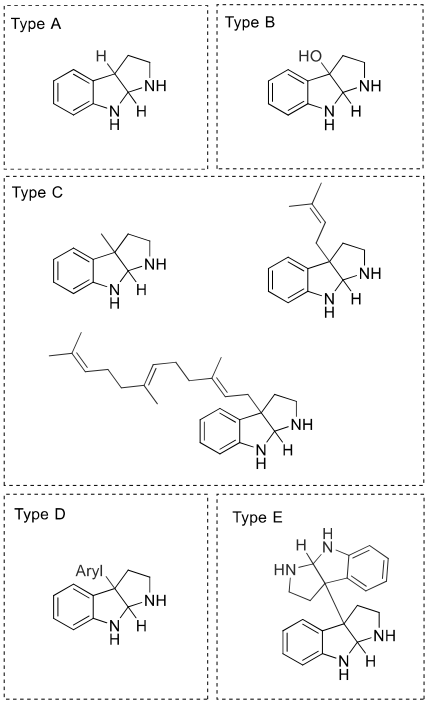

Figure 5. The classification of pyrroloindole-based natural products: type A-E, based on their structure.

There is more information about the enzymatic routes for the biosynthesis of types B, C, D and E, as the elucidation of the biosynthetic gene clusters (BGCs) of multiple pyrroloindole-containing natural products was achieved in recent years. In type B okaramine,[113] himastatin,[104] and asperlicin E,[114] flavin-dependent monooxygenases or cytochromes P450 catalyze the 2,3-epoxidation of the indole, which leads to the subsequent intramolecular cyclization. In the case of type C, the enzymatic transfer of methyl (physostigmine,[105] nocardioazine A[106, 115]), prenyl (acetylaszonalenin,[116] ardeemin[107]) or farnesyl

(drimentine[117]) triggers the pyrroloindole-forming intramolecular cyclization. Type D PiNPs can be divided into C3-indole substituted and C3-purine substituted. New information about the biosynthesis of naseseazine[118] and tetratryptomycin B[119] revealed that the pyrroloindole is formed through a radical mechanism in a reaction catalyzed by P450 enzymes. Similarly, the dimerization and pyrroloindole formation in type E compounds dibrevianamide[120] and (**−**)-ditryptophenaline[120] is catalyzed by cytochromes P450 through the formation of indole radicals.

The stereospecific synthesis of chiral pyroloindoles is challenging using chemical synthesis and is most often performed using transition metal catalysts and chiral ligands.[98] Biomimetic approaches were developed, focusing on the catalytic asymmetric dearomatization of indoles, comprising most of the synthetic pathways reported in the literature. In this case, the reactions start from tryptophan, tryptamine or their derivatives in the presence of various electrophiles. The pyrroloindole ring is formed after the transfer of functional groups on the 3-position of the indole ring, triggering the subsequent intramolecular cyclization (Scheme 3A). The formation of the pyrroloindoles can be achieved by chemical alkylation, allylation, arylation, amination, hydroxylation, or halogenation. Additionally, pyrroloindole synthesis can also be achieved through intramolecular dearomatization-cyclization cascades. The biomimetic approach allows for the incorporation of various electrophiles, expanding the chemical and structural diversity of the available pyrroloindoles.[121-123] Another path to the creation of the pyrroloindole ring includes the catalytic dearomative [2+3] cycloaddition of indoles in the presence of carbon-carbon-nitrogen (CCN) 1,3-dipoles (Scheme 3A).[124] Substituted anilines, bearing an activated alkene, can also be used as substrates instead of indoles, using isocyanoacetates in addition-cyclization reactions (Scheme 3B).[125] An alternative approach uses 3,3-disubstituted oxindoles as precursors in reductive cyclizations, yielding pyrroloindoles (Scheme 3C).[126, 127] Finally, a more recent synthesis route towards chiral pyrroloindoles uses indoline imines as substrates in a stereoselective iridium-catalyzed double allylation followed by a reduction (Scheme 3D).[121, 128, 129]

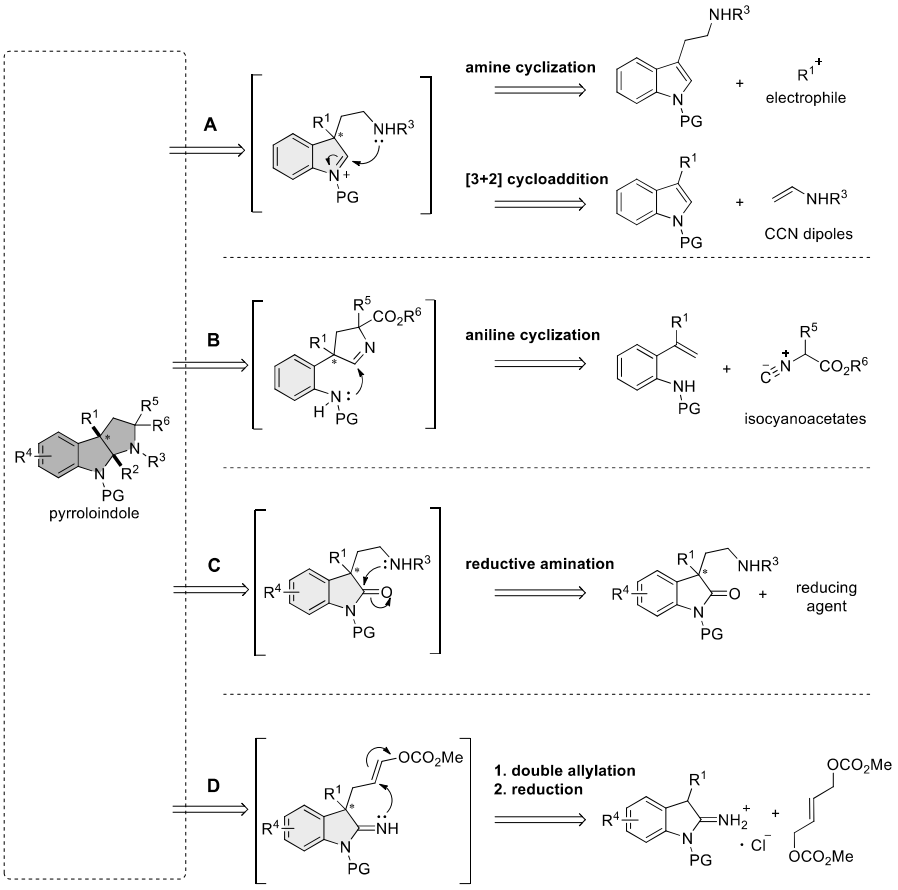

Scheme 3. Overview of several chemical synthetic paths for the stereoselective synthesis of pyrroloindoles. The mechanism for the formation of the pyrroloindole ring is illustrated for each case. **A**. Intramolecular cyclization of tryptamine derivatives after the addition of an electrophile or after the [3+2] cycloaddition of CCN dipoles to indoles. **B**. Formation and intramolecular cyclization of substituted anilines containing activated alkenes. **C.** Intramolecular reductive amination of 3-substituted oxindoles. Under acidic conditions, a water molecule is eliminated after the amination. **D**. The double allylation of indoline imines followed by a separate reduction step produces the pyrroloindoline scaffold. PG=protecting group.

The rigid framework of the pyrroloindoles, combined with the availability of a variety of functionalization options, make this scaffold an attractive template for the development of new drug candidates. The prevalence of pyrroloindoles in natural products displaying biological activity is a promising hint towards the potential of these compounds as new therapeutic agents. Considerable efforts were dedicated to the stereoselective generation of this scaffold

through chemical synthesis. The enzymatic asymmetric synthesis of pyrroloindoles presents a potentially greener alternative, enabled by the ongoing advancements in the discovery, characterization, and application of pyrroloindole-forming enzymes.

2.1.5 AChE inhibitors

Acetylcholinesterase is a hydrolase with a crucial biological role in the nervous system of many organisms, regulating the quantity and effects of the acetylcholine neurotransmitter. The enzyme catalyzes the fast hydrolysis of acetylcholine at the synaptic junctions, terminating acetylcholine-mediated neurotransmission. Maintaining precise neuronal signals is essential for cognitive function and muscle contraction. The inhibition of acetylcholinesterase leads to an accumulation of acetylcholine in the synapses, resulting in an elongated stimulation of muscles and nerves. This can lead to cholinergic poisoning, with symptoms such as muscle twitching, respiratory issues, seizures and eventually death. The accumulation of acetylcholine in the nervous system can be caused by nerve agents or organophosphates and is usually treated using competitive reversible inhibitors.[130, 131] Butyrylcholinesterase is a similar, albeit less specific enzyme, which can also hydrolyze acetylcholine and can serve as a decoy target for natural anticholinergic compounds. While AChE is predominantly found in the synaptic cleft of neurons, BChE is more abundant in plasma, liver and lungs, and displays a broader substrate scope, detoxifying a variety of neurotoxins and contributing to drug metabolism and neuroprotection.[132] BChE is more resistant to inhibition by nerve agents and organophosphates, making it an important target in pharmacology due to its potential as a bioscavenger.[133, 134]

The abnormal activity of AChE can contribute to neurodegenerative conditions, such as Alzheimer's disease. There is research suggesting other physiological roles of AChE in cell adhesion and neuronal development.[135] It was also found that AChE and BChE contribute to the formation of amyloid plaques in Alzheimer's disease.[136] While research on these two enzymes and their physiological and therapeutic roles is still ongoing, their potential as therapeutic targets is evident.

From a structural standpoint, AChE belongs to the α/β hydrolase family and contains a highly conserved Ser-His-Glu catalytic triad, responsible for the hydrolytic activity. The high specificity of AChE is influenced by the active site gorge, which is lined with hydrophobic aromatic residues. There is a peripheric anionic binding site at the outer periphery of the gorge, playing the main role in substrate recognition (Figure 6).[137, 138] Although mechanistically, the

hydrolysis takes place following a classic serin protease mechanism, the AChE catalysis still holds unanswered questions.

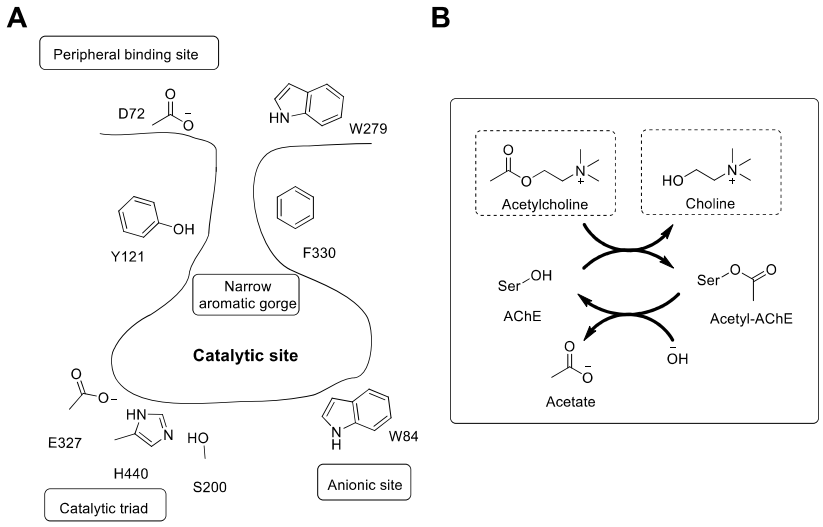

Figure 6. A. Scheme of the catalytic site of AChE. **B.** Reaction scheme of the AChE reaction.

Although the substrate needs to navigate a relatively long tunnel to the catalytic site, AChE is one of the fastest known enzymes, with an acetylcholine turnover number of $1.5*10^4\ s^{-1}$.[139] A suggested reason for this high rate is the unusually strong electric field of the enzyme creating a gradient, which presumably pulls the substrate down the gorge.[140]

Due to its role in neural communication, AChE is a target for the treatment of various neurological conditions, such as Alzheimer's disease, glaucoma and anticholinergic poisoning, with several therapeutic inhibitors on the market. Inhibitors such as donepezil, galantamine and rivastigmine help increase acetylcholine levels in the brain, compensating for the deficit of cholinergic neurons (Figure 7). However, more recent studies suggest that the benefit of these treatments might not be clinically significant. Moreover, because of the important side effects associated with these drugs, pharmacological studies are being conducted to improve their properties. The search for new inhibitors is ongoing.[141, 142]

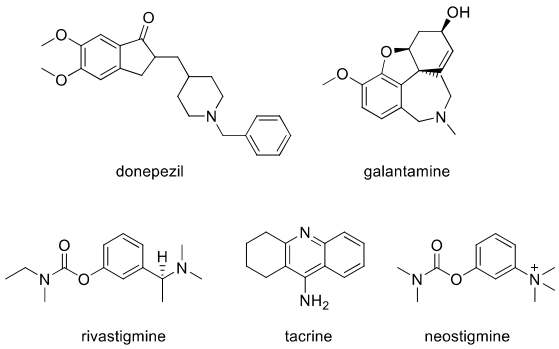

Figure 7. Examples of commercially approved AChE inhibitors used in the treatment of neurological diseases.

2.1.6 Physostigmine and its derivatives

Physostigmine (also known as eserine) was the first identified pyrroloindole displaying a reversible AChE inhibitory effect (Figure 8). It was isolated from the Calabar bean (*Physostigma venenosum*), a plant species from West Africa, and initially described in 1864 as an antidote for atropine poisoning. There are records of the past use of the calabar bean as an ordeal poison.[143] It is nowadays used as a treatment for glaucoma and myasthenia gravis as well as an antidote against anticholinergic poisoning. Other uses for physostigmine involve the reversal of the effects of overdoses of benzodiazepines, antipsychotics, antihistamines and tricyclic antidepressants. As it was found to improve short-term memory, it was explored as a treatment for Alzheimer's disease. However, clinical trials revealed severe side effects, including tremors, nausea, vomiting, diarrhea, and loss of appetite. Combined with the development of other better-tolerated AChE inhibitors, these issues led to its abandonment as a potential treatment for Alzheimer's disease. [144]

Phenserine is a synthetic physostigmine analog, containing a phenyl ring attached to the carbamate side-chain of the pyrroloindole core. Besides its AChE inhibitory effect, phenserine was found to reduce the synthesis of the amyloid β precursor protein (APP), which is associated with the formation of amyloid-beta plaques.[145] Although it was considered a promising candidate for the treatment of Alzheimer's disease, its mixed results in efficacity analyses and significant gastrointestinal side effects stand in the way of its clinical

applications.[146] The action of the (+)-enantiomer – posiphen was also investigated. Since it retains the ability to lower APP production without displaying AChE inhibition, it remained under investigation as a potential treatment for Alzheimer's.[147]

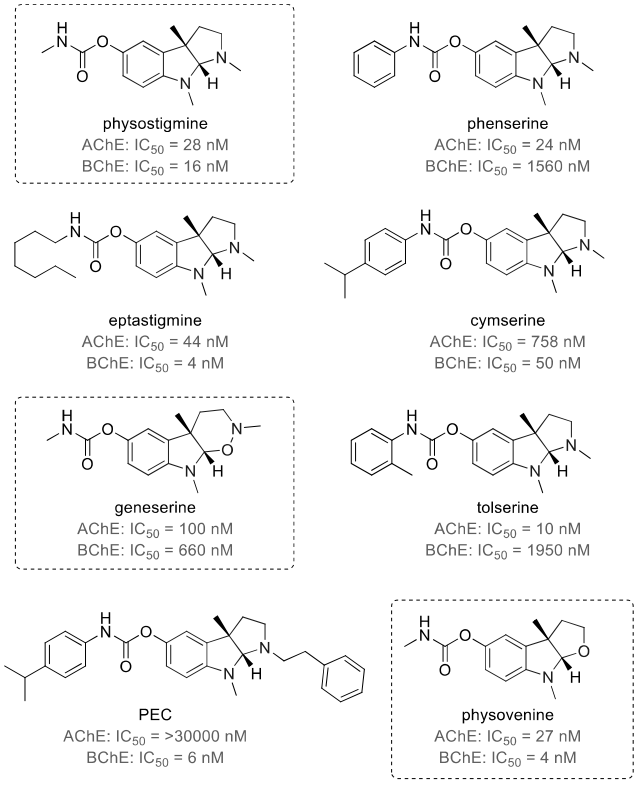

Figure 8. AChE and BChE inhibitors including derivatives of the pyrroloindole scaffold or its derivatives, along with their determined IC_{50} for AChE and BChE. The framed compounds are natural products; the rest are synthetic derivatives.

Physovenine is a less-known physostigmine natural analog, replacing the peripheral pyrrolidine ring with a tetrahydrofuran (Figure 8). It was also isolated from the Calabar bean, but no information about its biosynthesis has been acquired so far. Although its AChE and BChE inhibitory actions are known, the pharmacological profile and therapeutic potential of physovenine are largely unexplored.[148] Similarly, geneserine is another physostigmine analog found in the calabar bean. As its inhibitory effect is reduced compared to other similar compounds, geneserine has not found significant therapeutic applications.[149, 150]

The structure-activity relationship of physostigmine provides insight into its AChE inhibition mechanism. The carbamate group plays a crucial role: the carbamylation of the serine residue of the AChE catalytic triad temporarily inactivates the enzyme, preventing the entry and breakdown of acetylcholine. Pyrroloindoles are a structural feature present in a variety of compounds displaying AChE inhibitory activity. Their tricyclic core structure contributes to the affinity of AChE for physostigmine analogs, through the formation of hydrophobic interactions within the hydrophobic gorge of the enzyme.[151] Additional modifications on the pyrroloindole rings or the side chains were found to influence the target selectivity of physostigmine analogs. After developing and testing new physostigmine analogs, it was observed that longer carbamate or amide alkyl side chains increase the affinity towards BChE, while the presence of an ortho- or meta-substituted phenyl ring improves AChE selectivity (Figure 9).[152, 153] However, the modification of other sites remains elusive, due to the limited synthetic methodologies. Similarly, it might be interesting to evaluate the pharmacological effects of different alkylations on the chiral sites of the pyrroloindole or the two pyrroloindole nitrogen atoms. Given that the structural diversification of the physostigmine scaffold already produced new AChE and BChE inhibitors with various properties, the further diversification of this scaffold can be a promising strategy for developing more effective and selective inhibitors, while possibly reducing the associated side effects.

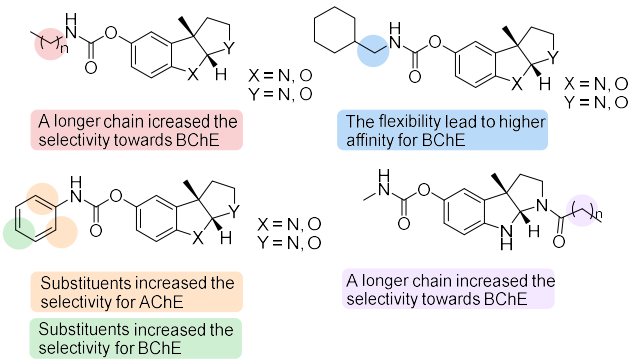

Figure 9. SAR of physostigmine analogs. Observed effects of structural features of physostigmine derivatives on AChE and BChE activity.

2.2 Late-stage methylation in medicinal chemistry

The late-stage modification of bioactive compounds is used in pharmaceutical research for the diversification and optimization of leads. Usually, small functional groups are attached to a lead, affecting properties that are relevant for the pharmacological performance, such as polarity, solubility, target selectivity, metabolic stability and potency. This approach allows researchers to access a wide range of structural modifications without repeating the synthesis of the entire molecule, accelerating the drug development process. Some of the most common late-stage functionalizations in medicinal chemistry include halogenation (most often fluorination), methylation, hydroxylation, amination, and amidation.[154]

The small and mostly chemically inert methyl group is ideal for the fine-tuning of drug candidates without strongly affecting their chemical properties. According to a 2011 analysis of the 200 best-selling drugs, 67% contained methyl groups.[155] Methylation can significantly influence the pharmacokinetic and pharmacodynamic properties of therapeutic agents. This effect can be caused by multiple phenomena, and is prevalent enough to be included under the term “magic methyl effect”.[9, 156] The stereoelectronic effects of methyl groups can have a great impact on bioreceptor recognition, and the magic methyl effect can also be found in nature. The most important example is the difference between DNA and RNA, in which the presence of one methyl group on thymine influences the stability, conformation and interactions of the nucleic acid, with effects on biological processes such as transcription, translation and gene regulation (Figure 10).[157, 158] Other natural examples include secondary metabolites that change properties with methylation, such as caffeine and theobromine or morphine and codeine (Figure 10).

The properties that can be influenced through methylation include:

- Solubility: methyl groups increase the lipophilicity of compounds, generally increasing the logP values, leading to a reduction of water solubility and the enhancement of hydrophobic interactions. The increased lipophilicity will also often improve biomembrane permeability. However, counterintuitively, in some cases, methylation can lead to increased water solubility by disrupting intramolecular hydrogen bonds, changing the ionization states of functional groups, or disrupting the crystalline network.

- Metabolic stability: methylation on metabolic “soft spots”, such as the vicinity of heteroatoms can hinder the activity of metabolic enzymes, prolonging the half-life of the drug molecule in the organism, which helps decrease the necessary dose.

- Binding affinity: introducing a methyl group can improve the target affinity by increasing the hydrophobic and van der Waals interactions with the hydrophobic residues in the active site of the receptor.

- Electronic effect: the inductive electronic effect of the methyl group can in some cases influence the charge distribution of the target molecule, affecting the acidity or the tautomeric state of the molecule. This can in turn alter the type of interactions the bioactive compound establishes with the target receptors.

- Conformational effect: the most extreme activity improvements after methylation were often achieved in compounds that can be sterically "locked" into a favorable conformation through methylation. This can significantly alter the target selectivity and affinity.[9]

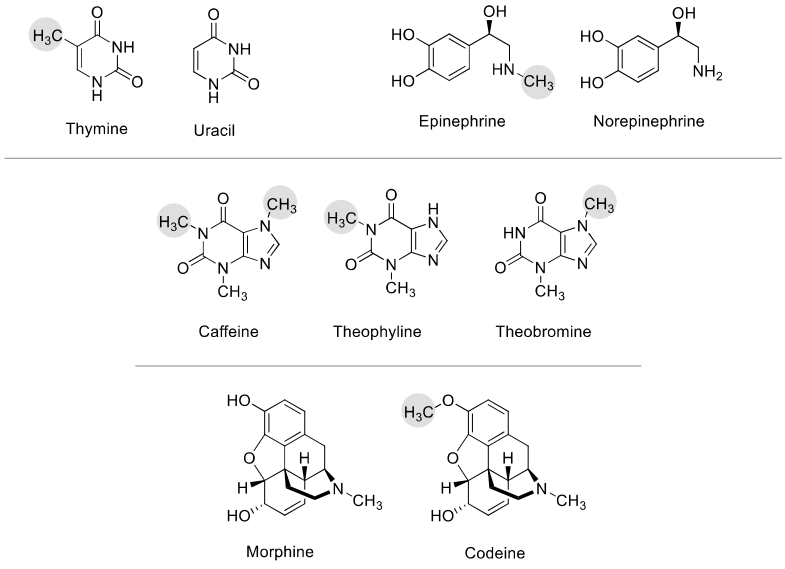

Figure 10. Natural examples of the methylation effect on bioactive compounds.

The literature provides numerous examples of drug candidates significantly improving efficacy after methylation, typically due to a combination of multiple methyl effects, instead of one single factor (Figure 11).[159] A literature study from 2012 of published SAR reports revealed that a 10-fold activity boost from methylation occurs in 8% of the cases, while a 100-fold increase in activity occurs with 0.4% frequency.[160] Several successful examples include the development of the FDA-approved anticancer drug tazemetostat, where the methylation of the lead

compound provided a dramatic increase in potency (Figure 11A).[161] The 4-methylated analog of a tetrahydroisoquinoline κ opioid receptor agonist led to an 18-fold increase in the affinity, compared to the non-methylated compound (Figure 11B).[162] An example of the methylation effect on water solubility comes from the development of N-acylhydrazones as histone deacetylase 6/8 (HDAC6/8) inhibitors for cancer treatment, where the conformational effect of an N-methylation leads to an increase in solubility (Figure 11C).[163] Finally, the metabolic optimization of a quinazoline derivative involved in phosphoinositide 3-kinase-δ (PI3Kδ) inhibition revealed that the methylation of a "metabolic soft spot" on the pyrrolidine linker increased the half-life in human liver microsomes (HLM), while maintaining similar efficacy (Figure 11D).[164]

An illustrative example of the conformational effect of methylation is the development of biaryl mitogen-activated protein 3 (MAP3) kinase inhibitors by the drug discovery team of GSK. Adding a methyl group on the ortho position of one of the aryl units caused a 200-fold increase in target binding affinity (Figure 12). Computational analysis revealed that the dihedral angle of the methylated inhibitor resembles the conformation of the protein-bound parent compound.[165]

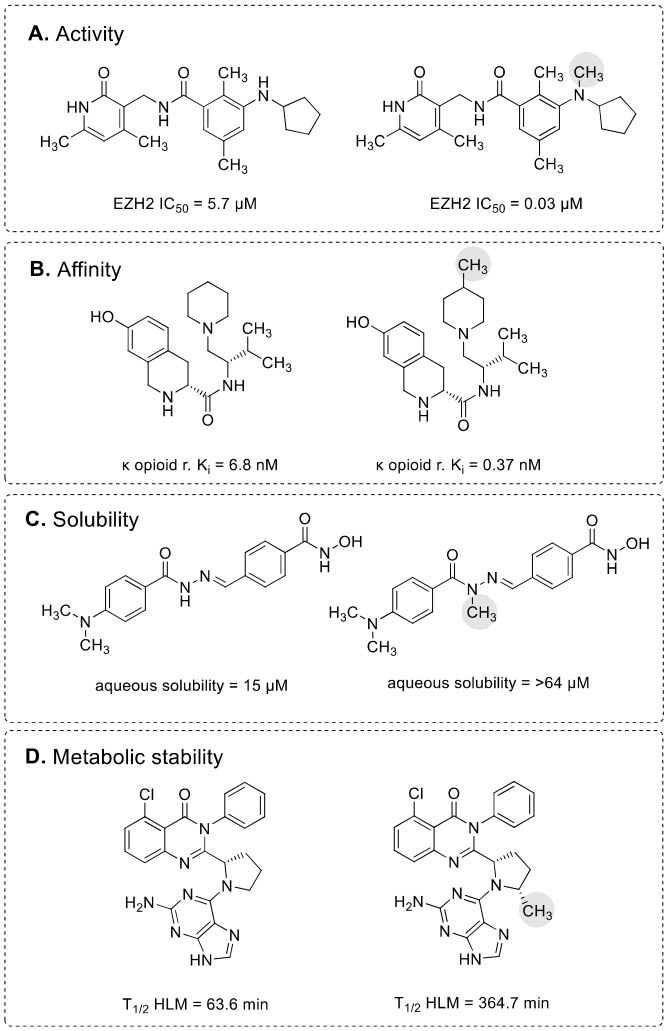

Figure 11. Examples of different effects of the methylation of lead compounds on their pharmacological properties. **A.** IC_{50} increase after the methylation of a lead compound in the development of tazemetostat.[161] **B.** Effect of methylation on the target affinity of κ opioid receptor inhibitors.[162] **C.** Solubility change after the methylation of an HDAC6/8 inhibitor.[163] **D.** Effect of methylation on the metabolic stability of PI3Kδ inhibitors.[164]

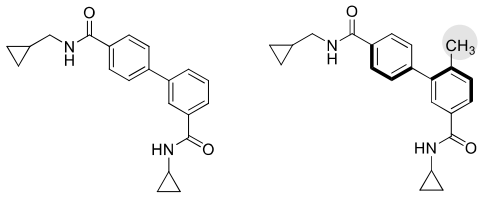

Figure 12. Example of a conformational "locking" caused by methylation of a biaryl inhibitor of the MAP3 kinase, leading to a significant increase in affinity.

The search for C-methylation options

The traditional synthetic routes for late-stage C-methylation have generally been limited to the deprotonation of acidic C-H bonds, followed by methyl transfer from an electrophilic donor, such as methyl iodide. In the absence of acidic protons in the target position, the methyl group must be incorporated early in the synthetic sequence, dramatically increasing the experimental efforts for the structure diversification of lead compounds.[10] More recently, advances in C-C bond formation enabled new pathways for the chemical late-stage methylation. These advances often include the use of transition metal-catalyzed methylation of aromatic sp^2 carbons, usually in the presence of directing groups.[166-168] For the *C*-methylation of aromatic heterocycles, radical addition strategies stemming from the Minisci reaction provided a solution, with various radical-generating options being explored.[10, 169] An important achievement of the radical methylation field was the photocatalytic activation and use of methanol as a methylation agent.[170] However, the need for harsh oxidative conditions limits the use of this strategy for more sensitive heterocyclic compounds. Other options include the nucleophilic aromatic substitutions of electron-deficient *N*-activated heteroarenes,[171] Catellani-type reactions[172], or metal-catalyzed cross-coupling reactions.[10, 173]

The methylation of sp^3 carbon centers is more challenging due to the higher energy requirement for C-H activation, relying heavily on the presence of directing groups. Regioselective methylation can be directed by the presence of nitrogen-based directing groups in the presence of metal catalysts, while oxidative methylation of saturated heterocycles on the α-position is possible using a combination of metal and photocatalysis.[174] The options presented so far require activated C-H bonds. The methylation of unactivated C(sp^3)-H bonds, was reported using highly reactive carbenes adsorbed on GaN nanowires.[175]

Direct asymmetric *C*-methylation remains a challenge for many starting materials. Most often, diastereospecific methylations are achieved using directing groups, from chiral starting molecules.[176] When possible, the stereoselective methylation of prochiral molecules is usually performed using either metal catalysis and chiral ligands, or chiral organocatalysts.[177] Several strategies for the asymmetric late-stage methylation of saturated *N*-heterocycles or α-stereogenic carbonyls were established, with various stereoselectivities.[178] However, the stereospecific late-stage attachment of methyl groups on prochiral molecules is so far out of reach for most targets.

Although important progress was made in the past years in the C-H activation and the selective alkylation of carbon atoms, the vast majority of successful examples are limited to activated positions on the target molecules, requiring transition metal catalysts and/or complex organic ligands. Selective *C*-methylation remains a challenging endeavor for synthetic chemistry, but an important area of study, given the potential of late-stage methylation for drug development and the remarkable advancements achieved in recent times. In the past few years, biocatalytic methods using SAM-dependent methyltransferases have emerged as an alternative for the selective methylation of various molecular scaffolds. Although the research in this area is still in the relatively early stages, promising examples of highly selective methylations using methyltransferases can be found in the literature. The biocatalytic methylation options are discussed in detail in Chapter 2.4.

2.3 Biocatalysis as a synthetic tool

Biocatalysis has been gaining ground as a state-of-the-art synthetic tool, mostly in the pharmaceutical and fine chemical industries. The high selectivities of enzymes, mild reaction conditions and natural variety have established them as tools for building complex molecules. In pharmaceutical research, the need for rapid development and high optical purity in complex compounds has driven the interest in biocatalytic methods. To ensure the economic viability of biocatalytic processes, the productivity must be comparable to chemical processes.[179] While achieving a high product yield per gram of catalyst is important for chemical production, it is most often not the focus of natural evolution. Therefore, innovations in process development and protein engineering are essential for the scaling of biocatalytic processes.

The practical limitations of enzyme use, such as reduced productivity, stability and propensity to inhibition have not yet made biocatalysis a viable competition to fossil-based bulk chemical production. There are however several successful examples of ton-scale use of enzymes, such as the use of nitrile hydratases to produce acrylamide,[180] the production of high fructose corn syrup from starch and the use of hydrolases in detergents.[181] The option to modify catalyst properties through molecular biology, combined with the use of renewable catalysts and feedstocks, might drive a shift in the bulk chemical production strategies in the future. This is particularly important as climate change remains a major issue for humanity, with the reliance on fossil fuels requiring a drastic reduction in the near future.[182] However, to make biotechnological production economically feasible, ongoing efforts are required to enhance the efficiency and productivity of biocatalysts and microbial processes.

Using recombinant DNA technology, scientists can expand the range of available biocatalysts and reaction types. All enzyme classes have been successfully used as biocatalysts for a large variety of reactions.[181, 183] One of the most prominent examples in the field is the application of transaminases to produce optically pure amines from ketones, particularly useful in the synthesis of active pharmaceutical ingredients (APIs).[184] Flavin-dependent monooxygenases have found many applications in the synthesis of natural products, due to their ability to perform highly selective oxidations.[185] Ketoreductases are widely used for the asymmetric synthesis of chiral alcohols from ketones, while lipases have long been utilized for the synthesis of chiral alcohols through kinetic resolution.[186, 187] Important developments were also achieved in the use of lyases and amino acid dehydrogenases for the stereoselective preparation of chiral amino acids.[188] Enzymatic late-stage functionalization is particularly important in API development, with many enzymes being identified and engineered to efficiently transfer functional groups such as hydroxyl, halogens, alkyl, or aryl with high selectivity.[189] The discovery of PETases, which can hydrolyze polyethylene terephthalate (PET) brought

important progress in plastic depolymerization and recycling, with ongoing efforts to optimize the activity through protein engineering.[190] Polyketides are a complex and varied class of natural products produced naturally by polyketide synthases from carboxylic acids. The engineering of extremely large polyketide enzymatic assembly lines has gained attention recently due to the polyketide diversity in terms of structures and biological activities.[191] Only several prominent examples from recent years have been presented here to illustrate the current trends and advancements in biocatalysis research. However, the scope of the research, enzyme and reaction types developed by the scientific community in the last years is much wider, with important advances across all the enzyme classes (Figure 13, Table 2).[183, 192, 193]

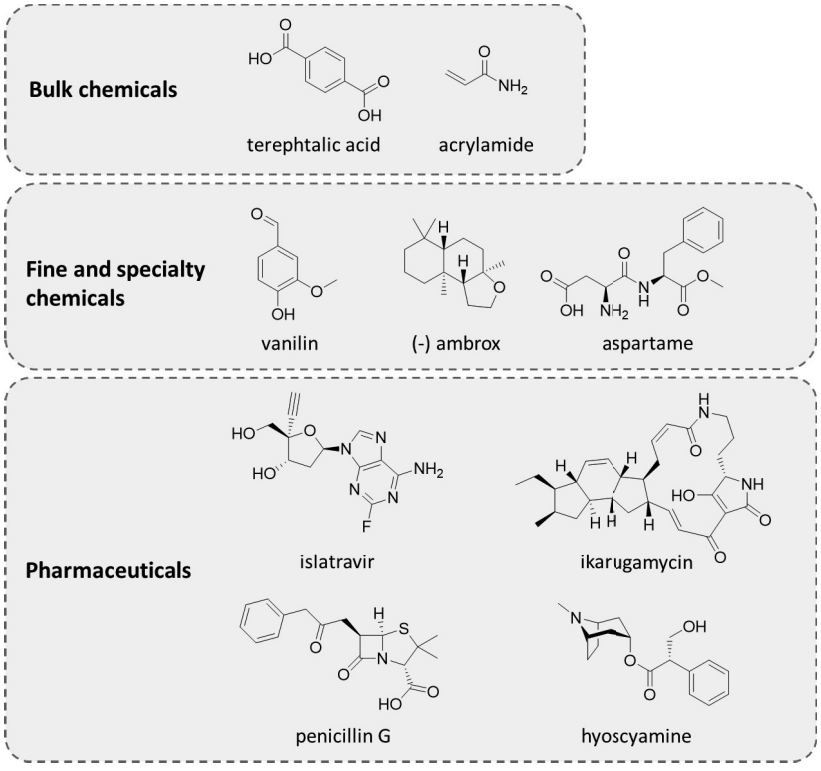

Figure 13. Examples of applications of biocatalysis in the production of industrially relevant chemicals.

One of the most notable uses for enzymes as biocatalysts is in the synthesis of complex pharmaceuticals and natural products.[7] Enzymatic cascades were proposed recently for the synthesis of the AIDS drug candidate islatravir,[194] for the diversification of cannabinoids,[195]

the antibiotics ikarugamycin[196] and enterocin[197], and for hyoscyamine and scopolamine (treatments for neuromuscular disorders).[198] The development of new enzyme cascades has become easier with the use of computational retrosynthesis tools. Multiple computer-aided synthesis planning tools have been developed in the previous years for chemical retrosynthesis (ex. Chematica),[199] while other tools specialize in the identification of new metabolic routes for the production of target molecules (ex. RetroPath).[200] A targeted alternative tool for biocatalytic synthetic routes is RetroBioCat,[201] which identifies potential routes for multistep biocatalytic reactions, considering factors such as commercial availability, cofactor requirements, and solvent tolerance.

The supply and regeneration of cofactors

Many enzymatic reactions require cofactors, which are organic or organometallic molecules (coenzymes) or inorganic metal ions. They play a critical role in the catalytic function of many enzymes, enabling the transfer of electrons (e.g. NAD(H), FMN, FAD) or acting as chemical group donors (e.g. ATP, SAM, coenzyme A, THF).[158] The supply and regeneration of cofactors is a critical aspect of industrial and pharmaceutical biocatalytic processes. As coenzymes are complex and often unstable molecules, the chemical synthesis for supply is not always economically viable. Innovations in enzymatic cofactor recycling systems have provided an elegant solution for achieving high conversions from cofactor-dependent enzymes in a more sustainable and cost-efficient manner. Examples include the developments in the regeneration of NAD(P)H using alcohol, glucose or formate dehydrogenases in the presence of a sacrificial substrate. This is now a well-established and widely used method in biocatalytic reactions with a variety of oxydoreductases.[202, 203] Acetate and pyruvate kinases are used to regenerate ATP, transferring a phosphate group from acetyl phosphate or phosphoenolpyruvate (PEP) to ADP.[204] For the regeneration of the reduced $FADH_2$, reduction by flavin reductases is performed using NAD(P)H as an electron donor, usually in the presence of a NAD(P)H recycling system.[203, 205, 206] SAM can be recycled using halide methyltransferases in the presence of a methyl donor, such as methyl iodide.[207] Chemical and electrocatalytic cofactor recycling methods have also been developed as alternatives to enzymatic cascades, with varying efficacy levels.[203] Recycling strategies play an important role in enhancing the efficiency and sustainability of cofactor-dependent enzymatic processes.

Table 2. Examples of prominent biocatalysts from different enzyme classes and their applications.[11, 180, 190, 208-212]

EC	Enzyme	Reaction	Importance	Ref.
1	D-amino acid dehydrogenase	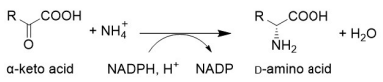	Stereoselective production of non-canonical D-amino acids	[209]
2	Catechol O-MTase		Selective late-stage functionalization of polyphenols	[212]
3	PETase	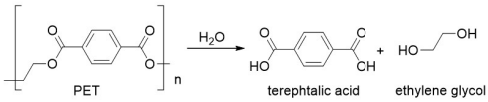	PET plastic depolymerization	[190]
4	nitrile hydratase	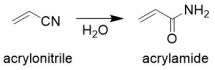	Production of acrylamide and removal of nitriles from waste water	[180]
5	glucose isomerase	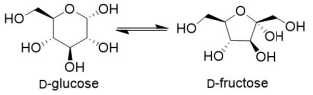	Industrial production of high-fructose corn syrup	[210]
6	T4 DNA ligase	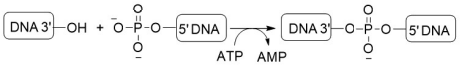	Tool for genetic engineering	[211]

The development of new-to-nature biocatalytic functions

Nature provides a vast variety of enzyme activities that can be modified and combined to create artificial pathways. However, the range of chemical mechanisms available in natural enzymes is limited. As a result, the development of enzymatic transformations that have not evolved in nature took an important role in the recent biocatalysis research. This enables the use of new-to-nature chemical mechanisms in the chiral enzymatic environments. The incorporation of non-canonical amino acids in the catalytic sites of enzymes using orthogonal translation systems has helped improve their stability, understand their mechanism and enable access to new reactions. This technique can improve the catalytic activity by changing the reactivity of residues in the catalytic site, creating new metal binding sites or enable new enzyme reactivities altogether.[213, 214] For example, new-to-nature hydrazine and oxyme formation was achieved by incorporating a 4-amino-phenylalanine residue into the structure of the multidrug transcriptional regulator LmrR from *Lactococcus lactis* (Figure 14A).[215] In another instance, the substrate selectivity of PikC P450 enzyme, involved in the biosynthesis of macrolide

antibiotics, was altered by the incorporation of 4-acetyl-phenylalanine in the catalytic pocket (Figure 14B).[216]

Photobiocatalysis is a recent development in the creation of novel enzyme reactivities, where light is used to drive the selective conversion of small molecules through radical mechanisms, under mild conditions. This can be achieved through multiple routes: by using natural photoenzymes, enabling photoreactivity in enzymes containing photosensitive cofactors such as FMN, combining chemical photocatalysis with biocatalaysis in cascade, developing artificial photoenzymes containing covalently linked photocatalysts, or conjugating a photosensitizer within the protein scaffold.[217, 218] FMN-dependent ene-reductases have shown promiscuous reactivities in the presence of light irradiation, achieving the asymmetric reductive cyclization of lactams or the intermolecular hydroalkylation of olefins (Figure 14C).[219, 220] NADPH-dependent ketoreductases were used for the radical dehalogenation of halolactones in the presence of light (Figure14D).[221] Finally, a *de novo* approach to enzyme design allowed the incorporation of unusual metal centres. This produced new enzyme functionalities by combining the advantages of metal catalysis with the selectivity of enzymes. For example, the photoredox radical C-C cleavage of 1,2-diols was enabled by a fully artificially designed cerium containing metalloenzyme (Figure 14E).[222]

The adoption of biocatalytic methods for chemical production can produce significant economic and environmental benefits, by reducing energy consumption, lowering greenhouse gas emissions, and minimizing waste. The large-scale implementation of these methods still meets regulatory, market and financial barriers.[223] However, it is likely that the technology will be further developed and adopted as part of the global transition toward sustainability and greener chemistry practices.[224]

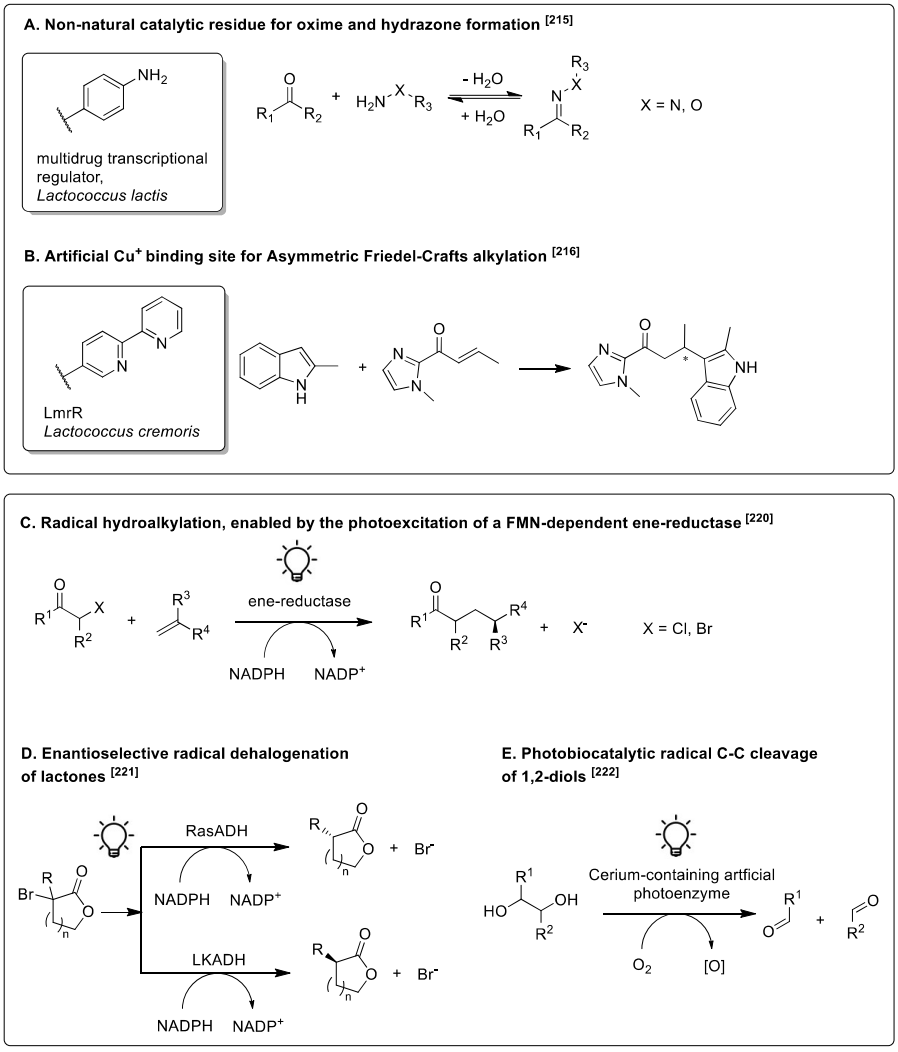

Figure 14. Examples of new enzymatic funtions enabled by the incorporation of non-natural amino acids (A and B) or by the use of photobiocatalysis (C, D and E).

2.3.1 Protein engineering

The advances in molecular biology and emergence of recombinant DNA technology in the 1970's allowed an unprecedented capacity for altering the properties of biocatalysts and pushing them outside of their evolutionary boundaries. Through protein engineering, one can improve properties such as the activity, selectivity and stability, obtaining more effective catalysts.[192] Early efforts foscused on site-directed mutagenesis, in which rationally designed point mutations allowed scientists to begin altering the properties of enzymes. In the 1990s directed evolution emerged as a powerful approach, mimicking natural selection through iterative rounds of random mutagenesis and selection.[6] Today, protein engineering techniques continue to evolve and diversify, incorporating computational prediction tools.[225] Enzyme engineering has found significant applications in scientific research, industry, medicine and environmental protection, becoming a crucial part of the development of most of the industrial biocatalytic processes of today.[226]

Site-specific mutagenesis

The current practices for protein engineering range from a targeted site-specific approach (few variants) to semi-rational methods (specific mutation sites but randomized amino acids) and finally to full randomization (large number of variants and extensive selection) (Figure 15). Each of these methods have their own variations and specific strengths. The choice of strategy needs to be considered according to the circumstances of the engineering project. A rational design approach requires prior knowledge about the structure and mechanism of the enzyme of interest. It requires significant input from the scientist, as predictions need to be made about the effects of the changed amino acids. The major advantage of this method is that it requires minimal resources for enzyme production and screening, as it generates only a small number of variants. A disadvantage is the difficulty in making accurate predictions in the context of the dynamic nature of enzymes, as well as high chances of overlooking the cumulative effects of mutations. Recent successful examples of site-directed mutagenesis include the modulation of stereoselectivity of the polyketide synthase ketoreductase domain[227] and the improvement of catalytic efficiency and thermostability of a glucoamylase from *Talaromyces leycettanus* for industrial saccharification.[228]

Directed evolution

The directed evolution strategy is found at the other end of the spectrum, requiring minimal prior structural and mechanistic information about the targeted protein. As a result-driven method, it helps eliminate bias and explore a much larger structural diversity. In a reverse conceptual order from site-directed mutagenesis, random mutations are applied to the whole gene sequence and the best fits are identified after a selection process targeting the desired property. After the hits are identified, the genetic information of the best mutants is determined by sequencing, which might explain the effects of the discovered mutations. The most common methods for *in vitro* gene randomization are error-prone PCR (epPCR) and DNA shuffling,[229, 230] but multiple strategies have been developed over the years. *In vivo* gene diversification can be achieved through recombination strategies, the use of mutator strains or plasmids, and using CRISPR-Cas9-assisted gene editing.[231] The directed evolution of enzymes is nowadays a key technique in industrial biocatalysis process development.[226] For example, the evolution of the monoamine oxidase MAO-N from *Aspergillus niger* significantly expanded the substrate scope for the deracemization of amines, maintaining high stereoselectivity.[232] Some notable successful examples of directed evolution include the development of PETase (*Ideonella sakaiensis*) variants with significantly improved its thermostability and activity for PET plastic depolymerization[233] or the improvement of a glucose dehydrogenase and a ketoreductase activity for their use in a 2-step biocatalytic synthesis of a key precursor of atorvastatin.[234] The evaluation of large mutant libraries requires high-throughput screening strategies. They need to be tailored for each enzymatic process, and are often the bottleneck of applying this technique, due to the high cost of development and implementation. However, the recent evolution of high-throughput screening technology (described in Chapter 2.3.2) has enabled the screening of extensive mutant libraries.

Semi-rational design

Semi-rational design can be considered a compromise between the site-directed and fully randomized mutagenesis approaches. Site-saturation mutagenesis is a powerful technique for exploiting the effects of amino acid modifications in a given position. The chosen residue is systematically replaced with all the 20 canonical amino acids using degenerate primers, allowing the identification of the effects of mutations on the enzyme properties in a focused manner. This leads to a significant reduction of the size of the mutant libraries, reducing the necessary production and screening efforts. In order to select relevant mutation sites, prior information about the target protein is required. To account for possible cooperative effects,

multiple sites can be mutated at the same time. The mutant library size can be reduced by the use of modified degenerate primers, coding for only a fraction of the 20 possible amino acids, chosen based on information such as the conservation trends in known homolog sequences.[235] A workaround for the saturation-based optimization of multiple sites while reducing the size of the mutant libraries is iterative saturation mutagenesis (ISM).[236] In this technique, multiple sites are mutated separately using saturation mutagenesis, in a sequential approach: the best performing single mutant from one round of mutagenesis is used as a template for subsequent rounds, allowing for the gradual accumulation of possible cooperative effects of mutations in different positions. The first successful example of the ISM strategy was the thermostability enhancement of the lipase LipA from *Bacillus subtilis*. In this case, 10 amino acid positions were initially targeted for saturation mutagenesis. After 5 rounds of mutagenesis and the screening of a total of 8000 variants, the T_{50} value was increased by 45 °C.[236] Other examples include the reversal of the enantioselectivity of alcohol dehydrogenase from *Lactobacillus kefiri* for the chemoenzymatic synthesis of enantiopure styrene oxide[237] and the engineering of a nitrilase from *Pyrococcus abissy* for the dynamic kinetic resolution of 2-chloromandelic acid.[238]

Combined methods

Some strategies combine directed evolution with rational or semi-rational design. Methods such as ProSAR[239] or KnowVolution[240] integrate computational protein design and analysis with experimental directed evolution. This can help gain information about the causes of beneficial random substitutions and, in turn, make better predictions for rational design. These strategies typically start with directed evolution and screening of mutant libraries for the identification of beneficial positions, followed by site saturation mutagenesis and/or computational analysis, and finally, rational recombination of the beneficial mutations, for achieving the desired effect. ProSAR was used to improve the productivity of a halohydrin dehalogenase for the biocatalytic production of atorvastatin,[239] while the KnowVolution method was proven a powerful tool for enzyme evolution campaigns, leading to the improvement of a variety of biocatalysts. Several successful applications of KnowVolution include the 40-fold improvement of the catalytic efficiciency of the prodigiosin ligase PigC from *Serratia marcescens*,[241] a 7.7 °C increase in melting temperature for the GH5 cellulase from *Penicillium verruculosum*[242] and the improvement of the alkaline tolerance of the laccase from *Melanocarpus albomyces*.[243] The combined methods and the integration of computational analysis and prediction methods can help improve the efficiency of mutagenesis projects, while better understanding the underlying reasons for the beneficial screening results.

In vivo laboratory evolution

Laboratory *in vivo* evolution can also produce significant improvements of biotechnological processes, particularly in strain development. In these cases, specific biocatalysts are not the direct targets, but the strains themselves are subjected to multiple continuous rounds of evolution under the desired growth conditions. After the desired strain is developed, the genetic changes are often reverse engineered, to identify the specific biocatalyst changes leading to the successful result. This strategy has been successful in developing new bacterial strains with important applications such as plastic degradation or the bioproduction of bulk chemicals from renewable sources.[244, 245]

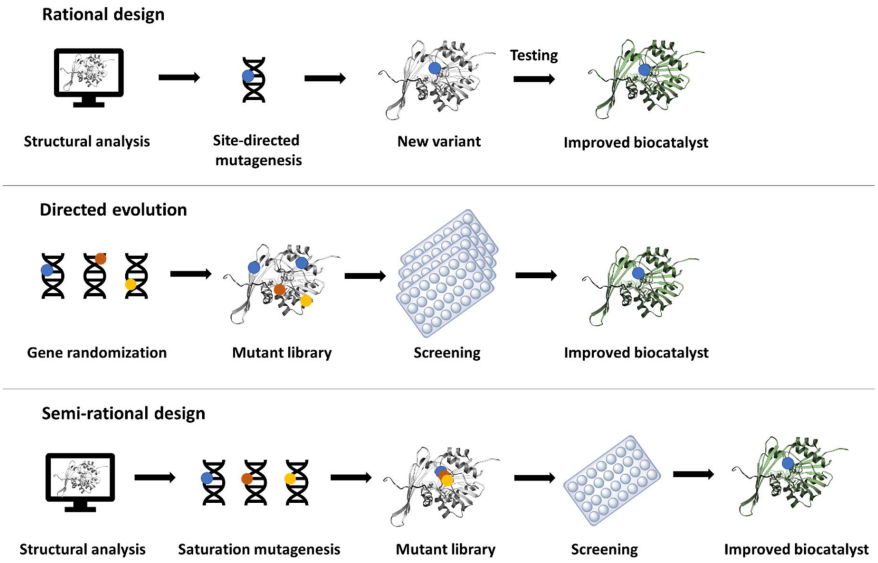

Figure 15. General schemes of the current main strategies for enyzme engineering.

Computational tools for protein engineering

To reduce the screening efforts and enhance the quality of mutant libraries, computational tools have been developed for *in silico* pre-screening. These tools help lower the mutant library size and identify potential promising targets and mutations. Based on the type of information utilized, they can be classified into several types:

- **Sequence-based.** These tools predict the effects of mutations based on amino acid sequence alignments with homologs from experimental databases. The andvantage of these methods is that they only require sequence information and they are computationally inexpensive. Examples include PoPMuSiC,[246] which predicts the effect of site mutations on protein stability, and PROVEAN, predicting the functional effect of mutations.[247]

- Structure-based. They are particularly useful for identifying hot spots for engineering. Using 3D structural data as input, these tools make predictions analyzing properties such as surface features or interatomic interactions. Web tools such as CAVER 3.0,[248] Funclib,[249] or HotSpot Wizard 3.0[250] can predict relevant mutation targets and provide information about the function and mechanism of the target enzymes.

- Molecular dynamics (MD). MD simulations calculate the movement of individual atoms within a biomolecule over time, offering valuable insights into the dynamic behavior of proteins, in contrast with the static structural information generally obtained through experimental methods.[251] This allows for more accurate identification of important targets for mutagenesis.

- Machine learning. The rapid development of data science triggered the development of machine learning methods for protein engineering. Machine learning can identify patterns among enzyme sequences, properties or atom interactions and make predictions, reducing the library screening requirements. It is a powerful tool, which was already used for multiple enzyme engineering projects.[225, 252, 253] The development of the deep-learning AlphaFold tool for protein structure prediction has represented a paradigm shift for protein engineering, as accurate structural information became accessible to an unprecedented level.[254] Large language models (LLMs) have seen a rapid evolution in the recent years, and have also found applications in protein property prediction and the generation of novel proteins.[255]

2.3.2 Mutant library screening

Directed evolution and semi-rational design have enabled unprecedented possibilities for the optimization of biocatalysts. One of the crucial requirements for the implementation of these techniques is the mutant selection process, based on the desired effect of the mutagenesis. In order to identify hits out of thousands of variants, the development of high-throughput screening (HTS) has been crucial.[256, 257] Nowadays, the HTS method development is based on several important properties:

- **High-throughput**: a screening strategy needs to allow the analysis of a large number of samples in a short time. This requires a different experimental set-up, compared to regular biocatalyst laboratory characterization techniques.
- **Specific and reproducible**: a HTS strategy should be specific for the desired tested property, assuring a strong differentiation from the background signal.
- **Automated (optional)**: while manual handling of large sample libraries is possible, it is not advisable, as it is time-consuming and labor-intensive, while carrying a high risk of errors. The automation of high-throughput library screening is the current state-of-the art for handling mutant libraries while maintaining high standards of precision and reproducibility.[256, 258, 259]
- **Quantitative (optional)**: quantitative assays are desirable for providing more information on the relative performance of potential hits. However, it is not an absolute requirement. In the case of ultra high-throughput screening methods this can often be impractical due to the experimental set-up. Initial screenings of large libraries are often performed with qualitative assays, for the efficient initial filtering of desirable variants.[260, 261]
- **Adaptable (optional)**: ideally, a high-throughput screening strategy should allow the adaptation for other (similar) biocatalysts and chemical transformations.[262]
- **Efficient analytic method**: the analytic method is important for the overall cost of the screening process. While UV/Vis, mass and flurescence spectroscopy tend to assure lower costs, they are not feasible for all screening projects.[256] Although more cost and time intensive, chromatographic analysis is still sometimes used for large libraries, as it provides comprehensive information about the performance of the tested variants.[263, 264]

High-throughput screening is also a key step in drug and target discovery in the pharmaceutical industry, benefitting from intensive technological advancements in the last decades (Figure 16). While the 96-well microplate has been the main sample handling format at the start of HTS development in the 1990's, there has been a strong push for the miniaturization of samples for an increase in productivity and cost efficiency. This triggered the development and adoption of 384 (30-100 µl) and 1536-well plate formats (2.5-10 µL), with many assays easily adaptable to smaller volume formats. This allowed for the significant improvement of efficiency. While 3456-well plate formats (1-2 µl) were also reported, the industrial trends favored the use of 384-well and low-volume 384-well formats (10-20 µL), as they could be handled using existing infrastructure.[265] Recent technological advances in liquid handling have enabled the analysis at volumes of nL and pL (microfluidics, acoustic liquid handling) or at the level of single cells (cell sorting techniques).

Fluorescence-activated cell sorting (FACS) is a technique used to sort and separate cells based on their fluorescence or light-scattering properties. The cells are labeled with fluorescent dyes or antibodies, which bind to targeted molecules on the cell surface. The labeled cells pass through a laser beam in a flow cytometer, where their fluorescence is detected and measured, providing information on cell characteristics such as size, shape, and molecular composition. The system can then apply an electric charge to droplets containing the hits, directing them into separate containers for further analysis. FACS can achieve ultra-high sorting speeds allowing the screening of up to 10^8 variants per day.[256] The limitation of FACS is the low range of available reactions, either limited by the cell survival or product retention in the cells. Nevertheless, due to their versatility and high efficiency, FACS systems have found applications in enzyme engineering, immunology and medical science.[266-269]

Drop-based microfluidics allow the analysis of aqueous mixtures at picoliter volumes and rates of thousands of droplets per second. This leads to an increase in screening speed of orders of magnitudes, compared to usual high-throughput screening strategies. Microfluidic systems and FACS can be combined for the analysis of physically separated whole-cell reactions, allowing the analysis of the whole reaction “vessel”, instead of the cell characteristics.[270] The detection is most often performed by optical methods, such as fluorescence, absorbance, or light scattering, but other analytical methods such as mass spectrometry, NMR, or electrochemical analysis have also been successfully employed.[271] The combination of ultrahigh-throughput droplet screening with next-generation sequencing and deep learning technologies has started to be implemented in protein engineering projects, showing great promise for the acceleration and cost reduction of biocatalyst development.[231, 272-274]

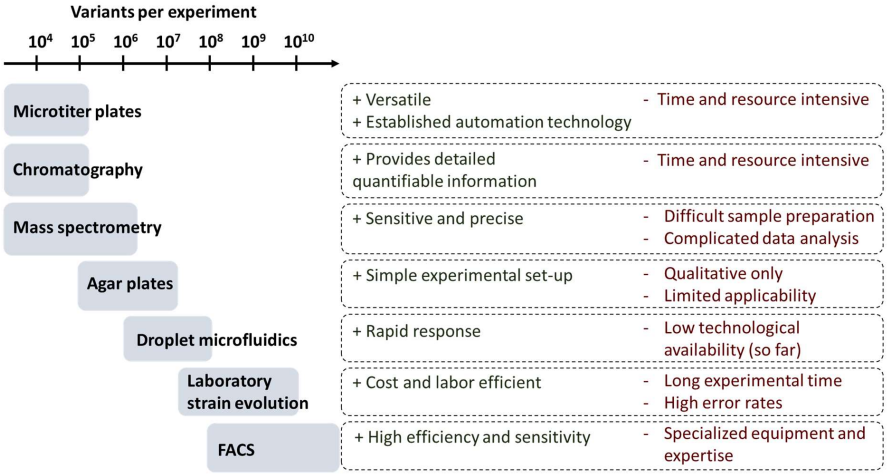

Figure 16. Achievable throughput for various screening strategies, their advantages and disadvantages.

HTS strategies have known important advancements in the last decades, with a great range of adaptation options. The extensive diversity of biocatalytic processes requires high adaptability when it comes to the screening of mutant libraries. Due to the technological advancements in experimental handling, the sample processing time and costs were reduced considerably. Some of the main time-consuming steps of high-throughput screening today are the assay development, data analysis and hit validation.[265] Therefore, the development of new assays that can accommodate the vast diversity of biocatalytic reactions is essential, with significant benefits to be gained from creating "generalist" assays that are applicable across entire classes of enzymes or chemical transformations.

2.3.3 Scaling biocatalytic processes

Scaling biocatalytic reactions from laboratory to industrial levels presents opportunities for the development of more environmentally friendly chemical processes, as they typically require mild reaction conditions and fewer toxic reagents, compared to traditional chemical synthesis. Enzymes are attractive as catalysts as they often exhibit high specificity, lowering the need for protective groups and reducing the purification steps. However, scaling biocatalytic reactions poses several challenges, such as maintaining enzyme activity and stability over extended periods under harsher industrial conditions, the generally low productivity and the propensity

for inhibition.[182] Additionally, many enzymes require expensive cofactors in stoichiometric amounts. Mass transfer limitations may also arise in larger reactors, negatively impacting productivity. Besides the engineering of the biocatalyst itself, process engineering is important for providing solutions to these challenges, by optimizing the enzyme formulations, reaction parameters and reactor set-up.

When scaling a biocatalytic process from laboratory to industrial scale, several considerations take the central stage. As in any commercial endeavor, the production costs must be reduced as much as possible. This can be achieved by the optimization of factors such as overall productivity, biocatalyst production strategy and downstream processing. The process efficiency and sustainability can further be increased by recycling the catalyst and the cofactor and using renewable feedstocks. Global guidelines and policies are driving the transition towards green chemistry practices, a necessary step towards reducing the reliance on fossil fuels and mitigating their impact on the climate.[275]

Enzyme formulation

The choice of the biocatalyst formulation is an important stage in the development of biocatalytic processes (Scheme 4). The enzyme can be used inside the host cell, in a cell-free mixture or isolated. If enzyme isolation is required, it is important to determine what degree of purity is needed, as isolation steps greatly increase the production price. A majority of industrially used biocatalysts are in whole-cell format (either free or immobilized).[276] Using whole cells, biocatalytic processes can take place through fermentation, usually starting from sugars and using the modified metabolic pathways of the host organism to produce the desired product. In this case, the production is tied to the growth curve of the production organism.[277] A wide range of chemicals are now produced in this way, including bulk chemicals such as succinic acid, lactic acid or isoprene, fine chemicals such as amino acids, vanillin or squalene, biopolymers such as polylactic acid (PLA), or biofuels including alcohols or fatty acids.[278] The other option includes using “resting cells” as carriers for the expressed enzyme. When using resting cells, the fermentation phase required for cell growth and enzyme expression is separated from the production phase. Although the cells might still be metabolically active, they are separated from the growth media and simply used as catalysts. While this simplifies the downstream processing, the stability of the enzyme is an important factor, affecting the production yield. While whole-cell biocatalysts provide an important production cost advantage, issues regarding mass transfer, selectivity, membrane permeability, or competing metabolic processes can disqualify them from certain processes.[279] However, as the high

production costs are a major challenge for implementing biocatalytic processes in the chemical industry, whole-cell biocatalysis holds significant potential for reaction scaling and bulk chemical production, provided that productivity can be enhanced through improvements in the biocatalyst and expression levels.[275, 280]

The use of isolated enzymes generally provides the highest catalyst productivity. However, the costs of enzyme purification through chromatography are too high for economically viable large-scale processes, due to the high cost of the resin materials and solvents.[208, 275] The crude enzyme solution obtained after the lysis of the cell membrane is sometimes used as a compromise.[281] However, a literature estimation shows that adding a cell disruption step after protein expression increases the catalyst production costs by approximately a factor of 2, while purifying the enzyme leads to about 10-fold higher costs, compared to whole cells.[275] This can be circumvented by developing extracellular protein production systems. Targeted protein secretion systems are in development and have found uses in biocatalyst production.[282, 283] Another option is enzyme immobilization, which can enable the catalyst separation and recycling after the reaction. However, the large-scale use of immobilized enzymes remains limited due to the high costs of immobilization materials.[284] Carrier-free immobilized enzymes are being explored as a more cost-efficient alternative.[285]

The design of processes to include reagent, catalyst or cofactor recycling, and efficient heat exchange distribution can further improve the efficiency of the biocatalytic system and reduce costs. One of the major issues of chemical production in general is the downstream processing and product isolation.[275] This is an even more pressing problem in biocatalytic reactions, which tend to take place in an aqueous environment, with reduced substrate and product concentrations. In this case, the sustainability impact of the mild reaction conditions might be canceled by the necessity for large amounts of extraction solvents or complex purification steps. These issues can be addressed by attempting to improve the substrate tolerance and the productivity of the biocatalysts, both through enzyme and formulation optimization, as well as optimizing biocatalytic reactions in unusual environments, such as organic solvents or multiphase systems. Flow reactors can also help overcome some of the issues, through the continuous removal of side products and the recirculation of remaining or regenerated reactants.

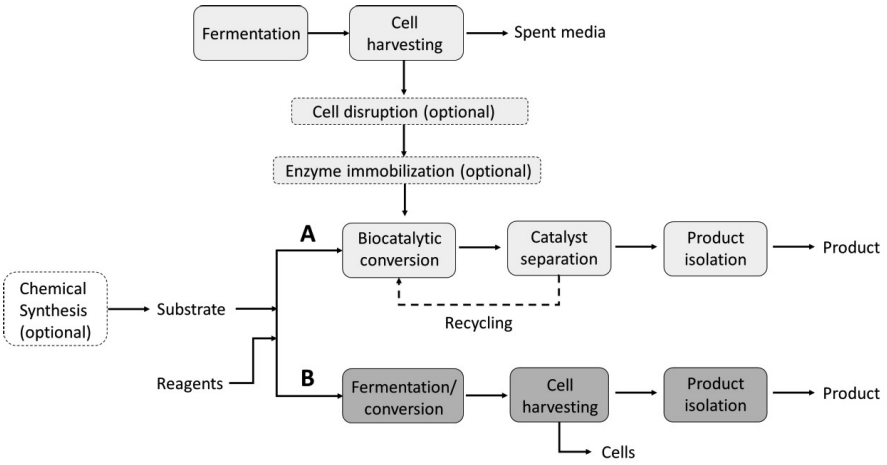

Scheme 4. General process scheme for biocatalytic processes in which the fermentation is separated from the target biocatalytic reaction (**A**) or in which fermentation is coupled to the desired biocatalytic process (**B**). The enzyme preparation steps depend on the desired formulation. In case A, the catalyst can sometimes be separated and reused.

The development of biocatalytic processes can help advance sustainable industrial practices, providing an alternative to traditional chemical synthesis. Large-scale implementation of biocatalysis has been adopted in various sectors such as pharmaceuticals, agriculture, specialty chemicals, food chemistry, and biofuels.[179] It was estimated that the bioeconomy contributed to 5% of EU's GDP in 2021, with a total value added of 728 billion euro, compared to 474 billion euro in 2009.[286] Within the bioeconomy umbrella, the manufacturing of bio-based pharmaceuticals and bio-based chemicals have registered significant positive trends since 2009, with approx. 60 billion euro (bio-based pharmaceuticals) and 10 billion euros (bio-based chemicals, excepting bio-fuels) added value in 2021. Within this scenario, scaling biocatalytic processes could lead to more sustainable supply chains, lower environmental footprints, and reduced reliance on petrochemicals. In this context, addressing the challenges of scaling up enzymatic reactions remains a key development target in biocatalysis.

2.4 Methyltransferases

C-C bond formation is a fundamental process in chemical synthesis and the basis of many biochemical processes. In living organisms, the attachment of methyl groups to biomolecules is one of the most common reactions, with implications for a variety of biological processes, such as gene regulation, molecular signaling, or secondary metabolite synthesis.[287] *S*-Adenosyl-L-methionine (SAM)-dependent methyltransferases are found throughout all natural systems, targeting a wide range of biological molecules. They typically transfer a methyl group from the SAM cofactor to nucleophiles through an S_N2-type mechanism. The enzymatic transfer of small alkyl units is becoming attractive in pharmaceutical and fine chemical industries due to the improved selectivity - when compared to most chemical methods.[12, 156] Small molecule methyltransferases can catalyze the methylation of various scaffolds with excellent chemo-, regio- and stereoselectivity. Besides the selectivity advantage, methyltransferases can provide greener synthetic paths to fine chemicals, by acting in aqueous solutions and mild conditions.[11] As illustrated in Chapter 2.2, methylation can significantly influence the biological and biophysical properties of a biologically active molecule, making efficient methylation strategies important for drug development. Stereo- and regioselective methylation poses a challenge for chemical synthesis, often requiring toxic reagents and complex catalysts. A shift toward biocatalytic methylation offers a promising approach to developing more effective synthetic strategies for methylated compounds.[10]

Methyltransferases have evolved to fulfill various roles, contributing to many biological functions and the biosynthesis of a wide range of secondary metabolites. Consequently, various classifications can be established, based on different criteria. In regards to the type of target biomolecule, there are three main categories:

- Protein methyltransferases catalyze the transfer of methyl groups to specific amino acid residues in proteins, mostly lysine and arginine. Most known protein methyltransferases methylate histones, acting as key mediators for the regulation of gene transcription.[158] This makes these enzymes particularly attractive drug targets. The two major protein methyltransferase families involved in histone methylation are lysine methyltransferases (PKMTs) and protein arginine methyltransferases (PRMTs). Dysregulation of protein methyltransferase activity has been linked to various diseases, including cancer, neurological, inflammatory and metabolic disorders, highlighting their importance in maintaining cellular homeostasis.[288]

- Nucleic acid methyltransferases catalyze the methylation of cytosine or adenine bases, leading to gene silencing and contributing to cellular differentiation, epigenetic

regulation, and cancer progression. DNA and RNA methylation are epigenetic markers present across species, at all developmental levels. In prokaryotes, it has the role of differentiating between self and foreign DNA, while in eukaryotes, it is used for DNA fragment silencing.[158] Due to their critical role in the development and survival of living organisms, DNA methyltransferases are intensely regulated through various inhibitory mechanisms. Some of these mechanisms, when dysregulated, have been associated with cancer proliferation.[289] This makes this class of enzymes a particularly important target for the development of new inhibitors as therapeutics, and extensive research is focusing on understanding their influence and mechanisms in epigenetic regulation.[290]

- Small molecule methyltransferases are involved in metabolic pathways, usually playing a role in the functionalization of secondary metabolites. They are often involved in the biosynthesis of natural products with various biological activities. Due to their substrate diversity, they are attractive as catalysts for the late-stage modification of complex molecules.[287]

Several SAM-dependent methyltransferases have been successfully utilized in the synthesis and diversification of clinically relevant natural products.[212, 291-298] However, engineering natural product methyltransferases is challenging due to the low reaction rates, limited substrate availability, and the relatively small number of characterized enzymes in this class. Additionally, the requirement for stoichiometric amounts of the SAM cofactor presents a significant obstacle, due to its high cost and chemical instability, hindering extensive screening efforts.[11] Nevertheless, the potential of biocatalytic methylation for the production of industrially relevant compounds is becoming more noticeable.[10-12] Late-stage enzymatic methylation for the synthesis of natural products and pharmaceuticals has seen an abundance of successful examples in the past years. Some of the latest examples of the successful enzymatic methylation of biologically or industrially relevant molecules will be discussed in detail in this chapter.

2.4.1 Structural and mechanistic aspects of SAM-dependent methyltransferases

Five main structural classes of SAM-dependent methyltransferases have been described.[299] However, within the same class, the amino acid sequences can differ greatly. Most known methyltransferases belong to the structural class I (Figure 17A), which is characterized by a Rossmann-like fold containing central parallel β-sheets, flanked by α-helices, and a

characteristic GXG motif allowing a loop bend that creates the cofactor binding domain. A strongly conserved position in class I methyltransferases is an acidic residue forming hydrogen bonds with both of the ribose hydroxyl groups of the cofactor (Figure 17C).[299] Catechol *O*-methyltransferase (COMT) is one of the smallest methyltransferases, showcasing the specific class I structural core (Figure 17A).[300] Class II methyltransferases contain a central long antiparallel β-sheet, with groups of helices at both ends, and was first identified in the cobalamin-dependent methionine synthase.[301] Class III structures are similar to class I, but contain two αβα domains, binding the cofactor between each other. Several protein methyltransferases are known to be part of this structural fold.[299] The SPOUT family of RNA methyltransferases are representatives of class IV, with the core structure containing a homodimer with the active site at the subunit interface.[302] Class V methyltransferases are the SET-domain proteins, which are best known to methylate lysine residues at the tails of histones, regulating chromatin function. The SET domain is a conserved region containing the catalytic site of these enzymes. The cofactor binds to a concave region on the enzyme surface in the vicinity of a conserved tyrosine residue, involved in the catalytic mechanism.[299, 303]

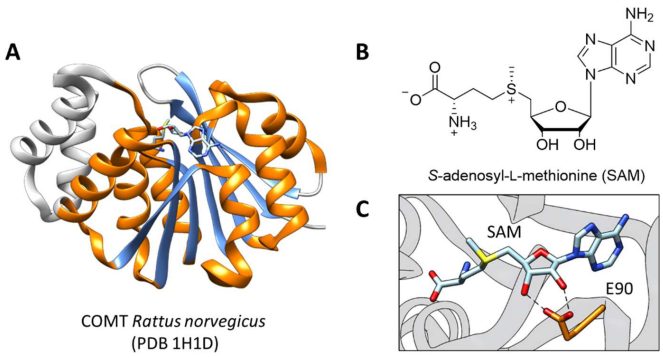

Figure 17. A. A representative example of a class I small molecule methyltransferase, catechol *O*-methyltransferase (COMT) from *Rattus norvegicus*. The Rossmann fold-like domain is represented in blue (β-sheets) and orange (α-helices). The bound SAM cofactor is represented in light blue. **B.** Representation of the SAM cofactor structure. **C.** Hydrogen bonding between the SAM ribose and the highly conserved acidic residue (E90 in this case) in the catalytic site of COMT from *Rattus norvegicus*.

Mechanisms of action

Most methyltransferases use the SAM cofactor as a methyl donor (Figure 17B), methylating their targets through a nucleophilic S_N2 substitution on N, O, C, S or halogen atoms of the target molecules. Several structural features are required for this reaction to take place. The methyl acceptor needs to be placed close to the cofactor methyl group, usually within

approximately 3 Å.[304] A compression motion within the catalytic site of methyltransferases has been proposed to promote the S_N2-type enzymatic methylation by lowering the energy barrier to the transition state.[305-308] Class I methyltransferases often contain structural features such as N-terminal extensions and active site caps. Their roles have not been extensively explored so far, but studies have implied their importance for the dynamic activation of the methylation mechanism, with some also playing a role in substrate recognition.[304, 309] The acceptor molecule should serve as the most chemically reactive nucleophile in the vicinity, which often demands the enzymatic activation of the substrate. This can be achieved through several mechanisms:

- Proximity and desolvation. This mechanism does not require the direct participation of amino acid residues, but the environment of the active site should assure close proximity to the cofactor, a suitable orientation of the substrate, and the exclusion of water molecules from the reaction site (desolvation).

- Acid/base catalysis. Typically involves the presence of a catalytic residue acting as a base to deprotonate the methyl acceptor, activating it for the nucleophilic attack. Often, other residues adjacent to the catalytic base act in a concerted manner for the substrate activation, forming a proton shuttle system. The role of the primary base is most often fulfilled by a histidine or tyrosine residue, accompanied by an adjacent acidic amino acid, such as aspartate or glutamate.[310, 311]

- Metal-dependent catalysis. Metal-dependent methyltransferases can either require a metal ion for the coordination of the substrate, with a nearby amino acid residue acting as a base for substrate activation or display a mechanism in which the metal ion contributes to the deprotonation of the substrate by perturbing the pK_a of the targeted methyl acceptor group. The latter mechanism is specific to phenol *O*-methyltransferases from plants.[304]

There are also several methyltransferases using radical mechanisms for methylation. They belong to the radical SAM superfamily and they use a [4Fe-4S] cluster for the generation of the 5'-deoxyadenosyl radical, which enables the methylation of various targets, such as rRNA,[312] chlorophyll[313] or secondary metabolites such as the chemotherapy agent bleomycin[314] and the antibiotic thiostrepton.[315, 316]

SAH inhibition

The demethylated cofactor *S*-adenosyl-L-homocysteine (SAH) was shown to strongly inhibit many methyltransferases, as it binds to the SAM binding pocket with high affinity. Engineering methyltransferases to reduce SAH inhibition is difficult as this also impacts their affinity for SAM. A potent strategy for avoiding SAH inhibition is utilizing SAH-degrading enzymes from the natural methionine cycle, such as SAH hydrolase (SAHH) or nucleosidase (MTAN). Another strategy for reducing SAH inhibition is the use of SAM recycling systems, which consume the SAH formed after the methylation, regenerating the active cofactor.[317] Alternatively, the SAH inhibitory effect has been used as inspiration for the development of SAH analogs as therapeutical methyltransferase inhibitors.[318]

2.4.2 Small molecule methyltransferases as catalysts

This chapter will describe several examples of small molecule methyltransferases that have been successfully utilized *in vitro* for the synthesis of natural products, building blocks, pharmaceuticals, and other industrially relevant compounds (Figure 18).

Catechol *O*-methyltransferases (COMTs) are some of the best-documented methyltransferases and have been successfully used in multiple biocatalytic or chemoenzymatic synthesis strategies. COMT from *Rattus norvegicus* was recently used for the regioselective structural diversification of tetrahydroisoquinoline alkaloids in cascade with the *O*-methyltransferases SafC from *Myxococcus xanthus*, 6-OMT from *Coptis japonica* and the *N*-methyltransferase CNMT from *Coptis japonica*.[298] The synthesis and diversification of protoberberine and tetrahydroprotoberberine natural product scaffolds were performed using an enzymatic cascade containing a pictet-spenglerase, COMT and chemical Pictet-Spengler reactions in a continuous sequential manner.[295] Rat COMT was also used in cascade with a tyrosinase for the post-translational modification of tyrosine residues from various peptides and proteins.[319]

NovO and CouO *C*-methyltransferases are part of the biosynthesis of the novobiocin and coumermycin antibiotics and were shown to regioselectively methylate a range of non-natural substrates.[320] NovO was also used with a glycosyltransferase in a one-pot cascade to obtain aminocoumarin antibiotic derivatives.[293] Rebeccamycin *O*-methyltransferase (RebM) was used to generate a number of analogs of the anticancer agent rebeccamycin.[321]

The *N-methyltransferase* PsiM was used for the enzymatic synthesis of 6-methylpsylocibin, in a cascade sequence with a tryptophan synthase, a decarboxylase, a monooxygenase and a kinase.[296] Human nicotinamide *N*-methyltransferase (NNMT) was reported to possess a wide substrate scope containing substituted pyridines.[322] A library of NNMT analogs was obtained through enzyme engineering and the identification of natural homologs. Several of the selected variants exhibited activity in the methylation of various aromatic N-heterocycles.[323]

The production of tryptophan-based diketopiperazines, which are a common structural feature of several bioactive natural products such as lansai B and nocardioazine B, was enabled by a stereoselective indole *C*-methyltransferase in the presence of a cofactor recycling system.[292] Furthermore, the radical *C*-methyltransferase TsrM was shown to possess unusual promiscuity. While it can methylate a range of tryptophan and tryptamine derivatives in the 2-position on the indole ring, it was also reported to catalyze the C-methylation in the 4-position of the indole and the N-methylation of tryptamines.[324, 325] Multiple variants of the *C*methyltransferases SgvM and MarI were used for the stereoselective methylation of a variety of α-ketoacids.[326] A generally promiscuous SgvM variant was engineered for more efficient promiscuous alkylation activity, while maintaining stereoselectivity.[327] SgvM and MarI were also used in cascade with transaminases for the stereoselective production of methylated non-canonical amino acids.[328]

While the methylation of thiols is unusual in nature, two catechol *O*-methyltransferases (COMT) from *Myxococcus xanthus* and *Rattus norvegicus* and a caffeate *O*-methyltransferase (CaOMT) from *Prunus persica* were used for the methylation of various aromatic thiols. The study also suggests a potential physiological function for these enzymes in the metabolism of thiol-containing drugs or other endogenous molecules.[294]

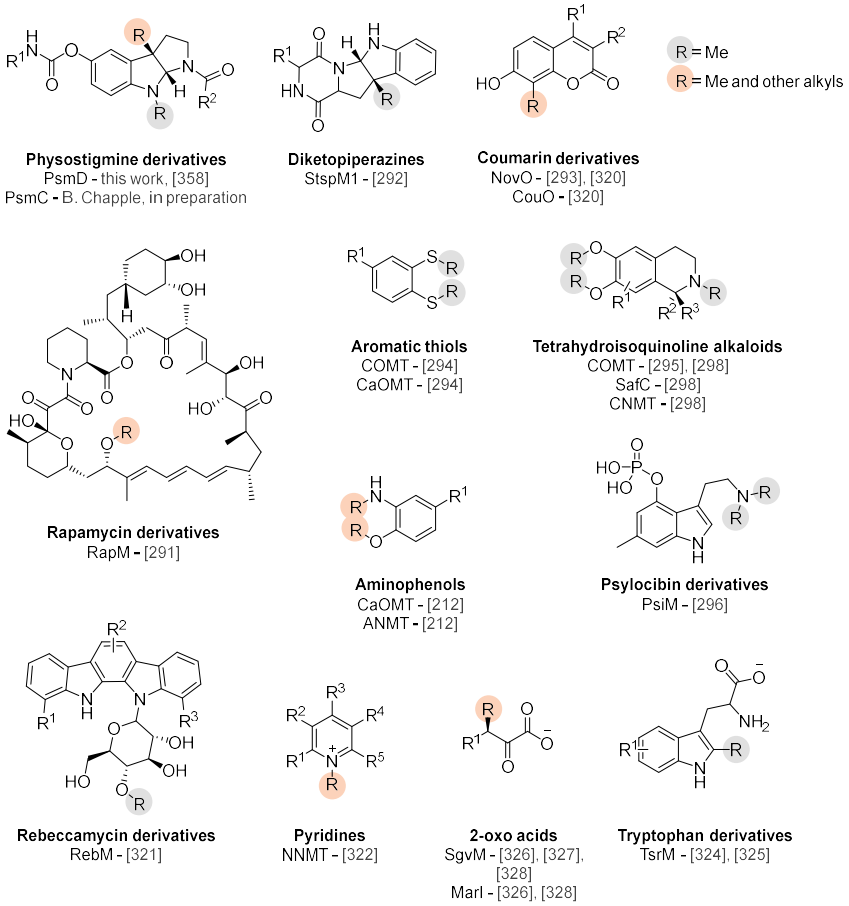

Figure 18. Structural scaffolds that can be alkylated using SAM-dependent small molecule methyltransferases. The position of the enzymatically installed methyl groups is highlighted on each molecule. The positions shaded in grey represent sites of methylation only, while those marked in orange indicate instances where other enzymatic alkylations were also achieved, using SAM cofactor analogs.

2.4.3 Cofactor supply and recycling

The widespread use of methyltransferases as biocatalysts has been limited by the requirement of a stoichiometric amount of the SAM cofactor, for the enzymatic methylation to occur. The SAM molecule is unstable and difficult to produce chemically.[329] Because of its instability, an excess of SAM is often necessary, which can lead to high costs.[12] This prompted the recent development of multiple options for SAM *in situ* enzymatic supply or recycling systems. Despite the significant reduction in the cost of SAM in recent years, challenges such as the low stability, reduced atom economy, and the need to prevent SAH inhibition, have made enzymatic SAM supply and recycling systems essential tools for many biocatalytic methylations. Besides its role as the major natural methyl donor, SAM was found to enable the enzymatic transfer of other groups such as methylene, amino, ribosyl and aminopropyl, showcasing the chemical versatility of this cofactor.[330, 331] In this chapter, the different options for enzymatic SAM generation are discussed, along with their specific advantages, disadvantages and use cases.

SAM enzymatic supply

One of the first enzymatic SAM supply systems used the enzyme SalL, naturally involved in the biosynthesis of chloroethylmalonyl-CoA, to generate SAM from 5'-ClDA and L-methionine (Scheme 5). SalL was used in combination with the *N*-methyltransferase MtfA from *Amycolatopsis orientalis* for the methylation of the antibiotic teicoplanin and with NovO to produce methylated and ethylated coumarin compounds.[320, 332]

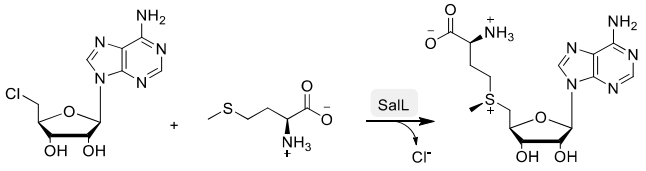

Scheme 5. SAM enzymatic production using SalL.

In nature, the formation of SAM from ATP and L-methionine is catalyzed by methionine adenosyltransferases (MAT) (Scheme 6). These enzymes were successfully used for the *in-situ* cofactor supply in several enzymatic methylations. MAT-COMT/SafC-MTAN cascades were used for the regioselective O-methylation of catechols.[333] MAT was also used for the cofactor supply in the RapM-catalyzed methylation of rapamycin precursors[291] and the RebM-catalyzed diversification of indolocarbazoles.[334]

This supply system has several drawbacks. ATP is required in stoichiometric amounts and is relatively expensive, while MATs are naturally selective for L-methionine, requiring either enantiopure amino acids or wasting half the quantity when using a racemic mixture. Furthermore, the accumulation of SAH after the reaction can lead to the inhibition of the methyltransferase, demanding a SAH removal strategy. However, a major strength of the MAT-based supply is the possibility to produce cofactor analogs by replacing the amino acid. The discovery and development of several promiscuous MATs have rendered this system a reliable source of SAM cofactor derivatives, which can otherwise be difficult to produce. The MAT-based cofactor analog production will be discussed in Chapter 2.4.4. Another advantage of the MAT supply system is the selectivity of the methylation, as no chemical methylating agents are required. This is especially important when the substrate molecule contains additional nucleophilic sites, as it helps prevent non-selective methylation.

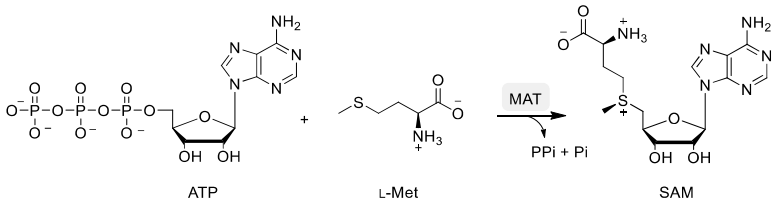

Scheme 6. Scheme of SAM production from ATP and methionine using MAT.

The MAT SAM production system has also been coupled with in vitro ATP generation from adenosine, using the adenosine kinase (ADK) from *Saccharomyces cerevisiae* for the first phosphorylation and polyphosphate kinase 2 from *Acinetobacter johnsonii* (PPK2-I) and *Sinorhizobium meliloti* (PPK2-II) to phosphorylate AMP and ADP (Scheme 7).[335]

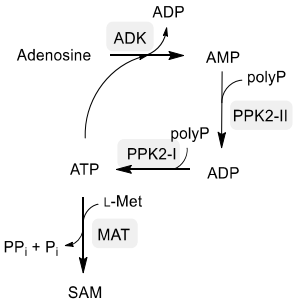

Scheme 7. Scheme of the MAT cofactor supply system, coupled with enzymatic *in situ* ATP production.

SAM recycling

The natural metabolic cycle of SAM is ATP-dependent and it involves six distinct enzymes. It has been successfully reconstituted *in vitro* and used as a SAM recycling strategy in parallel with methylations catalyzed by COMT from *Rattus norvegicus*, anthranilate *N*-methyltransferase (ANMT) from *Ruta graveolens* and SafC from *Myxococcus xanthos* (Scheme 8).[335] The biomimetic SAM recycling cascade achieved up to 25% conversions, corresponding to 10 cycles of SAM regeneration. Using an extensive enzyme cascade is not an ideal solution for an efficient methylation system, as it increases resource demands and the complexity of the process. Further modifications of the biomimetic recycling system were subsequently developed. The integration of homocysteine *S*-methyltransferase (HSMT) from *Saccharomyces cerevisiae* allowed the regeneration of L-methionine from L-homocysteine, increasing the efficiency of the system.[336]

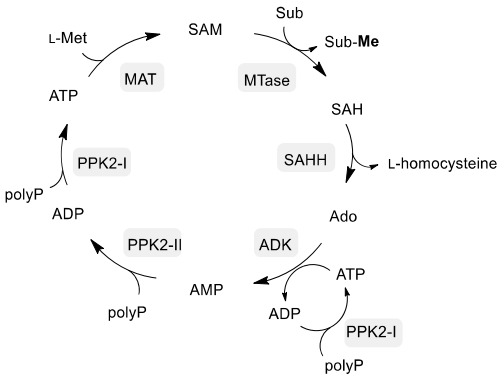

Scheme 8. The biomimetic SAM recycling cascade.

A streamlined one-enzyme SAM recycling system was first reported in 2019, harnessing the capacity of halide methyltransferases (HMTs) to generate SAM from SAH in the presence of methyl iodide as a methyl donor (Scheme 9).[207] This system provided a useful tool for the scaling of enzymatic methylations, as it uses a low-price methyl donor and the SAH generated as a side product in the enzymatic methylation reactions. As such, only catalytic amounts of the cofactor need to be supplemented. The development of HMT-based SAM recycling generated significant progress in methyltransferase biocatalysis, and extensive efforts have since been dedicated to the discovery of new HMT variants and the engineering of the existing ones.

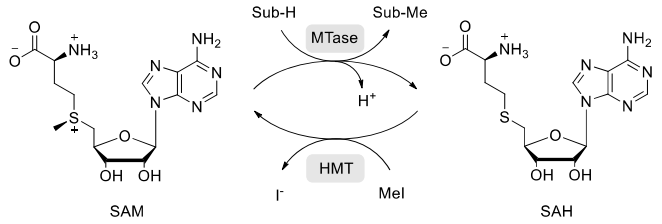

Scheme 9. The HMT cofactor recycling system.

HMT from *Chloracidobacterium thermophilum* (*Ct*HMT) was the first variant shown to perform the SAH methylation in the presence of methyl iodide and has since been used successfully in cascade with other methyltransferases.[207] Other active HMT homologs have since been identified, most notably from *Arabidopsis thaliana*, *Aspergillus clavatus, Batis maritima*, and *Synechococcus elongates*.[337] Enzyme sequence mining of *Pseudomonas* HMTs yielded several homologs displaying better methylation performance. The (so far) best HMT from *Pseudomonas aeruginosa* (*Pa*HMT) performed better than the other previously described HMTs in the SAM production using MeI. *Pa*HMT was used in cascade with SgvM for the C-methylation of α-keto acids.[327]

The main disadvantage of the HMT-based cofactor system is the requirement for methyl iodide as a methyl donor. Methyl iodide is highly toxic, and its low boiling point (42 °C) increases the risk of evaporation under standard enzymatic reaction conditions, requiring excess amounts.[338] Additionally, its low polarity causes it to dissolve in organic solvents, contaminating the extracted products. To counteract these problems, several HMT variants were explored using different methyl donors, with methyl-toluene sulfonate showing the most promise. Active homologs were identified, with the best performing originating from *Ustilago maydis* (*uma*HMT), *Aspergillus clavatus* (*Ac*HMT) and *Kordia algicida* (*kal*HMT).[339]

The development of enzymatic SAM supply and recycling systems has created new opportunities for the practical application of methyltransferase-catalyzed reactions. While the optimization of these systems is still underway, their progress has made the efficient scaling of methyltransferase biocatalysis an attainable goal.

2.4.4 Alkylation using small molecule methyltransferases

Late-stage methylation is appealing due to the "magic methyl" effect, but other alkylations may also provide unexpected benefits when it comes to API diversification. With the advent of SAM analog production strategies, the use of methyltransferases for alternative functionalizations has emerged as a topic of growing interest. Natural SAM analogs were identified as general methyltransferase inhibitors displaying therapeutic applications, such as the antimicrobial agent sinefungin or the epigenetic regulator methylthioadenosine.[340] Multiple other analogs were since synthesized for the targeted inhibition of therapeutically relevant methyltransferases, such as COMT or PRMTs. Double-activated cofactors were also synthesized by replacing the methyl group with activated groups such as allyl or propargyl. This enabled the functionalization of methyltransferase substrates with a reactive tag for subsequent attachments, allowing the production of selective probes for imaging applications.[318] For biocatalytic applications, the use of enzyme cascades for the *in-situ* production of cofactor derivatives is attractive as a solution for the lack of accessibility and poor stability of SAM analogs. Additionally, the stereoselective nature of enzymatic SAM analog synthesis improves the atom economy of the process. All of the previously discussed enzymatic SAM production strategies have been successfully used for the production of SAM analogs (Figure 19).

Alkylations using SalL

SalL was used to produce SAM analogs starting from methionine analogs and 5'-CIDA, and used in cascade with a range of small molecule (NovO, PRMT1) and DNA methyltransferases.[320, 332] The site-directed mutagenesis of SalL from *Salinispora tropica* and the fluorinase FDAS from *Streptomyces cattleya* yielded slight increases in their activities for the synthesis of SAM analogs. [341, 342] The modification of the cofactor nucleotide also provided an improvement in the efficiency and substrate scope of enzymatic alkylations using SalL and NovO.[343]

Alkylations using MAT

The screening of methionine analogs in the presence of ATP and MAT from humans, *Escherichia coli* (*Ec*MAT) and *Methanocaldococcus jannaschii* (*Mj*MAT) homologs revealed the capacity of MATs to produce a wide range of cofactor analogs.[344, 345] Furthermore, all studied enzymes were also able to use Se-Met analogs as substrates. The human MAT hMAT2 was successfully used in combination with RebM for the alkylation of indolocarbazole analogs.[334] The engineering of human MAT2A revealed mutant I117A with improved activity using bulky methionine analogs. This variant was used in combination with protein

methyltransferases G9a and GLP1 for the post-translational modification of chromatin.[346] Methionine analogs can however be difficult to produce chemically, and only the L-enantiomer is accepted by MATs as substrate.[347] In a recent study, *Sc*OAHS, a PLP-dependent *O*-acetyl-L-homoserine sulfhydrolase from *Saccharomyces cerevisiae*, was used to produce methionine analogs in a cascade involving *Ec*MAT for cofactor production, COMT or ANMT for alkylating the target aromatic substrates, and *Ec*MTAN to degrade the resulting SAH, preventing methyltransferase inhibition.[348] MAT from *Cryptosporidium hominis* (*Ch*MAT) was engineered for the generation of SAM analogs with aromatic photocaging groups. The best mutant, I122A/I330A was used for the photocaging of plasmid DNA.[349] Furthermore, the directed evolution of *Ec*MAT revealed variant I303V/Q22R displaying a 2-fold increase in activity, compared to the wild type.

Alkylations using HMT

Driven by the goal of expanding the range of cofactor analogs available through HMT production and recycling, several promiscuous active HMT homologs have been identified, most notably from *Arabidopsis thaliana*, *Aspergillus clavatus*, *Baris maritima* and *Synechococcus elongatus*.[337] The substrate profiling of a range of anion methyltransferases revealed multiple promiscuous HMT homologs from various organisms. Out of the tested enzymes, *Ac*HMT showed the highest promiscuity towards a wide range of halogenated alkyl, allyl and aryl donors and was used in casacades with engineered *N*-methyltransferases for the regioselective allylation of pyrazoles.[350] HMT from *Burkholderia xenovorans* was used for the generation of fluorinated SAM from SAH and fluoromethyl iodide and used in combination with several small molecule methyltransferases, generating fluoromethylated compounds.[351] Directed evolution of *At*HMT resulted in the identification of the V140T mutant, which exhibited an approximately 6-fold increase in catalytic efficiency for producing *S*-adenosyl-L-ethionine (SAE) compared to the wild type, along with enhanced activity for other cofactor alkylations.[352] Later, a structure-based directed evolution of HMT from *Aspergillus clavatus* yielded mutant V27F/P8L/V265W, which improved the ethylation activity by 38-fold compared to the wild type, reaching up to 421.5 mU/mg ethylation activity, 16-fold higher than *At*HMT(V140T).[353]

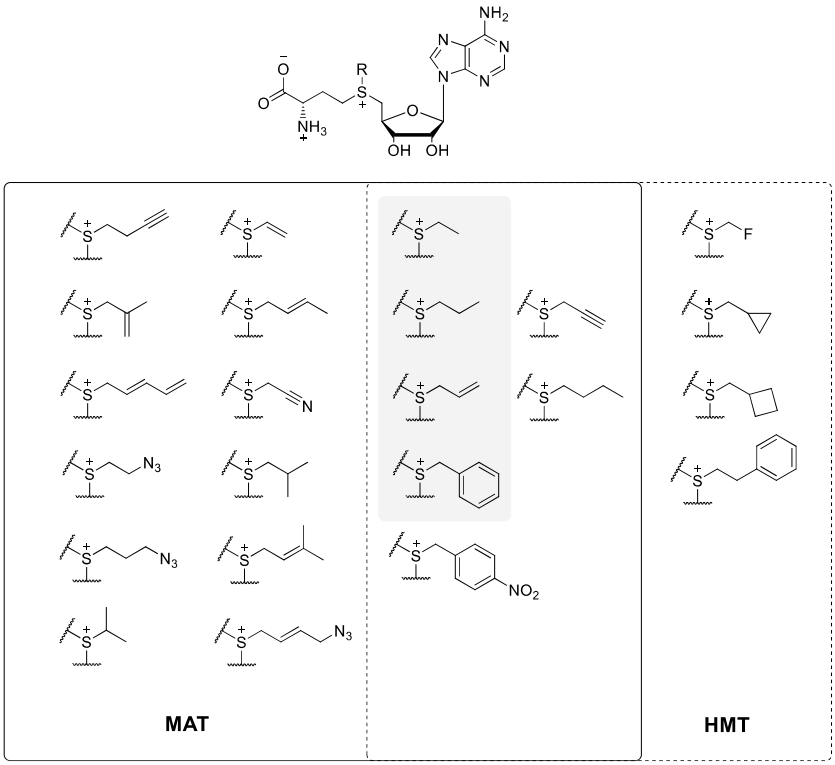

Figure 19. Enzymatically produced cofactor analogs reported in the literature so far using MATs (full line box) or HMTs (dashed line box). The overlapping derivatives have been produced using both MATs and HMTs. In addition to MAT and HMT, the highlighted cofactor derivatives were also synthesized using SalL.

A comparative study evaluated *Ac*HMT and *Mj*MAT (mutant L147A/I351A) for cofactor analog supply in coupled reactions with NovO, for the regioselective alkylation of coumarins. While methylations occurred with similar efficiencies, the MAT system performed significantly better for all the other tested alkylations.[354] However, a direct comparison between the two systems cannot be reliably drawn based on the experimental conditions presented in the study. As the authors note, the cofactor is generated and regenerated in catalytic amounts in the HMT recycling system, creating a kinetic barrier due to the lower affinity of the target methyltransferase for the cofactor analogs. That is not the case for the MAT system, in which the cofactor was directly produced in excess from its precursors. Furthermore, the MAT setup used MTAN for the degradation of the spent cofactor SAH, mitigating its inhibitory effect. It is likely that the lower affinity of methyltransferases for cofactor analogs is a significant obstacle

to the HMT-based recycling of these analogs. Using them in catalytic amounts may not overcome the kinetic disadvantage, while higher concentrations result in increased levels of inhibitory SAH in the mixture. This would require either the development of faster HMTs or the increase of the target methyltransferase affinity for cofactor analogs.

A variety of small molecule methyltransferases were successfully used for alkylations in combination with all of the enzymatic cofactor analog production systems presented in this chapter. The recombinant *O*-methyltransferase RapM, involved in the biosynthesis of the immunosuppressant rapamycin was used for the production of rapamycin analogs through the regioselective alkylation using cofactor derivatives produced in a coupled system with MAT.[291] NovO and CouO were used for the alkylation of coumarins with non-natural cofactors.[297] A range of new caffeate *O*-methyltransferases (*Ca*OMTs) and anthranilate *N*-methyltransferases (ANMTs) were shown to provide promiscuous methylation activity for aminophenols, as well as an acceptance of multiple cofactor analogs, expanding the available product pool.[212] The *C*-methyltransferase SgvM from *Streptomyces griseovidris* has been the first documented application of a methyltransferase in the catalysis of stereoselective C-alkylation, using SAM cofactor analogs and α-ketoacids as substrates.[355] Engineered nicotinamide, phenylethanolamine and histamine *N*-methyltransferases allowed the N-ethylation and propylation of pyrazoles.[356]

Selective alkylation using SAM-dependent methyltransferases in the presence of cofactor analogs is a new and fast-growing opportunity in methyltransferase biocatalysis. Recent advances in cofactor analog production and cascade optimization led to the apparition of multiple successful examples of enzymatic alkylations using methyltransferases. Although the research on the topic is still in the initial stages, the benefits of enabling these transformations have been acknowledged.

2.5 The indole *C*-methyltransferase PsmD

Besides its original source - the Calabar bean, physostigmine was found to be naturally produced in several *Streptomyces* species.[357] The biosynthetic cluster responsible for physostigmine formation in *Streptomyces griseofuscus* was identified in 2013 (Scheme 10).[105] The biosynthetic route originates from L-tryptophan (**6**), which is hydroxylated in the 5-position by a tryptophan hydroxylase, located outside of the biosynthetic gene cluster. The product **7** is decarboxylated by a PLP-dependent decarboxylase (PsmH), obtaining serotonin (**8**). An acetyltransferase (PsmF) performs the N-acetylation of serotonin, leading to normelatonin (**9**), which is further carbamoylated by the carbamoyltransferase PsmE. Then, the carbamoyl is N-methylated by the SAM-dependent methyltransferase PsmA, leading to **10**. The installation of the stereogenic center and formation of the pyrroloindole ring is catalyzed by the SAM-dependent *C*-methyltransferase PsmD.

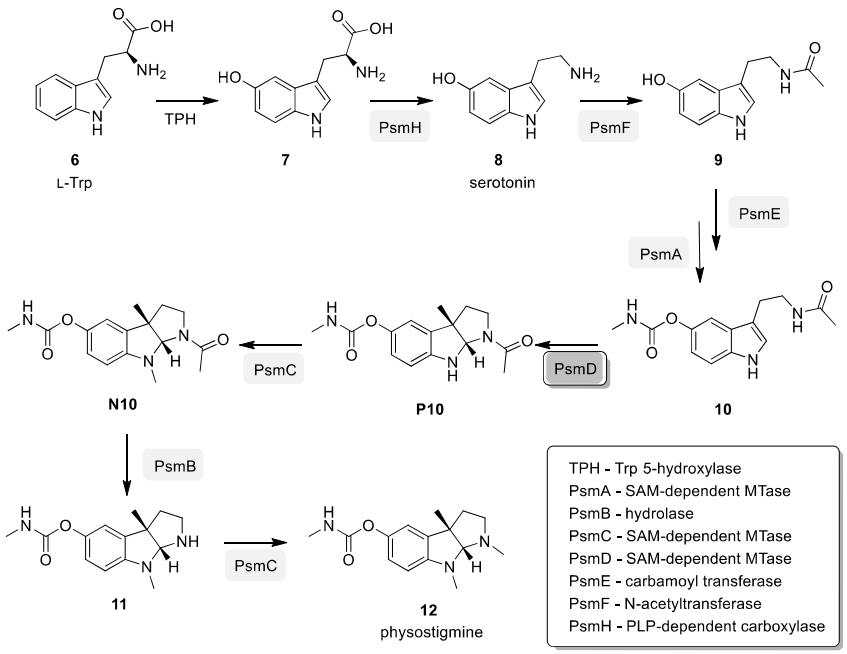

Scheme 10. Physostigmine biosynthetic pathway.

PsmD catalyzes the stereoselective C-methylation in the 3-position of the indole ring, disrupting the conjugated indole ring and triggering a spontaneous intramolecular cyclization.

Finally, a deacetylation of **P10** is catalyzed by the hydrolase PsmB and the remaining free nitrogens are methylated by the SAM-dependent *N*-methyltransferase PsmC.

The *C*-methyltransferase PsmD has attracted attention as a biocatalyst due to its stereoselectivity and role in the construction of the pyrroloindole ring from indoles. In a previous study, PsmD from *Streptomyces griseofuscus* (PsmD_*Sg*) was heterologously expressed and characterized.[358] The enzyme was used in a chemo-enzymatic process for the diversification of the chiral pyrroloindole products. The stereoselectivity of the enzyme was confirmed by chiral HPLC analysis. A three-step chemical synthesis route was established for the production of the natural PsmD substrate and its analogs. The substrate scope of the enzyme was explored, and several trends were identified: while the enzyme accepts a range of substrates substituted on the amide and the carbamate, the activity decreased with a larger substituent size (Figure 20). Furthermore, it was observed that in the absence of the substrate carbamate, the enzyme activity is severely hindered. Finally, PsmD was used in parallel with an HMT-based cofactor recycling system for the preparative chemoenzymatic synthesis of the natural PsmD product and two other derivatives, using lysates for the biocatalysis. The obtained product derivatives were shown to display AChE and BChE inhibitory effects (Table 3).[358] This study demonstrated the potential of PsmD as an effective biocatalyst for stereospecific indole methylation and pyrroloindole production.

The later steps of physostigmine biosynthesis (PsmD, PsmB and PsmC) were used for a mutasynthetic approach to produce physostigmine derivatives in *Myxococcus xanthus,* using chemically synthesized PsmD substrate analogs. The obtained pyrroloindoles were tested for AChE and BChE activities. The obtained IC_{50} values revealed a high selectivity of the ethyl-carbamate compounds for BChE, while the butyl-amide derivative provided lower IC_{50} than physostigmine for both receptors (Table 3).[153]

Table 3. IC_{50} values towards AChE and BChE for the PsmD natural product and several analogs, as well as the known inhibitors physostigmine and rivastigmine.

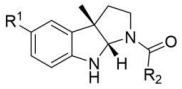

R^1	R^2	AChE IC_{50} (µM)	BChE IC_{50} (µM)	Ref.
Me-carbamoyl	Me	0.09	0.01	[358]
Me-carbamoyl	*t*-Bu	90	20	[358]
H	Me	17	400	[358]
Et-carbamoyl	Me	1.1	0.1	[153]
Me-carbamoyl	Pr	0.1	0.006	[153]
physostigmine		0.13	0.12	[358]
rivastigmine		36.1	1.0	[358]

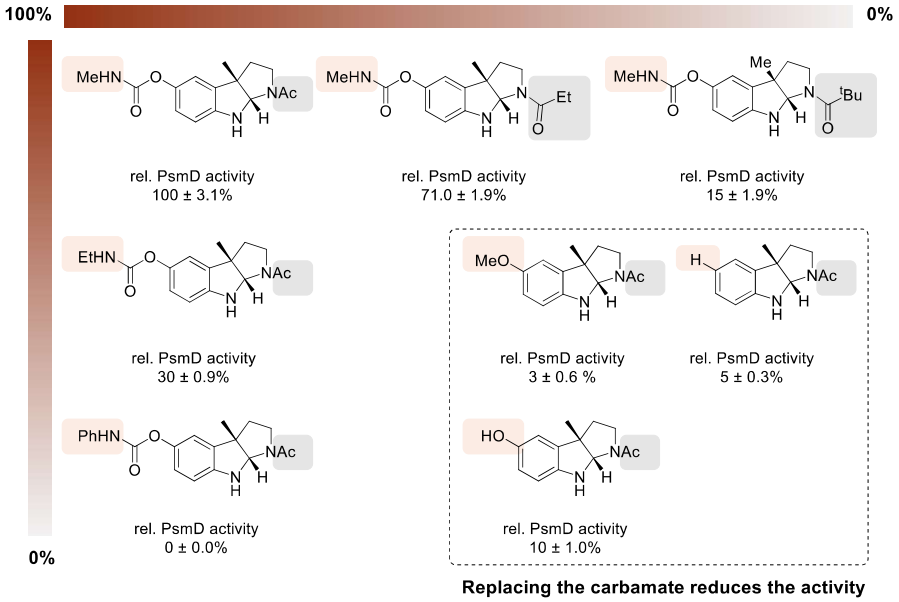

Figure 20. Activity trends of PsmD_*Sg* as a function of substrate size. The relative conversions are represented as percentages.

Furthermore, a PsmD analog was identified in *Streptomyces albulus* (PsmD_*Sa*) and heterologously expressed in *E. coli.* Initial analysis showed a significant boost in the enzyme time and temperature stability, compared to PsmD_*Sg*, while maintaining the same stereoselectivity of the methylation. This provided a promising candidate for the further

development of this type of enzymes as efficient biocatalytic tools for the stereoselective late-stage methylation of indoles.[359] The analysis and development of PsmD_*Sa* enters the scope of the present work and will be detailed in the following chapters.

3. Results and discussion

3.1 Characterization of a PsmD homolog from *S. albulus*

PsmD from *S. griseofuscus* (PsmD_*Sg*) displayed biocatalytic activity for the stereoselective C-methylation of various substrate analogs (Scheme 11). However, its limited stability can hinder its use, especially in preparative applications. A protein sequence BLAST (NCBI database) revealed a protein with high sequence similarity (90% identity, Figure 21), originating from *Streptomyces albulus* (PsmD_*Sa*). This organism was not previously known to produce physostigmine. The *Streptomyces albulus* strain has been reclassified as *Streptomyces noursei* since the time of this study.[360] However, it will be referred to as *Streptomyces albulus* throughout this work to maintain clarity and consistency with the published data.

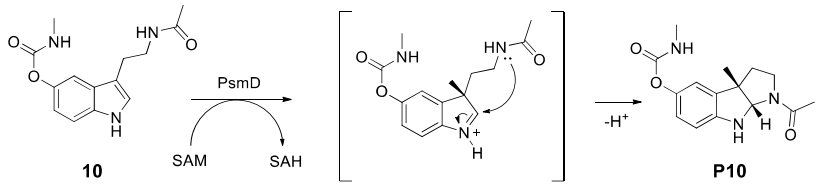

Scheme 11. The reaction catalyzed by PsmD_*Sg* and PsmD_*Sa* in the presence of the SAM cofactor.

Figure 21. Protein sequence alignment for PsmD_*Sa* and and PsmD_*Sg*. Alignment visualization was performed using Jalview Desktop App.

3.1.1 PsmD substrate synthesis

According to the information gained from the biosynthetic pathway elucidation, the natural substrate of PsmD_*Sg* and its homolog PsmD_*Sa* is 3-(2-acetamidoethyl)-1H-indol-5-yl methylcarbamate (**10**). A three-step synthetic route was established for its production, starting from 2-[5-(benzyloxy)-1H-indol-3-yl]acetonitrile (**13**).[358] In the first step, the nitrile group is reduced to amine in the presence of a $NaBH_4$, after which the acylation with acetic anhydride takes place, in the presence of $NiCl_2$, to obtain **14**. The second step is a Pd-catalyzed deprotection of the phenol, leading to N-acetylserotonin (**9**). Finally, in the third step, the phenol is deprotonated using triethylamine, and the carbamate group is attached using methylcarbamoyl chloride in the presence of DMAP. The substrate used for the characterization and mechanistic analysis of PsmD_*Sa* was synthesized directly from N-acetylserotonin (**9**), using the last step from the described sequence, with a 47% yield (Scheme 12). N-acetylserotonin was synthesized according to the procedure described in literature[358] and kindly provided by Pascal Schneider (Institute of Bioorganic Chemistry, Heinrich Heine University Düsseldorf).

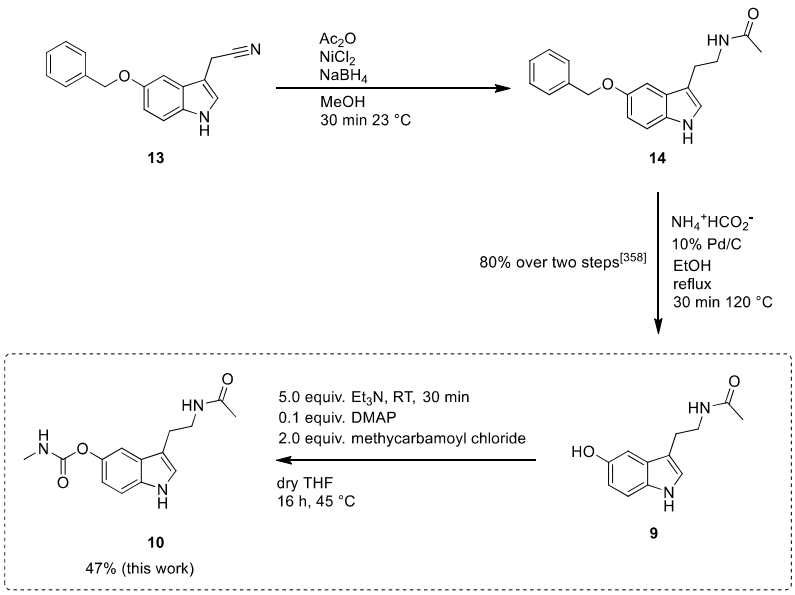

Scheme 12. Synthetic sequence for the production of the PsmD natural substrate **10,** used for PsmD_*Sa* characterization. N-acetylserotonin (**9**) was produced by Pascal Schneider for [358]. The final carbamoylation step was performed in this work, according to the literature procedure.[358]

3.1.2 Expression and purification of PsmD_*Sa*

The synthetic gene for the wild-type PsmD from *Streptomyces albulus* (PsmD_*Sa*) was purchased from a chemical vendor and was flanked with the recognition sites for the NdeI and XhoI commercial restriction enzymes. The gene was introduced into the pET21a(+) vector by restriction/ligation, introducing a C-terminal His_6-tag into the sequence and using a T7 promoter system and a *lac* operator. The expression was performed in the *E. coli* BL21 Gold (DE3) strain (Agilent Technologies, USA), which allows simple genetic manipulation as well as increased efficiency for protein T7 expression due to protease deficiency and the presence of the phage T7 polymerase.[361-363] The Gold-type strains are engineered to improve transformation efficiency due to the Hte (high transformation efficiency) phenotype and reduce plasmid degradation due to the inactivation of the gene coding for the endonuclease I (*endA*).[364-367] The initial cloning and expression of PsmD_*Sa* were performed by Nadiia Pozhydaieva (Institute of Bioorganic Chemistry, Heinrich Heine University, Düsseldorf)

The *E. coli* BL21 Gold (DE3) cells were cultured in TB medium, in the presence of ampicillin for plasmid uptake selection. The pET21a(+) vector contains the AmpR gene coding for beta-lactamase, leading to the ampicillin resistance of the successfully transformed cells. Heterologous protein expression in IPTG-induced systems relies on the Lac repressor to inhibit the gene expression before induction. The expression was triggered by the addition of 100 µM IPTG in the exponential growth phase, corresponding to an optical density (OD_{600}) of 0.5-0.8 (Figure 22). The OD_{600} at induction as well as the increase of the IPTG concentration did not significantly influence the expression efficiency. Furthermore, glucose supplementation (0.2% w/v) did not improve the expression. The isolation of PsmD_*Sa* was performed by affinity chromatography on Ni-NTA resin-packed columns, using an imidazole gradient for elution. This method yielded the target protein with high purity, typically producing about 3-4 mg of pure protein per gram of cells.

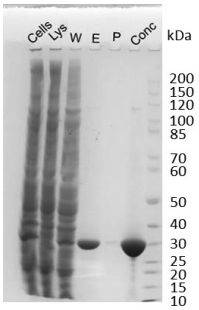

Figure 22. SDS gel showing the steps in the purification of PsmD_*Sa* by Ni-NTA affinity chromatography. Legend: Cells – *E. coli* cells containing the expressed PsmD_*Sa*; Lys – cell-free extract after lysis; W - column washing fractions at 50 mM imidazole; E – elution fraction at 150 mM imidazole; P – column purging fraction, at 1 M imidazole; Conc – final concentrated protein solution.

3.1.3 Biochemical characterization of PsmD_*Sa*

The most prominent feature of PsmD_*Sa* is its increased stability, compared to its homolog, PsmD_*Sg*. This became most obvious when it was observed that the methylation activity of PsmD_*Sa* remained constant after the incubation of the enzyme at 35 °C for 24 h (Figure 23a). In contrast, PsmD_*Sg* started becoming inactivated after 4 h of incubation, with a complete loss of activity after 24 h. A temperature screening was performed, showing that PsmD_*Sa* performs better than its homolog at higher temperatures, with an optimal temperature of 45 °C (Figure 23c). This tendency is also visible in the thermostability study, revealing a melting temperature of 58.6 °C, compared to 55.3 °C for PsmD_*Sg* (Figure 23b). The conversion was assessed under different pH conditions. The enzyme maintains most of its activity in the 6-8 pH range, with an optimum at pH 7.5 (Figure 24).

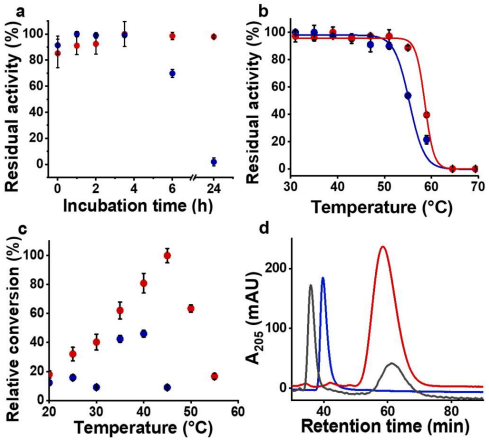

Figure 23. Biochemical characterization of PsmD_*Sa* (red) and PsmD_*Sg* (blue). **a**. Activity over time at 35 °C. **b.** Thermal inactivation. **c.** Conversion as a function of temperature**. d.** Chiral HPLC chromatogram showing substrate **10** (blue), racemic standard **P10** (grey) and the **P10** enantiomer obtained from the PsmD_*Sa* reaction (red). The stability in time and melting temperature experiments were performed by Nadiia Pozhydaieva (Institute for Bioorganic Chemistry, Heinrich Heine University Düsseldorf). The figure was produced for [1] and used here with the agreement of the American Chemical Society.

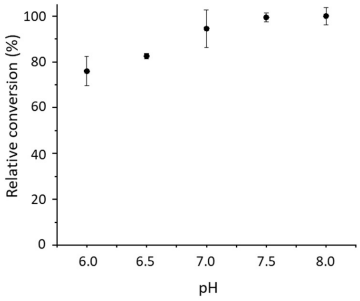

Figure 24. pH screening of PsmD_*Sa* activity. The conversions were determined via normal-phase high-pressure liquid chromatography (NP-HPLC). The figure was produced by the author for [1] and used in this work with the agreement of the American Chemical Society.

3.1.4 Substrate scope and selectivity

PsmD_*Sa* was shown to perform the C3 methylation in a stereoselective manner, similarly to PsmD_*Sg*. HPLC analysis of the reaction mixture, using a chiral stationary phase, shows that

the same enantiomer was exclusively formed as in the case of the *S. griseofuscus* homolog. Although the exact configuration of the enantiomer could not be determined experimentally, the *S*-enantiomer of physostigmine is naturally produced by *S. griseofuscus*.[105, 368] It is then reasonable to conclude that the methylation catalyzed by both PsmD homologs results in the *S*-enantiomer of **P10** (Figure 23d).

The substrate scope of PsmD_*Sa* was evaluated by comparing the specific activities calculated from the conversion of SAM to SAH, which was measured using the commercially available MTase-Glo™ assay. The MTase-Glo™ assay measures the SAH concentration based on luminescence measurements. The SAH formed after a methyltransferase-catalyzed methylation is converted enzymatically to ADP, and then to ATP. Finally, a luciferase catalyzes the conversion of luciferin to oxyluciferin using the previously obtained ATP, leading to measurable luminescence (Scheme 13).[369] The assay is highly sensitive, allowing the analysis of methyltransferase reactions in analytical scale. However, due to the multiple preparation and incubation steps and the prohibitive cost, it is not suitable for high-throughput analysis.

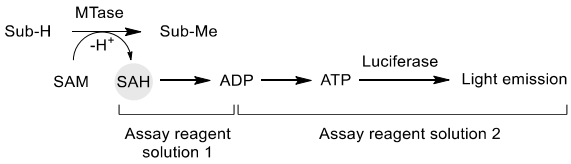

Scheme 13. MTase-Glo™ assay steps and functioning principle.

PsmD_*Sa* was tested in reaction with a variety of substrates bearing substituents either on the amide or the carbamate, as well as substrates substituted in the 5-position, lacking the carbamate (Figure 25). This included natural products such as melatonin (**25**) and N-acetylserotonin (**9**). The overall trends are consistent with those observed in the case of PsmD_*Sg*.[358] Although PsmD_*Sa* displays a relatively broad substrate scope, the activity profile shows a decrease in activity with the increase of the substituent volume. Furthermore, the carbamate appears to be an important structural feature of the substrate, its removal leading to a significant reduction of activity (compounds **9**, **25**-**30**). Unexpectedly, substrates halogenated at the 7-position are methylated at a relatively high rate. In particular, the enzyme retains 63% relative activity towards the 7-chlorinated substrate **31**. Overall, despite, the high sequence similarity, PsmD_*Sa* displays slightly higher activities for the less favored substrates, indicating a higher flexibility of the catalytic site.

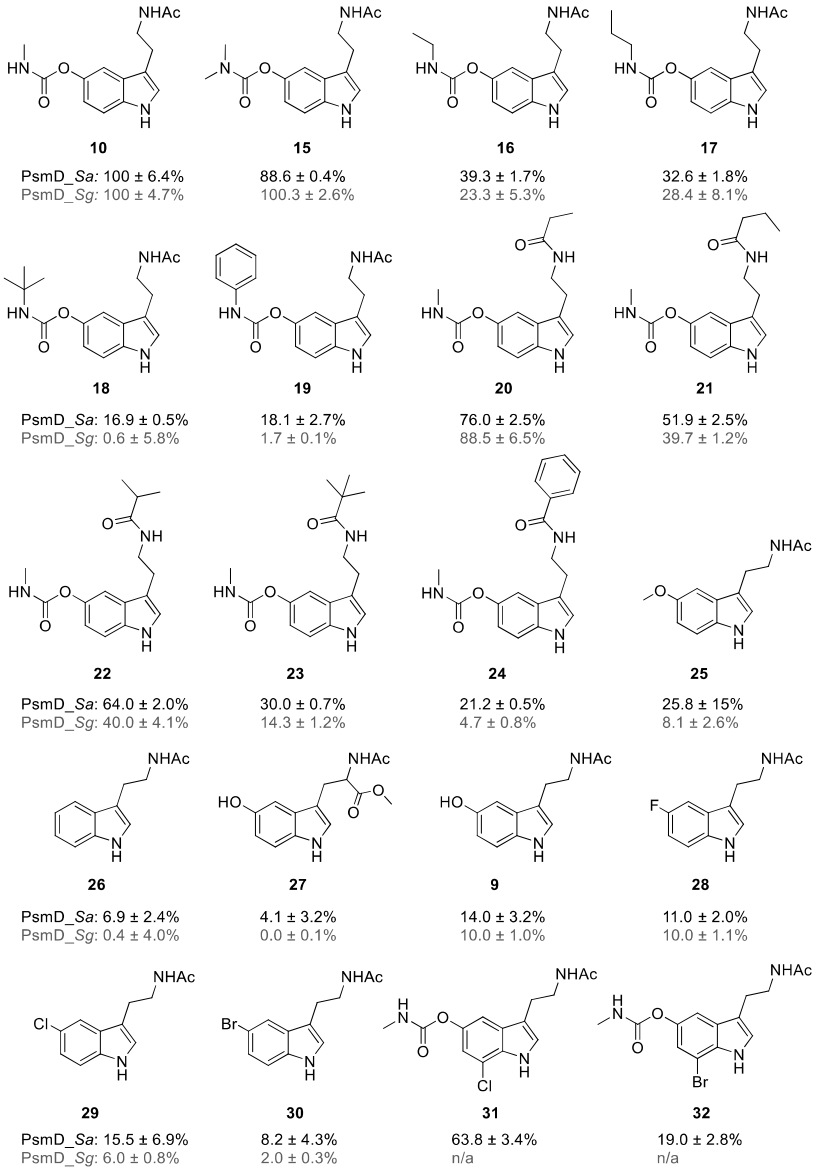

Figure 25. Substrate scope and relative activities of PsmD_*Sg* and PsmD_*Sa*. The conversion of SAM to SAH was determined using the MTase-Glo™ assay**.** The reactions were performed on a 20 µL scale, using 1 µg enzyme, 20 µM substrate and 30 µM SAM. The mixtures were incubated for 15 min at 35 °C. This experiment was realized in collaboration with Nadiia Pozhydaieva (Institute of Bioorganic Chemistry, Heinrich Heine University Düsseldorf).

3.1.5 Kinetic parameters of PsmD_*Sa*

The analysis of the kinetic parameters at 45 °C revealed a few differences between PsmD_*Sa* and its homolog. PsmD_*Sg* displays a slightly higher turn-over number and catalytic efficiency, as well as a higher affinity for both the natural substrate and the SAM cofactor (Figure 26, Table 4). However, PsmD_*Sa* exhibits better performance with longer reaction times due to its higher stability. This compensates for the kinetic disadvantage, resulting in overall higher yields across different substrates. For the sake of data completeness, the missing kinetic analysis as a function of the cofactor concentration for PsmD_*Sg* (at 35 °C) was also performed (Figure 27).

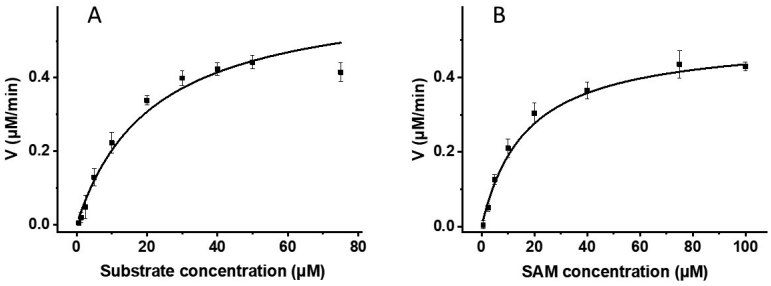

Figure 26. A. Michaelis-Menten kinetic model for PsmD_*Sa* and substrate **10**. Michaelis-Menten model was used as the fit function: $v=v_{max}*[S]/(K_M+[S])$. Fit parameters: R^2: 0.982; Adj. R^2: 0.979; Reduced Chi^2: 1.751. **B.** Michaelis-Menten kinetic model for PsmD_*Sa* and SAM. Michaelis-Menten model was used as the fit function: $v=v_{max}*[S]/(K_M+[S])$. Fit parameters: R^2: 0.993; Adj. R^2: 0.991; Reduced Chi^2: 1.209.

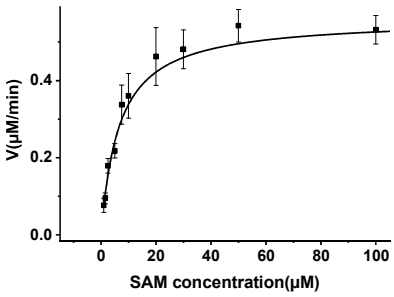

Figure 27. Michaelis-Menten kinetic model for PsmD_*Sg* and SAM. Michaelis-Menten model was used as the fit function: $v=v_{max}*[S]/(K_M+[S])$. Fit parameters: R^2: 0.984; Adj. R^2: 0.982; Reduced Chi^2: 0.790.

Table 4. Kinetic parameters of PsmD_*Sa* and PsmD_*Sg*.

Enzyme	Substr.	v_{max} (µmol * min^{-1} * g_{enz}^{-1})[a]	K_M (µM)[a]	k_{cat} (min^{-1})[b]	k_{cat}/K_M (µM^{-1} * min^{-1})[b]	Ref.
PsmD_*Sa*	**10**	6.1 ± 0.4	14.5 ± 3.1	0.19 ± 0.01	(13 ± 3.7) * 10^{-3}	This work
	SAM	5.5 ± 0.2	16.8 ± 2.2	0.18 ± 0.01	(10 ± 1.8) * 10^{-3}	This work
PsmD_*Sg*	**10**	18.3 ± 0.4	11.3 ± 1.1	0.54 ± 0,01	(93 ± 14.9) * 10^{-3}	[358]
	SAM	11.2 ± 0.4	6.6 ± 0.6	0.36 ± 0.01	(54 ± 7.0) * 10^{-3}	This work

[a] errors from least square fitting including replicates, [b] errors result from error propagation

3.1.6 Chapter summary

◊ A new homolog of PsmD from *Streptomyces griseofuscus* (PsmD_*Sg*) was identified, originating from *Streptomyces albulus* (PsmD_*Sa*). The new enzyme was successfully expressed and isolated, exhibiting similar activity and stereoselectivity to its homolog.

◊ Despite the high sequence similarity, PsmD_*Sa* displays markedly higher overall stability.

◊ Biochemical characterization revealed that the optimal reaction conditions of PsmD_*Sa* include a neutral pH and a preference for higher temperatures, compared to its homolog.

◊ PsmD_*Sa* accepts a variety of substrates, but its activity decreases with the increasing volume of the substituents on the amide and the carbamate. The presence of the carbamate in the 5-position on the indole ring is important for the activity. Overall, PsmD_*Sa* displays a slightly higher activity towards the less favored substrates compared to PsmD_*Sg*.

◊ The kinetic parameters of PsmD_*Sa* were determined and revealed lower affinity to the natural substrate and the cofactor, as well as lower catalytic efficiency, compared to PsmD_*Sg*, when used under the same conditions. However, the higher stability and greater substrate promiscuity outweigh the kinetic differences, leading to higher conversions using PsmD_*Sa*.

3.2 The structural study of PsmD

3.2.1 Quaternary structure determination

Mass photometry and size exclusion chromatography revealed that PsmD_*Sg* and PsmD_*Sa* are dimers under usual reaction conditions (Figures 28 and 29). Dynamic light scattering (DLS) revealed a monodisperse distribution consistent with a dimeric species of PsmD_*Sa*, while PsmD_*Sg* formed aggregates under the same conditions. The observed differences in protein surface amino acid residues may explain the observed disparity in the stability and crystallization patterns.

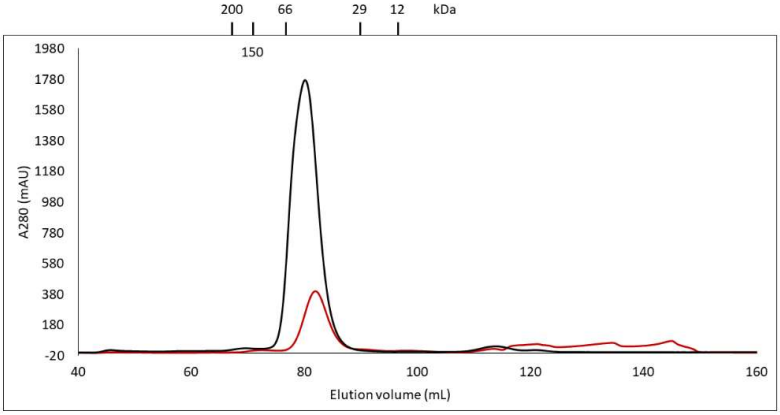

Figure 28. Size-exclusion chromatograms of PsmD_*Sg* (black) and PsmD_*Sa* (red), with the positions of standard calibration proteins, and their molecular weight. The expected size of the PsmD dimer is 61 kDa. The figure was produced by the author for [1] and used here with the agreement of the American Chemical Society

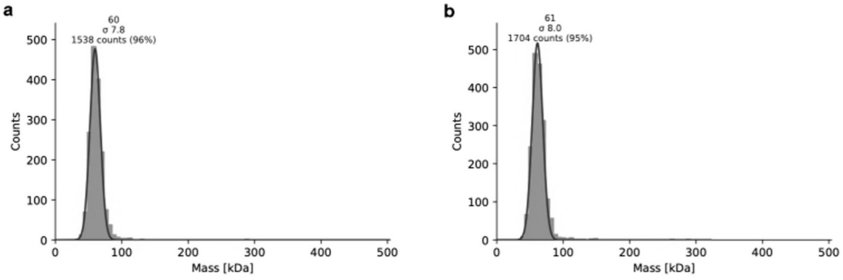

Figure 29. Mass photometry of PsmD_*Sa* (a) and PsmD_*Sg* (b). The figure was produced for [1] and used here with the agreement of the American Chemical Society.

3.2.2 Crystallization and structure determination of PsmD_*Sg*

In order to analyze the structural and mechanistic features of PsmD, the crystallization of both *S. albulus* and *S. griseofuscus* variants was attempted, in the presence of the cofactor and the natural substrate. Crystals were obtained for both variants in the apo form and in combination with SAH. However, despite extensive optimization efforts, PsmD_*Sa* crystals of a productive size and shape for high-resolution diffraction could not be obtained within the scope of this study. Two crystal forms were observed in the case of PsmD_*Sg*, and three crystal structures were determined: crystal form 1 – apo (PDB: 7ZGT, resolution 2.05 Å), crystal form 1 – containing SAH (PDB: 7ZKH, resolution: 1.40 Å) and crystal form 2 – containing SAH (PDB: 7ZKG, resolution 2.30 Å). The crystallization optimization experiments were performed in collaboration with Dr. Oliver Weiergräber (IBI-7, Forschungszentrum Jülich) and Nadiia Pozhydaieva (Institute of Bioorganic Chemistry, Heinrich Heine University Düsseldorf).[359] The X-ray diffraction experiments were performed at the DESY synchrotron (Hamburg, Germany), and the crystal structure determination and refinement were performed by Dr. Oliver Weiergräber (IBI-7, Forschungszentrum Jülich) and provided for this work.

3.2.3 Structural features of PsmD_*Sg*

Unless specified otherwise, the structural discussion refers to the crystal form 1 of PsmD_*Sg*, in the presence of SAH. The crystal structure of PsmD_*Sg* reveals two major domains: a Rossmann fold, characteristic to class I methyltransferases, involved in the cofactor binding, and a substrate binding domain, containing the catalytic site of the enzyme and likely the principal contributor to the substrate specificity (Figure 30a).[299, 370]

The substrate binding domain displays several noteworthy features. The first is the presence of a four-stranded antiparallel β-sheet surface (strands β1′ through β4′) between the β5 strand and αE helix of the Rossmann fold. The area was termed the β-cap domain and directly flanks the catalytic pocket, as well as forming the dimerization domain. The β-sheets of the two monomers intersect at an approximately right angle, forming a square area of overlapping nonpolar residues which are inaccessible to the solvent (Figure 30b). The dimeric complex is stabilized by the π-stacking of the central F201 residues, further hydrophobic interactions in the middle (I182), and a multitude of hydrogen bonds and salt bridges at the periphery, involving D175, T199, Y211, Y213 and R215 (Figure 30c).

Similar to other Rossmann-fold protein families, the nucleotide cofactor binding site contains a GTG motif at the positions 66-68 in the β1-αB loop, accommodating the SAM molecule, while

an aspartic acid residue (D85) stabilizes the cofactor position by forming hydrogen bonds with the ribose hydroxyl groups (Figure 31a, 31b). The homocysteine portion of SAH forms a salt bridge with R39 and hydrogen bonds with hydroxyl groups of Y23 and T123 and the main chain carbonyl of C64. The adenine ring is positioned in a hydrophobic pocket between the side chain of C64, the aliphatic chains of R86, and L109. A Glu-His-Tyr triad is present in the catalytic pocket of PsmD (Figure 31c). The amino acids are in close vicinity to each other and likely take part in an acido-basic mechanism of substrate activation, commonly found in other SAM-dependent methyltransferases (Chapter 2.4.1).

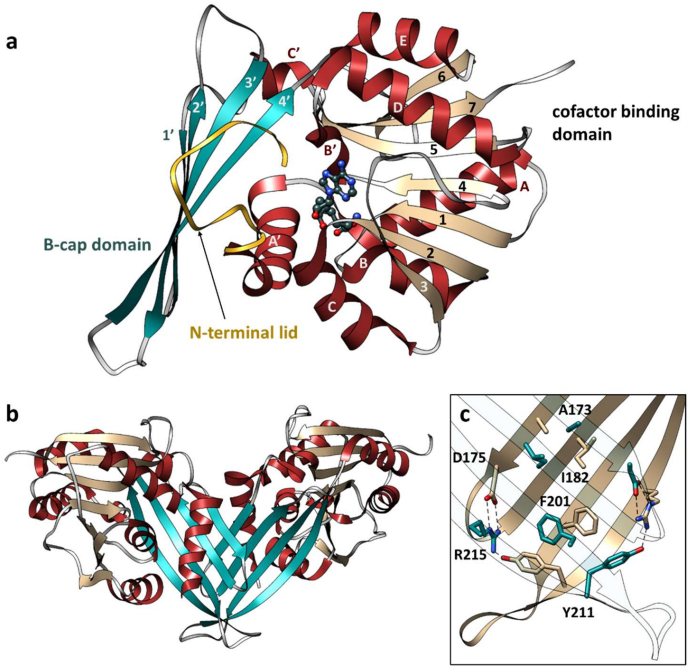

Figure 30. X-ray structure of PsmD_*Sg* in complex with SAH (crystal form 1, "closed" conformation). **a.** Ribbon representation showing the two main structural domains: the Rossmann-type α/β fold - the cofactor binding domain (red/beige) and the β-cap dimerization domain (blue). The N-terminal loop (lid) is marked in gold. The helices and strands are labeled by upper-case letters and numbers, using a prime symbol for elements outside the core Rossmann fold. The active center, as indicated by the cofactor (ball-and-stick, dark grey), is located at the interface between the two domains. **b.** Dimeric quaternary structure (apo) – the monomers are connected by the β-cap domain, as found in all PsmD_*Sg* crystal forms. **c.** Close-up view of the dimerization interface. The amino acid residues are represented in two colors (tan or blue), corresponding to the respective monomer of origin. For clarity, the residues are only labeled once. The correspondent for each amino acid, belonging to the other protein monomer, has an identical position. The X-ray crystal structure was solved by Dr. Oliver Weiergräber and published in the RCSB PDB database (PDB: 7ZKH, 7ZGT) and in [1]. The structural analysis was performed by the author in collaboration with Dr. Oliver Weiergräber. The figure was produced by the author.

An unusual structural feature of PsmD is a tryptophan cluster at the end of the catalytic pocket, formed by W34, W167, W172 and W183, which interact with each other primarily through π-stacking (Figure 31d). This cluster could presumably be involved in maintaining the folding of the substrate binding domain. However, multiple natural product methyltransferases display a similar protein fold containing different amino acids in the same positions (Chapter 5.1). When performing a sequence alignment with structurally similar methyltransferases, it becomes apparent that these tryptophan residues are generally not conserved, except for W34. Considering that introducing tryptophan in the sequence of proteins has a high metabolic cost, the presence of four residues in close proximity to each other in the catalytic pocket is likely to play a role in substrate binding and selectivity.[371] Furthermore, at least two of these residues (W34 and W167) appear to influence the dynamic motion driving PsmD catalysis, being involved in the product egress (discussed in Chapter 3.3).

Finally, the N-terminal segment was disordered in the apo form but ordered in the crystal form 1 in complex with SAH. This section acts as a lid, covering the entrance of the catalytic site in crystal form 1. As such, two conformational states of PsmD were identified: “open” and “closed”, determined by the position of the N-terminal lid in relation to the catalytic pocket. The lid closure corresponds to a conformational change of the cofactor, leading to a more favorable orientation of the methyl group toward the substrate methylation site (discussed in Chapter 3.3). As such, the closed conformation of PsmD likely corresponds to the catalytic activity. Tyrosines 16 and 23 also suffer a significant conformational shift between the open and the closed states. In the closed conformation, both orient their hydroxyl groups towards the homocysteine segment of the cofactor, forming a tyrosine cluster with Y129 closely surrounding the cofactor (Figure 31c). The role of this cluster is unclear but it can be presumed that the high local electron density has a stabilizing effect on the positive charge of the SAM cofactor, contributing to its productive conformation.

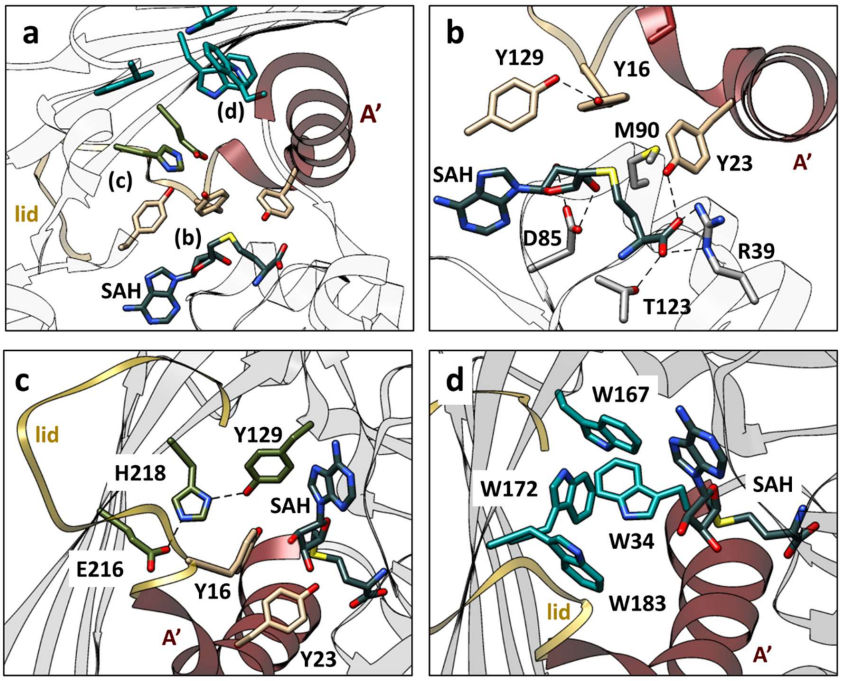

Figure 31. The active site of PsmD from *S. griseofuscus* (crystal form 1, in complex with SAH). **a.** The overview, featuring (from bottom to top) the docked SAH cofactor (dark gray), a tyrosine cluster (light beige) a presumed proton shuttle system (olive), and a tryptophan cluster (blue). Lowercase letters refer to the close-up views in subsequent panels. **b.** The cofactor binding site. The tyrosine cluster residues are light beige. The other main residues involved in the binding of SAH are displayed in gray. **c.** The Glu-His-Tyr proton shuttle triad (olive) and their position relative to the cofactor and the tyrosine cluster. Residue Y129 is part of both the catalytic triad and the tyrosine cluster. **d.** The tryptophan cluster (blue), positioned at the far end of the catalytic pocket. The X-ray crystal structure was solved by Dr. Oliver Weiergräber and published in the RCSB PDB database (PDB: 7ZKH) and in [1]. The structural analysis was performed by the author in collaboration with Dr. Oliver Weiergräber. The figure was produced by the author.

3.2.4 Homology modelling of PsmD_*Sa*

Considering that the efforts for experimental crystal structure determination of PsmD_*Sa* were unsuccessful, a homology model was generated, using the PsmD_*Sg* crystal form 1 (closed) as template. Due to the high sequence similarity and the shared catalytic function, it was reasonable to assume that the two enzymes share similar folding and structural features. The homology model was obtained by Dr. Benoit David (IBG-4, Forschungszentrum Jülich) using Modeller.[372] The results of the modeling show a high structural identity between the two homologs, sharing all the important features discussed in Chapter 3.2.3 (Figure 32a). The analysis of the sequence differences in relation to the protein structure reveals that most of the variations appear at the surface of the protein (Figure 32b). This can be expected when considering the differences in stability, as surface residues generally play a crucial role in protein solubility and intermolecular interactions. These factors influence the tendency to aggregate, which was observed for PsmD_*Sg* in our DLS experiments, but not for PsmD_*Sa*. Ultimately, identifying a surface modification pattern that could explain the stability boost is challenging and would likely require extensive mutagenesis efforts.

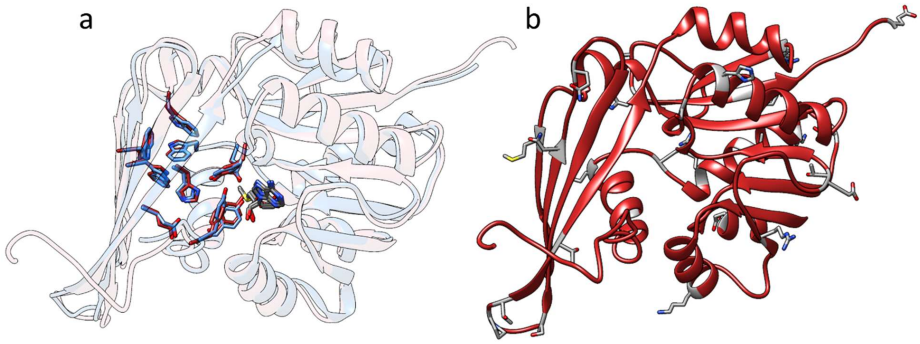

Figure 32. a. Overlap of the crystal form 1 of PsmD_*Sg* in complex with SAH (blue) and the homology model of PsmD_*Sa* containing docked SAM (red). The main amino acid residues in the catalytic pocket were highlighted and overlap to a high degree. The cofactor was marked in dark grey. **b.** Homology model of PsmD_*Sa*. The amino acids differing from the PsmD_*Sg* homolog were highlighted. The PsmD_*Sg* mutations corresponding to the PsmD_*Sa* structure are: D28A, E33Q, C37S, Q41R, V46I, A51K, H55Q, Q73E, Q96K, H105R, D115G, G116D, A117T, A131S, R134H, R141H, V171M, D184N, E188Q, H204S, A208P, A210T, V214T, Q239R, T254A, R256H, V261F, R267S.

3.2.5 Chapter summary

- ◊ DLS, MS and size exclusion chromatography indicate that PsmD_*Sg* and PsmD_*Sa* are dimers under regular reaction conditions.
- ◊ The crystal structure of PsmD_*Sg* was determined by X-ray diffraction in the apo form and in complex with SAH.
- ◊ X-ray diffraction revealed two crystal forms, likely corresponding to two conformational states of the enzyme: open and closed. The N-terminal loop acts as a lid, determining the conformational state of PsmD.
- ◊ Similar to other class I methyltransferases, PsmD possesses a Rossmann-fold domain involved in the binding of the cofactor. The substrate binding domain contains several noteworthy features such as a β-sheet “cap”, which also serves as a dimerization domain and a tryptophan cluster closing the catalytic pocket.
- ◊ The homology model of PsmD_*Sa* was obtained, using the PsmD_*Sg* crystal structure as template. Although the sequences of the two enzymes overlap to a high degree, most of the differences in the amino acids are found at the surface of the protein.

3.3 The mechanistic study of PsmD

After the structural analysis of PsmD, the next step was an assessment of the importance of the amino acid residues lining the catalytic pocket. To achieve this, each amino acid was replaced with alanine, with the focus on the PsmD_*Sa* homolog, as the intended working biocatalyst. However, the conclusions can be also reasonably attributed to PsmD_*Sg*, due to the high similarity in structure and catalyzed reactions. Therefore, the mentioned residues are similarly found in PsmD_*Sg*, with the numbering offset by +1. Unless mentioned otherwise, all further discussions will refer to PsmD_*Sa*. The conversion to the methylated product **P10** was tested for all mutants, to observe the effects of the substitutions on the enzymatic activity. This served a double role: better understanding the catalytic process of PsmD, as well as identifying potential mutagenesis targets for future enzyme engineering.

To further elucidate the catalytic mechanism, molecular docking and molecular dynamics simulations of the natural substrate within the active pocket of PsmD revealed the probable substrate position and substrate-enzyme interactions involved in the PsmD catalysis. The computational and experimental steps presented in this chapter made it possible to shape an overall picture of the PsmD catalysis.

3.3.1 Site-specific mutagenesis for catalytic site mapping

The genes bearing the desired mutations for the alanine scan were produced by site-directed mutagenesis of the pET21a(+) plasmid containing the wild-type (WT) PsmD_*Sa* gene. The QuikChange strategy (Stratagene, USA) was initially selected for the primer design, but a change towards the inverse PCR ("round-the-horn") approach was necessary for later mutants, to achieve consistent positive amplification results (Figure 33). The QuikChange approach uses two complementary primers containing the mutation of interest. The amplification is linear, only takes place on the template, and leads to blunt-end products that can hinder transformation efficiency.[373] In the case of inverse PCR, the primers are phosphorylated at the 5' end and sticky-end products are obtained after the amplification. The inverse PCR strategy includes a subsequent intramolecular ligation step before the transformation of the competent cells with the obtained plasmid, requiring the obtained PCR products to be phosphorylated at the 5' end. This can either be achieved by introducing the phosphate post-PCR using a kinase, or by using phosphorylated primers from the start. The use of circular plasmids substantially improves transformation efficiency. Most importantly, within the inverse

PCR method, the plasmid amplification is exponential, leading to significantly higher yields.[374, 375] This is also particularly important for the production of mutant libraries with randomized mutations.

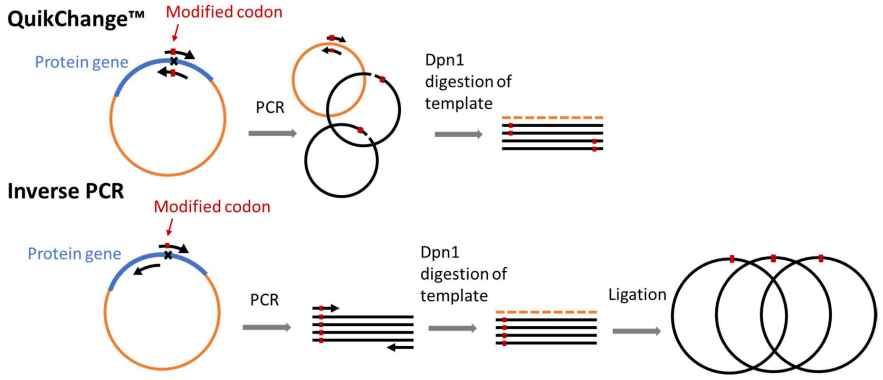

Figure 33. Comparison between the QuikChange and inverse PCR strategies for site-directed mutagenesis.

3.3.2 Alanine scan of the catalytic site

The mutated alanine scan PsmD variants were expressed in *E. coli* BL21 Gold (DE3), and used as whole-cell biocatalysts in reaction with the natural substrate **10**, in the presence of SAM. The conversion was measured after 16 h, allowing an evaluation of the importance of each amino acid for catalysis. For the validation of the whole-cell reaction results, several variants were isolated and their specific activity was also determined using the commercial MTase-Glo™ assay.

This allowed the mapping of the catalytic pocket of PsmD_*Sa*, revealing some of the functions of the amino acid residues present in the catalytic pocket (Table 5, Figure 34). The alanine scan revealed that the Glu-His-Tyr triad plays an essential role in catalysis. Replacing H215 and Y128 with alanine eliminated the activity, while Y128F led to a 10% conversion to the methylated product. In this case, it can be assumed that H217 or a water molecule could deprotonate the substrate indole instead of Y128, although at a much lower rate, while the phenyl ring could still fulfil a steric role in the catalytic pocket. H217A and E215A also lost most of the activity, leading to 6.8% and 18.9% conversion of **10**. E215 was also replaced by aspartate, which achieved 36.4% conversion (Table 5).

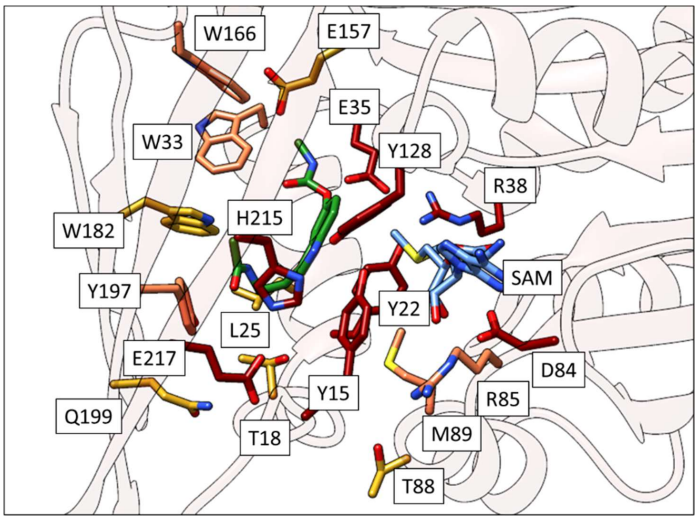

Figure 34. Amino acid residues in the catalytic pocket of PsmD_*Sa*, which were targeted for the alanine screen, in the presence of SAM (blue) and the natural substrate in pose 1 (green, pose described in Chapter 3.3.3). Their color corresponds to the enzymatic activity loss upon replacement with alanine: red = most or all activity lost; orange = some activity lost; yellow = minor loss of activity. The residues colored in orange and yellow can be considered appropriate targets for enzyme engineering.

The complete loss of activity in Y15A and Y22A highlights their importance. The significant shift of their position between the open and closed conformational states of the enzyme suggests an important role of these residues. It is unclear if this role is related to the motion of the lid or the activation of the cofactor. Interestingly, mutants Y22F and Y15F achieved high conversions (66.5% and 99%), suggesting that the steric effects of the phenyl rings play a major role in the catalytic action of these residues, rather than the hydroxyl groups. The position of Y22 and Y15 in the closed state of the enzyme, in contact with the cofactor, correlated to its favorable conformation.

Mutants W33A, E35A, R38A and D84A also lost most if not all of their activity. The role of W33 is not obvious when analyzing the docking poses, but it could be important for protein folding, due to its π-stacking within the local tryptophan cluster. Likewise, due to its position in close proximity to the substrate, it might play a significant role in shaping the steric environment of the catalytic pocket. The carboxylate of E35 likely forms a hydrogen bond with the substrate. The hypothesis regarding the importance of the interaction between the protein and the carbamate was supported by the substrate scope analysis, which showed that removing the carbamate significantly hinders the enzymatic activity. Mutant E35D lost all activity despite containing a carboxylate. Presumably, the shorter carbon chain might prevent the interaction

with the substrate altogether. R38 and D84 are involved in the binding of the cofactor, with R38 forming a hydrogen bond with the homocysteine rest and D84 forming hydrogen bonds with the cofactor ribose.

Table 5. Determined conversion for PsmD_*Sa* variants after 16 h of reaction, and specific activity for selected variants for method validation. The conversion was determined using whole cells and RP-HPLC analysis. The cells were incubated at 35 °C, in the presence of 1 mM **10** and 1.5 mM SAM in KP_i buffer (50 mM, pH 7.5). The specific activity was determined for isolated enzymes, using the MTase-Glo™ assay. 1 µg enzyme was incubated with 20 µM 1 and 30 µM SAM in MTase-Glo™ 1X buffer (20 µL final volume) for 15 min at 35 °C.

Variant	Conversion (%)	Specific activity (U/mg)	Proposed function of the original amino acid
Y15A	-	n/a	Lid closure, cofactor activation
Y15F	>99%	n/a	
T18A	73.5 ± 2.2	n/a	
Y22A	-	n/a	Lid closure, cofactor activation
Y22F	66.5 ± 3.5	n/a	
Y22E	-	n/a	
L25A	>99%	n/a	
W33A	14.8 ± 5.32	n/a	Protein folding, substrate binding
E35A	5.3 ± 0.1	n/a	Substrate binding, stabilization of closed conformation
E35D	-	n/a	
R38A	-	no activity	Substrate binding, stabilization of closed conformation
D84A	-	n/a	Cofactor binding
R85A	55.8 ± 9.6	n/a	
T88A	>99%	n/a	
M89A	48.6 ± 6.2	n/a	
Y128A	-	n/a	Proton shuttle - base
Y128F	10.2 ± 1.9	n/a	
Y128E	1.1 ± 0.46	n/a	
Y128S	-	n/a	
E157A	94.0 ± 7.0	$8.2 \pm 1.8 * 10^{-4}$	
W166F	60.5 ± 4.39	n/a	
W182A	85.7 ± 8.4	n/a	
W182F	84.1 ± 11.5	n/a	
Y197A	60.5 ± 9.66	n/a	
Q199A	96.1 ± 3.76	n/a	
E215A	18.9 ± 1.9	$1.6 \pm 1.3 * 10^{-4}$	Proton shuttle - acid
E215D	36.4 ± 3.2	n/a	
H217A	6.8 ± 0.6	n/a	Proton shuttle - base
WT PsmD_*Sa*	>99%	$81.3 \pm 10.0 * 10^{-4}$	
EV	-	n/a	

EV = empty pET21a vector in E. coli BL21 (DE3) Gold strain
"-" = no product peak was observed after RP HPLC measurements
n/a = specific activity was not determined

Finally, mutants R85A, M89A, W166F and Y197A converted around half of the substrate amount, while T18A, L25A, T88A, E157A, W182A and Q199A led to high or full conversion,

revealing that their function is not vital and can be considered as targets for further protein engineering (Figure 34).

3.3.3 Catalytic mechanism of PsmD

The molecular docking of the natural substrate **10** in the catalytic sites of PsmD_*Sg* and PsmD_*Sa* provided insight into the substrate binding and interactions, as well as the possible mutagenesis targets within the catalytic site. The substrate was modeled and docked into the catalytic site in the closed conformation of PsmD_*Sa*, presumed to correspond to activity. The docking considered the amino acid residues rigid, but was followed by molecular dynamics simulations for the refinement of the poses and the substrate interactions with the solvent. The molecular docking and molecular dynamics simulations were performed by Dr. Benoit David (IBG-4, Forschungaszentrum Jülich).

Since PsmD_*Sa* was the intended target for mutagenesis, the mechanistic analysis focused primarily on this homolog. As such, the computational simulations were performed on the PsmD_*Sa* homology model.

Two plausible substrate poses were obtained after docking, corresponding to the *S*-configuration of the methylated product, and respecting the distance and angle requirements for methylation (Figure 35).[305, 307, 376] The first pose shows the indole nitrogen aligned with the Glu-His-Tyr triad. The carbamate side of the substrate molecule is oriented towards the tryptophan cluster at the end of the catalytic pocket, and stabilized by a hydrogen bond with the side chain of E35. The amide side of the substrate is folded towards the lid. In the second pose, the indole nitrogen forms a hydrogen bond with the carboxylate of E35 and the substrate is flipped, the amide side oriented towards the tryptophan cluster and the carbamate pointing towards the lid. As there was no strong argument for disregarding any of the two poses, both were considered plausible for mechanistic elucidation.

Pose 1 supports the hypothesis of the Glu-His-Tyr triad acting as a proton shuttle, involved in the electronic activation of the substrate in an acid-base type of mechanism (Figure 35a). More precisely, it is proposed that the hydroxy group of Y128 is deprotonated by the activated H217, leading to the formation of a strong base, which in turn can deprotonate the indole in the 3-position, activating the adjacent double bond prior to the nucleophilic attack. Variations of this system were reported in other methyltransferases, with histidine mostly in the role of the

base, sometimes in the presence of an activating acid. The substrate activation is sometimes performed by a tyrosine residue, as is the case of PsmD, directly by the catalytic histidine, or by an activated water molecule present in the catalytic site.[304, 310, 311, 377-381] In the case of PsmD, substrate activation could be presumably achieved either by complete deprotonation or by hydrogen bonding. Considering that the chemical methylation of this substrate requires the presence of a strong base, it is likely that the substrate deprotonation would be required within the mechanism of the enzymatic methylation.[358, 382]

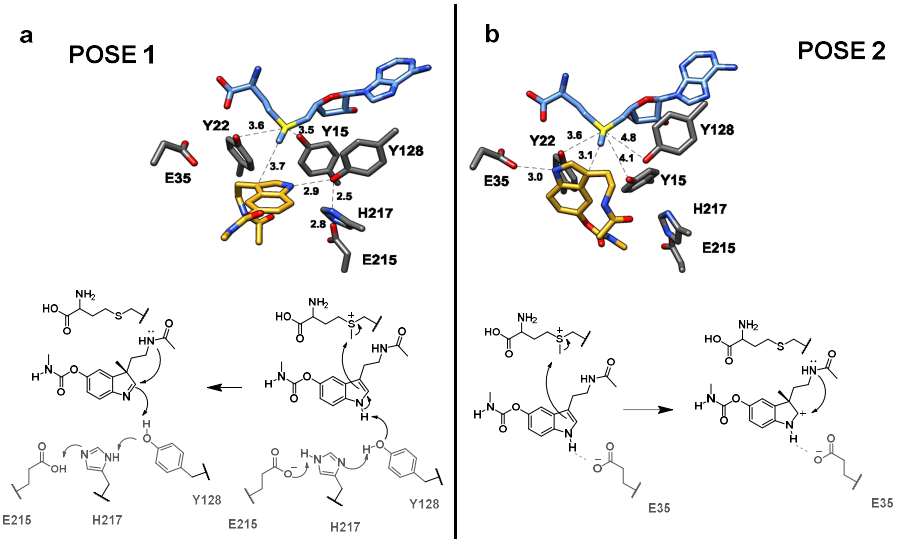

Figure 35. View of both substrate docking poses in the PsmD_*Sa* active site (taken from snapshots extracted from the MD simulations of the closed conformation) and the proposed mechanisms of methylation and subsequent intramolecular cyclization for each case. **a.** Substrate docking pose 1. **b.** Substrate docking pose 2. The carbon atoms of the substrate and the SAM cofactor are colored in gold and blue respectively. The dashed lines illustrate relevant distances with the surrounding active site residues. The figure was produced by the author for [1] and used here with the agreement of the American Chemical Society.

In the second pose, a similar activation of the substrate indole could be achieved by hydrogen bonding of the indole nitrogen with the carboxylate of E35 (Figure 35b). However, glutamate by itself is not a strong enough base (pKa ~ 6.5) to deprotonate the indole amine (pKa ~ 17). A similar mechanism was reported for the CdpNPT prenyltransferase. In that case, a glutamate residue forms a hydrogen bond with the indole amine increasing the electron density on the C3' of the indole and promoting the prenylation and subsequent intramolecular cyclization.[383] E35 could participate in a similar mechanism, also contributing to the productive orientation of the substrate in the catalytic site. However, it must be noted that there is a substantial

difference in the reactivity of methyl and prenyl groups. Prenyltransferases use dimethylallyl pyrophosphate (DMAPP) as the prenyl donor. In this case, the double bond stabilizes the positive charge formed after the cleavage of the pyrophosphate, creating a stronger electrophile than the SAM-attached methyl group.[384] As a consequence, methylation requires a stronger driving force than prenylation.

In the MD simulations, pose 2 provides a shorter distance between the methyl group of the cofactor and the C3' of the substrate indole, compared to pose 1. Additionally, the angle distribution between the sulfonium ion, the transferred methyl and the C3' site on the substrate aligns more closely with the transition state of the S_N2-type mechanism typically described in SAM-dependent methyltransferases (162-170°), (Figure 36).[305, 380]

Although both poses must be reasonably considered, the alanine scan results highlight the importance of the Glu-His-Tyr triad, which cannot be fully explained when referring to pose 2. Considering the literature examples of acid-base activation in methyltransferase catalysis and our subsequent mutagenesis and docking results (Chapter 3.3.2), the evidence seems to favor the likelihood of pose 1 as the productive binding mode (Figure 35a). However, pose 2 cannot be definitively excluded with the information available so far.

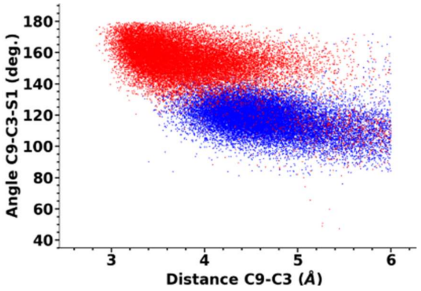

Figure 36. Geometry of the substrate docking poses 1 (blue) and 2 (red) in relation to the SAM cofactor. The distance between the C3 (substrate) and C9 (SAM) atoms over 380 ns of MD simulation is reported on the x-axis. The angle measured between the S1 and C9 atoms of the cofactor and the C3 atom of the substrate is reported on the y-axis. Each point refers to a single snapshot taken over the course of the PsmD MD trajectories starting from the functional (closed) conformation. The figure was produced by Dr. Benoit David for [1] and used in this work with the agreement of the American Chemical Society.

3.3.4 Conformational dynamics of the PsmD catalysis

An overlap of the open and closed crystal structures of PsmD_*Sg* bound to the cofactor revealed a conformational shift of the cofactor itself. Although the obtained crystal structures only contain SAH, SAM could be digitally modeled by adding the missing methyl group, respecting the natural *S*-conformation of the natural cofactor. This, in combination with the docked substrate and subsequent MD simulations, shows that the closing of the lid is associated with a favorable shift in the cofactor position, pointing its methyl group towards the methylation site on the substrate (Figure 37a). This could be part of a regulatory metabolic pathway, where the transformation of the substrate is controlled by the closure of the lid, in turn triggered by the binding of the substrate within the catalytic site. There is an argument for the evolutionary utility of such regulation, as producing secondary metabolites at an uncontrolled rate could generate a too high metabolic cost and prove toxic to the host organism.[385-387] The SAM conformational shift as a regulatory mechanism has been reported for the tRNA methyltransferase TrmD. In this case, a Mg^{2+} ion drives the cofactor conformational exchange and stabilizes the negative charge of the deprotonated amine methylation site on the substrate.[388] Furthermore, similar N-terminal lid structures have been reported particularly in sugar *O*-methyltransferases, such as MycF, involved in the biosynthesis of mycinamicin, the novobiocin biosynthetic methyltransferase - Nov-P, and TylF, the methyltransferase involved in the biosynthesis of tylosin.[389-391] Although not specifically identified as lids, similar N-terminal loop structures can be found in the reported structures of other methyltransferases with a variety of substrates and methylation targets such as NNMT (nicotinamide *N*-methyltransferase), NovO (coumarin *C*-methyltransferase) and StspM1 (tryptophan diketopiperazine *C*-methyltransferase).[292, 309, 392]

The S_N2 mechanism of methylation requires the formation and stabilization of a transition state, as previously shown by density functional theory (DFT) simulations and kinetic isotope effect (KIE) measurements.[393] Previous studies have shown that KIEs are influenced by the conformational changes of the cofactor upon protein binding, as well as the interactions between the protein and the substrate. Besides the electronic effects of the residues in the catalytic site, a “compression effect” has been proposed, postulating that the mechanical compression of the enzyme might destabilize the reactants more than the transition state. This hypothesis was formulated in response to KIE results for COMT, which suggested that the enzyme might be able to distinguish the S_N2 transition state and stabilize it specifically.[394] Although the theory is controversial in the scientific community, with studies showing contradictory conclusions on the matter, more recent computational and experimental analyses on SAM-dependent methyltransferases such as COMT and GNMT, are in favor of the existence of a protein compression effect, associated with the electrostatic stabilization

within the catalytic site, as necessary for the activation of the methyl transfer.[395] The requirement for a catalytic site compression for the stabilization of the transition state could provide another plausible explanation for the presence of the N-terminal lid and its closing motion within the catalytic process of PsmD. The closure of the lid presumably reduces the space in the catalytic pocket, while triggering the formation of the methylation transition state through the conformational shift of the cofactor. KIE experiments on PsmD could perhaps bring more insight into the matter.

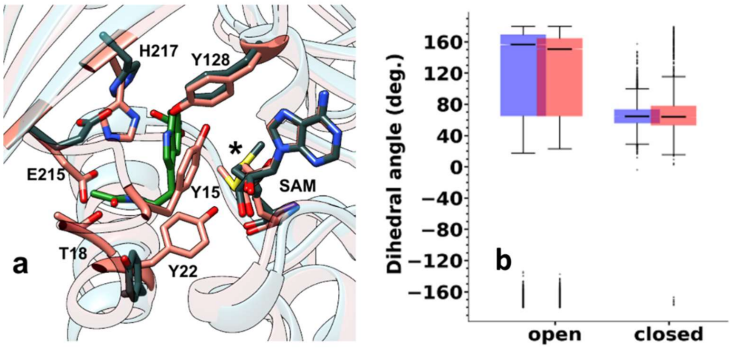

Figure 37. Significance of the Y22 residue. **a.** Location of Y22 in relation to SAM in the open (gray) and closed (pink) conformations of the PsmD_*Sa* homology model. The substrate (green) is represented in docking pose 1. The SAM cofactor (methyl group marked by asterisk) was modeled based on the position of SAH in the respective crystal structure of each conformation in PsmD_*Sg*. **b.** Influence of the conformation (open/closed) of the N-terminal lid (blue: substrate pose 1; red: substrate pose 2) on the fluctuations of the Y22 C*α*-C*β* torsion angle over the course of the simulations. The figure was produced by the author in colaboration with Dr. Benoit David for [1] and used here with the agreement of the American Chemical Society.

In order to obtain more insight into the dynamic motion involved in PsmD catalysis, a comparative analysis of the MD trajectories of the dimeric PsmD_*Sa* in both conformational states was performed, in the presence of both substrate poses. This revealed a high mobility of the Y22 side chain in the open conformation, in contrast to the high conformational stability of this residue in the closed state (Figure 37b). It is plausible that the position shift of Y22 upon lid closure influences the conformational change of the cofactor, stabilizing the productive conformation through the electrostatic interaction between its hydroxyl and the positively charged sulfonium ion on the cofactor. This effect is heightened by the hydroxyl groups of Y15 and Y128, positioned in the close vicinity within the closed catalytic pocket and forming a partially negatively charged area. This activation is likely essential for PsmD activity and similar tyrosine residues emerge in the structures of multiple methyltransferases with a variety of target substrates (Figure 38).[292, 311, 377-379, 396, 397] A literature analysis based on quantum

chemistry calculations shows evidence of CH···O hydrogen bonds coordinating the SAM methionine residue across all classes of methyltransferases. These interactions are stronger than typical hydrogen bonds and are believed to be important for the binding of SAM and for the stabilization of the transition state.[398, 399] This is in agreement with and could explain the observed importance of Y22, Y15 and Y128 in the structure of PsmD.

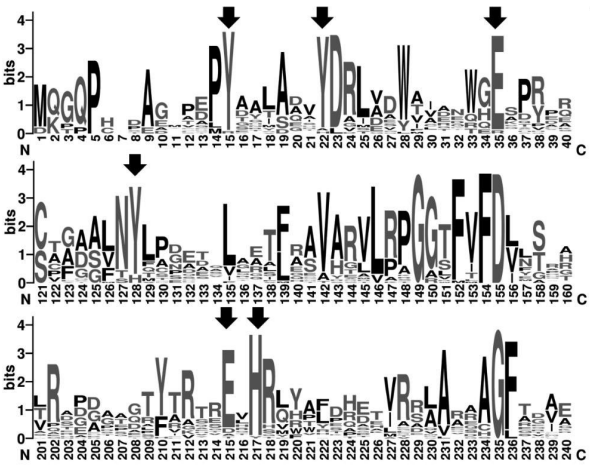

Figure 38. Conservation of key residues in selected PsmD sequence homologs. The conservation scores (bits) were derived from a multiple sequence alignment built using ConSurf and processed using the WebLogo server.[400-402] The arrows indicate essential residues for PsmD activity. The conservation analysis and figure were produced by Dr. Benoit David (IBG4, FZJ) for [1] and used here with the agreement of the American Chemical Society.

Principal component analysis of the conformational landscape within the MD simulation time revealed a possible third conformational state of the enzyme, in which after the lid closure, a channel opens between the A' and C' α-helices on the opposite side of the catalytic site. This was observed after approximately 100 ns in all simulation iterations. This motion could be involved in the egress of the product, after the methylation. The crystallographic data supports this hypothesis, as the closed state features notable mobility of this region, revealing alternate conformations of the C' helix and the adjacent tryptophan residues. The interaction between W33 and W166 may play a critical role in this motion, functioning as a "latch" on the catalytic pocket, opening after the product is synthesized and facilitating its removal (Figures 39, 40).

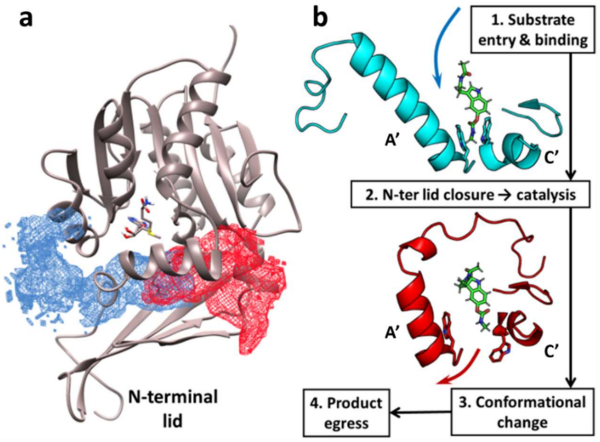

Figure 39. Consequences of the conformational state of the N-terminal lid on the dynamics of the substrate (calculated from the simulations including the substrate pose 1). **a.** Computed volume occupied by the substrate indole ring during the simulations of the PsmD_*Sa* dimer in complex with both SAM and substrate. Both open (blue mesh) and closed (red mesh) states were simulated. The SAM cofactor is represented in sticks. The structure of PsmD in its closed state is shown in the gray cartoon. **b.** Proposed product egress mechanism. The impact of both opening (blue) and closing (red) conformations of the N-terminal lid on adjacent structural motifs and on the orientation of W33 and W166 side chains is shown. The analysis and figure were produced by Dr. Benoit David for [1] and used here with the agreement of the American Chemical Society.

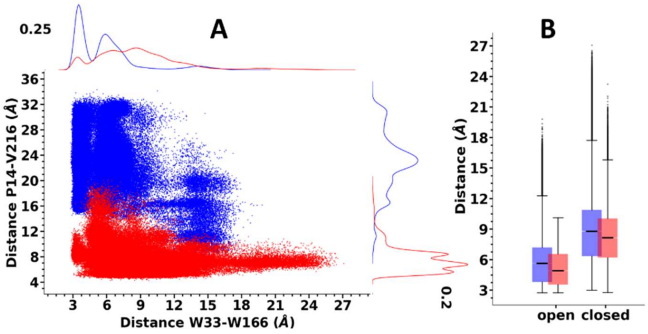

Figure 40. A. The closure of the N-terminal lid is quantified by the distance between P14 and V216 C atoms and between W33 and W166. Each point refers to a given snapshot extracted from 380 ns MD simulations of the PsmD dimer, considering both substrate docking poses and N-terminal lid in either open (blue) or closed (red) conformations. The normalized distance distributions are shown on the top and right sides of the plot. **B.** Influence of the conformation (open/closed) of the N-terminal lid on the distance between W33 and W166 sidechains Cβ atoms considering the simulations with the substrate docking pose 1 (blue) or 2 (red) separately. The analysis and figure were produced by Dr. Benoit David (IBG4, FZJ) for [1] and used here with the agreement of the American Chemical Society.

3.3.5 Chapter summary

- The molecular docking of the natural substrate into the catalytic site of PsmD_*Sa* and subsequent MD simulations provided two plausible poses of the substrate within the catalytic site.
- An alanine scan was performed, highlighting the importance of E215, H217 and Y128 as a proton shuttle, likely involved in substrate activation. The importance of other residues such as Y15, Y22, W33A, E35A, R38A and D84A was revealed and their roles were discussed.
- Two mechanisms of action were proposed, corresponding to the two identified substrate poses. The first involves the electronic activation of the substrate by a deprotonation of the indole amine, driven by the activated tyrosine in the Glu-His-Tyr catalytic triad. For the second pose, the activation takes place via a hydrogen bond between the indole amine and the carboxylate of E35
- The apparent significance of the catalytic triad, along with the similarity to the mechanisms of other SAM-dependent methyltransferases reported in the literature, supports the first pose and its corresponding mechanism.
- MD simulations revealed the significance of Y22 and Y15 position shifts upon lid closure, correlating with the conformational change of the cofactor. A third conformational state of the enzyme was identified, in which a channel opens on the inner end of the catalytic channel. This conformation is likely associated with the product egress.

3.4 Development of a colorimetric assay for indole detection

3.4.1 The Ehrlich reagent in indole detection

The Ehrlich reagent was originally developed at the beginning of the 20th century and used for the detection of indoles in biological samples.[403] It is based on the coupling of 4-(dimethylamino)benzaldehyde (DMAB) with two indole rings under acidic catalysis, forming a colored iminium cationic compound, stabilized by extended electron resonance. The reagent is currently used for diagnosing liver disorders through the detection of urobilinogen and has been suggested as a potential tool for screening various types of cancer.[404-406] It is also used as a test for tryptophan production in bacterial cultures, as a detection method for psychoactive compounds in forensic samples, and for the detection of hydrazine, pyrroles and porphobilinogen. [407-412] The original Ehrlich reagent uses HCl as a catalyst and EtOH as a solvent. Its scope is however limited to simple indoles, prompting the later development of multiple variations, using the same principle but various replacements of acids (most notably H_2SO_4) and solvents (MeOH or *i*PrOH).[413, 414]A modified Ehlich reagent was used as a developing agent for thin layer chromatography (TLC), with the addition of oxidants ($FeCl_3$ or H_2SO_4).[415] An enzymatic activity assay was developed based on the Ehrlich reagent, for the determination of amine transaminase activity, in which 2-aminoethylaniline was used as the amine donor, generating indole *in situ*, which was then detected using the Ehrlich reagent.[416]

The indole aromaticity is disrupted after the PsmD methylation. Because of that, a selective assay for indoles was an attractive option for PsmD mutant activity screening. However, when attempted, the original Ehrlich reagent as well as the modified versions available in the literature, did not provide reliable results, if any, for the PsmD substrates. As such, new modifications of the assay conditions were necessary. A key goal of this project was to develop an assay applicable in aqueous environments, allowing for easy use in the buffered environment typical for most enzymatic reactions. Most of the reported Ehrlich assay variations use alcohols exclusively as solvents for the analytes, occasionally containing small amounts of water. One instance was reported in which synthetic cannabimimetics were quantified using a modified Ehrlich test in which the samples were dissolved in 70:30 (v/v) MeOH:H_2O mixtures, using H_2SO_4 immobilized on silica as catalyst.[413]

The mechanism of the reaction between the Ehrlich reagent and indoles is still debated, and the identity of the colored product obtained from the condensation with indole derivatives is unclear, based on current reports. A crystal structure of the DMAB condensation product with indole was determined, showing the carbonyl of the DMAB molecule binding to two indole molecules in the 3-position, forming a β-bis(indoyl)methane derivative as the colored

product.[417] However, this conclusion cannot be freely applied to indoles substituted in the 3-position, such as the PsmD substrates, where steric constraints are likely to cause the binding of the DMAP molecule to the 2-position of the indole rings instead.[413] More insight into the formation of the condensation product could be found in the descriptions of triphenylmethane dyes, particularly their light-driven ionization. Considering this as a parallel, the oxidation of the central carbon atom could cause electron delocalization contributing to the absorption of light in the visible spectrum (Figure 41). This phenomenon was observed in various triphenylmethane dyes, such as crystal violet and malachite green (Figure 42). In an aqueous environment, an equilibrium forms between the colored cation and a colorless carbinol. Increasing the pH shifts the equilibrium toward carbinol formation. This matches the observations in this work, where an increase in pH corresponded to a reduction of color intensity (Chapter 3.4.3). The possibility of the carbinol and the cation forming a colorful complex was also hypothesized.[418] Notably, in the case of triphenylmethane dyes, photophysical and photochemical deactivation was also observed.[419]

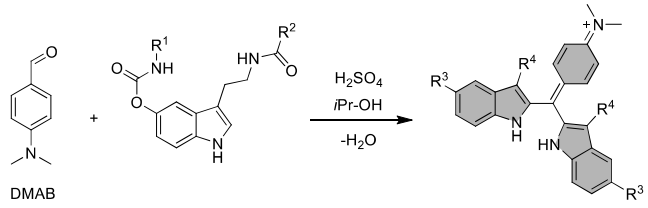

Figure 41. Reaction scheme showing the reaction between a substituted indole derivative and DMAB, and the putative colorful complex. The figure was originally produced for [2] and was used without modifications, according to the Wiley CC licensing.

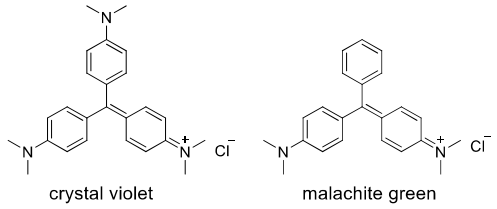

Figure 42. Examples of known triphenylmethane dyes. The figure was originally produced for [2] and was used without modifications, according to the Wiley CC licensing.

3.4.2 The role of light in the color formation

The optimization of the indole assay started from the cannabimimetic assay described by Durmuş et al., using H_2SO_4 as the acid, and *i*PrOH as the alcohol.[413] This version of the assay was selected due to the structural similarity between the targeted analytes and the PsmD substrates. The attempts to use the reported assay as described in the literature did not yield adequate results in terms of color intensity and reproducibility for the compounds used in this work. All the optimization efforts and tests were applied to solutions of 1 mM analyte in KP_i buffer (50 mM, pH 7.5), unless specified otherwise. The assay was optimized and performed in 96-well microtiter plates, to allow for easy automation when necessary.

An initial experiment showing the influence of light on the formation of the color was prompted by the lack of method reproducibility in the early stages. The role of light in the formation of the colored compound in various Ehrlich assay variants has mostly been overlooked and has only been scarcely referenced in the literature.[416] An early experiment, in which the final incubation step with DMAB was simultaneously carried out either in the dark or exposed to 365 nm UV light revealed significant efficacy differences. The absorbance of compound **10** was measured after 10, 30 and 60 minutes of incubation with DMAB (Figure 43B). The irradiated samples consistently provided higher absorbances than the ones incubated in the dark. The evolution in time also showed an opposing trend between the two procedures. The samples incubated in the dark were subjected to discoloration, corresponding to the decrease in the absorbance at 580 nm. For the samples exposed to UV light the absorbance increases in time. The color formed after UV exposure was stable for at least an hour after the light exposure was interrupted (Figures 44, and 45).

Multiple sources of light were tested in order to identify the best setup for the assay. Samples containing 1 mM melatonin (**25**) were irradiated by white and green LED light panels, a UV lamp at 365 nm and a LED lamp at 405 nm. The absorbance at 600 nm was measured after 10 min of irradiation, providing a maximum absorbance after the 405 nm irradiation. Lower irradiation wavelengths performed better, suggesting that higher energy boosts the formation of the colored product (Figure 43A). This energy might be required for the oxidation of the DMAB condensation product, leading to the colored iminium ion. In other reported cases, this was achieved by adding supplementary oxidation agents such as $FeCl_3$ or silica-immobilized H_2SO_4 to support color formation when using more structurally complex indoles.[413] It must be noted, however, that the addition of these oxidizing agents did not improve color yields for the substrates tested in this work.

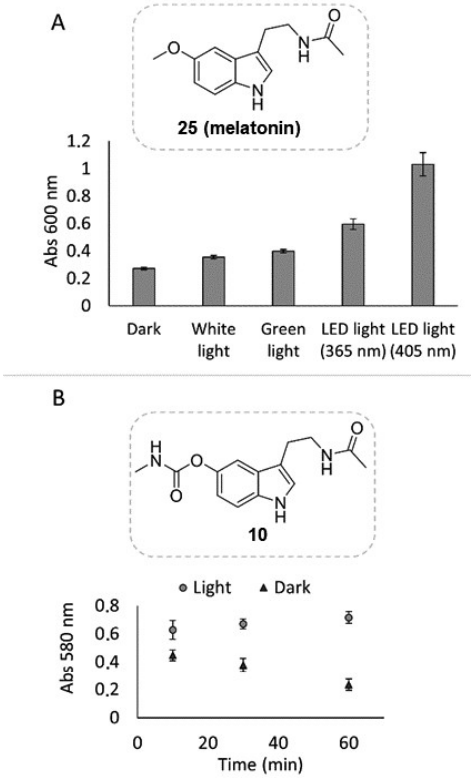

Figure 43. A. Absorbance of the colorimetric complex formed by 1 mM melatonin (**25**) and DMAB after 10 min of incubation under different types of light irradiation **B.** Evolution in time of the absorbance of the samples containing 1 mM compound **10** after 10 min of incubation with DMAB in the dark (triangles) or under UV light irradiation at 365 nm (dots). The figure was originally produced for [2] and was used according to the Wiley CC licensing. The compound numbering was modified, to correspond to the current work.

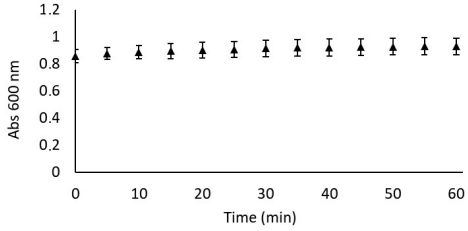

Figure 44. Stability of the color of the melatonin (**25**) complex with DMAB in time, after the stop of light irradiation. The figure was originally produced for [2] and was used without modifications, according to the Wiley CC licensing.

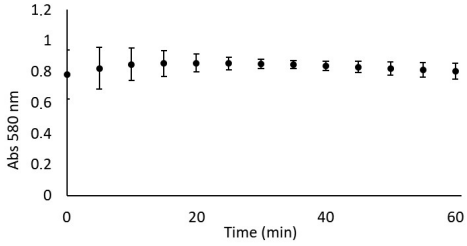

Figure 45. Stability of the color of the **10** complex with DMAB in time, after the stop of light irradiation. The figure was originally produced for [2] and was used without modifications, according to the Wiley CC licensing.

In order to facilitate the practical implementation of the optimized activity assay, an LED array adapted for 96-well microplates was designed and built by Martin Wäscher (Institute of Bioorganic Chemistry, Heinrich Heine University Düsseldorf). The device case was produced by 3D printing, using low-cost materials, and the light was produced using commercially available 405 nm LEDs (Figure 46). The digital construction plans are publicly available along with the published assay data, for easy reproduction of the device.[2]

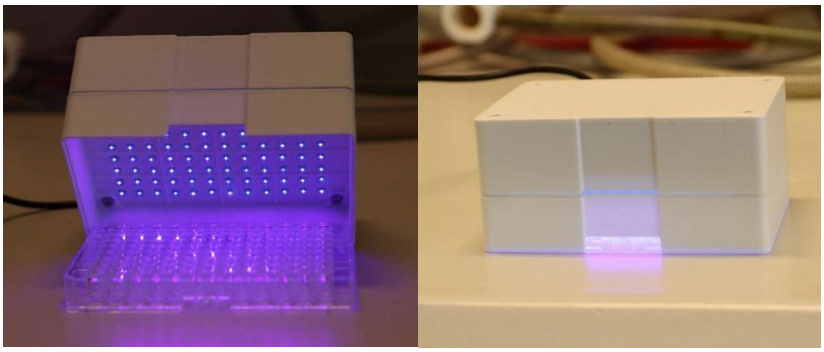

Figure 46. The UV-LED array used for the irradiation of the 96-well plates within the indole assay. The lamp was designed and built by Martin Wäscher (IBOC, Heinrich Heine University Düsseldorf) for this work. The photos were originally produced for [2] and were used without modifications, according to the Wiley CC licensing.

3.4.3 Assay parameter optimization

Melatonin (**25**) was selected as a model compound for the assay components optimization due to its similarity to the PsmD substrates, and its commercial availability. The reaction with DMAB needs strong acidic conditions to take place. Several highly concentrated acids were tested, and various alcohols were screened as solvents for DMAB. In the acid screening experiment, discrepancies in the absorbances appeared between melatonin and the PsmD substrate **10**. Although the samples containing melatonin provided high absorbances in the presence of HCl and H_2SO_4, the reaction with substrate **10** only performed well in the presence of H_2SO_4 (Figure 47A). The choice of alcohol did not cause significant variance in the final sample absorbances, regardless of the analyte. The screening indicated that all tested alcohols can be used in the assay, with *i*PrOH leading to the highest color formation. In the end, the combination of H_2SO_4 and *i*PrOH was chosen for broader assay applicability.

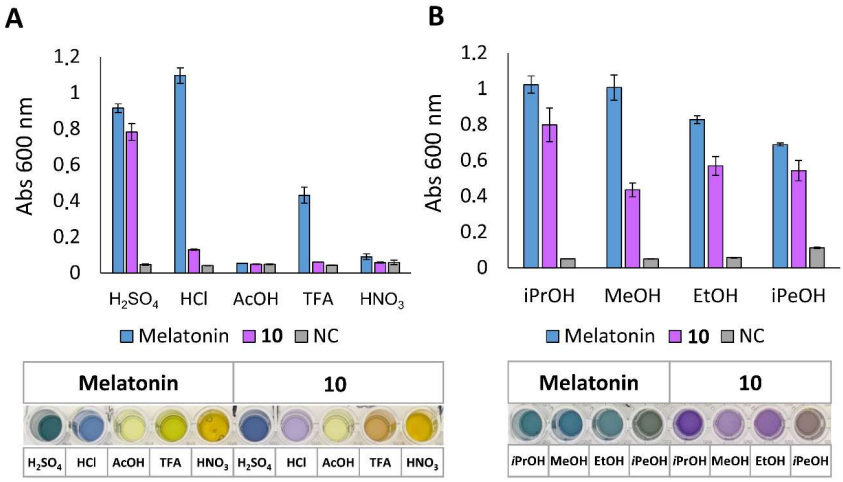

Figure 47. A. The influence of different acids on the read-out. **B.** The influence of different alcohols on the read-out. Blue: DMAB complex with melatonin (**25**); violet: DMAB complex with compound **10**; grey: negative controls (the negative controls contain all the components, except for the substrate). The figure was originally produced for [2] and was used according to the Wiley CC licensing. The compound numbering was modified to correspond to this work.

The necessary DMAB concentration was also tested, revealing a linear dependence. Absorbance at 600 nm increased with DMAB concentration in *i*PrOH (Figure 48A). The 300 mM concentration was chosen for the optimized assay. Higher concentrations were limited by the solubility of DMAB in *i*PrOH. Finally, the effect of the substrate solution pH was assessed. Various pH values typically used in enzymatic reactions were tested, ranging from 5 to 10 (Figure 48B). The pH shift resulting from the addition of concentrated H_2SO_4 seems to erase most of the effects of the initial buffers. After performing the assay, the absorbances at 600 nm were similar across most tested samples, regardless of the initial pH of the analyte solution. However, a drop in absorbance was observed at pH 10, resulting in decreased assay sensitivity. Nonetheless, the assay is applicable across the pH conditions most commonly used in enzymatic reactions, in the presence of various buffers, including sodium acetate, potassium phosphate and sodium bicarbonate.

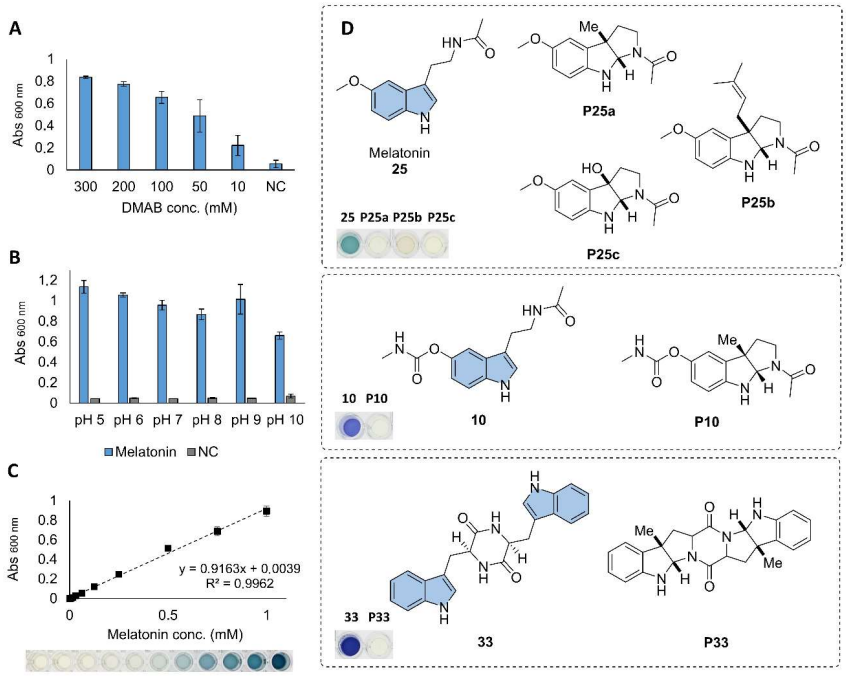

Figure 48. A. The influence of the DMAB concentration on absorbance; **B.** The influence of sample pH on the absorbance of melatonin (**25**) complex at 600 nm. NC stands for negative control, in the absence of **25**; **C.** The linear range of the indole assay with melatonin (**25**) in 96-well plate format and 150 µL total volume, with absorbance measured at 600 nm. The linear response occurs between 7.8 and 1000 µM melatonin (**25**); **D.** Substrates and products of known cyclization reactions producing pyrroloindoles. The photographs of microplate wells show their respective color response within the assay. The figure was originally produced for [2] and was used according to the Wiley CC licensing. The compound numbering was modified to correspond to this work.

Using the optimized conditions, the relationship between the absorbance at 600 nm and the melatonin concentration in the initial sample follows a linear model up to 1 mM melatonin, with a limit of detection of 7.8 µM (Figure 48C). Similarly, a linear calibration of PsmD substrate **10** was achieved to a maximum concentration of 2 mM and a limit of detection of 62 µM (Figure 49). In both cases, the linear response corresponds to the range of concentrations normally used for analytical scale enzymatic reactions. The optimized assay in the presence of melatonin was also tested for reproducibility, producing under 10% deviation of absorbance at 600 nm, across 8 measurements (Figure 50).

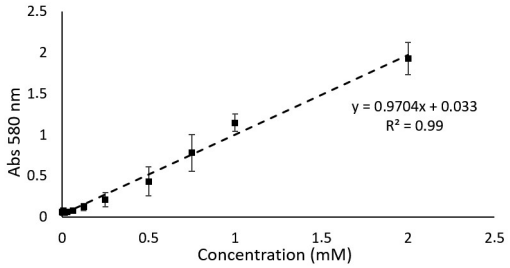

Figure 49. The linear range of the indole assay with **10** in 96-well plate format and 150 µL total volume, with absorbance measured at 600 nm. The linear response occurs between 62 and 2000 µM **10**. The figure was originally produced for [2] and was used without modifications, according to the Wiley CC licensing.

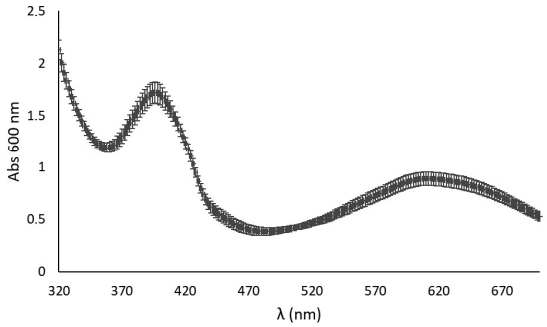

Figure 50. Reproducibility study of the absorbance spectrum of the complex formed with melatonin 1 mM, using the indole assay. 8 samples from 3 different batches were compared. At 600 nm there was an 8.6% standard deviation. The figure was originally produced for [2] and was used without modifications, according to the Wiley CC licensing.

In the optimized procedure, 50 µL sample solutions in buffer were transferred to the plate wells, after which 50 µL 98% H_2SO_4 were carefully added and mixed thoroughly. The plate was incubated at room temperature for 10 min, and then 50 µL DMAB solution (300 mM in *i*PrOH) was added to the samples and mixed thoroughly. The plate was then incubated for 10 min under LED irradiation at 405 nm. The resulting colors ranged from pink to blue, depending on the analyzed substrate, allowing for absorbance measurements using a plate reader (Figure 51).

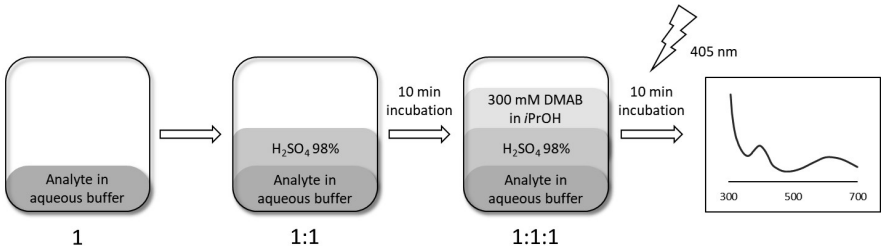

Figure 51. General optimized procedure for the indole assay. The figure was originally produced for [2] and was used without modifications, according to the Wiley CC licensing.

There is a variety of enzymes capable of catalyzing group transfers on the 3-position of indole-containing substrates, leading to spontaneous intramolecular cyclization to pyrroloindole (described in Chapter 2.1.4). The assay was tested with various indoles and pyrroloindoles, to assess its applicability range. Its use is not limited to the activity determination of the PsmD methylation, but is applicable to any enzyme catalyzing the formation of pyrroloindole from indoles, regardless of the transferred group or enzymatic mechanism. To test this, melatonin was tested, along with its potential methylation, hydroxylation, and prenylation products. The melatonin-derived pyrroloindoles were chemically synthesized by Mona Haase (Institute of Bioorganic Chemistry, Heinrich Heine University Düsseldorf), starting from melatonin using methyl iodide or prenyl bromide in basic conditions, to produce the methylated and prenylated compounds. The hydroxylated compound was synthesized in four steps using a 3-brominated intermediate followed by oxidation, as described in the literature.[2] None of the pyrroloindoles reacted with DMAB, demonstrating the selectivity of the assay for indoles and its applicability for multiple types of pyrroloindole-forming enzymatic processes. For validation, the PsmD substrate **10** and natural product **P10** were tested, as well as the natural dipeptide substrate **33** and product **P33** of the methyltransferase StspM1.[292] Only the compounds containing the aromatic indole rings lead to color formation after the assay (Figure 48D).

3.4.4 Substrate scope of the new colorimetric assay

To determine the structural range of possible analytes leading to positive results, several indole-containing natural metabolites were analyzed using the optimized assay. Free and protected tryptophan (**6**, **34**, **35**), serotonin (**8**), tryptamine (**36**), and melatonin (**25**) reacted

with DMAB, forming compounds that strongly absorb in the 580-600 nm range (Figure 52). This makes them excellent candidates for detection and quantification using the indole assay. Compounds **10**, **23** and **29** as well as the tryptophane dipeptide **33**, also led to intense color formation. The samples containing indole (**5**), 4-hydroxyindole (**37**) and indole pyruvic acid (**38**) displayed slight orange coloration after the assay was used, with a lower local maximum absorbance around 0.5 mAU and a shift towards lower wavelengths. Other heterocyclic compounds, adenine (**39**) and 8-hydroxyquinoline (**40**) did not form any colored product in the presence of DMAB. The lack of coloration of compound **19** was unexpected, and might occur due to the low solubility of **19** in water. Compound **19** was of interest for PsmD engineering, so a modification of the assay was tested, supplementing the sample with *i*PrOH to improve the solubility. In this case, a color change could be detected using a 1:1 *i*PrOH:buffer ratio of the initial sample (Figure 53). This allows for the detection of **19** using the modified indole assay, albeit with lower sensitivity.

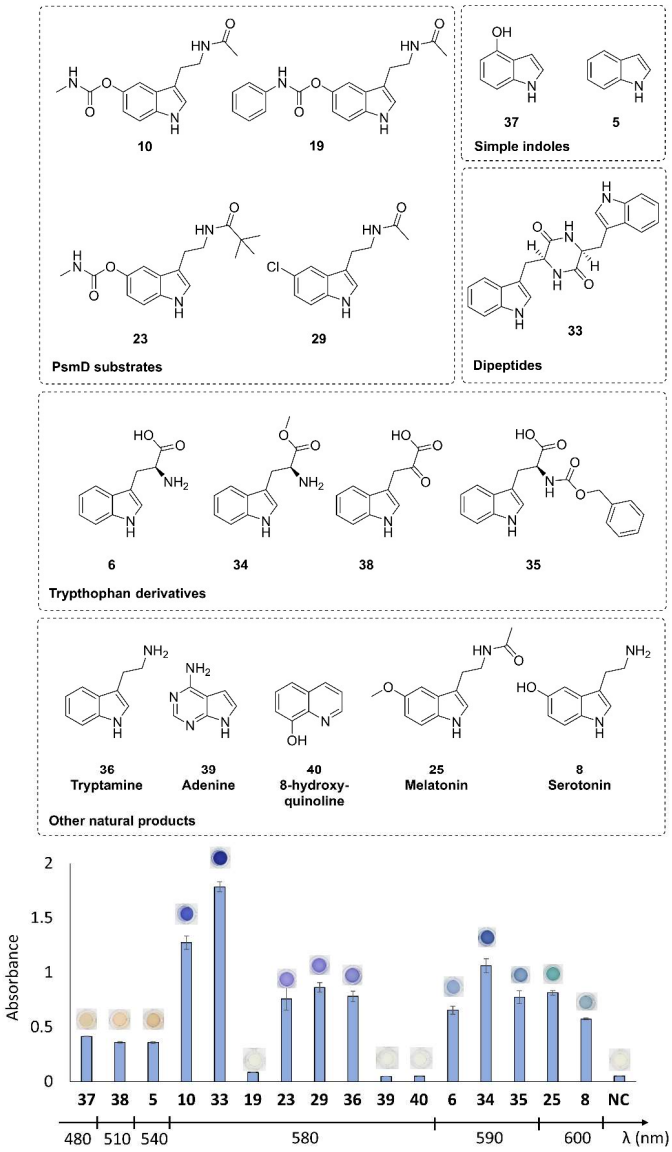

Figure 52. Substrate scope used to test the indole assay. The graph shows the absorbance at the chosen peak wavelength of each substrate, with a 1 mM initial sample concentration; the photographed plate wells show the corresponding color. NC stands for "negative control" (absorbance measured at 580 nm). The figure was originally produced for [2] and was used according to the Wiley CC licensing. The compound numbering was modified to correspond to this work.

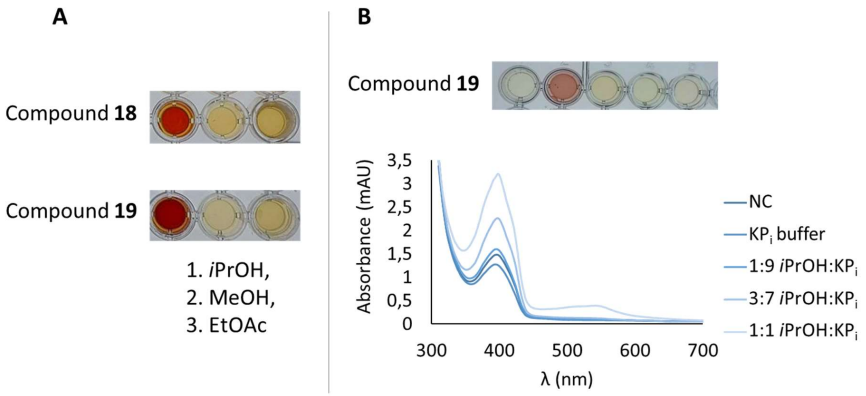

Figure 53. A. Wells containing compounds **18** (*t*-Bu-carbamate) and **19** (Phe-carbamate), after performing the modified assay with different dilution solvents. The initial 1 mM sample in KP_i buffer (50 mM, pH 7.5) was diluted with an equal amount of solvent, after which 50 µL of the mixture was used in the usual assay protocol. **B.** Effect of the dilution ratio with *i*PrOH on the sample color in the wells containing 1 mM **19**, after the completion of the assay procedure. The sample diluted to a 1:1 ratio provided the highest absorbance at 550 nm.

3.4.5 Application of the colorimetric assay for PsmD activity determination

The indole assay was developed specifically for the high-throughput activity screening of PsmD-catalyzed methylation reactions. To assess its utility in enzymatic reactions, it was tested with the PsmD_*Sa* reaction mixture in two different formulations. In the initial test, the reaction was performed using isolated PsmD_*Sa* in the presence of 1 mM substrate **10** and SAM. The reaction was stopped at different time points and the conversion of **10** to **P10** was assessed in each case. The consumption of the substrate followed a linear trend.

A newly developed pyrroloindole assay was used in parallel, to monitor the product formation.[2] The pyrroloindole assay was developed by Mona Haase (Institute of Bioorganic Chemistry, Heinrich Heine University Düsseldorf) and it requires the use of cerium sulfate under acidic conditions for the detection of pyrroloindoles. Both assays can be utilized for monitoring the PsmD reaction progress, from different directions: the indole assay detects the substrate consumption, while the pyrroloindole assay monitors the product formation. When used in the same experiment, the obtained enzymatic activity should coincide. The conversion trends after the PsmD reaction followed by separate analysis using each assay were complementary

(Figure 54A), and specific activities could be calculated. The calculated specific activity was 0.06 ± 0.01 U/mg for the indole assay and 0.047 ± 0.001 U/mg for the pyrroloindole assay. For the validation of both assays, the conversion in time was also analyzed using RP-HPLC, obtaining a calculated specific activity of 0.046 ± 0.000 U/mg. Therefore, both assays can reliably be used for specific activity determination using isolated enzymes.

The use of isolated enzymes is typically avoided in the screening of mutant libraries due to the large number of variants. Instead, whole-cell formulations or protein extracts are usually chosen. For a proof of concept in this type of setting, the indole and pyrroloindole assays were used for conversion determination in PsmD_*Sa* reactions using whole-cell biocatalysts (Figure 54B). The wild type and mutants R85A and E35A were expressed in *E. coli* Bl21 Gold (DE3) cells, which were then harvested and resuspended in a reaction mixture containing 1 mM substrate **10** and SAM. The mutants were selected based on their activity relative to the wild type, as determined from the earlier alanine scan (Chapter 3.3.2). *E. coli* cells containing the empty vector were used as a negative control. After 16 h of incubation, the reactions were stopped and the cells were removed by centrifugation. The supernatant was used without further processing in the regular assay protocol. The RP-HPLC conversion in the samples was also determined for validation. The conversion trends between variants correspond between all the analytical methods used. As expected, WT PsmD_*Sa* reached the highest conversion, followed by mutant R85A and E35A. In the case of E35A, the low conversion could not be detected with either assay, resulting in absorbance readings below the background levels. The background can be attributed to the proteins and cell debris present in the mixtures. The tryptophan present in the samples can also be responsible for the background absorbance, as it was shown to form colored condensation compounds with the DMAB. While the conversions detected by the pyrroloindole assay were significantly different from the HPLC analysis, the trends were maintained, allowing its use for a qualitative analysis using whole cells. In the case of the indole assay, the higher conversions were comparable with the HPLC results, with the sensitivity decreasing at lower conversions. Considering this limitation, the indole assay is compatible with (at least) a semi-quantitative high-throughput screening using whole-cell biocatalysts.

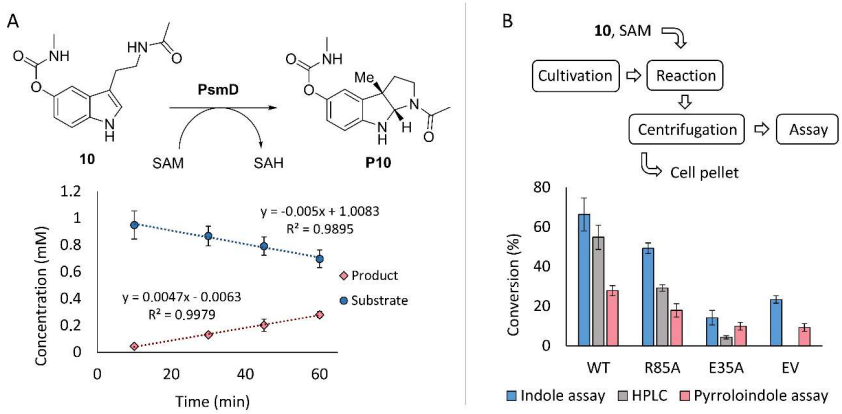

Figure 54. A. Reaction scheme of the reaction catalyzed by PsmD_*Sa* in the presence of the SAM cofactor. Variation of substrate **10** and product **P10** concentration in time during the reaction catalyzed by isolated PsmD_*Sa*. The substrate consumption was monitored using the indole assay, while the product formation was quantified using the pyrroloindole assay. The slopes correspond to comparable activity, displayed here as the variation of concentration in time, from both the perspective of the substrate and the product. **B.** Process scheme of the PsmD_*Sa* mutant screening using whole-cell biocatalysts. The graph shows the conversion to **P10** for the tested mutants, determined from the supernatant using the indole assay (blue), the pyrroloindole assay (pink) and RP-HPLC (grey). The figure was originally produced for [2] and was used according to the Wiley CC licensing. The compound numbering was modified to correspond to this work.

3.4.6 Chapter summary

- ◊ The Ehrlich reagent detects indoles through the coupling with DMAP in the presence of an acid and alcohol, forming a colored product. Various versions of the assay have been developed, with applications ranging from diagnostics to forensic science and microbiology.
- ◊ The available Ehrlich test versions are not applicable for the detection and quantification of the PsmD indole-containing substrates. For this reason, a new iteration of the assay was developed.
- ◊ It was found that light irradiation plays a crucial role in color formation, likely triggering the oxidation of the condensation product with DMAB.
- ◊ The system parameters (component types and concentrations, pH, light source) were optimized, enabling its applicability for a range of substituted indoles.
- ◊ The assay is selective for indoles, enabling its use with pyrrolindole-forming enzymes. Its substrate scope includes metabolites such as melatonin, serotonin, tryptamine and tryptophan.
- ◊ The assay was successfully used to determine the substrate conversion and activity of multiple PsmD variants in isolated form and as whole-cell biocatalysts, demonstrating its utility for the high-throughput screening of mutant libraries.

3.5 Directed evolution of PsmD_*Sa*

The mechanistic analysis of PsmD_*Sa* revealed a dynamic mode of action, triggered by important conformational shifts of the enzyme. In order to modify the substrate scope of the enzyme in a productive manner and take into account the unexpected effects of amino acid substitutions within the catalytic site, a semi-rational design approach was chosen for the engineering of PsmD, using saturation mutagenesis. This allowed for a reduction of bias, by exploring the effects of all the possible amino acid residues in the chosen positions while producing concentrated mutant libraries, which could be efficiently screened within the scope of the project.

3.5.1 Mutagenesis strategy

Two substrates were used for the screening of mutant libraries, containing voluminous functionalities on either side of the molecule (Figure 55). Although physostigmine derivatives containing phenyl-carbamates are known to possess AChE inhibitory effects, not much is known about the effect of substituents on the amide side (Chapter 2.1.6). Derivatives containing longer alkyl chains such as ethyl and butyl were shown to possess AChE and BChE inhibitory effects, but the available data for similar structures remains limited.[153] For this reason, we chose substrate **23** containing a *t*-butyl residue on the amide, in the hope of further expanding the available diversification options in this position. Product **P23** is also known to inhibit AChE and BChE.[358] Substrate **19**, containing a phenyl-carbamate rest is a precursor of the AChE inhibitor drug phenserine. Since phenserine and its derivatives are synthetic drugs, a chemo-enzymatic route towards phenserine would be attractive, providing an alternative option for its stereoselective production.

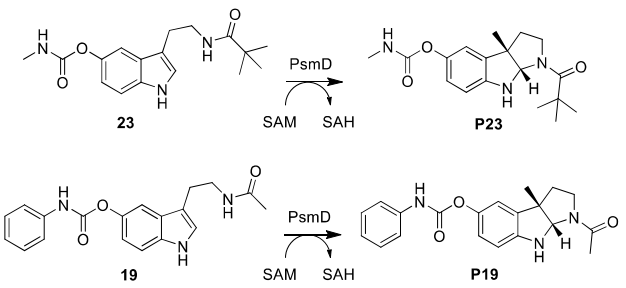

Figure 55. Substrates chosen for the mutant library screening and their respective enzymatic methylation products.

The choice of saturation mutagenesis sites was driven by the aim of increasing the available space for bulky substrate substituents, while maintaining a compact enough catalytic pocket for the methylation to take place. Multiple studies have shown the importance of compression within the catalytic site of methyltransferases for the S_N2-type methyl transfer (see Chapter 3.3). As such, we targeted bulky amino acid residues positioned at the extremities of the catalytic pocket, which were shown to not be vital in the alanine scan. Two residues were chosen from the previously identified “tryptophan cluster” (Chapter 3.2), W166 and W33, as well as Y256 in their vicinity, as they pose a significant steric hindrance on the carbamate side of the substrate. Y15 and Y197 were also targeted from the lid area (Figure 56).

Iterative saturation mutagenesis allows the creation of focused libraries and reduces bias by taking into account possible cooperative effects of different mutations. As such, iterative mutagenesis and screening steps were planned with the aim of harnessing the potentially cumulative effect of beneficial mutations. To combat codon redundancies and reduce the resources needed for the screening we chose the 22c trick for the primer design within the saturation mutagenesis approach, using a specific set of degenerated primer mixtures (Table 6).[420]

Table 6. Comparison between saturation mutagenesis primer design strategies

Saturation strategy	Degenerated codon	Colonies screening requirement for 95% aa coverage[420]
Regular	NNK	96
22c trick	NDT, VHG, TGG mix	66

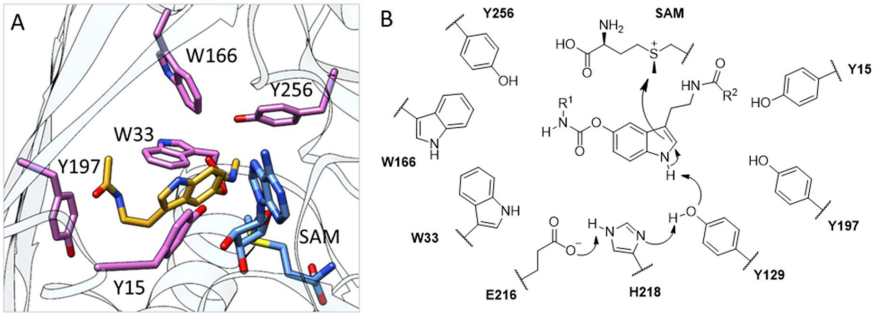

Figure 56. A. Catalytic site of PsmD_*Sa* with the docked SAM and the natural substrate **10**. Saturation mutagenesis targets are highlighted in pink. **B.** Scheme of the catalytic site of PsmD and the positions of saturation mutagenesis targets relative to the substrate and the catalytic triad.

3.5.2 Mutant library generation

The use of the 22c trick for primer design involves mixing the degenerated primers in a specific ratio. Throughout the optimization efforts, inverse PCR, also known as “round-the-horn” mutagenesis functioned in a consistent manner (Figure 32, Chapter 3.3.2). This method uses back-to-back primers, amplifying the whole plasmid in opposite directions. Only one of the primers contains the degenerated codons. At the end of the PCR amplification, linear amplicons are produced, requiring a subsequent ligation step for the generation of circular plasmids. The high GC content of the PsmD gene rendered the optimization of annealing temperatures difficult. To accommodate the variety of mutation targets and primer sequences without the necessity of extensive PCR condition optimization, a “touch-down” approach was employed. This involves the reduction of annealing temperature by 1 °C with each cycle, within a given set of boundaries. The method can present several disadvantages, such as the higher cost of phosphorylated primers and the higher chance of random mutations occurring when amplifying a whole plasmid, as opposed to genes or gene fractions. Nevertheless, in this case, the inverse PCR primer design method combined with the “touch-down” PCR approach proved to be the most versatile and reliable for the amplification of the PsmD gene libraries.

3.5.3 Development of an automated screening process

An automated process for the mutant library generation and screening can greatly improve the speed and precision of directed evolution. To increase the versatility of the process and enable its use for the engineering of other similar enzymes, the process was split into three modules: protein expression, enzymatic reaction and activity assay (Figure 57). The automated process starts with colony picking of the mutant library transformants on agar plates. A robotic arm and liquid handling system can then perform all the steps sequentially, until the end of the enzymatic reaction module. Depending on the enzymatic process and the type of assay used, the next module could be continued on the same platform, or separated. The newly developed indole assay (Chapter 3.4) was used for the evaluation of the substrate consumption. Due to the necessity of concentrated H_2SO_4, the assay module was moved to a separate Opentrons (NY, USA) liquid handler robot, to avoid the corrosion of the laboratory platform components.

The automated process in its current form can be applied to enzyme libraries which fulfil several conditions. In this study, the protein expression was performed by autoinduction in the *E. coli* production strain BL21 Gold (DE3). While generally, lac-induced expression systems can function via autoinduction, the expression needs to be confirmed and optimized if

necessary in each case, prior to the screening. If a later induction is required, OD_{600} monitoring systems could be implemented, along with an extra induction step. The enzymatic reactions were performed in whole-cell format. Depending on the membrane permeability of the substrates and products, this might often not be a possibility. High-throughput cell lysis steps can be considered, using a combination of lysozyme and detergents. Finally, the indole assay can provide appropriate fast screening strategies for other pyrroloindole-forming enzymes. For methyltransferases, in the absence of a UV/Vis or fluorescence assay, one can consider the use of mass spectrometry for the screening of the focused mutant libraries.

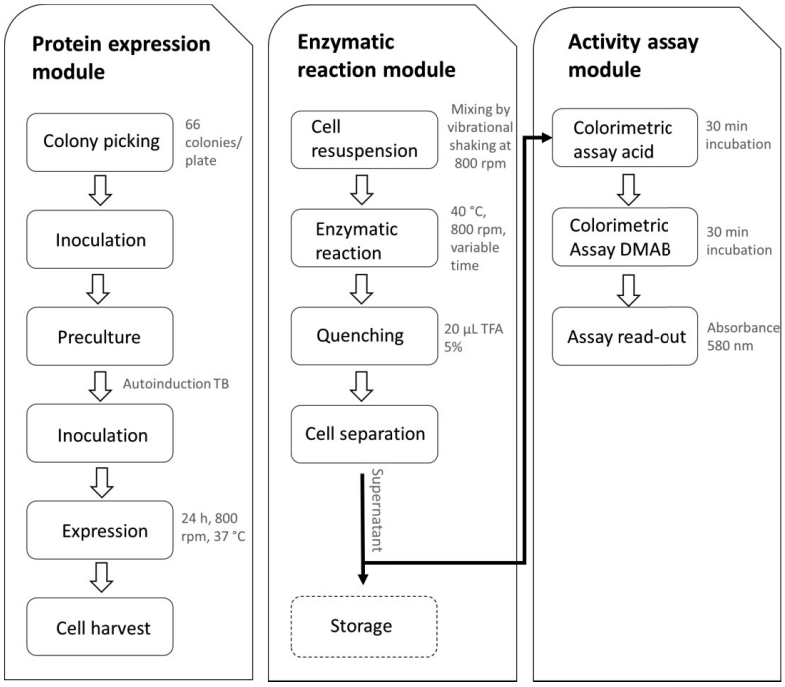

Figure 57. Process scheme of the automated mutant library production and screening process.

3.5.4 Synthesis of the PsmD substrates used for screening

Substrates **23** and **19** were synthesized according to the literature.[358] A three-step synthesis route starting from 2-(5-(benzyloxy)-1H-indol-3-yl) acetonitrile (**13**) has been employed for both substrates, with minor differences (Scheme 14). In the first step, a reduction of the nitrile to amine in the presence of a $NaBH_4$ takes place *in situ*, followed by the acylation with the corresponding anhydride (di-*tert*-butyl-dicarbonate for **41** and acetic anhydride in the case of **14**), in the presence of $NiCl_2$. Next, a Pd-catalyzed deprotection of the phenol is necessary, before the carbamate attachment in the final step. A deprotonation of the phenol using triethylamine is followed by the DMAP-catalyzed carbamate formation. For substrate **23,** methylcarbamoylchloride was used as a reagent, while in order to obtain the phenyl-carbamate in substrate **19**, phenyl isocyanate was used. Although isocyanates are highly effective in carbamate synthesis with alcohols and phenols, their high toxicity limits their suitability for larger scale processes. In the end, the isolated substrates were obtained with a 21% overall yield for substrate **23** and a 22% yield in the case of **19**.

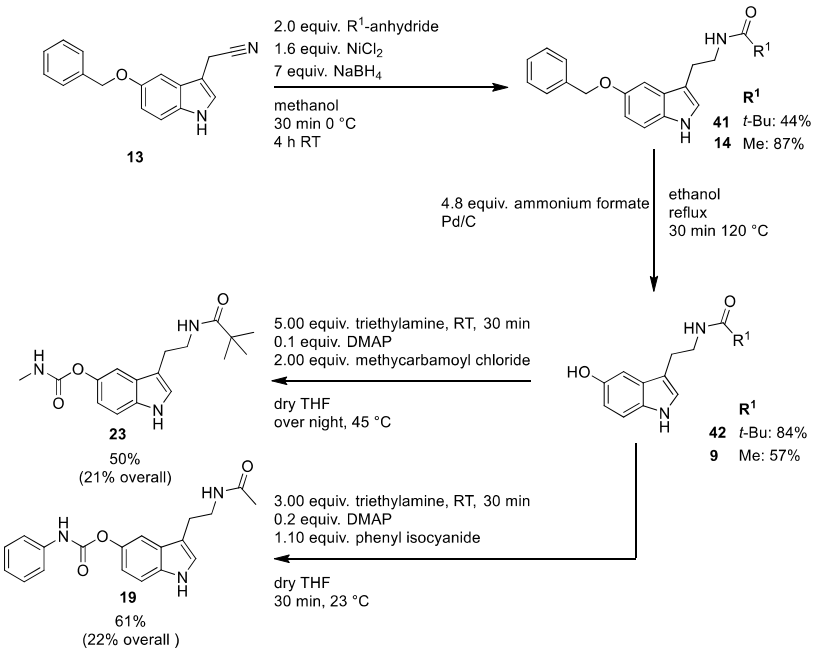

Scheme 14. Synthesis routes to PsmD substrates **23** and **19**.

3.5.5 Hit identification and characterization

After the activity assay step, heat maps were generated based on the absorbance values at 580 nm. Since the indole assay detects the PsmD substrate, the hits were selected from the wells with the lowest absorbance at 580 nm, corresponding to the highest conversion of the substrate by the PsmD variant (Figures 58, 59).

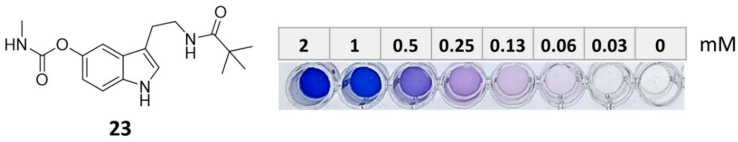

Figure 58. Example of the relationship between the analyte concentration (substrate **23**) and color intensity after applying the indole assay.

For each library, the wells with the five lowest absorbances were selected and the corresponding gene sequences were analyzed. Then, all the identified hits were re-cultivated, expressed and purified for specific activity determination and comparison, using the MTase-Glo™ assay to determine the SAH cofactor formation. A comparison between the absorbance values obtained from the colorimetric assay and the specific activity determined from the MTase-Glo™ assay shows a similar trend between the hit variants. Small differences in the activity ranking of the colorimetric assay were observed. Some errors are not unexpected, due to the high absorbance background of the whole-cell reaction mixtures, as well as the multiple steps required in the high-throughput screening. A test run was performed using the natural substrate and the Y197X mutant library in order to validate the results of the colorimetric assay under the conditions used within the automated process. After the colorimetric assay step, several wells were picked randomly and the absorbance of the samples at 580 nm was compared with the RP-HPLC conversions of **10** to **P10** (Table 7). The absorbance values decrease correlates to the increase of conversions, and the order of mutant activities was similar in both analysis methods. This confirmed the accuracy of the colorimetric assay for ranking mutant activities. Ultimately, after considering repeated hit mutations and false positives, several active mutants could be selected from each library in the screenings targeting **23**. The screening for activity against **19** yielded one library with active mutants.

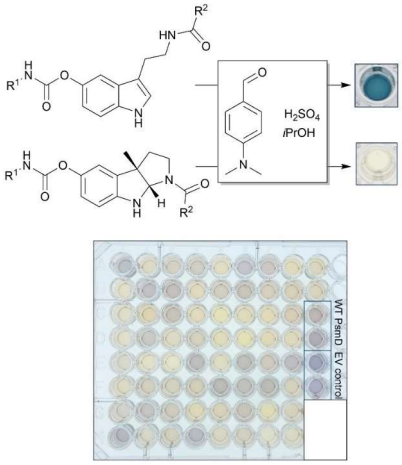

Figure 59. General scheme of the colorimetric assay used for the detection of the substrate indole and example of a library plate after the entire automated screening process. EV refers to the "empty vector" negative control. The figure was produced for [3] and used without modifications according to the CC licensing of the Royal Society of Chemistry.

Table 7. Validation of the colorimetric assay as a screening strategy for mutant libraries. Wells were randomly selected and the absorbance at 580 nm after the indole assay was compared to the RP-HPLC conversions of the natural substrate **10** to the methylated product **P10**.

Sample	Conversion in RP HPLC	Absorbance at 580 nm
C8	100%	0.1088
F4	100%	0.1077
F12	95%	0.1203
E2	80%	0.1333
D6	66%	0.1601
C2	0%	0.1821
C10	0%	0.2033
F6	0%	0.2381

After the elucidation of the hit sequences, the selected mutants were isolated for specific activity determination and comparison. The purification of a larger number of mutants using the regular Ni-NTA affinity chromatography method is time and resource-intensive, therefore a small-scale chromatographic purification method was developed. This allowed the purification of a larger number of different enzymes in parallel and significantly reduced the necessary time. The parallel purification of 5-10 mutants became possible, yielding approx. 200-300 µg protein/run, enough for analytical scale enzymatic activity determination. The

detailed small-scale purification protocol is described in the experimental section (Chapter 7.3.3).

3.5.6 Screening for *t*-Bu-amide activity (23)

The screening using substrate **23** provided the most successful hit in the first round of saturation mutagenesis. While mutations of Y15, Y197 and W33 led to a reduction in PsmD activity, mutant W166C provided a 3-fold increase in specific activity towards **23**, compared to the wild type. Considering the possibility of synergistic effects with mutations in the other positions, we continued the iterative approach. A series of mutants were identified which display more activity towards **23** compared to the wild type: W166C/W33L, W166C/Y15F, W166C/Y197F, W166C/Y197F/W33F, W166C/Y197F/W33M, W166C/Y197F/Y15F and W166C/Y197F/Y15F/W33L. Nevertheless, none surpassed the activity of the initial hit, W166C. Subsequent mutations to the other chosen positions reduced the activity of W166C (Figure 60). In particular, mutations to Y15 and W33 seemed to generally reduce the activity. The only active mutation of Y15 was to phenylalanine, which supports the earlier mechanistic hypothesis about the steric requirements of the PsmD lid closure (Chapter 3.3). Similarly, the presence of W33 might be necessary for the proper folding in the “tryptophan cluster” area of the catalytic site. Interestingly, W166 is part of the cluster as well, but the position displays much more versatility for mutations. Further saturation mutagenesis strategies might benefit from focusing on the area in the vicinity of W166 (Figure 61).

The activity towards the PsmD natural substrate **10** was also determined and a clear decreasing effect is observable in the mutants active towards **23** (Figure 62). This is expected, as the increase in space in the catalytic pocket can also reduce the probability of substrate **10** orienting in a productive position in the catalytic site. The enantioselectivity of the reaction was evaluated for each hit using chiral HPLC. Only one enantiomer was detected in each case, suggesting the conservation of the enzyme stereoselectivity upon engineering.

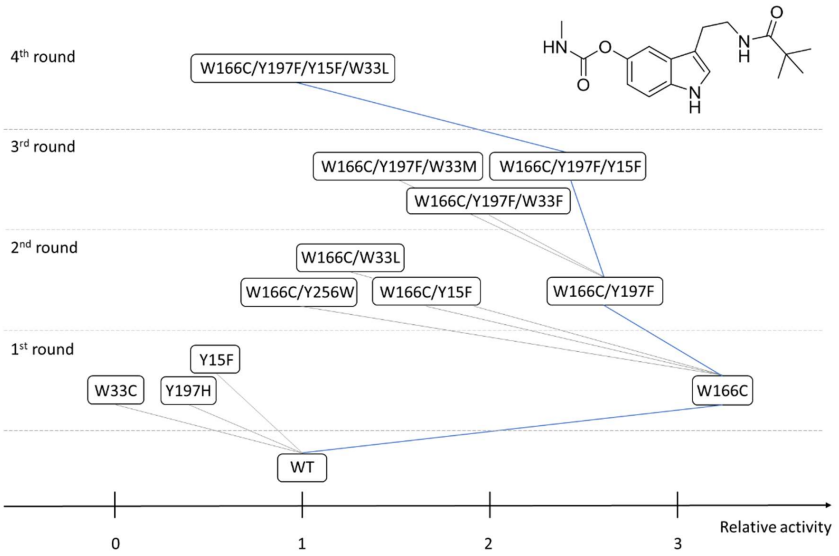

Figure 60. Mutagenesis and screening rounds using substrate **23**. The iterative saturation mutagenesis progression path is highlighted.

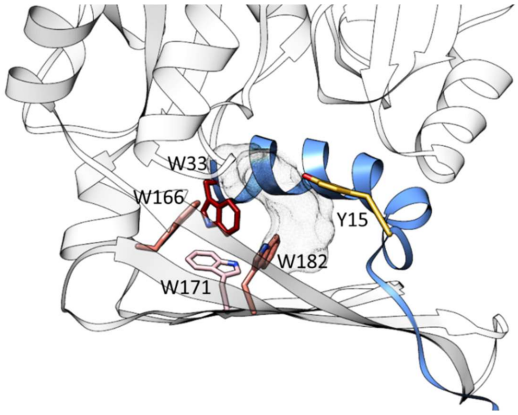

Figure 61. Homology model of PsmD_*Sa* with the docked natural substrate **10** (surface shown as a mesh). The tryptophan cluster is depicted in relation to the enzyme's catalytic site. The color intensity correlates to the conservation of tryptophan residues across methyltransferase homologs, with higher conservation scores corresponding to more intense colors, as calculated using the ConSurf web server.[402] The tryptophan cluster is thought to anchor the α-helix supporting the N-terminal lid (shown in blue). Structurally, we propose that this substitution might disrupt the lid motion, affecting the positioning of Y15 within the catalytic site (shown in yellow). The figure was produced for [3] and used without modifications according to the CC licensing of the Royal Society of Chemistry.

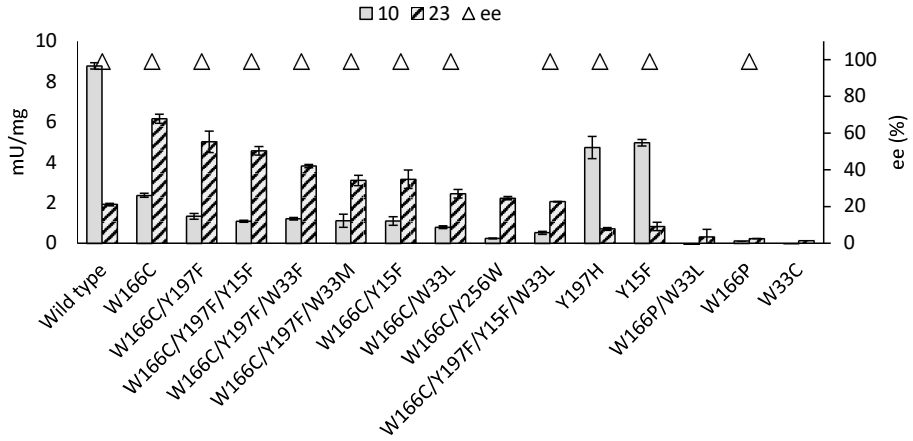

Figure 62. Specific activities towards the *t*-Bu-amide (**23**) and the natural PsmD substrate (**10**) of hits from the screening using **23** as a target substrate. The specific activity was measured using the MTase-Glo™ commercial assay. Conditions: 20 μM substrate, 30 μM and 1 μg isolated PsmD variant were incubated in 20 μL MTase-Glo™ 1X buffer at 45 °C for 15 min. Then, the reactions were quenched with 5 μL TFA 0.5% (v%, in water) and the assay was performed according to the manufacturer's protocol. The enantiomeric excess (*ee*) was evaluated using chiral RP-HPLC.

The selected mutants were tested in reaction with substrate derivatives displaying different chain lengths attached to the amide (Figure 63). Mutant W166C outperforms WT PsmD on substrates **21** and **23**, but predictably, its activity towards the smaller **20** is reduced. None of the other mutants outperform W166C and WT PsmD in the reaction with **20** and **21**.

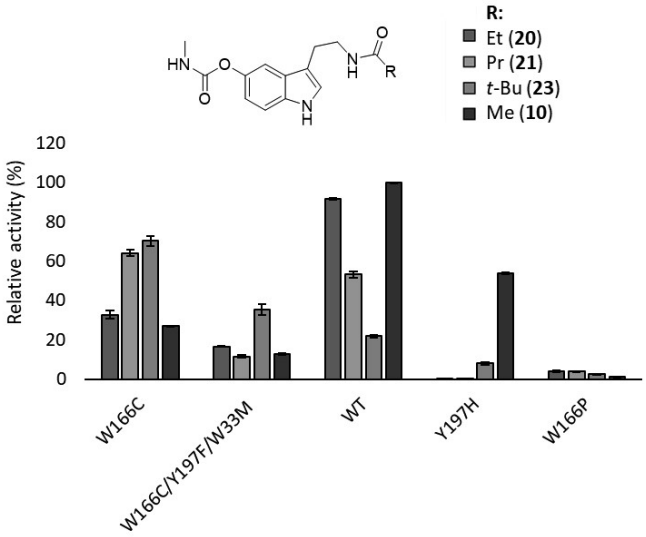

Figure 63. Relative activity of selected mutants towards other PsmD substrates with substituted amides. The activity was measured using the MTase-Glo™ commercial assay. Conditions: 20 μM substrate, 30 μM and 1 μg isolated PsmD variant were incubated in 20 μL MTase-Glo™ 1X buffer at 45 °C for 15 min. Then, the reactions were quenched with 5 μL TFA 0.5% (v%, in water) and the assay was performed according to the manufacturer's protocol.

3.5.6.1 Docking of 23 in WT PsmD_*Sa* and mutant W166C

In order to uncover the structural basis of the improved activity of W166C towards substrates with voluminous substituents, we performed an extensive docking of substrate **23** in the catalytic site of W166C and WT PsmD_*Sa*. The docking, dimensional data extraction and principal component analysis were performed by Dr. Thomas Classen, from the Institute of Bioorganic Chemistry, Heinrich Heine University Düsseldorf. The homology model of PsmD_*Sa* was obtained using the "closed" crystal structure of the homolog PsmD_*Sg* (PDB: 7ZKG) as a reference (Chapter 3.2.4). The mutation was introduced using the "rotamers" function of UCSF Chimera, and the amino acid conformation was chosen based on the highest probability according to the Dunbrack 2010 library.[421, 422]

A comprehensive probing of the catalytic site docking poses was performed to observe the substrate binding trends of **23** and **19** within WT PsmD_*Sa* and mutants W166C and W166P. The binding energy range was restricted to 3 kcal/mol in order to filter for only the highest

affinity binding. To thoroughly explore the conformational space within the catalytic site for qualitative analysis, each docking combination was repeated 40 times, with 50 poses for each session. In the end, a total of 11567 binding poses were obtained for the six combinations, due to the energy restraint.

For the comparative analysis, several representative atoms were selected from each substrate, in order to reduce the dimensionality of the data set. The atoms were chosen to represent the entire degree of freedom of the conformation, as well as the atom corresponding to the methylation site. This reduced data set was then subjected to principal component analysis, independent of substrate type or enzyme, extracting three principal components resembling 67% (PC1), 9% (PC2), and 6% (PC3). The data was then clustered by distance into 10 clusters, representing different types of binding poses (Figure 64). The putative productive binding pose was selected based on the structural and mechanistic information previously acquired for PsmD_*Sg* (Chapters 3.2 and 3.3) and corresponds to cluster 6 in all enzyme-substrate combinations. Information such as the enzyme variant, binding energy and the distance between the substrate and the methylation site could be projected onto the data set, and the trends were correlated with the observed changes in enzymatic activity.

The comparative cluster analysis of the obtained poses of **23** in WT PsmD_*Sa* and mutant W166C correlate to the experimental activity results for the two enzyme-substrate combinations. Cluster 6, associated with the productive pose, is mainly populated by poses of **23** in W166C. The cluster is generally associated with lower distances between C3 of the substrate indole and the methyl group of SAM, as well as lower binding energy (Figure 66). From a structural point of view, the reduced activity of WT PsmD_*Sa* correlates with the low occupation of cluster 6. Studying the representative binding pose of **23** in W166C, a small channel forms between C166 and W33, accommodating the carbamate rest of the substrate and leading to a more relaxed conformation, that is not achieved within the catalytic site of WT PsmD_*Sa* (Figure 65). Our MD simulations of PsmD_*Sa* showed the opening of a channel between W166 and W33 driven by the motion of the two α-helices connected to the residues. This motion seems to be involved in the removal of the product after the enzymatic reaction takes place (Chapter 3.3.4). The replacement of W166 disrupts the π-stacking interaction with W33, potentially affecting the dynamics of product egress and influencing the enzyme's activity.

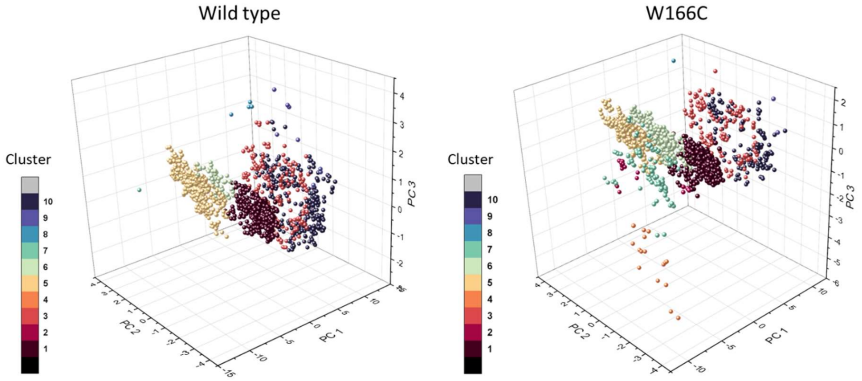

Figure 64. Cluster representation after principal component analysis of the obtained docking poses of **23** in the catalytic site of WT PsmD_*Sa* and mutant W166C. The figure was produced for [3] and used without modifications according to the CC licensing of the Royal Society of Chemistry.

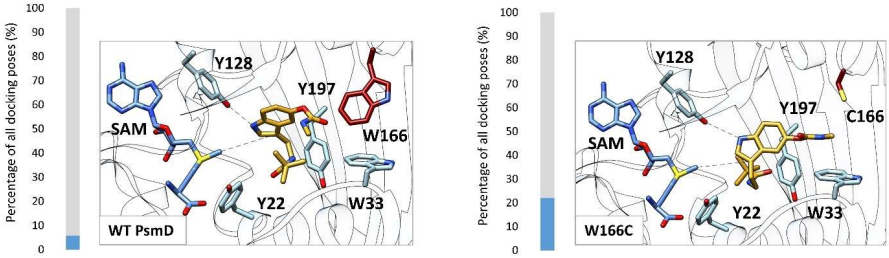

Figure 65. Docked **23** in WT PsmD_*Sa* and mutant W166C. The bars represent the percentage of the productive poses obtained after the docking of **23**, relative to the entire data set for each variant. A higher percentage corresponds to a higher chance of obtaining a docking pose corresponding to enzymatic activity. A total of 1999 poses were analyzed for each variant. The displayed poses were chosen based on their similarity to the previously determined active pose of the natural substrate, representing activity. The residue at position 166 is highlighted in red. The figure was produced for [3] and used without modifications according to the CC licensing of the Royal Society of Chemistry.

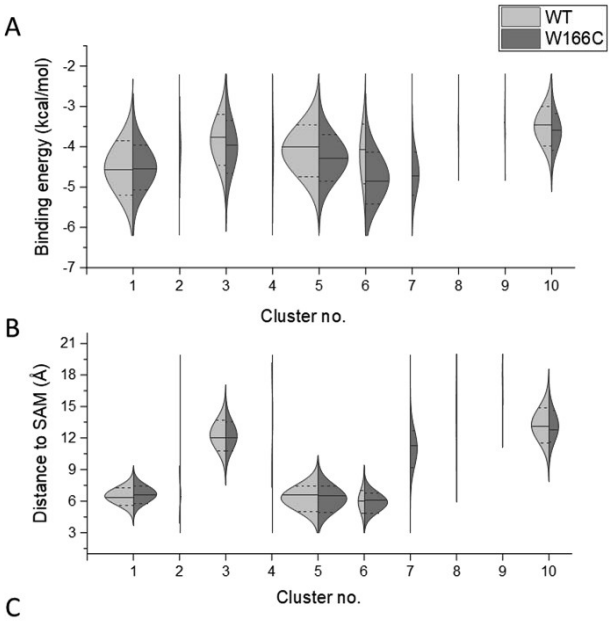

Cluster	1	2	3	4	5	6	7	8	9	10
N [WT]	541	0	297	0	701	114	1	7	8	330
N [W166C]	441	23	216	16	543	442	130	2	2	184

Figure 66. Clustering of substrate **23** poses in WT PsmD_*Sa* and the mutant W166C and the normal distribution of calculated parameters in each cluster. The median is represented as a solid line; the dashed lines indicate the standard deviation. Cluster 6 is considered the active binding mode, according to previous studies on PsmD_*Sa*. **A.** Distribution of calculated binding energies per pose cluster. **B.** Distribution of distances between the SAM methyl group and the methylation site per pose cluster. **C.** Number of samples assigned to each cluster in the principal component analysis. The figure was produced for [3] and used without modifications according to the CC licensing of the Royal Society of Chemistry.

3.5.7 Screening for Phe-carbamate activity (19)

A narrower screening was performed with substrate **19** containing a phenyl ring attached to the carbamate, a precursor of the AChE inhibitor phenserine (Figure 67). Due to its low solubility in water reducing the assay efficacy and presumably the enzymatic reaction rate, a focused test screening was performed for mutant libraries in positions 166 and 33, most likely

directly involved in the carbamate accommodation within the catalytic site of PsmD (Chapter 3.3.5). In this way, we intended to test the feasibility of the process towards this type of substrate. In order to differentiate between the substrate conversion values, the use of the modified version of the indole assay was necessary (described in Chapter 3.4.4). The automated expression and reaction steps were performed as described earlier. After the enzymatic reaction and cell separation, the reaction mixture was diluted with isopropanol (1:1 v/v) prior to the addition of the acid and DMAB. This way, hits were identified in one of the three tested libraries. The mutation W166P was identified as a hit. Upon isolation and activity testing with the MTase-Glo™ assay, the mutant provided a 28-times increase in specific activity. No hits could be identified from the W33 library testing with substrate **19**. Although a hit was identified upon the initial screening of the W166P/W33X library having the double mutation W166P/W33L, no activity towards substrate **19** was detected upon isolation and testing. The false positive results within the initial assay could be a consequence of the decreased sensitivity of the assay with substrate **19**, diminishing the absorbance differences compared to the background.

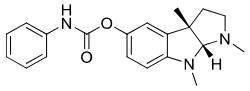

phenserine
AChE: IC_{50} = 24 nM
BChE: IC_{50} = 1560 nM

Figure 67. Structure of AChE inhibitor phenserine and its IC_{50} values for AChE and BChE inhibition.

The activity towards substrate **19** was also evaluated for the isolated hits of the screening rounds using **23** as a target. Surprisingly, two mutants, Y197H and W166C/Y197F/W33M, were active towards substrate **19**, with Y197H displaying a 5-fold increase in activity and W166C/Y197F/W33M increasing the specific activity 18-fold, compared to WT PsmD_*Sa* (Figure 68A). As expected, this led to a reduced specific activity towards the natural substrate in all tested mutants. Although a significant improvement in activity was achieved, particularly by the mutagenesis of W166, the comparison to the usual WT PsmD activity towards the natural substrate shows that there is still a need for further optimization until an efficient enzyme-catalyzed production of **P19** can be achieved (Figure 68B).

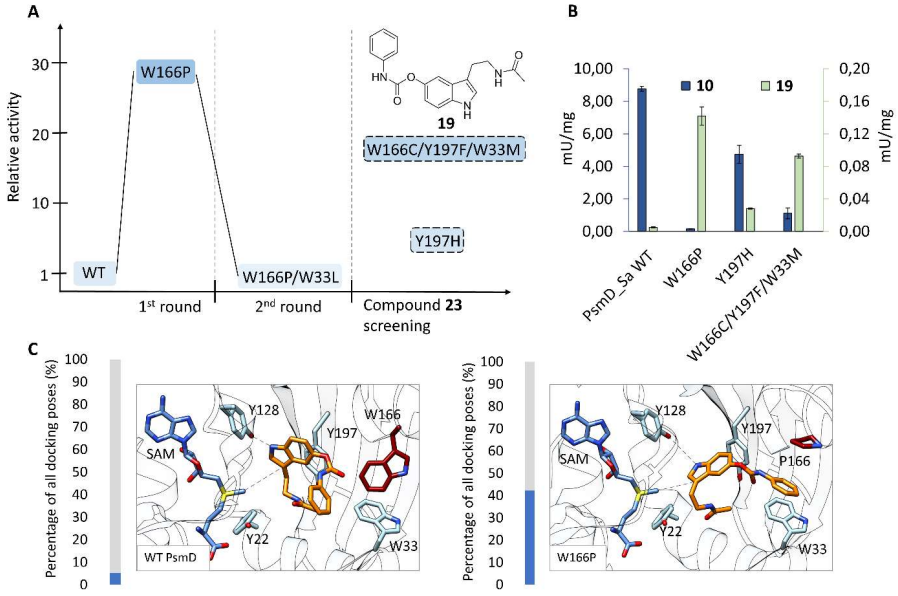

Figure 68. A. Results of the saturation mutagenesis screening rounds using **19** as substrate. **B.** Specific activity of hit mutants towards the natural substrate **10** (blue, left axis) and towards **19** (green, right axis), compared to WT PsmD_*Sa*. **C.** Comparison of the docked active pose of substrate **19** in the catalytic pocket of WT PsmD and the W166P mutant. The percentage of active binding modes from all obtained docking poses is shown in blue. A total of 1861 poses were analyzed for WT PsmD with substrate 3a, while 1791 poses were analyzed for W166P. The displayed poses were chosen based on their similarity to the previously determined active pose of the natural substrate, representing activity. The residue at position 166 is highlighted in red. The figure was produced for [3] and used according to the CC licensing of the Royal Society of Chemistry. The compound numbering was modified to correspond to this work.

The activity of the selected mutants was also tested for substrates **16** and **17** containing an ethyl and a propyl-carbamate functionality (Figure 69). Whereas WT PsmD_*Sa* and W166P have similar activities towards **16**, the difference becomes significant with the increase in the size of the chain attached to the carbamate. It appears that W166P shows no difference in activity between **16** and **15**, while the activity towards **19** decreases. None of the other selected mutants outperform WT PsmD or mutant W166P in reaction with **16** or **17**.

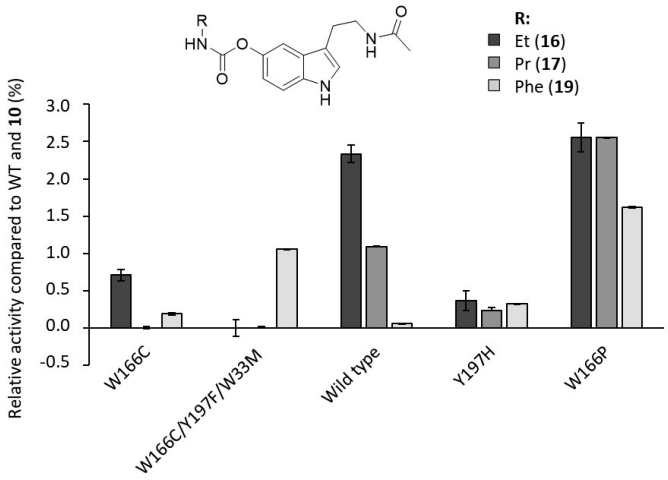

Figure 69. Relative activity of selected mutants towards other PsmD substrates with substituted carbamates. The activity was measured using the MTase-Glo™ commercial assay. Conditions: 20 μM substrate, 30 μM and 2 μg isolated PsmD variant were incubated in 20 μL MTase-Glo™ 1X buffer at 45 °C for 30 min. Then, the reactions were quenched with 5 μL TFA 0.5% (v%, in water) and the assay was performed according to the manufacturer's protocol.

3.5.7.1 Docking of 19 in WT PsmD_*Sa* and mutant W166P

A docking of substrate **19** in the catalytic site of WT PsmD_*Sa* and mutant W166P was performed using the method described in Chapter 3.5.6.1. Upon cluster analysis, the most likely productive position within the catalytic site was chosen as part of cluster 6. The cluster trends are similar to the analysis after the docking of **23**. While cluster 6, associated with the productive substrate pose is populated mainly by poses of **19** in W166P, it is generally associated with the lowest distances between C3 of the substrate indole and the methyl group of SAM and with the lowest binding energies (Figures 70, 71). These differences are confirmed by the experimental activity observations. The collected data points suggest a much higher probability of an active position of **19** in the catalytic site of W166P, compared to the WT PsmD_*Sa*. Similar to the observations from substrate **23**, the docked pose of substrate **19** in W166P shows a gap forming between P166 and W33, allowing the voluminous carbamate side of the molecule to accommodate in the open tunnel (Figure 68C). The π-stacking of the phenyl ring with the indole of W33 offers a supplementary stabilizing effect. Although

significantly less populated, cluster 6 also yielded docking poses of **19** in the catalytic site of WT PsmD_*Sa* (Figure 70). Even though the substrate appears to be in the productive position in those cases, the steric constraints within the closed catalytic pocket result in higher distances between C3 of the substrate indole and the SAM methyl group. The cluster distribution was correlated with the binding energies and distances between the methylation site and the cofactor. Similar trends were observed for substrate **19**, as with the previously discussed docking of substrate **23** (Figure 71).

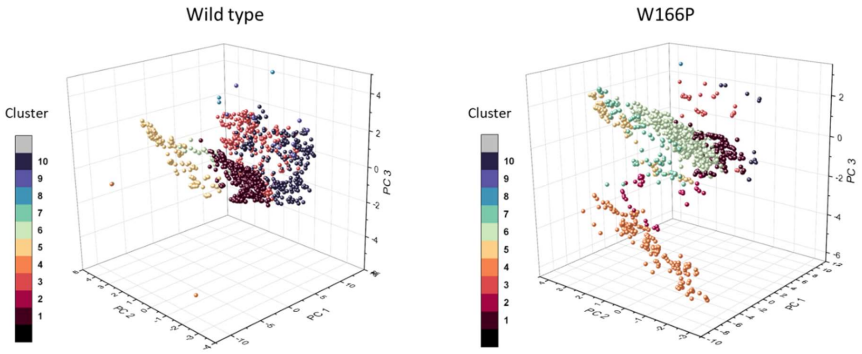

Figure 70. Cluster representation after principal component analysis of the obtained docking poses of **17** in the catalytic site of WT PsmD_*Sa* and the mutant W166P. The figure was produced for [3] and used without modifications according to the CC licensing of the Royal Society of Chemistry.

Although the preparative scale methylation of **19** by W166P was attempted in lysate and immobilized form, very limited **P19** formation was observed and no product could be isolated. Beyond the low activity of the enzyme itself, the expression of W166P in the production strain *E.coli* BL21 Gold (DE3) is also reduced. Further optimization through expression, reaction and enzyme engineering is required for the enzymatic preparative synthesis of **P19**. This work provides the first successful test of the evolvability of PsmD for this type of carbamates.

The identification of position W166 as the main hit of both mutagenesis and screening sequences described in Chapter 3.5 revealed an important role of this residue in the substrate specificity of the enzyme. These results suggest that the tryptophan cluster area inside the catalytic pocket of PsmD provides a relevant target for future substrate scope modulation through protein engineering. The saturation mutagenesis of W171 and W182 in particular, have the potential to provide new substrate selectivities (Chapter 3.5.6, Figure 61).

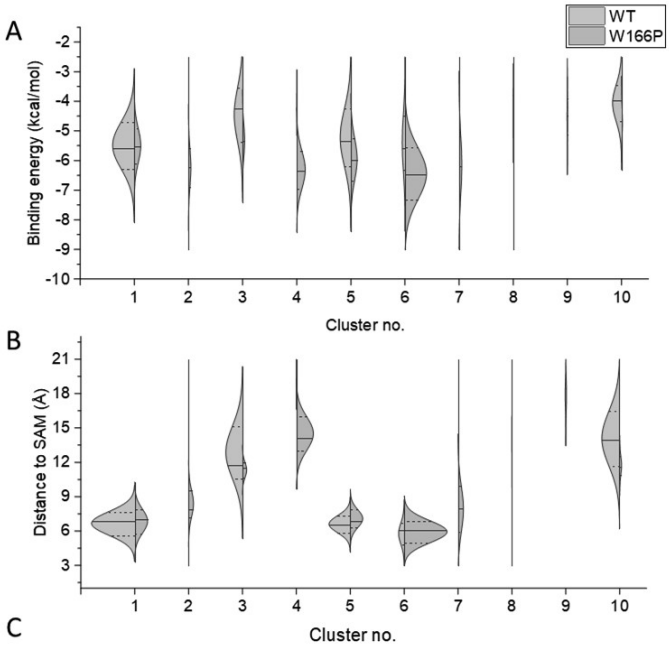

Cluster	1	2	3	4	5	6	7	8	9	10
N [WT]	762	0	294	2	375	98	1	3	11	315
N [W166P]	227	86	73	300	220	757	95	1	0	32

Figure 71. Clustering of substrate **19** poses in WT PsmD_*Sa* and the mutant W166P and the normal distribution of calculated parameters in each cluster. The median is represented in a solid line; the dashed lines indicate the standard deviation. Cluster 6 is considered the active binding mode, according to previous studies on PsmD_*Sa*. **A.** Distribution of calculated binding energies per pose cluster. **B.** Distribution of distances between the SAM methyl group and the methylation site per pose cluster. **C.** Number of samples assigned to each cluster in the principal component analysis. The figure was produced for [3] and used without modifications according to the CC licensing of the Royal Society of Chemistry.

3.5.8 Chapter summary

◊ Iterative site saturation mutagenesis was used for the modification of five residues in the catalytic pocket in order to expand the substrate scope of PsmD_*Sa*.

◊ The mutant library was generated using the 22c trick, reducing the number of colonies needed for screening.

◊ A modular screening process was developed using a robotic liquid handling platform for the automated protein expression, enzymatic reaction and activity analysis of the obtained mutant libraries. The system can be easily adapted for the screening of other pyrroloindole-forming enzymes.

◊ Two voluminous PsmD substrate derivatives (*t*-Bu-amide derivative **23** and Phe-carbamate derivative **19**) were chemically synthesized and used as targets for the mutant activity screening.

◊ The screening of the mutant libraries provided hits for both of the tested substrates. In the case of substrate **23**, mutant W166C achieved a 3-fold increase in specific activity, compared to the wild type. Mutant W166P was found to perform the methylation of substrate **19** with a 28-fold increase in specific activity.

◊ The structural effects of these mutations and the role of the key position 166 in substrate accommodation were explored by performing an extensive docking study of the two substrates in the wild-type PsmD_*Sa* and mutants W166C and W166P.

3.6 Further alkylation of indoles using PsmD

The potential for stereoselective alkylations using PsmD offers a unique opportunity to access previously unexplored structural diversifications of physostigmine. The effect of these transformations on the AChE and BChE inhibition would be worth exploring. Furthermore, stereoselective C-alkylation using SAM-dependent methyltransferases in the presence of cofactor analogs has been mostly unexplored, with only one successful example of an alkylating *C*-methyltransferase currently in the literature.[355] In this context, through a combination of cofactor supply, reaction and protein optimization, the PsmD-catalyzed alkylation of the natural substrate **10** became possible. All optimization efforts were focused on ethylation (Scheme 15), and the optimized conditions were later successfully applied to attach propyl and allyl groups, using the respective cofactor analogs.

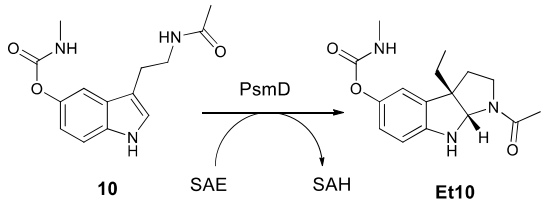

Scheme 15. Reaction scheme of the ethylation catalyzed by PsmD_*Sa* in the presence of substrate **10** and the ethylated cofactor derivative SAE.

3.6.1 Production strategies for SAM cofactor derivatives

Multiple production strategies for SAM cofactor derivatives were described in the literature, mostly using biocatalytic processes. The ethylated cofactor (SAE) is at the moment of writing this work unavailable commercially. Most often, it is produced enzymatically using either a halide methyltransferase (HMT) from SAH and ethyl iodide or using an *S*-adenosylmethionine synthetase (MAT) with ATP and L-ethionine as precursors.

In order to produce the stoichiometric amount of SAE for the PsmD reaction (1 mM), both production systems were tested and optimized. For the first system, purified HMT from *Aspergillus Clavatus* (*Ac*HMT), known for its substrate promiscuity, was incubated in the presence of SAH and EtI (Scheme 16).[337, 350] The conversion in time was evaluated, using 10 µM *Ac*HMT, 1 mM SAH and 10 mM EtI. After 2 h, the conversion reached a plateau between 20 and 30% (Figure 72). Although stability issues cannot be excluded, it is more likely that an equilibrium was reached due to the low affinity of the enzyme for EtI. Indeed, *Ac*HMT is known

to display limited catalytic activity for ethylation, compared to methylation. Although so far limited, engineering efforts for HMTs recently led to reaching 25.8 mU/mg for SAE production using HMT from *Arabidopsis thaliana* and a 38-fold improvement of SAE production capacity of *Ac*HMT, with 421.5 mU/mg, using the W27F/P8L/V265W mutant.[352, 353] As such, the use of the mutated *Ac*HMT variant instead of the wild type could benefit the SAE production using this system in the future.

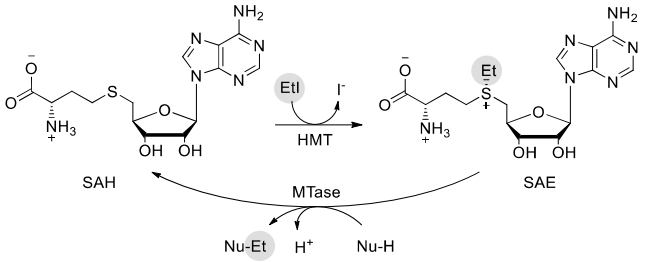

Scheme 16. Production of SAE using *Ac*HMT in a recycling system, in the presence of EtI.

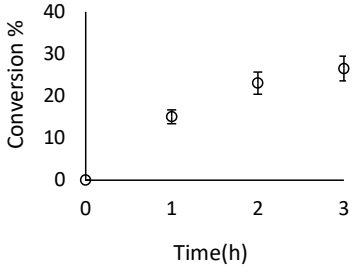

Figure 72. The evolution of the conversion of SAH to SAE in time, catalyzed by *Ac*HMT in cell-free extract.

The use of *Ac*HMT to produce SAE in a cofactor recycling system, in parallel with the PsmD-catalyzed ethylation was attempted, using catalytic amounts of SAH (10% catalyst loading). This produced no conversion to the ethylated product **Et10**. This can be attributed to the kinetic characteristics of the system, as the low affinity of PsmD towards the ethylated cofactor would require a higher starting concentration of SAE in the reaction mixture. The low rate of SAE production by *Ac*HMT exacerbates this effect. For this reason, the decision was made to use

*Ac*HMT in a separate step, before the PsmD reaction, as a supply system for producing stoichiometric amounts of SAE.

The second SAE supply option included the use of MAT from *Thermococcus kodakarensis* (*Tk*MAT), supplemented with L-ethionine and ATP (Scheme 17). The MAT from *Methanocaldococcus jannaschii* was particularly studied and engineered, leading to the improvement of its promiscuity towards different precursor amino acids and successful application for the production of various SAM derivatives.[344, 349, 354] Comparatively, MAT from *Thermococcus kodakarensis* is less common in literature. However, the enzyme was structurally and functionally characterized and its crystal structure was elucidated.[423] Due to its provenience from an extremophilic organism, *Tk*MAT showcases high thermostability and activity at high temperatures, peaking at 60-80 °C.[424] However, within this work, the temperature was reduced to 50 °C, as higher temperatures were found to accelerate the thermal degradation of the produced cofactor (Figure 73).

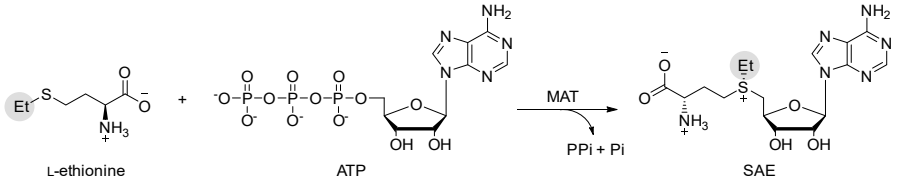

Scheme 17. Reaction scheme of the SAE formation catalyzed by *Tk*MAT.

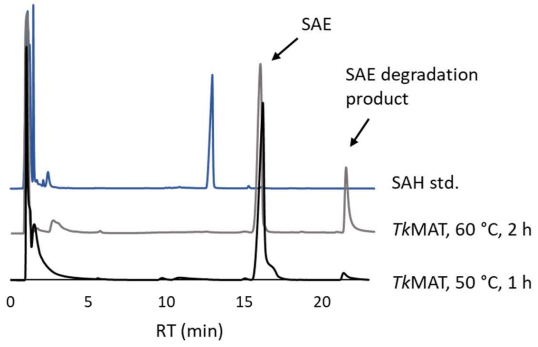

Figure 73. RT-HPLC chromatograms of the *Tk*MAT reaction mix after 1 and 2 h, showing the presence of the SAE (16 min) and the SAE degradation product, 5'-desoxy-5'-(methylthio)adenosine (MTA) at 21 min.

Several reaction temperatures (35-60 °C) and incubation times (1-2 h) were tested for both SAE production systems. While the *Tk*MAT conversion of SAH was complete after 1 h at 50 °C, the reaction catalyzed by *Ac*HMT required double the time and lower temperature for similar results (Table 8). Nevertheless, SAE was reproducibly obtained through both enzymatic routes, at a final concentration of approx. 7 mM (Figure 74). This provided a slight excess of the cofactor in the PsmD ethylation reactions, achieved by diluting the cofactor supply mixture 5-fold in the final reaction mixture. The *Tk*MAT system is considerably more effective for SAE production, due to the significantly higher reaction rate, requiring 10 times less enzyme, compared to *Ac*HMT (Table 8). The limitation of this procedure comes from the high cost of the precursors, as the enzyme only transforms the L-enantiomer of the amino acid. While L-ethionine is commercially available, larger derivatives are difficult to access in a stereoselective manner, which strongly limits the possibility of further alkylation by PsmD. Furthermore, while other MATs are known to produce other cofactor derivatives, the substrate selectivity of *Tk*MAT was not explored so far beyond the ethylated cofactor. In contrast, while *Ac*HMT generates cofactor derivatives at a much slower rate, its promiscuity is well-established. Moreover, the alkyl iodide precursors are readily available at much lower prices. Overall, while the *Tk*MAT supply system is clearly superior for the production of SAE in terms of efficiency, there is also a significant benefit to optimizing the *Ac*HMT as a supply strategy for other cofactor derivatives, that might be otherwise inaccessible.

Table 8. Optimized reaction conditions for the tested SAE supply systems.

	***Thermococcus kodakarensis* MAT**	***Aspergillus clavatus* HMT**
Enzyme	10 µM	100 µM
Temperature	50 °C	35 °C
Time	1 h	2 h
Buffer	100 mM TRIS, 20 mM $MgCl_2$, 200 mM KCl, pH 8.0	50 mM KP_i, pH 7.5
Substrates	L-ethionine, ATP	SAH, EtI
Cost of substrates/mmol SAE (€) *	81	63

* The prices for chemicals were extracted from the Sigma-Aldrich website on 15.04.2024

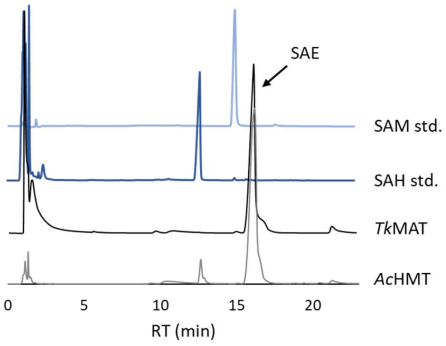

Figure 74. RP-HPLC chromatograms showing SAE formation by the *Tk*MAT and *Ac*HMT systems under the optimized conditions presented in Table 8. The broad peak at 2 min in the *Tk*MAT reaction corresponds to ATP. The peak at 21 min corresponds to the SAE degradation product, 5'-desoxy-5'-(methylthio)adenosine (MTA).

3.6.2 Structural basis of PsmD alkylation capacity and mutagenesis targets

For site-saturation mutagenesis, the target residues were chosen in the general vicinity of the SAM binding site (A123, A124, A125, F126, T138). Their potential steric constraints on the methionine rest of the cofactor were considered for the selection (Figure 75). Residues A123, A124 and A125 directly flank the catalytic methyl group of the SAM cofactor in the closed conformation of PsmD. To expand the available space for fitting larger cofactors, each of these residues was replaced with glycine. F126 is next in the sequence, and although its phenyl ring is oriented away from the cofactor, replacing it with a smaller residue could relieve significant steric constraints in the area. A substitution of this residue might also adjust the position of the cofactor-adjacent (AAA) loop. Valine was chosen to maintain the hydrophobic interactions in the area, with L135 and L139. T138 is found on the Dα-helix and was chosen for the possible effect on the position of the AAA-loop. This polar residue is located in a predominantly hydrophobic area. Replacing it with alanine aimed to disrupt the local partial charge and create more space in the cofactor area. The initial positive results for the A125G mutant prompted a second round of mutagenesis, introducing additional mutations: A125G/F126L, A125G/T138A, A125G/F154V, A125G/E157V, A125G/V227A, F126L/T138A, A125G/F126L/T138A.

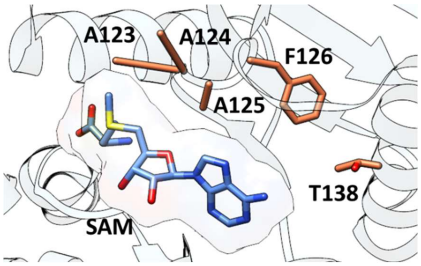

Figure 75. Representation of the PsmD_*Sa* cofactor binding site. Residues chosen for mutagenesis are marked in orange.

A protein sequence alignment with other methyltransferases known to accept cofactor analogs was performed to inform the rational design (Figure 76). However, it was inconclusive in identifying common trends that might determine the enzyme's potential for accepting larger cofactors. The amino acids in the selected positions tend to be poorly conserved. A structural alignment analysis was also performed using UCSF Chimera[421] and the crystal structures or, if not available, the AlphaFold[254] models of the selected methyltransferases (Table 9). This offered further insight into the positions of the residues, which would often not correspond to the sequence alignment equivalence. However, it remains challenging to establish definitive trends as the number of known methyltransferases presently known to ethylate is limited, and the residues are not highly conserved within the analyzed structures.

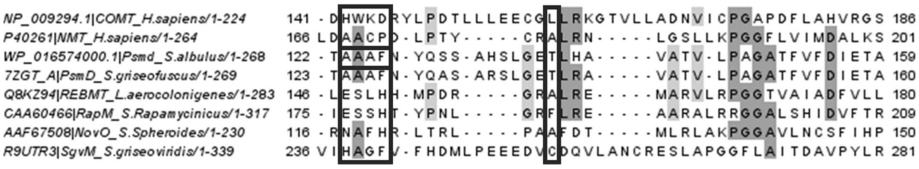

Figure 76. Sequence alignment of PsmD_*Sa* and PsmD_*Sg* with ethylating small molecule methyltransferases described in the literature. The descriptions contain the organism of origin and the protein accession numbers.

Table 9. Corresponding residues in the structures of small molecule methyltransferases, known to catalyze ethylation reactions in the presence of SAE. The corresponding residues were selected by superimposing the 3D structures of the selected enzymes, and not through sequence alignment. The amino acids most often encountered in the corresponding position are shaded.

Protein	PDB/AF model	Organism	Residues chosen from PsmD_*Sa*				
			A123	A124	A125	F126	T138
NNMT	2IIP	*Homo sapiens*	T	L	C	L	A
HNMT	1JQD	*Homo sapiens*	I	Q	M	L	T
COMT	3A7E	*Homo sapiens*	D	H	W	K	D
RebM	3BUS	*Lentzea aerocolonigenes*	L	E	S	L	A

NovO	5MGZ	*Streptomyces niveus*	R	N	A	F	A
RapM	AFQ54303	*Streptomyces hygroscopicus*	I	E	S	S	F
SgvM	8FTS	*Streptomyces griseovidris*	G	F	V	F	V

Ultimately, although the rational design choices were informed by structural data, they were still largely hypothetical, due to the limited available information. More extensive mutagenesis and testing of different methyltransferases is essential before any structural basis for the ethylation capacity can be established. This would support more informed decision-making for further site-directed mutagenesis.

3.6.3 Mutant generation and initial screening

Mutants A123G, A124G, A125G, F126L, F126C, T138A, and their combinations were produced using the inverse PCR method described in Chapter 3.5.1, and the “touch-down” approach for the amplification cycles. For an initial screening for ethylation capacity, the PsmD variants were expressed in *E. coli* BL21 Gold (DE3) by autoinduction (Figure 77A), then they were immobilized on Ni-NTA resin and used in this form for the ethylation reaction. Ethylation could not be detected reliably in lysate or whole-cell reactions due to competitive methylation caused by the presence of SAM in the cellular environment. As a result, enzyme immobilization from lysate offered a compromise between the efficiency of lysate reactions and the precision of using purified variants (Figure 77B). The SAE cofactor was produced before the screening using the *Tk*MAT supply system described in Chapter 3.6.1. After 20 h of incubation, the reaction mixture was analyzed by RP-HPLC. LC-MS confirmed that the peak at 14 min corresponds to the mass of the ethylated product (Figure 78). The attempts to chemically synthesize the ethylated PsmD product were unsuccessful, prompting the use of UV spectra for the comparison between the ethylated product and the double methylated pyrroloindole **N10**, previously observed in PsmD reactions.

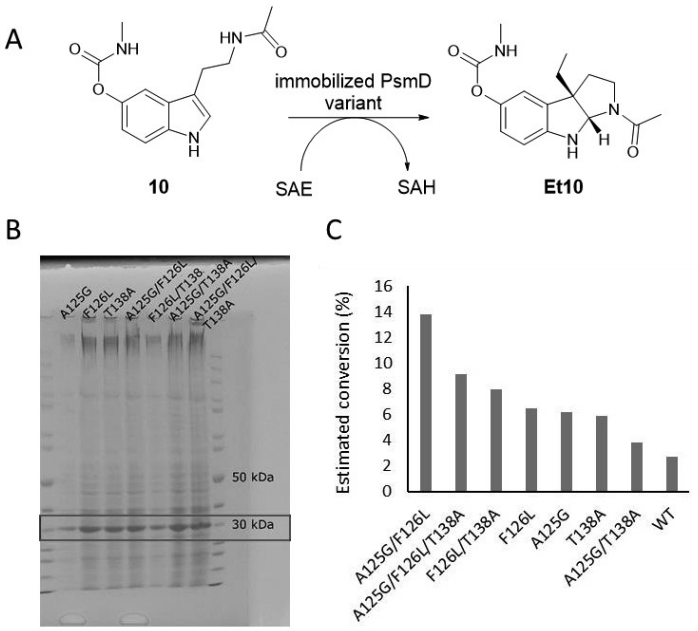

Figure 77. A. Reaction scheme of the ethylation catalyzed by the PsmD variants. **B.** Expression of the selected mutants in *E. coli* BL21 Gold (DE3), using autoinduction. The bands for the PsmD variants appear at 30 kDa. **C.** Results of the initial screening of immobilized PsmD mutants and WT with SAE. The variants were immobilized on Ni-NTA resin and incubated with 1 mM substrate **10** and 300 µL MAT-SAE mix for 20 h at 45 °C and 800 rpm. The conversion was estimated from the RP-HPLC signal areas, using the standard calibration of the methylated product analog, **P10**.

The results indicated that the spectra correspond to different compounds. The ethylation product was detected for several mutants, as well as the wild type. The mutants A123G, and A124G could not be expressed under the tested conditions. After testing the other mutants, the obtained conversions of **10** to the ethylated product **Et10** ranged from 2% (for the wild type PsmD) to 14% (double mutant A125G/F126L) (Figure 77B). The positive mutants were purified using the mini-protein isolation procedure described in Chapter 7.3.3.

Although promising, the low conversions hindered any practical applications of PsmD for other alkylations. As such, an optimization of the reaction conditions of the PsmD-SAE supply coupled reaction was necessary. In this context, the HMT system was selected as the main source of cofactor derivatives with the expectation that it would serve as a platform for using other cofactor analogs besides SAE.

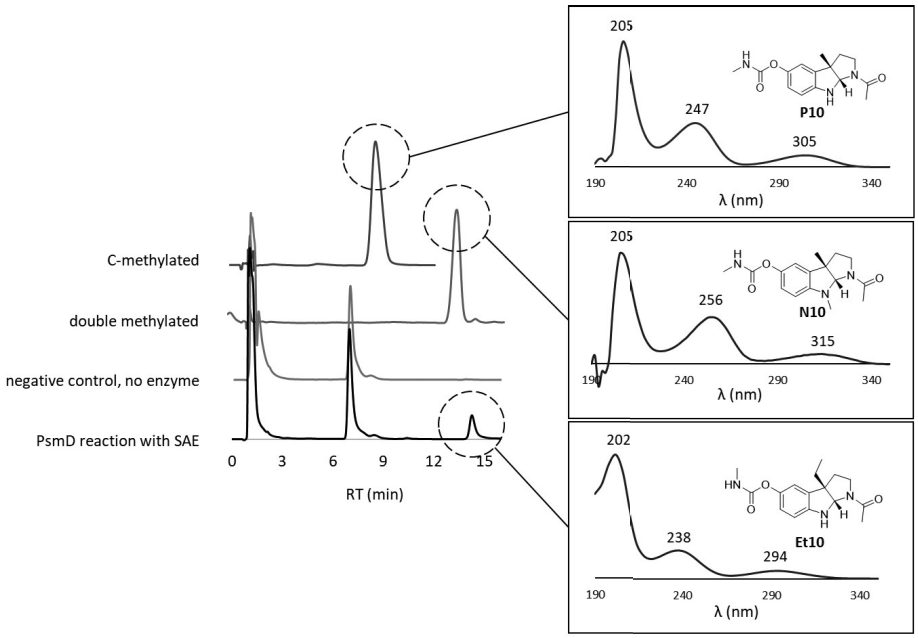

Figure 78. RP-HPLC chromatograms of the PsmD reaction mixture in the presence of SAE, the negative control without enzyme, single methylated **P10** and the double methylated **N10**. Comparison of the absorbance spectra of natural PsmD product **P10** (blue), double methylated **N10** (black) and ethylated product **Et10** (red).

3.6.4 Indole ethylation by PsmD

A reason for the low rate of PsmD ethylation, compared to methylation, can have kinetic origins. The affinity of PsmD for SAE is presumably much lower than for SAM, requiring a high concentration of SAE in the reaction mixture to initiate the ethylation. This could explain why the parallel reaction of PsmD and the *Ac*HMT cofactor recycling system did not produce any detectable ethylated product, as catalytic amounts of SAE might be simply under the K_M constant. However, the challenge of obtaining, purifying and storing SAE causes significant difficulties for conducting precise experimental kinetic measurements. Furthermore, the inhibitory effect of SAH was reported before for methyltransferases (described in Chapter 2.4). Although SAH inhibition did not pose a problem for PsmD-catalyzed methylation reactions, the lower ethylation rates are likely more affected by this inhibition. A way to address this issue is through the immediate degradation of SAH formed after the ethylation reaction. This can be performed enzymatically in a selective manner, using a SAH nucleosidase (MTAN) or SAH

hydrolase (SAHH). Indeed, supplementing the PsmD-SAE reaction mixture with MTAN from *E. coli* provided a 16-fold increase in conversion to **Et10** using WT PsmD (Figure 79).

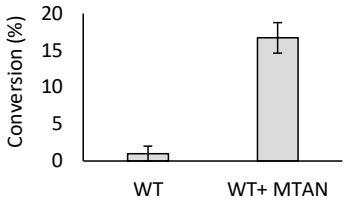

Figure 79. Effect of MTAN supplementation on the conversion of **10** to ethylated **Et10,** catalyzed by WT PsmD_*Sa*. Reaction conditions: 50% (v/v) AcHMT-SAE mix, 58 µM WT PsmD_*Sa*, 1 mM substrate **10**, 8 µM MTAN, in Kp_i 50 mM (pH 7.5) and 50 µL total volume. The reaction was incubated for 17 h at 37 °C and 1000 rpm and quenched with 5.5 µL TFA 5%. The analysis was performed by RP-HPLC.

The active mutants were isolated and their activity was tested, in the presence of MTAN and the SAE produced by each of the tested supply systems (Figure 80). The conversion differences observed between WT PsmD_*Sa* and its mutants were small. In the presence of SAE produced by the *Ac*HMT system, mutants A125G and F126L led to slightly increased conversions to **Et10** (20 and 17%), compared to the wild type (14%). In the case of the MAT-produced SAE, all the conversions were slightly higher, while maintaining the same trends among the variants. The difference in conversion when comparing the two supply systems can be explained by the slight difference in the SAE production yield, for which *Tk*MAT performed slightly better. Furthermore, in the case of the HMT system, any unconverted SAH could contribute to the inhibition effect discussed earlier. Nevertheless, the general activity trends correspond for both systems, and all tested variants displayed ethylating activity.

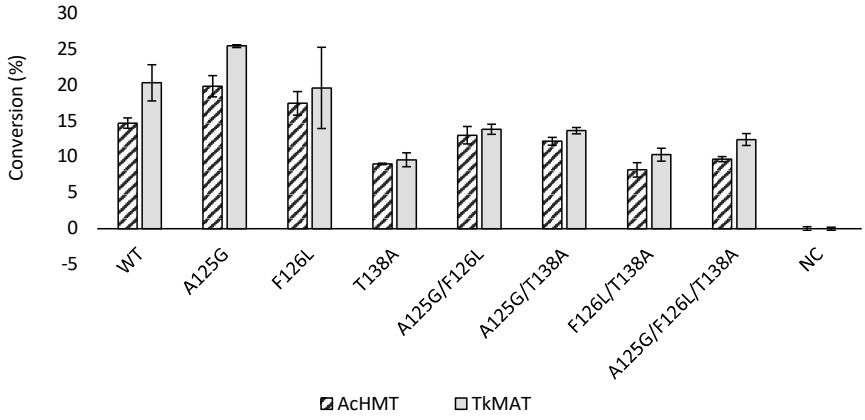

Figure 80. Conversion of WT PsmD_*Sa* and its mutants after the ethylation reaction, using SAE produced by *Ac*HMT and *Tk*MAT. Reaction conditions: 20% (v/v) TkMAT-SAE mix or AcHMT-SAE mix, 1 mM substrate **10**, 8 µM MTAN, 30 µM PsmD variant in Kp_i 50 mM (pH 7.5) and 50 µL total volume. The reaction was incubated for 17 h at 37 °C and 1000 rpm and quenched with 5.5 µL TFA 5%. The analysis was performed by RP-HPLC.

A design of experiment was performed in order to adjust the ratio of PsmD, MTAN and HMT-SAE mixture and obtain higher conversions (Figure 81). This method allows the building of a second-order (quadratic) model without needing to test all possible combinations of factors. It includes three types of points:

- factorial points – combinations of initially set high (+1) and low (-1) levels of each factor.
- center points – experimental runs corresponding to the median values of the variables, replicated to provide an estimate of the experimental error.
- axial points – experimental runs identical to the central points conditions with the exception of one factor which varies bellow and above the median, outside of the given range.

This model allows for the statistical determination of linear effects as well as the interactions between the process variables. The concentration of PsmD was found to have the greatest impact on the conversions, while the MTAN concentration and the HMT-SAE mixture volume could be reduced close to the lowest values used in the model. The MTAN concentration did not influence the conversion within the tested limits, suggesting that the rate of SAH degradation by MTAN surpasses the rate of SAH formation within the PsmD ethylation. As such, its concentration could likely be reduced further. Increasing the volume of the SAE mixture showed a correlation with a decrease in ethylation conversion within the system. The difference is small, making it difficult to determine whether it arises from a true inhibitory effect or from statistical or experimental errors. Within the design of experiment, a 35% conversion

was the maximum reached. For higher conversions, the PsmD concentration should be further increased. With the enzyme concentration of 30 µm, the catalyst loading in the reaction is at 3% (mol%). Further increasing this concentration would be impractical for the preparative use of PsmD or its mutants as catalysts in isolated form. In this scenario, enzyme engineering or changing the enzyme formulation (e.g. through immobilization) could be more advantageous approaches before increasing the enzyme concentration.

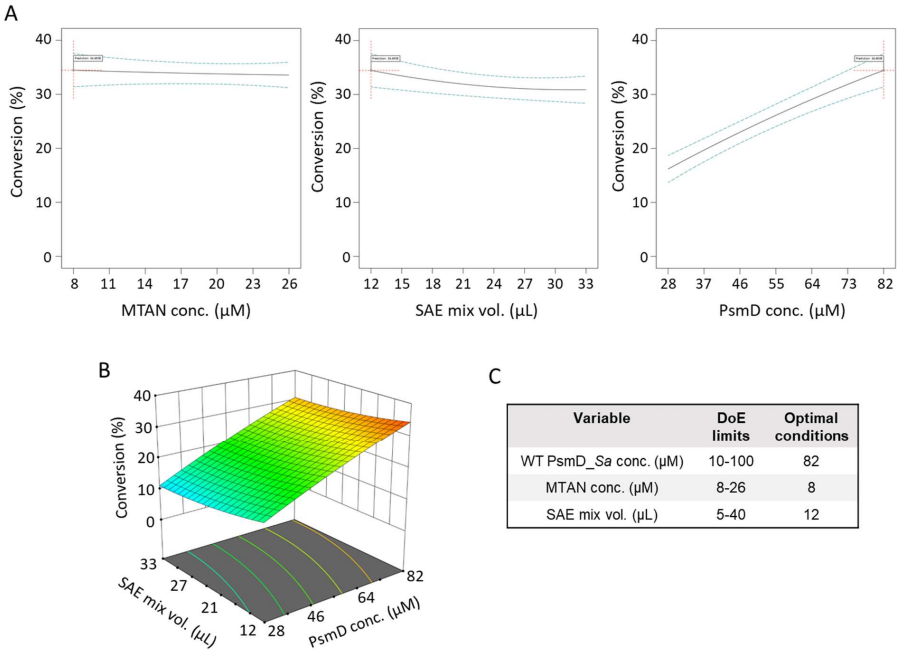

Variable	DoE limits	Optimal conditions
WT PsmD_*Sa* conc. (µM)	10-100	82
MTAN conc. (µM)	8-26	8
SAE mix vol. (µL)	5-40	12

Figure 81. A. Influence of all tested variables on the ethylation system, determined through the DoE. **B.** influence of the PsmD concentration and the SAE mix volume on the final conversion. **C.** Limits set for the variables within the DoE and the predicted optimal conditions. The optimal conditions correspond to a substrate conversion of 35%.

These results are however in line with previous reports of methyltransferase-catalyzed ethylation. PsmD_*Sa* is performing better than most of the other reported ethylating methyltransferases. 79% conversion to ethyl-vanillin was achieved after 24 h using COMT with a 30% (mol%) enzyme loading.[353] An engineered human NNMT was used for the ethylation of pyrazoles, leading to 9% conversion over 72 h with 2.5% (mol%) catalyst loading.[356] The best performance was achieved using the histamine methyltransferase HNMT, where N-ethylation was achieved with a 58% conversion with 2% (mol%) of enzyme over 48 h. In the case of RebM *O*-methyltransferase, the ethylation using SAE could be performed with a 40%

conversion using a 20% (mol%) catalyst loading. In this case, SAHH was supplemented for the SAH product elimination.[334] 20% (mol%) catalyst loading was also used in the case of the NovO-catalyzed ethylation using SAE, leading to 24% conversion, while a 7% (mol%) enzyme loading led to 19% conversion in the ethylation catalyzed by the RapM *O*-methyltransferase.[291, 343] Only one other *C*-methyltransferase, SgvM, was reported to catalyze the ethylation of α-keto acids with 10-30% conversion over 18-27 h, using 2% (mol%) catalyst loading, in the presence of MTAN.[355] Despite the variety of amino acid sequences, these reports reveal similar ethylation activities. This suggests that the limitations of methyltransferase-catalyzed ethylation may be mechanistic, stemming from the reactivity of the system, rather than the structural properties of the enzymes. The present work is the second reported instance of a *C*-methyltransferase catalyzing the ethyl transfer in the presence of the SAE cofactor derivative.

3.6.5 PsmD activity using other cofactor derivatives

Other cofactor derivatives were produced using the *Ac*HMT supply system in the presence of SAH and the respective iodides. Propyl and allyl groups were added to SAH in this manner and used further in the coupled reaction with the best performing variants - A125G and F126L, as well as WT PsmD_*Sa*. The attempts to produce the butyl- and isopropyl-cofactors using *Ac*HMT and the respective alkyl iodides were unsuccessful. The newly obtained cofactors were tested in the presence of the PsmD variants using the optimized conditions determined by the DoE. Interestingly, the propylation of **10** reached similar conversions with the ethylation (Table 10). This suggests that the lack of space around the cofactor was not necessarily the issue hindering PsmD-catalyzed alkylations. This hypothesis was further strengthened by the conversions to the allylated product. Almost full conversion (94%) was achieved by the WT PsmD in this case, with 80% conversion by A125G and 59% by F126L. The allyl group is larger in size than the ethyl group, suggesting that a possible reason for the conversion disparity might be the reactivity difference, rather than the size of the transferred group. The double bond on the allyl group activates the electrophile carbon in contact with the substrate through electron delocalization. In contrast, within the ethyl group, the contact carbon is influenced by the inductive effect of the second carbon atom, further reducing its electrophilicity. Thus, it can be hypothesized that the general low conversions obtained in methyltransferase-catalyzed ethylation are a consequence of the lack of reactivity of the cofactor. The steric effects within the catalytic sites of the enzymes might play a smaller role than expected.

Table 10. Conversion of **10** catalyzed by WT PsmD_*Sa* and mutants A125G and F126L in the presence of different SAM cofactor analogs, obtained using *Ct*HMT and the respective alkyl iodides. Reaction conditions: 20% (v/v) *Ac*HMT-SAR mix, 1 mM substrate **10**, 8 µM MTAN, 30 µM PsmD variant in Kp_i 50 mM (pH 7.5) and 100 µL total volume. The reaction was incubated for 17 h at 37 °C and 1000 rpm and quenched with 5.5 µL TFA 5%. The analysis was performed by RP-HPLC.

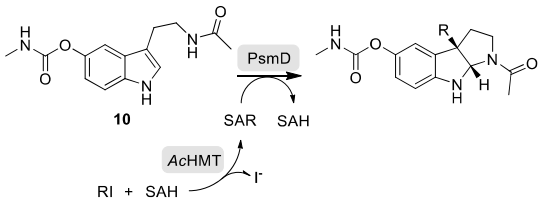

R	WT	A125G	F126L
	Conversion (%)		
Methyl	>99	>99	96 ± 4
Ethyl	15 ± 1	20 ± 1.5	17 ± 2
Propyl	19 ± 4	19 ± 1	16 ± 2
Allyl	94 ± 6	80 ± 5	59 ± 7.5
	Specific activity* (mU/mg)		
Methyl	8.7 ± 0.1	14.3 ± 0.4	5.3 ± 0.1

* The specific activity was determined using the MTase-Glo™ assay.

When the allylated cofactor was also incubated with substrate **10** in the absence of PsmD, no product was formed. Furthermore, only traces of the allylated product were observed after the incubation of substrate **10** with 14 mM allyl iodide, suggesting that the allylation is indeed catalyzed by PsmD (Figure 82). An unexpected effect of the A125G mutation was the increase in specific activity for the methylation reaction by 64% (14.3 mU/mg), compared to the wild type (8.7 mU/mg). The increase in overall activity could also explain the improved performance observed in the ethylation reaction.

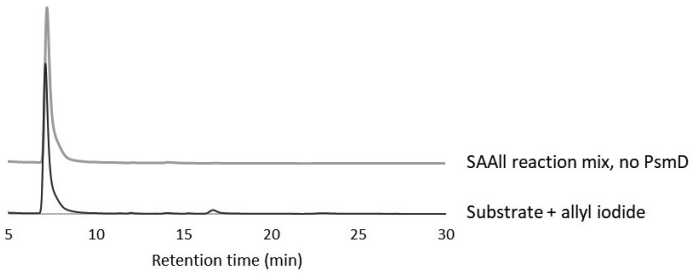

Figure 82. Evaluation of the background allylation. RP-HPLC chromatograms showing the results of the incubation of substrate **10** with the allylation reaction mixture (SAAll mix), in the absence of PsmD (top). Reaction conditions: 20% (v/v) SAAll mix, 1 mM substrate **10**, 8 µM MTAN, in Kp_i 50 mM (pH 7.5). The

SAAll mix resulted from the incubation of 100 µM *Ac*HMT with 7 mM SAH and 70 mM allyl iodide for 2 h at 35 °C (according to the procedure presented in Chapter 3.6.1). The bottom chromatogram was obtained after the incubation of 1 mM substrate **10** with 14 mM allyl iodide in KP_i 50 mM (pH 7.5). The peak at 7 min corresponds to substrate **10**, and the peak at 16 min corresponds to the allylated product. In both cases, the mixtures were incubated at 37 °C and 1000 rpm for 17 h.

Methyltransferase-catalyzed ethylation is only starting to become explored as a tool for selective structure diversification. In this chapter, the ethylation, propylation and allylation of indoles by PsmD were achieved, using two different cofactor analog supply systems. Overall, the reported conversions of methyltransferase-catalyzed ethylations relative to enzyme loading are similar to the literature reports for other small-molecule methyltransferases.

Two approaches could help solve the low productivity issue: enzyme engineering and reaction optimization. The first is the engineering of the enzyme in order to improve the ethylation activity. Making predictions about the effects of amino acid residues in the catalytic site on ethylation efficiency is challenging. The difficulty arises both from the lack of data on ethylating enzymes and from the dynamic mechanism of methyltransferases. In many cases, a compression motion is needed for the reaction to take place (details in Chapter 3.3). Due to this effect, freeing space to accommodate larger cofactors might in fact be detrimental to enzymatic catalysis. Because of this, a semi-rational approach might be more suitable as an engineering strategy. The screening of mutant libraries presents the challenge of supplying the cofactor in a reliable manner. The optimized supply systems described in this chapter could provide a solution to this problem. Apart from enzyme engineering, another opportunity for preparative ethylations (or other alkylations) would be adjusting the enzyme formulation. Enzyme immobilization could be a valuable approach for achieving high catalyst loading with improved stability over extended reaction times. Using immobilized methyltransferases in flow systems could further improve yields and reduce costs by enabling the reuse of the enzyme. Finally, studying the alkylation capacity of additional methyltransferases could provide valuable insights into the specific structural and chemical requirements of this process.

3.6.6 Chapter summary

◊ Some small molecule methyltransferases can catalyze other alkylations using cofactor derivatives. PsmD variants were not known to transfer larger alkyl groups.

◊ The ethylated cofactor (SAE) was successfully produced using two different enzymatic supply systems. The first uses a halide methyltransferase (*Ac*HMT), while the second uses an *S*-adenosylmethionine synthetase (*Tk*MAT) as a catalyst. Both supply systems were optimized for the rapid production of SAE.

◊ Several amino acid residues from the vicinity of the cofactor were modified through site-specific mutagenesis, in an effort to improve the ethylation capacity of PsmD_*Sa*. All variants, including the wild type, lead to detectable ethylated product using either of the optimized cofactor supply systems. Two mutants (A125G and F126L) provided an increase in the conversion to the ethylated product, compared to the wild type.

◊ Propylated and allylated cofactor analogs were also produced using the *Ac*HMT supply system, in the presence of SAH and the respective iodides. They were used in cascade with WT PsmD_*Sa* and the two best mutants. Propylation conversions were comparable to ethylation, while allylation reactions achieved conversions up to 94%. This highlights the importance of the transferred group reactivity for the catalytic process

◊ The PsmD ethylation cascade using the *Ac*HMT-based SAE supply system was optimized using a design of experiment, leading to a 150% increase in conversion to the ethylated pyrroloindole product.

3.7 Scaling enzymatic methylation – challenges and strategies

The use of methyltransferases in industry is limited by the cofactor availability and the generally low reaction rates. The recent developments in SAM cofactor recycling systems provided a necessary boost to the synthetic applications of methyltransferases, offering a solution to one of their most pressing problems. Besides enzyme engineering, the productivity issues can be tackled by process optimization and the exploration of different enzyme formulations. The study and optimization of methyltransferase cascades with cofactor recycling systems is important for realizing the potential of this enzyme class in industrial biocatalytic applications. Considering this, this chapter will focus on the preparative applications of PsmD in the presence of HMT-based cofactor recycling systems. The challenges, experimental and economical considerations will be described, in the context of bringing stereoselective enzymatic C-methylation to a preparative scale (50-1000 mg). This effort represents one of the early examples of preparative enzymatic stereoselective C-methylation and aims to offer some guidance for the practical applications of these processes.

As described in Chapter 3.1, the increased stability of PsmD_*Sa* can significantly improve the methylation yields compared to PsmD_*Sg*, due to its capacity for longer reaction times. However, the catalytic efficiency of PsmD_*Sa*, although similar to other small molecule methyltransferases, is too low for preparative applications using the purified enzyme. As such, alternative enzyme formulations were considered. The use of cell-free extracts containing the expressed enzymes was successful in the case of PsmD_*Sg*.[358] However, this system also presents several disadvantages, documented further in this chapter. As such, enzyme immobilization and whole-cell biocatalysis were also explored, as alternatives.

3.7.1 PsmD use in combination with a cofactor recycling system

The HMT-based cofactor recycling system, first described in 2019, has since been refined for greater efficacy and has been successfully applied in combination with various methyltransferases. The original HMT recycling system uses methyl iodide as a methyl donor and SAH as an acceptor. This allows for the in-situ recycling of the cofactor consumed in methyltransferase-catalyzed methylations. HMT from *Chloracidobacterium thermophilum* was successfully used for SAM recycling in parallel with the PsmD_*Sg*-catalyzed C-methylation of **10**, up to 50 mg scale, with 100% conversion.[358] Encouraged by these results, we sought to expand the biocatalytic methylation capacity by using the more stable PsmD_*Sa*, and increasing the substrate amount to 100 mg (Scheme 18). The enzymes were expressed separately in the *E. coli* BL21 (DE3) Δmtn strain, which has the native gene coding for the SAH

nucleosidase knocked out. This strain was specifically produced for use with the HMT cofactor recycling system.[207] The Δmtn strain was developed and kindly provided by the Seebeck research group from the University of Basel, Switzerland. *Ct*HMT is more efficiently expressed in this strain, compared to PsmD_*Sa*. Nevertheless, both enzymes were successfully expressed using the standard IPTG-induction strategy (Figure 83A). A temperature optimization revealed that the optimal temperature of the coupled system is 35 °C, lower than the optimal temperature of PsmD itself (45 °C) (Figure 83B).

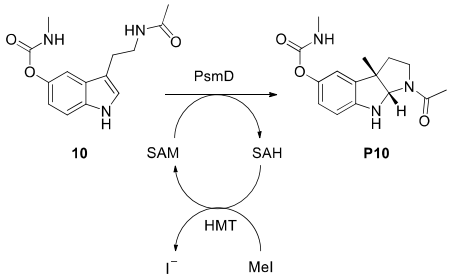

Scheme 18. Methylation of the natural substrate **10**, catalyzed by PsmD, in the presence of the HMT-based cofactor recycling system.

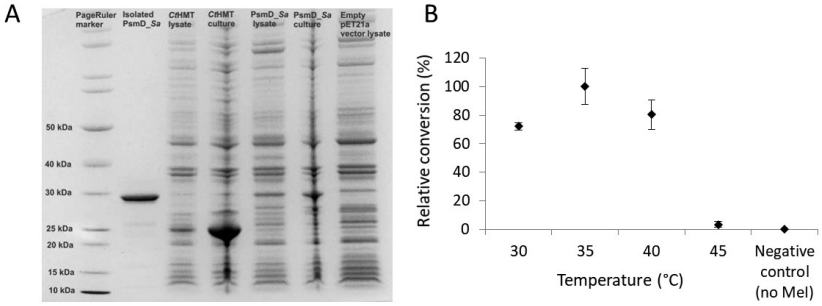

Figure 83. A. SDS-Page of PsmD_*Sa* and *Ct*HMT expression in *E. coli* DE3 Δmtn strain and PsmD_*Sa* after affinity Ni-NTA column purification. PsmD_*Sa* presents as a band at approx. 30 kDa, while the *Ct*HMT band is at approx. 25 kDa. **B.** Optimal temperature for the PsmD/HMT coupled system. The figures were produced by the author for [1] and used here with the agreement of the American Chemical Society.

3.7.1.1 Coupled methylation system optimization – design of experiment

A central composite design of experiment (DoE) was utilized to optimize the enzymatic cascade and assess the influence of each component on the preparative PsmD methylation of **10**, in the presence of the HMT recycling system. The variables chosen in this case were the PsmD and HMT lysate volumes and the concentrations (mM) of SAH and methyl iodide. The substrate **10** concentration was maintained constant at 1 mM. The reactions were performed in 500 µL scale in KP_i buffer (50 µM, pH 7.5) and incubated for 16 h at 35°C. The product formation was then analyzed by NP-HPLC. A reduced quadratic model was generated using Design Expert 12 (12.0.7.0), with an R^2 of 0.9097. A detailed description of the model can be found in Annex 8.6.

Interestingly, the DoE revealed that the supplemented SAH did not influence the final conversion (Figure 84). The lysates contain the endogenous SAH produced by *E. coli*, which is not degraded enzymatically in the Δmtn strain. Consequently, sufficient SAH is available as a substrate for HMT without the need for external supplementation. This is a significant advantage of the system, as SAH is one of the cost-limiting components. Out of the tested parameters, the PsmD lysate volume has the greatest impact on the final conversion. For both PsmD and HMT lysates, the conversion peaked and then declined at higher volumes (Figure 84). The optimal conditions leading to full conversion required 14% (v%) HMT lysate and 20% (v%) PsmD lysate (Figure 85D). A relatively high excess of methyl iodide is necessary, perhaps to compensate for its loss by evaporation. Too much methyl iodide also hindered conversion, with 13-18 equivalents yielding the best results. However, due to the observed non-specific methylation of the PsmD product, the working methyl iodide concentration was reduced to 10 mM. The model validation revealed higher conversions than those predicted (Figure 85C). Some variations between the experiments can be expected, since lysate composition cannot be controlled entirely, even under identical preparation conditions. Nevertheless, the optimized coupled methylation system offered a blueprint for the experimental design of the other preparative PsmD methylations.

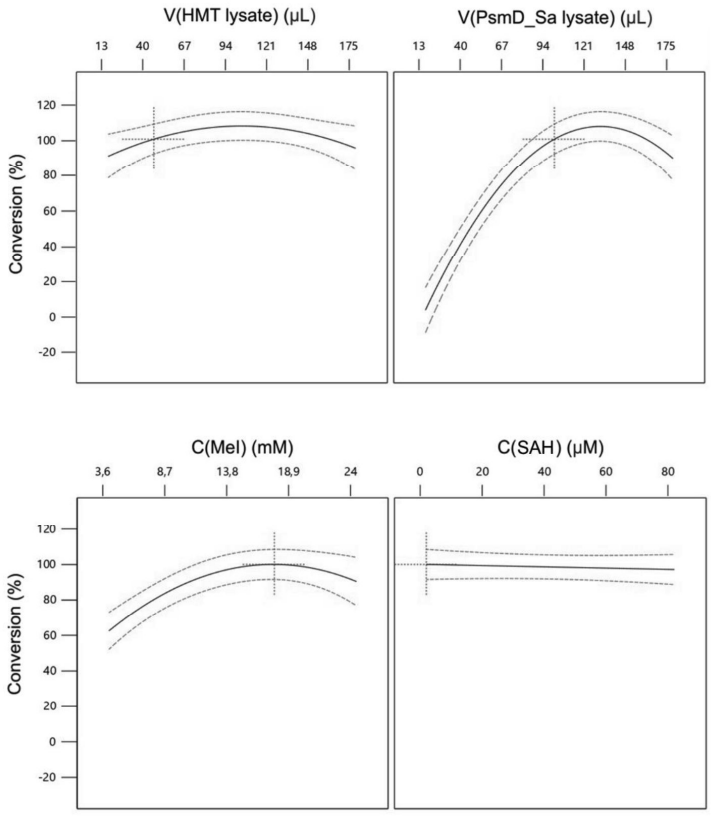

Figure 84. Influence of the parameters on the model of the coupled reaction using PsmD_*Sa* and *Ct*HMT, determined by a central composite design of experiment. The reactions were performed on a 500 µL scale. The figure was produced for [1] and used here with the agreement of the American Chemical Society.

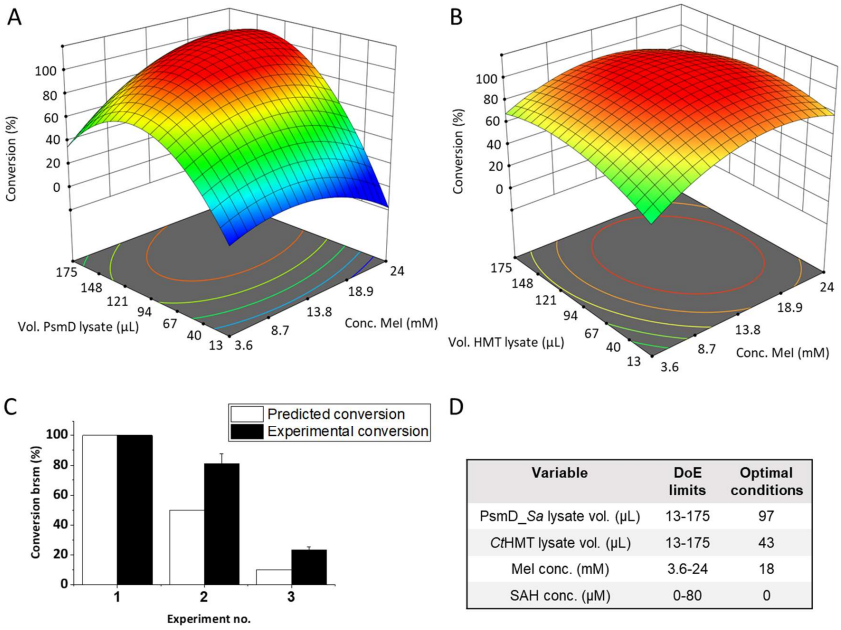

Variable	DoE limits	Optimal conditions
PsmD_*Sa* lysate vol. (µL)	13-175	97
*Ct*HMT lysate vol. (µL)	13-175	43
MeI conc. (mM)	3.6-24	18
SAH conc. (µM)	0-80	0

Figure 85. DoE results for the coupled PsmD-HMT lysate reaction. **A.** Interaction between the volume of PsmD lysate and MeI concentration, and their effect on the final conversion. **B.** Interaction between the volume of HMT lysate and MeI concentration, and their effect on the final conversion. **C.** Validation of the obtained DoE model. **D.** The parameter limits and the optimal conditions determined by the DoE model. The reactions were performed in 500 µL total volume. The conversions to product **P10** were determined by NP-HPLC, after 16 h of incubation at 35 °C, with 1 mM **10**.

3.7.1.2 SAM thermostability

The literature reports that the highest stability of SAM was observed between pH 3 and 8.[329] However, as no information about the temperature profile was available, the stability of SAM at 35, 45 and 55 °C was evaluated using ^{1}H NMR. While SAM is relatively stable at all the tested temperatures for the first 5 h, after 21 h most of the SAM is degraded at 55 °C. At 45 °C, 30% of SAM is degraded after 21 h, while almost 90% of SAM remains after the incubation at 35 °C (Figure 86). This information is important for planning the conditions for all the PsmD

reactions, as the determined optimal temperature of PsmD (45 °C) might not be productive with longer reaction times. In any case, an excess of SAM needs to be provided if the reaction is incubated for more than a few hours. The necessary excess increases drastically at higher reaction temperatures.

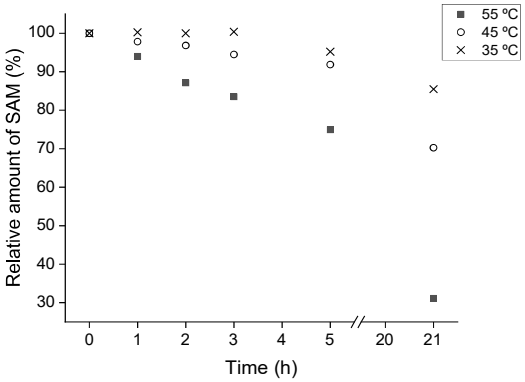

Figure 86. SAM stability in time at different temperatures. 5.5 mM SAM were incubated in D_2O. The degradation in time was analyzed using the ratio between the integral of its ^1H NMR signal and the TMS internal standard, at different time points. The figure was produced for [1] and used here with the agreement of the American Chemical Society.

3.7.1.3 Background N-methylation of the PsmD product

A noteworthy aspect of the biocatalytic methylation in the presence of the cofactor recycling system is the non-selective methylation of **P10**, leading to the double methylated compound **N10** (Scheme 19). The origins of the side product were investigated by incubating the PsmD natural product **P10** with different components of the coupled reaction. Although most of the background methylation was initially attributed to the excess of methyl iodide (10 equiv.), the experiment revealed that some N-methylation of **P10** occurs after 48 h incubation in cell-free extracts. Approximately 20% of **P10** was converted to **N10** in cell-free extracts containing HMT, with a negligible difference when methyl iodide was present (Figure 87A). The incubation of **P10** with only methyl iodide in KP_i buffer also led to approx. 11% N-methylation, similar to the incubation with the cell-free extract control containing the empty vector. All evaluated

components appear to facilitate the N-methylation of **P10** when provided sufficient incubation time. Interestingly, the presence of HMT in the mixture increases the rate of N-methylation. One could expect the methylation of the endogenous SAH present in the cell-free extracts, leading to higher concentrations of SAM. However, this should not be possible in the absence of methyl iodide. It is unlikely that HMT itself can catalyze the methylation of **P10** in the presence of SAM.

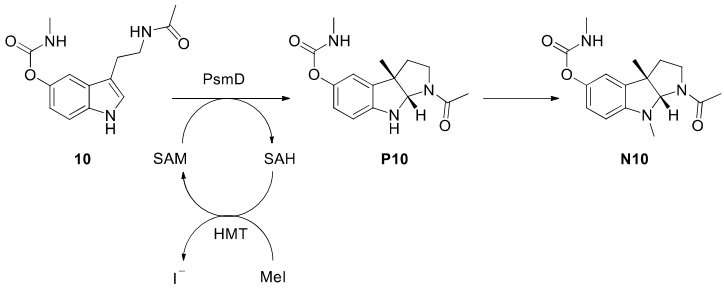

Scheme 19. Reaction scheme of the PsmD catalyzed methylation of **10** in the presence of the HMT-based recycling system and the subsequent N-methylation of the product **P10** to **N10**.

The hypothesis of the background methylation being caused by SAM was tested by incubating **P10** in the presence of SAM, with and without purified PsmD_*Sa* (Figure 87B). A small amount of N-methylated product formed when SAM was present (≈ 2%). However, approximately three times more N-methylation occurred in the presence of PsmD_*Sa*, indicating that the enzyme's promiscuity includes the methylation of its own product. It is not unexpected when examining the structures of PsmD and PsmC - the *N*-methyltransferase further along the biosynthetic pathway of physostigmine. The two enzymes exhibit similar structures, especially in their catalytic pockets, suggesting a similar mechanism of action.

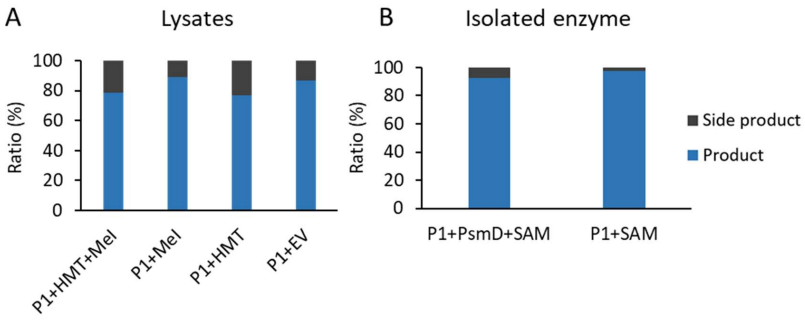

Figure 87. Background methylation in the presence of the HMT cofactor recycling system components. **A.** Control experiments in the absence of PsmD, showing the N-methylation of the product **P10**. The ratio of **P10** (blue) and N-methylated side product **N10** (grey) is represented, after incubation in the presence of 1 mM **P10** at 35 °C for 48 h. The samples were analyzed using NP-HPLC. HMT and the empty vector control (EV) were used as lysates. The amounts of lysates and MeI correspond to the optimal conditions determined in the design of experiment. N-methylation of the product could be observed in all cases. **B.** Background methylation in the presence of isolated PsmD_*Sa* and SAM. The ratio of **P10** (blue) and the N-methylated side product **N10** (grey) is represented, after the incubation at 35 °C for 24 h. The samples were analyzed using NP-HPLC.

The coupled PsmD-HMT reaction was performed using PsmD_*Sa* and *Ct*HMT cell-free extracts in the presence of methyl iodide. The reaction mixture was incubated at 35 °C for 72 h. Samples were taken at different time points, to assess the rate of formation of the side product. After 24 h, all of the substrate was converted, but 9% of the **P10** product was N-methylated, leading to **N10** (Figure 88).

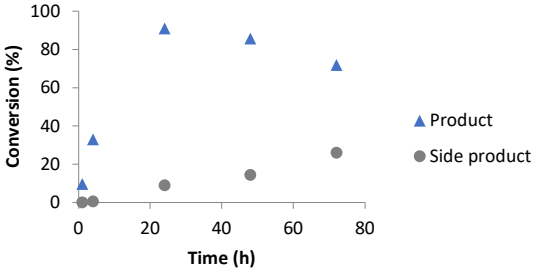

Figure 88. P10 product (triangles) and N10 side-product (circles) evolution in time. The coupled PsmD-HMT reaction using lysates was incubated at 35 °C in the presence of 1 mm substrate 10 and 10 mM MeI.

Further incubation led to an increase in **N10** concentration, reaching 26% conversion after 72 h. Therefore, long incubation times should be avoided for the lysate-based system, to prevent the formation of the side product.

The early experimental applications of PsmD_*Sa* revealed that the substrate concentration significantly impacts the preparative processes, with concentrations exceeding 2 mM leading to lower conversions and faster side product accumulation, compared to lower concentrations (Figure 89). The same lysate amounts were used in all cases. Substrate inhibition was not evident at the concentrations used in the kinetic study (up to 80 µM), but it could potentially become an issue at higher substrate concentrations. Therefore, the optimal working substrate concentrations for preparative experiments were set at 1-2 mM.

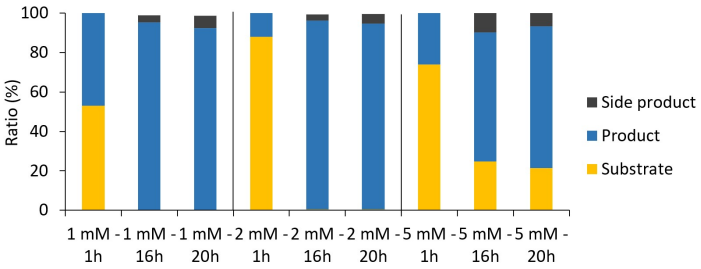

Figure 89. Evolution in time of the PsmD methylation of substrate **10** to product **P10** in the presence of the HMT recycling system at different substrate concentrations, and the accumulation of the N-methylated side product **N10**. Reaction conditions: 1, 2 or 5 mM substrate **10**, 14% (v%) HMT lysate, 20% (v%) PsmD lysate, 18 equiv. MeI in Kp_i 50 mM (pH 7.5) were incubated at 35 °C and 300 rpm.

3.7.1.4 Methyl iodide quenching

The use of the HMT cofactor recycling system provides an important advantage for the preparative enzymatic methylations using SAM-dependent methyltransferases, contributing to a significant reduction of the costs associated with the cofactor. However, methyl iodide is a toxic and volatile substance, and its use can be detrimental to the development of safe synthetic processes.[338] For this reason, several methods were explored for the degradation of methyl iodide after the enzymatic reaction.

Methyl iodide is relatively unpolar, being readily extracted into organic solvents, along with the PsmD substrates and products. Therefore, it is preferable to degrade the remaining methyl iodide in the aqueous reaction environment, before any extraction steps. It is sensitive to alkaline conditions and can be quenched through hydrolysis using a strong base. However, this is not applicable to the PsmD-HMT coupled system, as the sharp rise in pH is likely to cause the hydrolysis of the carbamate. For the removal of methyl iodide under milder

conditions, several options were explored. The supplementation of weaker bases, such as amines, was attempted. Soft nucleophiles such as thiosulfates might also provide a methylation target for the excess methyl iodide, without significantly altering the pH. As such, ammonium chloride and ammonium thiosulfate were tested as additives.

In order to explore the effects of the quenching strategies, 10 mM MeI were incubated at room temperature in KP_i buffer (50 mM, pH 7.5), simulating the coupled methylation reaction environment, in the presence of different additives. Then, it was extracted with deuterated chloroform and analyzed by ^{1}H NMR. The ratio between the methyl iodide peak intensity and the solvent peak was used for the comparison of the efficiency of the quenching methods. Out of the tested options, only ammonium thiosulfate was found to effectively degrade methyl iodide, with a 90% decrease in concentration after 10 min. The supplementation of 50 equiv. ammonium thiosulfate resulted in a reduction of 99.5% of the methyl iodide NMR peak and 100 equiv. caused the complete degradation of MeI after 10 min (Figure 90). As such, ammonium thiosulfate was chosen as a quenching agent for the preparative reactions using the PsmD-HMT coupled systems.

The methyl iodide quenching experiment was performed by Lisa Guo (Institute of Bioorganic Chemistry, Heinrich Heine University, Düsseldorf), as part of her bachelor thesis project.

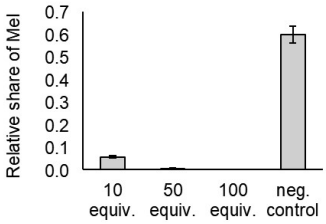

Figure 90. Effect of ammonium thiosulfate supplementation on the MeI content after 10 min of incubation at room temperature. The ratio between the MeI peak and the $CDCl_3$ peak after the ^{1}H NMR measurement was used for the comparison. The negative control contained MeI without any quenching agent.

3.7.2 Preparative methylation catalyzed by PsmD_*Sa* using lysates

Using the optimal conditions determined with the DoE, the preparative scale coupled reaction was attempted using two different substrate concentrations. 100 mg substrate **10** were incubated in a final concentration of 1 mM and 2 mM, in the presence of 10 equiv. methyl iodide,

14% (v%) *Ct*HMT lysate and 20% (v%) PsmD lysate in KP_i buffer (50 mM, pH 7.5). The substrate was chemically synthesized from N-acetylserotonin (**9**), according to the literature procedure, with 47% yield, as presented in Chapter 3.1.1 (Scheme 12).[1, 358] In both cases, all of the substrate was converted after 16 hours of incubation at 35 °C and 300 rpm. However, 25% of the product was N-methylated in the case of the 2 mM substrate loading, compared to 5% at 1 mM substrate (Table 11). The product isolation after the reaction was challenging, particularly during the extraction step. The proteins in the lysate precipitate upon contact with the extraction solvent (EtOAc), forming a gelatinous interface. This practical limitation resulted in reduced isolated yields - approx. 50%, despite achieving high conversions to the **P10** product (75 and 95%) (Figure 91).

Table 11. Comparison of the preparative scale methylation catalyzed by PsmD in the presence of the HMT cofactor recycling system using lysates and 100 mg substrate, at different concentrations.

Substrate concentration	2 mM	1 mM
Total volume	182 mL	363 mL
Conversion to nat. prod. P10	**75%**	**95%**
Conversion to side prod. **N10**	25%	5%
Isolated yield nat. prod. **P10**	50% (52 mg)	54% (57 mg)
ee	>99%	>99%
Isolated yield side prod. **N10**	7% (7.7 mg)	-

The product **P10** was purified and the optical rotation, as well as the normal phase HPLC analysis using a chral stationary phase, confirmed the enantioselectivity of the process (Figure 92). The product was isolated by column chromatography with 95% purity, according to qNMR.

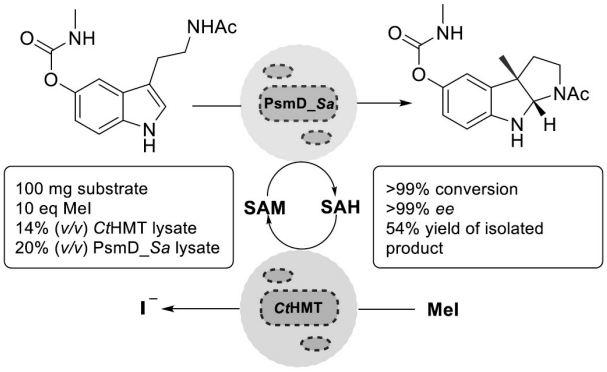

Figure 91. Representation of the coupled methylation system and the optimal composition of the reaction mixture using 100 mg substrate and 1 mM. The figure was produced by the author for [1] and used here with the agreement of the American Chemical Society.

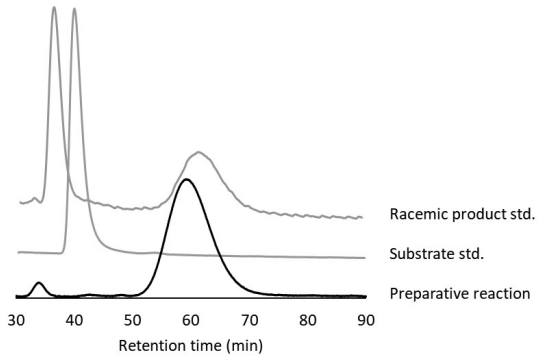

Figure 92. Chiral NP-HPLC chromatogram of the large-scale coupled reaction after 16 h, using 1 mM initial substrate **10**. At RT 33 min, the N-methylated side product **N10** was observed. The chromatogram of the racemic **P10** is shown for comparison.

3.7.3 Preparative methylation of derivative 23 using immobilized PsmD W166C

Mutant W166C was found to increase the activity of PsmD_*Sa* towards the substrate analog **23** three-fold, after the saturation mutagenesis and screening (Chapter 3.5). A new enzyme formulation was explored for the preparative methylation of **23**, using the mutant W166C, in the presence of the cofactor recycling system. The enzymes were immobilized on Ni-NTA resin directly from the lysate using their His-tags (Figure 93A). The lysate volumes used for

immobilization were calculated according to the DoE-optimized coupled reaction: 20% (v% of the total reaction volume) PsmD W166C and 14% (v% of the total reaction volume) *Ct*HMT. 10% (v% of the lysate volume) of commercial Ni-NTA resin slurry (Protino) was used for the immobilization in each case. After the reaction, the immobilized enzyme was removed by centrifugation, and the supernatant was used in the further purification procedure. This eliminated the separation issues encountered with lysate reactions, avoiding the formation of the protein interface. Starting from 50 mg substrate **23**, the process reached 65% conversion after 15 h. The N-methylated side product was not observed. The C-methylation product was extracted and purified by column chromatography, yielding 30 mg of pure compound **P23** (Figure 93B), corresponding to a 60% yield. This has shown the applicability of the system using immobilized enzymes, as well as the catalytic capacity of the newly found mutant W166C.

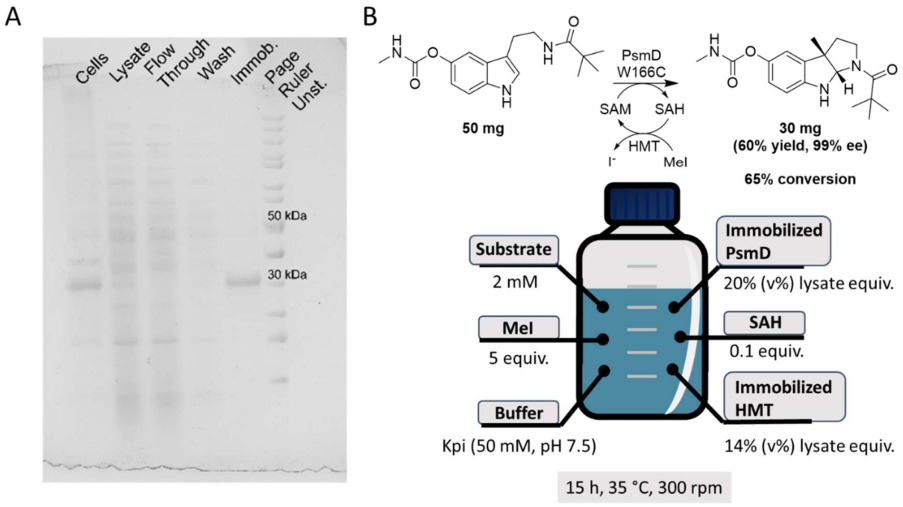

Figure 93. A. SDS-Page gel of the immobilization steps of PsmD_*Sa* W166C. The PsmD band is expected at 30 kDa. **B.** Conditions and results of the preparative methylation of **23** using PsmD_*Sa* mutant W166C, in the presence of the *Ct*HMT cofactor recycling system in immobilized format.

3.7.4 Preparative methylation of halogenated substrates

The optimized coupled reaction system was utilized for the enantioselective synthesis of halogenated C3-methylated pyrroloindoles. In the substrate scope analysis (Chapter 3.1.4),

WT PsmD_*Sa* displayed activity towards the 7-halogenated substrates **31** and **32**. This provides an important synthetic value, as the stereoselective methylation of halogenated substrates enables further coupling reactions of the chiral product. The Suzuki-Miyaura cross-coupling, in the presence of organoboron compounds and palladium catalysis, accommodates a wide range of coupling partners that can subsequently undergo further chemical functionalization.[425-427] This approach is valuable for generating new physostigmine analogs which can be linked with probes for target fishing, for the discovery of novel drug targets. The preparative methylation of 7-halogenated substrates was part of a collaborative project with Marcel Schatton (IBOC, Heinrich Heine University, Düsseldorf), who chemically synthesized and supplied the halogenated indole substrates. In a first experiment, WT PsmD_*Sa* was used in the presence of *Ct*HMT in lysate format for the C-methylation of the 7-chlorinated substrate **31**. The DoE-optimized parameters (Chapter 3.7.1.1) were used for the process. This resulted in full conversion of the substrate and a 46% yield after column chromatography purification (Figure 94A). The yield was again affected by the gelatinous protein interphase forming during the product extraction. Although the lysate formulation provided good conversion, purification issues led to a strategy shift toward using immobilized enzymes.

For the methylation of the 7-brominated substrate **32**, WT PsmD_*Sa* and *Ct*HMT were immobilized on Ni-NTA resin using the conditions described earlier (Chapter 3.7.3) and 16 mg substrate. After 20 h of incubation at 35 °C and 300 rpm, the conversion to **P32** reached approx. 57% (NMR) and 2.7 mg of product were obtained after purification (Figure 94B), corresponding to 17% yield. In this case, the low yield cannot be attributed to the phase separation during extraction, as using immobilized enzymes prevents the formation of a protein interface. The yield was a consequence of poor chromatographic separation between the substrate and product and can be improved in future attempts by the optimization of the chromatographic procedure (e.g. a different elution system).

The optimized coupled methylation system demonstrated its utility for the preparative biocatalytic synthesis of non-natural products, producing good conversions for **32**, a substrate for which PsmD exhibits low activity. This success supports its future application for the methylation of other structurally diverse substrates.

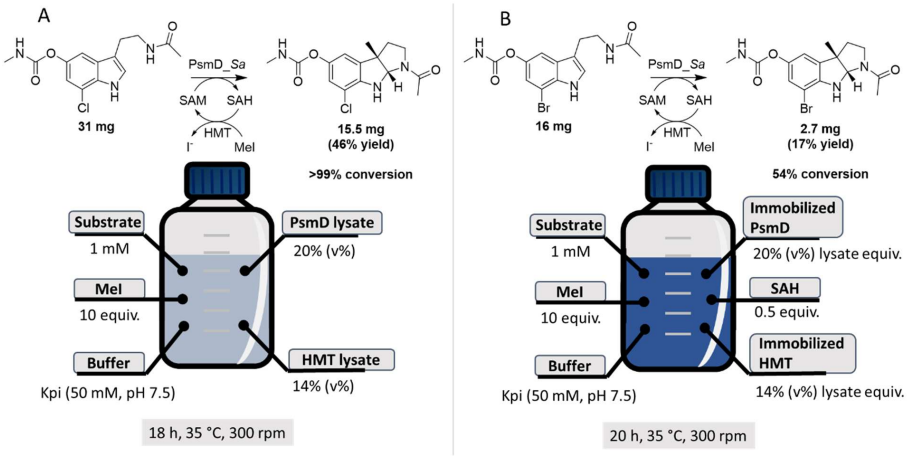

Figure 94. Preparative methylation of halogenated substrates in the presence of the *Ct*HMT cofactor recycling system. **A.** Conditions and results of the PsmD-catalyzed methylation of the chlorinated substrate **31**; **B.** Conditions and results of the PsmD-catalyzed methylation of the brominated substrate **32**.

3.7.5 Scaling further – 1 g scale enzymatic methylation using PsmD

Having successfully used the PsmD-HMT coupled reaction for 50-100 mg scale methylations, scaling up to 1 g appeared to be readily achievable. The two enzyme formulations used so far performed well enough on lab-scale transformations but still present major disadvantages at higher scales. The lysates, although easily prepared and scaled, lead to difficult product purification, while the immobilization on Ni-NTA is cost and time-intensive.

In this case, a third enzyme formulation option was explored: whole-cell biocatalysis. The experiments within this chapter were performed by Lisa Guo (Heinrich Heine University, Düsseldorf) as part of her bachelor project. Using resting or inactivated cells is common practice in the chemical industry when performing biocatalytic processes due to the lower production costs and easy catalyst separation. The use of whole-cell biocatalysts is conditioned by the membrane permeability of the substrate, product and cofactor. An initial test revealed that the PsmD substrate and product, as well as SAH and SAM, can readily pass the cellular membrane, leading to full conversion of **10** to **P10** over 16 h.

The substrate was chemically synthesized, according to the route described in the literature, obtaining 1.4 g **10**, corresponding to a 38% total yield (Scheme 20).[358]

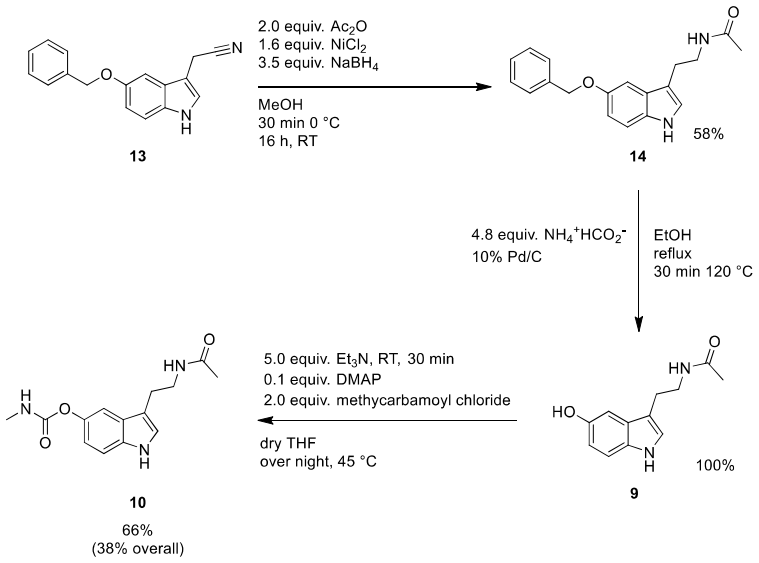

Scheme 20. Synthetic route to substrate **10**. The substrate synthesis for the gram-scale reaction was performed by Lisa Guo (Institute for Bioorganic Chemistry, Heinrich Heine University, Düsseldorf), as part of her bachelor thesis project.

Several reaction setups were tested on a smaller scale (10 mg substrate), to determine the best approach for using whole-cell biocatalysts in a gram-scale reaction. The physical separation of the cells from the reaction mixture was attempted by enclosing them in a dialysis bag, simulating a membrane reactor. The dialysis bag containing 1 g of PsmD_*Sa* and 1 g *Ct*HMT *E. coli* BL21 Δmtn (DE3) cells was suspended in 30 mL KP_i buffer (50 mM, pH 7.5), supplemented with 1 mM substrate **1** and 10 mM methyl iodide. The reaction took place in a closed glass flask. The mixing was performed using a magnetic stirrer, and a sand bath was used for temperature control. After 18 h incubation at 35 °C, the dialysis bag containing the cells was removed and the liquid reaction mixture was analyzed by RP-HPLC, revealing a 55% conversion to methylated product **P10** (Table 12).

The setup using cells which were freely suspended in the reaction mixture provided full conversion of the substrate to **P10**. The use of free cells likely improves the mass and temperature transfer throughout the system through better mixing of all the components. Furthermore, the cells are prone to lysis due to the mechanical forces, releasing the proteins into the reaction mixture. This setup resulted in a high protein content in the final solution, after

the cells were separated by centrifugation. This triggered the formation of an interphase during product extraction. Although it formed to a lesser extent than in lysate, the interphase still presented a significant obstacle to product purification. For this reason, the membrane setup was selected as the strategy for gram-scale methylation (Table 12).

Table 12. Test parameters of the whole-cells reaction set-up. All mixtures contained 1 mM substrate **10** and 10 mM methyl iodide.

Setup	Scale	Reaction volume	Cell weight	Conversion	Comments
Dialysis bag, magnetic stirring	8 mg	30 mL	1 g PsmD_Sa, 1 g HMT	55%	
Dialysis bag, magnetic stirring	16 mg	60 mL	2 g PsmD_Sa, 2 g HMT	41%	
Dialysis bag, orbital shaking 220 rpm	16 mg	60 mL	2 g PsmD_Sa, 1 g HMT	83%	1 mM EDTA was added to the buffer
Free cells, orbital shaking 220 rpm	16 mg	60 mL	3 g PsmD_Sa, 2 g HMT	>99%	Gelatinous protein interface formed at extraction

For the gram-scale process, 1 g substrate **10** was used, in a final concentration of 2 mM. This required 1.9 L of total reaction mixture. 30 g PsmD_*Sa* cells and 15 g *Ct*HMT cells were enclosed in a dialysis bag. The reaction mixture in KP_i buffer (50 mM, pH 7.5) containing 2 mM **10**, 20 mM methyl iodide and 1 mM EDTA, was incubated in a 2 L closed Schott Duran glass flask (Figure 95A). The reaction took place in an incubator with orbital shaking. For safety, the temperature was reduced to 30 °C, to prevent the evaporation of the methyl iodide, and the shaking rate was reduced to 120 rpm. A sample taken after 21 h of incubation revealed 13% conversion (RP-HPLC). Another dialysis bag containing fresh cells was added to the system, and the reaction flask was moved to a fume hood, which allowed for the increase of the temperature to 35 °C using a water bath for heating, and magnetic stirring. After another 21 h, the conversion to **P10** reached 29%. The reaction was halted after 43 h due to an increase in the formation of the N-methylated side product (**N10**) and was followed by the purification of the products (Figure 95B). Chiral NP-HPLC analysis confirmed that only one enantiomer was formed, indicating that the stereoselectivity of the methylation was maintained at larger scales (Figure 96). The product extraction was straightforward; however, the requirement for large quantities of extraction solvents is a major drawback when aiming to develop an environmentally friendly methylation route. 496 mg of low-purity product was obtained (74%, measured by qNMR) after three column chromatography steps, corresponding to a 35% yield. The low purity can be partially attributed to the formation of the N-methylated side product **N10**, which is difficult to separate from **P10** through regular silica column chromatography. For future

applications, an optimization of the downstream processing of **P10** at larger enzymatic reaction scales is necessary, to reduce waste and product impurities.

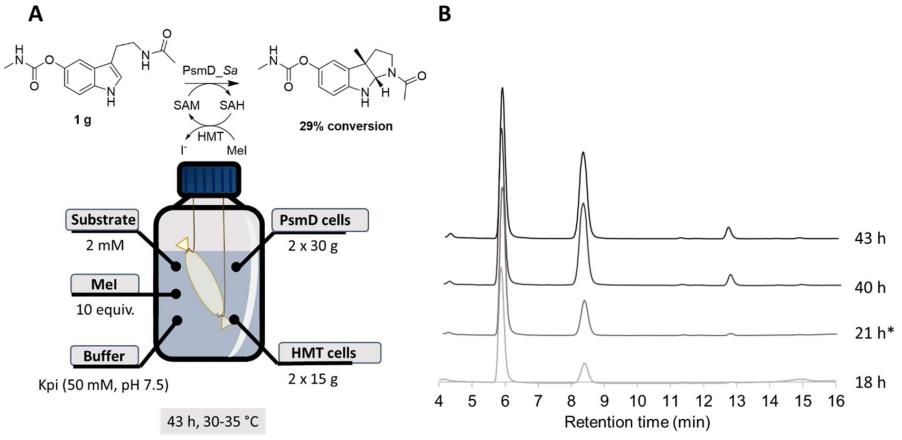

Figure 95. A. Conditions and results of the PsmD-catalyzed methylation of 1 g substrate **10**, in the presence of the cofactor recycling system, in whole-cells format **B.** RP-HPLC chromatograms showing the substrate conversion in time. The substrate peak has a retention time at 6 min, the PsmD methylation product **P10** has a retention time of 8.3 min and the N-methylated side product **N10** is represented by the peak at 13 min. *After 21 h, the reaction set-up was modified by increasing the temperature, changing the stirring and the heating methods and supplementing fresh cells.

In the end, the performance of the 1 g scale reaction using whole cells was not as good as anticipated. However, several lessons were learned. The low conversion can be attributed to a number of factors, which could be improved through process engineering:

- the reactor: most of the issues encountered in the gram-scale coupled process would likely be solved with another choice of the reactor, enabling better temperature control (e.g. through a mantle), and improved stirring.

- mass transfer: the enclosure of the catalyst made the mass transfer less efficient, requiring stronger stirring. Magnetic stirrers are insufficient for handling large volumes, so alternative stirring systems, such as anchor stirrers, could be considered. Orbital shaking worked well for smaller flasks (up to 1 L), but larger flasks require equipment with higher capacity than standard lab shakers. Scaling up orbital shakers may also not be energy-efficient.

- temperature control: assuring uniform temperature at a larger scale is challenging. It is likely that within the current setting, the desired reaction temperature was not consistent throughout the reaction volume, over time. The solution for this would be a reactor with a heating mantle, and sensors for real-time temperature control.

- cofactor reaction system: the cofactor recycling using methyl iodide limits the possible operational temperature, due to the low boiling point of methyl iodide (42 °C). Additionally, there are safety concerns when it comes to the use of the toxic reagent, as well as its removal after the reaction. A possible alternative would be the replacement of the HMT-MeI recycling system with alternatives allowing other methyl donors, such as methyl *p*-toluenesulfonate. Besides the lower toxicity, methyl *p*-toluenesulfonate is less volatile and would allow the increase of the reaction temperature closer to the PsmD optimum (45 °C), improving the methylation rate. This would additionally reduce costs by eliminating the methyl iodide quenching step.

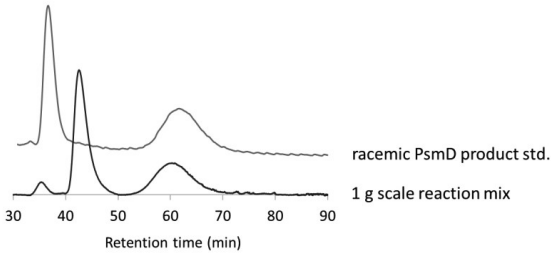

Figure 96. Chiral NP-HPLC chromatogram of the 1 g scale reaction mixture after 43 h, compared to the racemic standard of the C-methylated **P10** product. The substrate **10** peak appears at 42 min while the C-methylated **P10** product peak appears at 60 min. Although having a similar retention time with the other **P10** enantiomer (46 min), the peak at 45 min was confirmed to belong to the N-methylated side product **N10** by UV/Vis spectrum analysis.

Ultimately, with further process engineering, the gram-scale enantioselective methylation catalyzed by PsmD in whole-cell format is within reach, and could be a viable approach for the functionalization of physostigmine analogs at a preparative scale.

3.7.6 Practical and economic aspects of the preparative enzymatic methylation

The work presented in this chapter has provided several examples of the successful use of PsmD for the preparative methylation of indoles, in the presence of a cofactor recycling system. The coupled reactions were performed using different enzyme formulations, substrates and mutants, showcasing the versatility of the process. This section will present an overview of the methods used, their advantages and disadvantages, and the practical and economical considerations influencing their application (Table 13). The E-factor was calculated for the production of the biocatalyst starting from *E. coli* cells containing PsmD_*Sa*. The buffers and consumables used for the biocatalyst preparation were taken into account when calculating the E-factor as the *mass of waste/mass of product*, the product in this case being the biocatalyst in the final form supplemented to the enzymatic reaction mixture.

Each method provided overall good conversions. Most practical differences between the procedures arose either from the catalyst preparation or from the post-reaction processing. The costs of enzyme purification through affinity chromatography are prohibitive for the use in preparative or large-scale reactions. This is reflected in the calculated E-factor for the isolated enzyme preparation, which is higher by several orders of magnitude, compared to the other biocatalyst production methods.

The coupled PsmD-HMT reaction using lysates was the first choice for the preparative applications in this work and has consistently yielded the best reaction rates and conversions. It also has the advantage of easy preparation and versatility in regard to the enzymes or substrates used. However, its major disadvantage is the difficult post-reaction processing. Due to the high protein content, a gelatinous interphase forms upon product extraction with organic solvents, hindering the product recovery. Attempts at protein salting out with ammonium sulfate prior to the extraction did not produce significant differences. However, a potential solution was described in the literature, where the lysate proteins were precipitated with MeOH, followed by centrifugation and the vacuum removal of MeOH before the product extraction.[428] This could improve the final yields and allow the use of the lysate system at its full potential.

Using whole cells as catalysts is the most efficient method, in regard to catalyst preparation and post-reaction isolation, with higher storage stability. This formulation is however dependent on the membrane permeability of the substrate, the product and the cofactor. The use of whole cells was generally associated with the lowest conversions in the tested PsmD-HMT coupled systems, likely due to the less efficient mass transfer. Furthermore, depending on the reactor type and functioning parameters, cell lysis can occur, hindering the catalyst separation after the reaction. The yield of the final product formation was significantly affected by the difficult purification. The final product was obtained with moderate purity (approx. 75%)

after three column purification steps. The difficult product purification could be also attributed to the scale of the reaction, besides the extraction difficulties caused by the complex aqueous mixture. More options need be explored for the extraction and isolation of the product for gram scale enzymatic methylations, for an efficient process. Nevertheless, with further downstream processing optimization, the coupled process utilizing whole-cell catalysts holds the potential to offer an economically viable approach to enzymatic methylation.

Table 13. Comparison of the enzyme formulations used in this work for the PsmD-HMT coupled methylation reactions.

Method	Advantages	Disadvantages	Approx. catalyst preparation time	Comments on the post-reaction work-up	E-factor for the catalyst preparation/ unit
Isolated enzymes	Best activity, simple system	Expensive, time-consuming catalyst production	5-6 h	Regular product extraction and purification	$2712 * 10^3$
Lysates	Low cost, high conversion	Background methylation, high protein content hinders purification	1.5 h	Difficult extraction due to protein precipitation, significantly reducing yields.	$6.9 * 10^3$
Whole cells	Low cost, easy separation of the catalyst	Low conversion, hindered mass and temperature transfer	0 h	Cell removal can be achieved by centrifugation. After, regular extraction and purification.	$6.2 * 10^3$
Immob. enzyme	Simple system, easy separation of the catalyst	High cost of the resin, difficult preparation of the catalyst	3-4 h	Immobilized enzyme removal can be achieved by centrifugation. After, regular extraction and purification. The affinity resin can be regenerated and reused.	$8.6 * 10^3$

[a] the preparation time was estimated starting from *E. coli* cells containing the expressed enzymes, using the protocols described in the experimental section of this work. [b] The E-factor was calculated starting from *E. coli* cell cultivation and expression, taking into account the mass of media, buffer and additives used for the preparation of 1 U of catalyst. The activity observed for PsmD_*Sa* and the natural substrate **10** at 45 °C (8 mU/mg) was used as a reference, resulting in 125 mg of active enzyme corresponding to 1 U. The E-factor was calculated as the *mass of waste/mass of product*.

Finally, enzyme immobilization, although more cost-intensive, provides a good alternative for more sensitive processes, by reducing the complexity of the reaction mixture. This is relevant

for reducing the background methylation of the products, or for preventing the competitive methylation during alkylations with cofactor analogs. The immobilized enzyme could also be used for methylation in flow systems.

Each of the methods described here can lead to successful enzymatic methylation, and the choice of the system must be based on the particular necessities of the process. The conclusions presented here are based on the author's practical experience acquired for the PsmD-HMT coupled system and can differ when other methyltransferases and cofactor supply systems are used. Nevertheless, perhaps they can provide general guidelines for the future use of SAM-dependent methyltransferases as synthetic tools.

3.7.7 Chapter summary

◊ The methylation catalyzed by PsmD_*Sa* in the presence of the *Ct*HMT SAM recycling system using lysates was optimized using design of experiment. This revealed that SAH supplementation is not necessary when using lysates.

◊ Background N-methylation of the PsmD product was also observed and found to originate mostly from the lysate and the excess methyl iodide.

◊ The optimized coupled lysate system was used with 100 mg substrate, leading to full conversion of the natural substrate **10** and 54% final yield of the C-methylated product **P10**.

◊ PsmD_*Sa* mutant W166C and *Ct*HMT were successfully immobilized and used for the methylation of 50 mg substrate analog **23**, obtaining 65% conversion and 60% isolated product yield.

◊ Immobilized WT PsmD_*Sa* and *Ct*HMT were used for the methylation of 7-halogenated substrate analogs, leading to the full conversion of the chlorinated substrate (31 mg) and 54% conversion of the brominated substrate (16 mg).

◊ Further scale-up to 1 g substrate loading was attempted, using the enzymes in a whole-cell format. Multiple reactor arrangements and conditions were tested. In the end, the 1 g scale methylation of **10** achieved 29% conversion using whole cells enclosed in a membrane system.

◊ An overview of all the tested preparative methods provides their advantages, limitations and potential use cases.

4. Summary

This work provides a detailed insight into the utilization of methyltransferases for the C-methylation of indoles. The methyltransferase PsmD from *S. albulus* was biochemically characterized and analyzed from a structural and mechanistic perspective. The crystal structure of PsmD_*Sg* was determined experimentally, allowing for the precise modeling of its homolog, PsmD_*Sa*. A combination of site-directed mutagenesis, molecular docking and molecular dynamics simulation led to the elucidation of the catalytic mechanism of PsmD. The detection of two crystal forms, followed by MD simulations of the enzyme in the reaction environment, revealed the important role of the N-terminal "lid". Its closing motion triggers the start of the catalytic process after the binding of the cofactor and the substrate. A proton transfer generated by a Glu-His-Tyr catalytic triad electronically activates the substrate indole for the nucleophilic attack. The insights gained here have laid the foundation for the understanding, reaction optimization and enzyme engineering strategies for PsmD and other similar methyltransferases.

PsmD was engineered to improve its activity towards non-natural substrates containing various substituting groups on the carbamate and amide residues of the substrate molecule. A semi-rational design approach was used for the modification of the catalytic pocket. Iterative saturation mutagenesis was chosen as a strategy for the production of concentrated mutant libraries, replacing the residues in 5 different positions in a sequential manner. To assure the efficient screening of the mutant libraries we adapted the AutoBioTech integrated laboratory platform for the automated enzyme production and screening. The platform was optimized to perform the cell cultivation, protein expression, enzymatic reaction and activity screening automatically, with minimal human input. To assure the high throughput activity screening of the mutant libraries, a new colorimetric assay for the detection of indoles was developed. The assay takes inspiration from the Ehrlich test for indoles using 4-dimethylaminobenzaldehyde (DMAB) as a key reagent, expanding its application scope to substituted indoles and aqueous environments. The activatory effect of light irradiation on the indole reaction with DMAB was analyzed and harnessed in the new assay. This allowed the determination of the substrate conversion by PsmD, using isolated enzymes and whole-cell biocatalysts. The automated process aided in the identification of hit variants in the key position 166, providing up to a 3-fold increase in specific activity towards the *t*-Bu-amide substrate derivative **21** and up to 28-fold increase in specific activity towards the Phe-carbamate derivative **17**. This provided one of the first examples of the directed evolution of a stereoselective *C*-methyltransferase.

Enzymatic alkylation is an attractive target for the engineering of methyltransferases. The site-specific mutagenesis of PsmD was performed in an attempt to expand its capacity for

ethylation using a SAM cofactor derivative. Two enzymatic routes for the preparation of the SAE cofactor derivative were explored: using a promiscuous halide methyltransferase starting from SAH and ethyl iodide or using a *S*-adenosylmethionine synthetase with L-ethionine and ATP as precursors. Both methods were optimized to provide sufficient amounts of SAE for the evaluation of PsmD ethylation activity. The optimization efforts for the coupled PsmD-SAE supply systems led to a significant improvement of the conversion to the ethylated PsmD product using the wild type, while mutants A125G and F126L provided a small increase in conversion. The propyl- and allyl-cofactor derivatives were produced using the HMT enzymatic supply system, and tested in the cascade with WT PsmD and the best-performing variants. While the propylation attempts provided similar conversions to the ethylation, the conversion to the allylated PsmD product was significantly higher for all variants, reaching 95% for WT PsmD. This provides a clue into the mechanistic requirements for the PsmD catalysis (and for other similar methyltransferases), suggesting a potentially higher impact of the cofactor reactivity and enzyme dynamics, compared to the steric constraints of the catalytic pocket. This can help inform future engineering decisions aimed at expanding the alkylation capacity of similar methyltransferases.

Finally, the preparative enzymatic methylation using PsmD was performed using different enzyme formulations, in combination with a SAM cofactor recycling system. The practical applications and challenges of enzymatic methylations were explored and stereoselective methylation was achieved up to hundreds of milligrams scales. The combined system yielded good conversions using cell-free extracts, whole-cell biocatalysts and immobilized enzymes, showcasing some of the opportunities available for process engineering and optimization when it comes to scaling enzymatic methylations. A key objective of this study was to provide a positive example and several guidelines on utilizing SAM-dependent methyltransferases for the production of complex methylated compounds.

5. Outlook

5.1 Natural product methyltransferases – one family, many variations

Understanding the structural and mechanistic features of PsmD enabled the development of enzyme engineering strategies, as well as offering insights into the special needs and limitations of its catalytic process. This plays a vital role in the application of the enzymatic C-methylation in preparative synthesis, for the diversification of indole-containing compounds. Many of the features presented in this work are however not unique to PsmD. The presence of proton shuttles in the catalytic site of methyltransferases was reported before as a common mechanistic feature, with a histidine residue most often found in the vicinity of the methylation site, acting as a base.[304] Although not reported as often, disordered N-terminal regions controlling the access of the substrates in the catalytic site of methyltransferases were also found to occur in other methyltransferases.[379, 380, 429] Some of the vital amino acid residues identified in PsmD are highly conserved in other known small molecule methyltransferases, most prominently the tyrosines flanking the cofactor (in the case of PsmD_*Sa*, Y15, Y22 and Y128). The common ancestry of methyltransferase catalysis was postulated before and explains the observed similarities in the specifics of the reactions catalyzed by SAM-dependent methyltransferases. The similarities refer in particular to the electronic activation of the nucleophile, the binding and stabilization of the SAM cofactor and the lid function, which were described in detail in Chapter 3.3.

A global perspective on the structures and mechanisms of SAM-dependent natural product methyltransferases is proposed here, in an attempt to adapt their structural particularities within their overall shared features. In this way, it may be possible to identify which residues or sub-domains play important roles in the substrate selectivity, enzyme stability or dynamics, regardless of their specific methylation target. Further studies and new methyltransferase structures can help refine the collective knowledge and improve the economic viability of methyltransferase applications, by enabling more focused engineering strategies. For example, a literature search for other small molecule methyltransferases with published crystal structures reveals the similarities within this class of enzyme. The crystal structures of the human nicotinamide *N*-methyltransferase (NNMT), the *C*-methyltransferase NovO from *S. spheroides* and the *C*-methyltransferase StspM1 from *Streptomyces sp.* HPH0547 contain the same structural domains as PsmD, differing from each other in their specifics (Figure 97). These examples naturally target significantly different substrates. The Rossmann-fold domain is well-known as a conserved feature in SAM-dependent methyltransferases and is not the focus of this discussion. The substrate binding domains are substrate-specific and differ in secondary and tertiary structure.

The N-terminal lid can be identified in many structures, suggesting a similar regulation and/or activation pattern of the catalytic process (discussed in Chapter 3.3). The experimental identification of the N-terminal loop can be challenging due to its dynamic nature, often appearing disordered in X-ray analysis. This is likely why some methyltransferase crystal structures omit this region completely, and the issue extends to the structures predicted *in silico*. The structures predicted using AlphaFold for several literature-described methyltransferases, such as RapM from *S. hygroscopicus*, show the presence of a dynamic N-terminal loop. However, the confidence level of the predicted loop position is very low, a reflection of the experimentally observed variability of this region in other similar methyltransferases. The presence and importance of the lid need to be taken into account when planning enzyme engineering strategies, as disruptions in amino acid interactions at the lid level have high chances of affecting the enzymatic activities. However, if the compression motion caused by the lid closing is considered a driving force for the methyl transfer, the modification of carefully chosen amino acid residues on the lid (excluding the highly conserved ones) might have a positive effect on the overall reaction rate. It is speculative to infer that a stabilization of the closed enzyme conformation leads to higher catalytic efficiency but it is a possibility worth exploring. The lid function must also be considered when planning the practical applications of such methyltransferases, as affinity tags, restriction sequences or protease recognition domains attached at the N-terminal could affect the activity. The same applies to the enzyme immobilization, where the orientation of the enzyme on the support should be considered for optimal efficiency. Similarly, any sort of post-translational functionalization should be applied on the C-terminus instead, when possible.

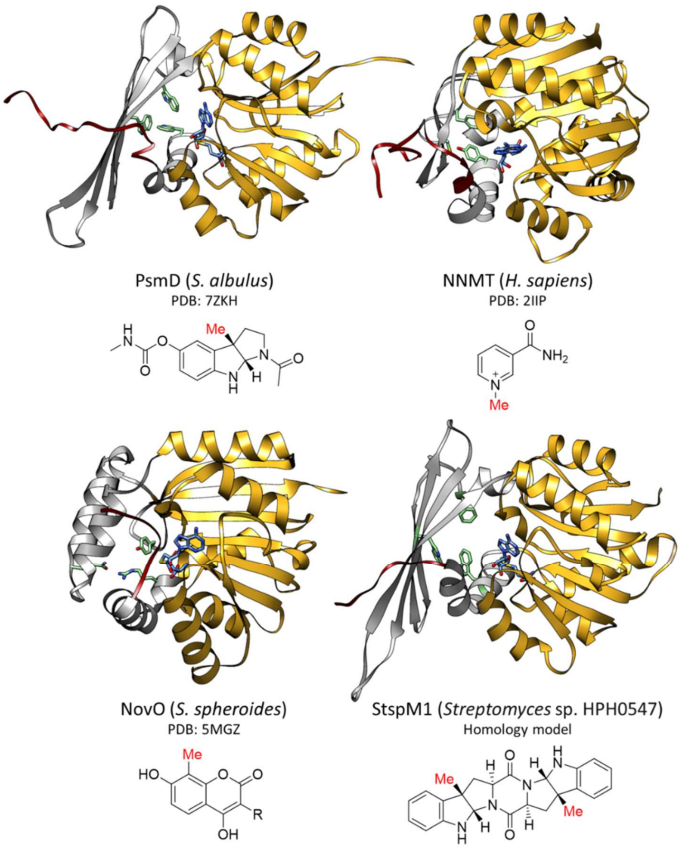

Figure 97. Examples of other small molecule SAM-dependent methyltransferases sharing the main structural features of PsmD: the Rossmann-fold cofactor binding domain (gold), the substrate binding domain (grey) and the N-terminal lid (red). The SAM or SAH cofactor is represented in blue. The putative "latch" residues are represented and colored in light green, and the structure of the methylation product of each enzyme is displayed underneath its name, species of origin and PDB code. The homology model of StspM1 was provided by Mona Haase (Institute of Bioorganic Chemistry, Heinrich Heine University, Düsseldorf), and initially generated for [292].

Another noteworthy structural aspect is the lining of the back end of the catalytic pocket. The "tryptophan cluster" of PsmD was described in Chapter 3.2, and its potential role in substrate binding and product egress was discussed. The residues lining the same area of the catalytic pockets of the other methyltransferases shown here differ significantly between the enzymes (Figure 97). The proposed "latch" function of the tryptophan cluster of PsmD, allowing the product egress after methylation, might be fulfilled by other amino acids and driven by various interactions. For example, in place of W166 and W33 of PsmD, NNMT contains two tyrosine residues, while StspM1 contains a phenylalanine and a tryptophan residue, arranged to

facilitate π-stacking interactions in a similar fashion.[292] In NovO, similar positions are occupied by an arginine and a tyrosine residue.[392] In Chapter 3.5, mutations of W166 from the "latch" domain of PsmD were shown to influence its substrate selectivity. Besides the substrate binding, the residues positioned there might influence the dynamics of the enzyme by the nature of their interactions. As such, further mutagenesis in this region is worth exploring in other methyltransferases, as a potential "hot spot" for the substrate selectivity modulation. MD simulations could help explain and even predict the effects of such mutations.

It must be noted that not all small molecule methyltransferases described in the literature display all of the mentioned structural features. The *O*-methyltransferase COMT from *Rattus norvegicus* (PDB: 5K09) lacks the distinct substrate binding domain and the N-terminal lid. Other methyltransferases used for biocatalytic methylations, such as the terpene *C*-methyltransferase TleD from *Streptomyces blastmyceticus* (PDB: 5GM1) and and the α-keto acid methyltransferase SgvM from *Streptomyces griseoviridis* (PDB: 8FTS) are also structurally different, displaying interlaced multimeric structures where the N-terminus flanks the catalytic site of another monomer. However, the common ancestry of small molecule methyltransferases often results in the structural patterns described in this chapter, and it is likely that the elucidation of more methyltransferase structures will add to the available diversity of targets associated with each structural sub-type.[299]

The information gained in this work about the structure and mechanism of PsmD has already been used as a foundation for the understanding and use of several other methyltransferases displaying a high degree of structural similarity, but different methylation targets. The first example involves the diketopiperazine *C*-methyltransferase StspM1, which was characterized and successfully used for the stereoselective methylation of tryptophan-containing dipeptides.[292] Its computational structure prediction and analysis revealed a similar dimeric structure of the enzyme and the presence of the N-terminal lid. An Asp-His-Tyr triad is present in the catalytic site, as well as the tyrosine residues flanking the cofactor, suggesting a reaction mechanism similar to PsmD. StspM1 was successfully immobilized using a C-terminal His-tag and used for preparative enzymatic C-methylation in the presence of a cofactor recycling system. Similarly, a new homolog of StspM1, was discovered and characterized. Its X-ray crystal structure was determined, revealing similar features (*Mona Haase, IBOC, Heinrich Heine University Düsseldorf, manuscript in preparation*). The second example is the *N*-methyltransferase PsmC from *Streptomyces griseofuscus.* This enzyme is involved in the biosynthetic sequence of PsmD, performing the N-methylation of the PsmD product **P10**. PsmC_*Sg* has a 48% amino acid sequence identity to PsmD_*Sg* and high structural similarity. The enzyme was recently used for the kinetic resolution of pyrroloindoles, and a crystal structure was determined. The structural and mechanistic insights from PsmD were used to

adapt the docking and post-processing strategy used in Chapter 3.5, aimed at explaining the stereospecificity of PsmC (*Benjamin Chapple, IBOC, Heinrich Heine University Düsseldorf, manuscript in preparation*). The information acquired for PsmD can hopefully help guide the engineering strategies for further natural product methyltransferases, with a wider range of targets.

5.2 PsmD as a tool for chiral pyrroloindole diversification – future prospects

5.2.1 Further mutagenesis targets for PsmD

The directed evolution of PsmD yielded an improvement of activity towards voluminous substrates, derivatized on the amide and the carbamate side of the substrate molecule. The saturation mutagenesis approach, combined with the automated production and screening system presented in Chapter 3.5 was shown to be a viable option for the substrate diversification of the PsmD-catalyzed methylation. Further improvements can be achieved by the expansion of the iterative saturation mutagenesis approach to other positions in the catalytic pocket (Figure 98). The alanine scan revealed more potentially interesting positions which could affect the substrate binding. The effects of mutagenesis on the other two residues in the tryptophan cluster - W171 and W182, would be interesting to explore, as they might influence the position of the substrate carbamate in the catalytic site. Furthermore, the alanine scan in the positions T18, L25, E157 and Q199 hinted at their potential as mutagenesis targets, as they all achieved high conversions to **P10** after being changed to alanine (Chapter 3.3.2). Finally, for ethylation using the SAE cofactor derivative, residues A125 and F126 have shown potential for altering the ethylation capacity of PsmD. Given the difficulty in predicting the outcome of changes to these residues, a saturation mutagenesis approach could provide better results.

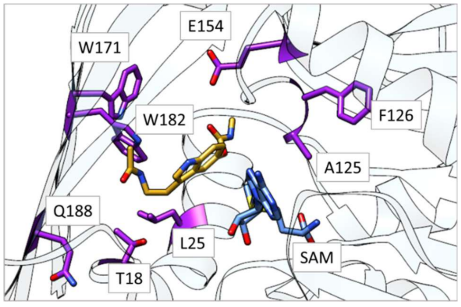

Figure 98. Amino acid residues (purple) in the catalytic pocket of PsmD_*Sa*, which are appropriate targets for further saturation mutagenesis and screening projects. The docked natural substrate **10** is represented in yellow. SAM is represented in blue.

Further diversification is within reach when it comes to other screening substrates (Figure 98). The mutagenesis-screening session using the Phe-carbamate substrate **17** presented in chapter 3.5 led to the significant improvement of the specific activity of PsmD. However, the methylation rate is not high enough for efficient preparative applications using the techniques

presented in this work. Further improvement of PsmD activity towards **17** would be significant, as it could provide a stereoselective option for the synthesis of phenserine. Subsequent saturation mutagenesis on the parent mutant W166P in the positions T18, L25, Q199, E157 and Y197 has the potential to improve the activity further.

Further substrate diversification

Although WT PsmD_*Sa* was successfully used for the preparative methylation of 7-halogenated substrates, its activity could be increased by directed evolution, particularly towards the 7-brominated substrate **30**. An increased efficiency towards the halogenated substrates is particularly useful for the chemical tagging of a larger variety of C-methylated products of PsmD for target fishing (Figure 99A).

Other substrates could be interesting targets for directed evolution approaches using the screening strategy presented in Chapter 3.5, such as 3-(2-hydroxyethyl)-1*H*-indol-5-yl methylcarbamate, a precursor of the AChE inhibitor physovenine (Figure 99B). Although physovenine is a natural product isolated from *Physostigma venenosum*, its biosynthetic origins are unclear. Publicly available comprehensive genetic data is still lacking for this organism, at the time of writing this work. Furthermore, the expansion of the carbon chain in the 3-position of the substrate to produce 6 or 7-member rings after the intermolecular cyclization is within reach (Figure 99D). This can lead to further physostigmine analogs in a chemical space largely unexplored so far.

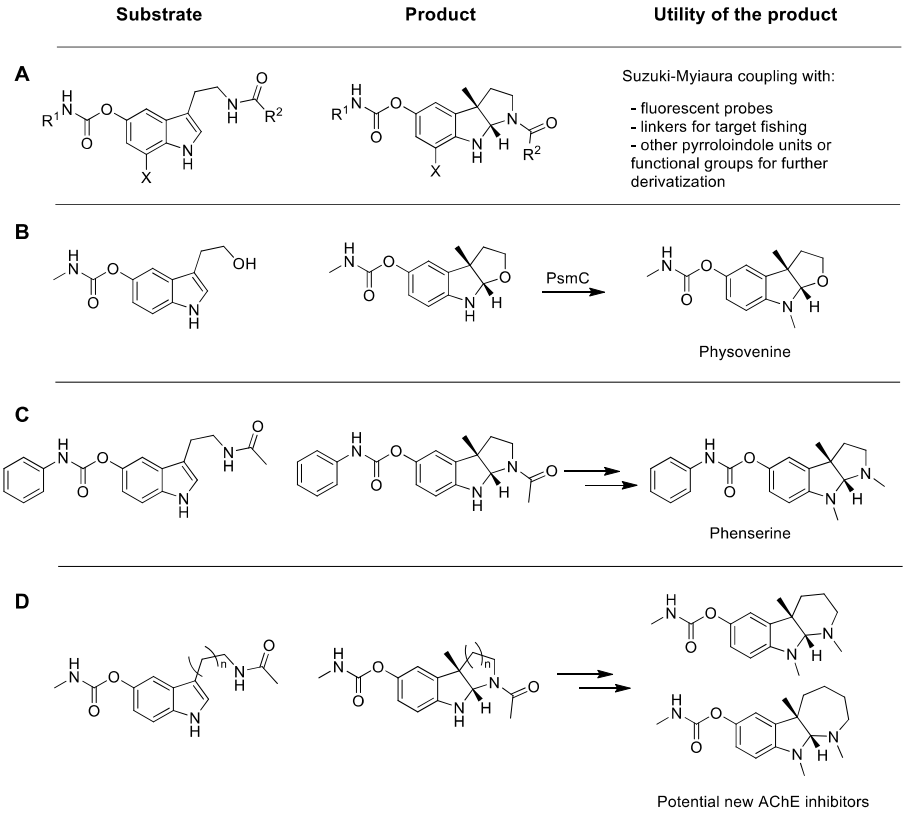

Figure 99. Examples of non-natural PsmD substrates of special interest, their products and their potential utility. **A**. The use of halogenated substrates can facilitate the chemical functionalization of the obtained pyrroloindoles for tagging with probes or linkers for target fishing. **B**. The replacement of the amide rest with a hydroxyl could enable the production of the AChE inhibitor physovenine. **C**. The stereospecific methylation of substrate 17 can provide an alternative route to phenserine. **D**. The elongation of the alkyl side chain of the PsmD substrates can lead to the stereoselective production of different ring systems. So far, there is little information on the effects of the ring size on the AChE inhibition.

PsmD_*Sa* can be a useful tool for the stereoselective synthesis of further AChE inhibitors, and the efforts made so far in its directed evolution have shown its potential for substrate diversification and synthetic versatility.

5.2.2 PsmD homolog identification

The search for other PsmD homologs can also provide useful tools for the stereoselective methylation of indoles. Several homologs of PsmD_*Sa* were identified through an amino acid sequence BLAST, predominantly in other *Streptomyces* species. PsmD from *Streptacidiphilus (Streptomyces) griseoplanus* and *Streptomyces cattleya* were expressed and tested with

several of the accepted PsmD substrates (Figure 100). While using the enzyme from *S. cattleya* did not lead to any detectable product, the homolog from *S. griseoplanus* was active towards multiple substrates, albeit approximately 2-fold slower than PsmD_*Sg* and PsmD_*Sa*. However, the presence of activity is promising, as the new homolog might provide a different selectivity and stability profile. Although other natural products such as erythromycin and anticapsin were detected after fermentation using *S. griseoplanus,* the organism is not known as a natural producer of physostigmine.[430, 431]

The identification of new PsmD homologs should not be limited to the amino acid sequence identity, as it is not necessarily an accurate way to predict the activity of unknown methyltransferases. A structure comparison using tools such as FoldSeek,[432] filtering for the PsmD "fingerprints" such as the substrate binding domain, the catalytic triad and the Trp cluster, can provide new active homologs with lower sequence similarity (Table 14).

Table 14. Structural homologs of PsmD_*Sa*, identified using Foldseek. All the identified homologs contain the catalytic triad residues in the corresponding positions. The shaded enzymes have already been expressed and tested with the PsmD natural substrate.

Genbank	UniProt ID	Organism	Sequence identity with PsmD_*Sa*	Activity
AEW99339.1	F8JMI0	*Streptomyces cattleya*	45%	No PsmD activity detected
WP_055591319	**-**	***Streptacidiphilus griseoplanus***	**55%**	**Yes**
AOM35479	A0A132ZFQ7	*Enterococcus faecium*	20%	n/a
AAG07565.1	Q9HWK3	*Pseudomonas aeruginosa*	17%	n/a
AAL00391.1	Q8DNR0	*Streptococcus pneumoniae*	19%	n/a
AAK80327.1	Q97GJ5	*Clostridium acetobutylicum*	20%	n/a

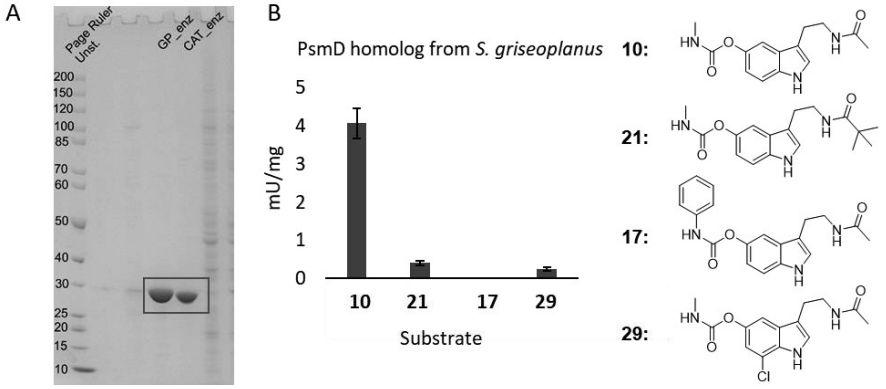

Figure 100. A. SDS-Page gel showing the two isolated putative PsmD homologs. The bands at approx. 30 kDa correspond to the homologs. **B.** Specific activity of *GP*_PsmD towards several substrates. The

activity was determined using the MTase-Glo™ assay, with the regular protocol. The reaction mixtures contained 20 μM substrate, 30 μM SAM, 1 μg enzyme in 1X MTase-Glo buffer, and were incubated at 40 °C for 15 min.

5.2.3 A chemoenzymatic synthesis route to phenserine

The AChE inhibitor phenserine is a synthetic drug which was developed as an alternative to physostigmine for the treatment of Alzheimer's disease, in order to reduce some of its associated side effects.[433, 434] The development of PsmD variants capable of performing the C-methylation of substrate analog **19** (Chapter 3.5.7) opens the path towards a new chemoenzymatic synthesis route to phenserine.

The chemical synthesis of the substrate **19** can be performed following the sequence presented in Chapter 3.5.4, or alternative options could be considered (Scheme 21A). The use of phenyl isocyanate for the carbamoylation of N-acetyl serotonin, although effective, is not ideal due to the necessity of the highly toxic isocyanate. An alternative carbamate synthesis routes could be considered, such as the coupling of phenols with amines in the presence of 1,1'-carbonyldiimidazole (CDI), which was shown to be possible under mild conditions (Scheme 21B).[435] Another option could be the generation of phenyl isocyanate *in situ*, in the presence of CO_2, trifluoroacetic acid anhydride (TFAA) and 1,8-diazabicyclo[5.4.0]undec-7-ene (DBU) (Scheme 21B).[436]

PsmD mutant W166P or further engineered variants can be used for the stereoselective methylation of the chemically synthesized **19**. The activity of W166P is still relatively low, posing difficulties in the preparative methylation of **19** through the strategies presented in Chapter 3.7. The optimization of the reaction conditions and enzyme formulation could help improve the final yields. Particularly, the stabilization through enzyme immobilization might allow the reaction to proceed for a longer time, increasing the conversion. Furthermore, it was observed that the inhibitory effect of SAH becomes significant in reactions with poorly accepted substrates. As such, the elimination of SAH immediately after formation - for example using MTAN, might improve the conversion to the product, as was the case for the PsmD-catalyzed ethylation (Chapter 3.6). Gradual substrate supplementation could also be beneficial to mitigate substrate inhibition. A promising strategy for the enzymatic methylation of **19** would be the use of flow chemistry. The immobilization of the enzyme on a column could enhance its stability, while a low flow rate would maintain a reduced substrate concentration and eliminate

the formed SAH. If necessary, the recirculation of the reaction mixture can also contribute to an increase in the overall yield (Scheme 22).

In the next step, the chemical deacetylation of the formed pyrroloindole is not advisable, as it might also lead to the cleavage of the carbamate. Instead, the enzymatic hydrolysis of the amide using PsmB might be a viable option. There is no information so far about the substrate promiscuity of PsmB, requiring further study and optimization of its hydrolytic action. The screening for commercially available promiscuous hydrolases might also provide an alternative. The final methylation of the pyrroloindole amides can be performed using methyl iodide as a methylating agent. Another option would be to perform the methylation enzymatically, using the *N*-methyltransferase PsmC. The recent characterization and analysis of PsmC from *S. griseofuscus* showed good performance in the presence of bulky substrates (*Benjamin Chapple, Institute of Bioorganic Chemistry, Heinrich Heine University Düsseldorf, manuscript in preparation*). Once established, this synthetic route could perhaps be adapted for the production of pharmacologically relevant phenserine derivatives, such as cymserine or tolserine.

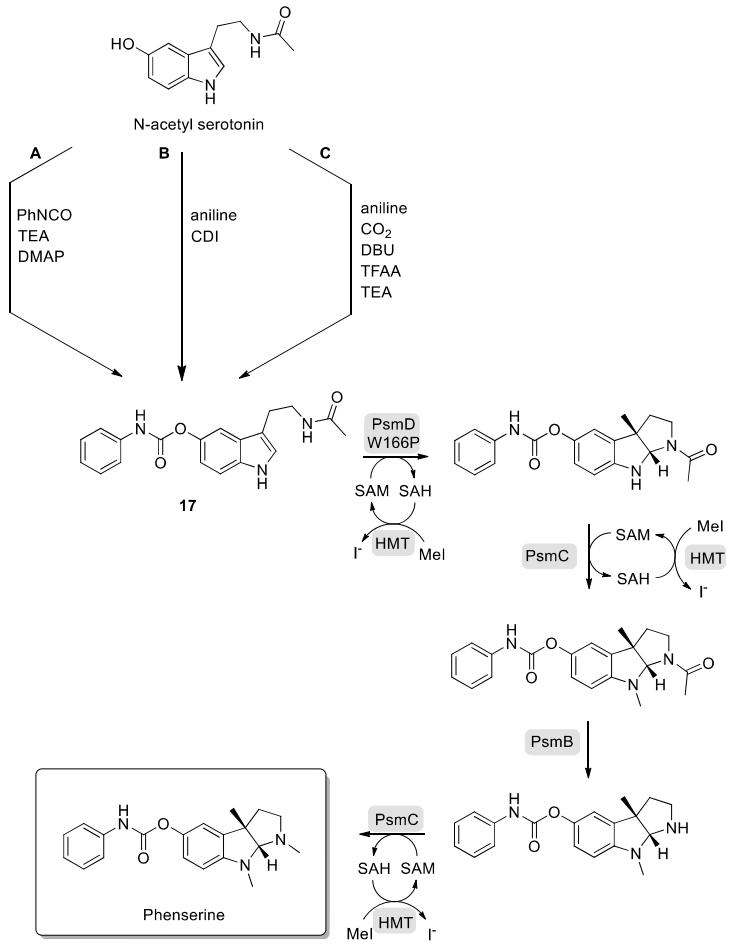

Scheme 21. Proposed chemoenzymatic synthetic path to phenserine, starting from N-acetyl serotonin. **A**. Chemical synthesis of **19** from N-acetyl serotonin using phenyl isocyanate (PhNCO) in the presence of a base (TEA) and DMAP catalysis. This was the route used in this work for the carbamate formation. **B.** Synthesis of **19** in a coupling reaction using aniline and CDI. **C.** Synthesis of **19** by generating phenyl isocyanate *in situ* from aniline in the presence of CO_2, TFAA and DBU.

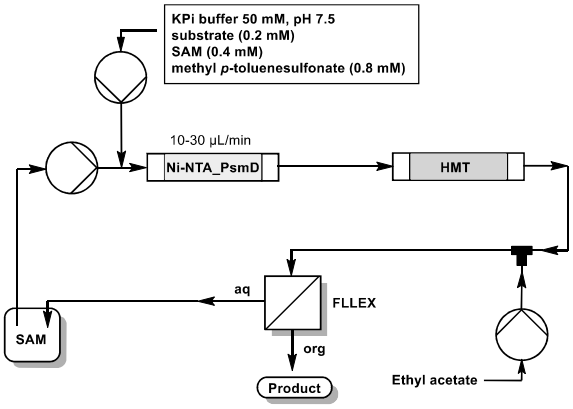

Scheme 22. The flow reaction set-up for the methylation of **19**, catalyzed by PsmD mutant W166P in the presence of the HMT cofactor recycling system using methyl *p*-toluene sulphonate as a methyl donor. The regenerated SAM cofactor is separated from the methylation product through a membrane liquid-liquid extraction module, and recirculated.

5.2.4 Enzymatic cascades containing PsmD

Enzyme cascades containing PsmD could open new paths for the synthesis of chiral indoles and pyrroloindoles. After performing the PsmD-catalyzed C-methylation of non-natural substrates, further physostigmine derivatives can be produced by continuing the biomimetic sequence of the methylated products, in the presence of PsmB and PsmC. While PsmC was recently characterized and its substrate scope is promisingly broad, not much is known about the hydrolase PsmB. Its characterization would bring valuable information for the optimization of an enzymatic cascade containing the three enzymes. An analysis of its substrate scope in particular, would help assess the achievable structural diversification using this strategy. PsmC and PsmB from *S. griseofuscus* have been expressed in an active form, but the use of their *S. albulus* counterparts could also be interesting, in case they benefit from a similar stability boost as PsmD. Since PsmD, PsmC and PsmB are part of the same biosynthetic pathway, their operational conditions are likely to be similar. As such, a one-pot PsmD-PsmB-PsmC enzymatic cascade starting from the indole PsmD substrates becomes a plausible strategy (Figure 101A). Adding an HMT-based cofactor recycling system is also a reasonable option, as one-pot PsmD-HMT enzymatic cascades were already shown to work well. The optimization of such a cascade for preparative synthesis would establish an easy-to-use biocatalytic platform for the structural diversification of physostigmine.

The use of the radical cobalamin-dependent TsrM *C*-methyltransferase can result in the further diversification of the PsmD substrates, methylating the C2 carbon on the tryptophan indole (Figure 101B). TsrM is part of the biosynthesis of the steroid thiostrepton A and was found to accept a range of substituted tryptophan derivatives as substrates. Although the enzyme was not tested for N-acetylated tryptamine derivatives, the reported results show promise for the potential indole C2-methylation of the PsmD substrates.[324] After the PsmD reaction, two methylated stereocenters would be formed. It would be interesting to assess if this transformation has any effects on the AChE inhibitory action of these molecules.

The chemical synthesis of PsmD substrate analogs could be replaced by an enzymatic cascade. Tryptophan synthases have been effectively used for the synthesis of a large variety of substituted tryptophan derivatives.[437] The use of a tryptophan synthase (TrpB) in cascade with a tryptophan decarboxylase (TDC)[438] and a serotonin *N*-acetyltransferase (SNAT)[439] could provide new PsmD substrates, using mild reaction conditions (Figure 101C).

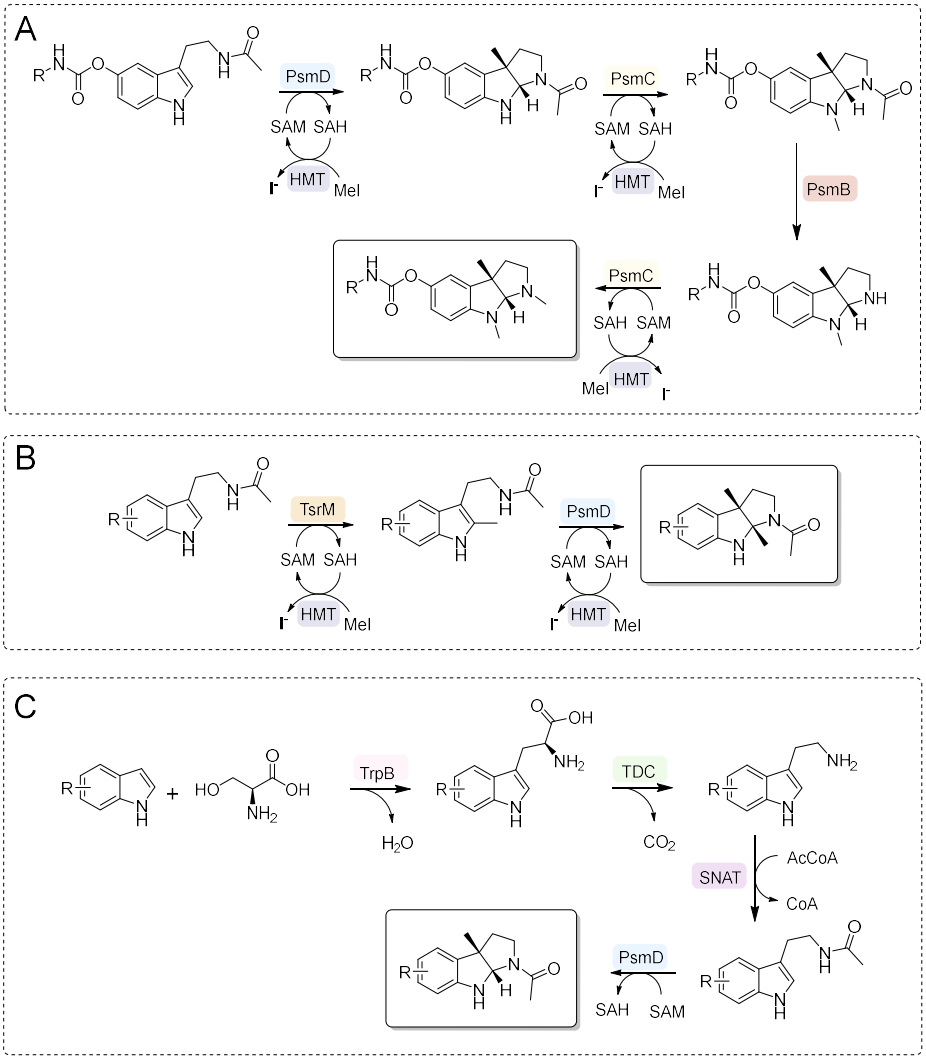

Figure 101. Possible enzymatic cascades using PsmD. **A**. Biomimetic cascade using PsmD substrate analogs. **B**. The use of TsrM *C*-methyltransferase for PsmD substrate diversification. **C**. The use of a tryptophane synthase (TrpB), tryptophan decarboxylase (TDC) and serotonin *N*-acetyltransferase (SNAT) for PsmD substrate derivative generation.

5.2.5 Is stereoselective biocatalytic ethylation within reach?

The biocatalytic alkylations using methyltransferases in the presence of SAM cofactor analogs were explored for multiple methyltransferases (described in Chapter 2.4.4). In recent years, significant progress was achieved in developing new production strategies for cofactor

derivatives that can transfer functional groups beyond methyl. The enzymatic production of cofactor derivatives profited from the recent discovery and engineering of new MAT and HMT variants, and as a consequence, the range of available SAM derivatives expanded considerably.

Multiple successful examples of alkylation and arylation cascades using MAT and HMT variants in combination with methyltransferases can be found in the literature. Although possible, one needs to note the generally low reaction rates, combined with the difficult production and control of the cofactor supply. Considering the low methyltransferase affinities for cofactor derivatives, the inhibitory effect of SAH becomes considerable and needs to be countered by removing the SAH from the reaction mixture. The enzymatic routes for this are the most advantageous, providing high selectivity for SAH. Most often, MTAN is supplemented, although SAHH is also a viable option. While the transfer of larger groups is in many cases more chemically accessible by coupling/reduction sequences, selective ethylation is even more challenging than methylation. The ethyl group is also interesting as it is small enough to provide a supplementary “magic (m)ethyl effect” in fine-tuning drug candidates. Because of this, although the transfer of larger groups from SAM derivatives can also be achieved using methyltransferases, this discussion will focus on ethylation.

The outcome of the efforts to improve the ethylation capacity of PsmD differed from the initial expectations. Due to the compact conformation of the enzyme in its active closed form, it seemed reasonable that opening the available space for a larger cofactor side chain would improve the ethylation activity. While this worked to a reduced extent, the differences in conversion between WT PsmD and the most active mutants A125G and F126L were small. The similar results for propylation and the much higher conversions obtained for the allylation of **10** supported another conclusion: steric constraints are not the main barrier to the biocatalytic ethylation using PsmD. This prompts a change of perspective for the future of PsmD engineering for ethylation. Considering the reactivity of the cofactor as the main limiting factor, enzyme engineering efforts should be targeted at the enhancement of the biocatalytic driving force. Counterintuitively, a reduction in the available space around the cofactor by replacing the surrounding amino acid residues with larger ones, might be more productive. A saturation mutagenesis approach in the positions A123, A124, A125 and F126 might be a better strategy, since not enough information is available for reliable rational design. Mutant library screening is challenging for ethylation, due to the cofactor supply limitation. This problem can be solved using the MAT-SAE supply system optimized in Chapter 3.6.1, to prepare the necessary cofactor. The more pressing issue is the requirement for pure enzymes. The ethylation reactions cannot be reliably analyzed in lysates or whole-cell systems due to the competitive methylation in the presence of endogenous SAM. The high-throughput His-tag

immobilization of the variants on microtiter plates could be a solution. This requires a slight change in the screening set-up, using Ni-coated plates and the addition of cell lysis and washing steps to the process. In this case, the screening can be achieved using the AutoBioTech platform and a similar strategy to the one described in Chapter 3.5.3 (Scheme 23).

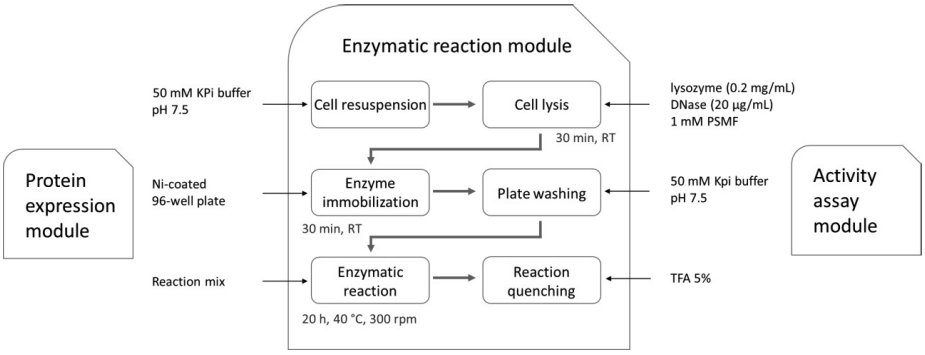

Scheme 23. Proposed process scheme for the automated production and screening of PsmD mutants for ethylation improvement. The protein expression and activity assay modules remain as presented in Chapter 3.5.3. The enzymatic reaction module requires several extra steps: cell lysis, enzyme immobilization and a washing step. The cell lysis can be performed enzymatically in 96-well plates using lysozyme. For the immobilization of PsmD, Ni-coated plates are required. They are commercially available or can be prepared using $NiSO_4$. After a washing step, the reaction can be started by adding the reaction mixture. The reaction mixture contains 1 mM substrate **10**, 8 µM MTAN, 10% (v/v) MAT-SAE mix (containing 7 mM SAE) in KP_i buffer 50 mM, pH 7.5. The MAT-SAE mix should be freshly prepared before the enzymatic reaction step. RT refers to "room temperature".

The optimized conditions from Chapter 3.5, as well as the evolution and screening strategy for ethylation, can be applicable to other methyltransferases. The emergence of more successful examples of methyltransferase-catalyzed alkylations and allylations is important for understanding the structural and chemical drivers of these reactions. This might help develop a general strategy for enabling enzymatic ethylations for more methyltransferases and targets. Indeed, the use of methyltransferase with SAM cofactor analogs is a rapidly evolving area of development and is likely to lead to a significant surge in the available range of biocatalytic alkylations in the near future. This can be streamlined by adopting a global overview of the origins of methylation and ethylation reactivities in small molecule methyltransferases.

5.2.6 Future PsmD engineering opportunities

5.2.6.1 Computer-assisted library design

The effects of mutations on the catalytic activity of enzymes are often difficult to predict, requiring extensive information on the structure, mechanism and dynamics of said enzyme. Even having this information, the dynamic nature of enzymes in solution can be easily overlooked and might produce effects that are not apparent in the structural experimental data. User-friendly computational tools for the prediction of productive mutations are emerging, helping create focused mutant libraries for different purposes such as the improvement of stability, solubility, or the modification of substrate scopes. An increase in the thermostability of PsmD and other small molecule methyltransferases might be achieved using the FireProt 2.0[440] tool for the mutant design. To improve overall protein stability in solution, the FoldX,[441] Dezyme's PoPMuSiC[246] and HOTMuSiC[442] or DeepDDG[443] tools can provide predictions of the effect of mutations on stability. Tools such as FuncLib[249] and Caver[248] can help expand the substrate scope of PsmD and similar enzymes.

Further discovery and characterization of small molecule methyltransferases can provide valuable data for the training of machine learning models, which could predict the target scope of unknown or unannotated methyltransferases from experimental databases. At the time of writing this work, there are over 2.7 million SAM-dependent methyltransferases in the UniProt database (19.08.24). Streamlining the target identification procedure using computational analysis would provide a great boost for expanding the available enzymatic methylation options.

5.2.6.2 Automation of mutant library production and screening

The automation of high-throughput mutant library production and screening is a staple of industrial enzyme engineering. Robotic liquid handling systems are becoming more common. The AutoBioTech platform was built for versatility, allowing for the construction of genetic libraries and production strains, as well as the screening of enzyme libraries.[444] The automated process reported in Chapter 3.5 can be used as described for the engineering of other enzymes. Beyond PsmD homologs, the system can directly be applied to any enzyme forming pyrroloindoles from indoles, provided it meets two requirements:

- The enzyme can be expressed by autoinduction
- The substrate, product and cofactor (if necessary) can pass the cell membrane

The AutoBioTech automated strategy described in Chapter 3.5 was successfully used for the engineering of an indole *C*-methyltransferase improving its activity towards halogenated dipeptides (Mona Haase, Marcel Schatton, IBOC, Heinrich Heine University Düsseldorf,

manuscript in preparation). In the future, other types of pyrroloindole-forming enzymes (for example prenyltransferases or monooxygenases) could be modified using the same strategy. The first two modules – the enzyme expression and reaction module, are applicable for the engineering of other methyltransferases fulfilling the requirements mentioned earlier. The replacement of the indole assay with another reaction-specific colorimetric or fluorescent activity assay is easily applicable to the robotic liquid handling platform. Recent advancements in high-throughput general methyltransferase assays monitoring SAH formation provided a valuable solution for general methyltransferase screening.[445]

The advances in microfluidic systems for enzyme engineering allowed for a dramatic increase in the screening throughput. The use of microfluidics can significantly accelerate the development of new enzyme variants, while reducing the necessary amounts of reactants.[270] This can be particularly important for methyltransferases such as PsmD, which require complex and commercially unavailable substrates, as well as expensive cofactors in stoichiometric amounts. While the price of SAM has decreased in the last years and it does not pose the problem it used to, the supply of SAM cofactor derivatives remains challenging. The derivatives need to be produced chemically or enzymatically, significantly raising the costs. Therefore, reducing the demand for cofactors would greatly lower the costs of methyltransferase engineering for further alkylations.

Nowadays, automation plays a crucial role in enzyme engineering, enabling faster, more efficient, and scalable workflows. High-throughput screening, robotic liquid handling, and data-driven design tools allow the exploration of large libraries of enzyme variants and the optimization of their properties with unprecedented speed and precision. This can help expand the methyltransferase engineering opportunities and provide new biocatalysts for the late-stage alkylation of biologically relevant complex molecules.

There are many opportunities for including PsmD and other similar methyltransferases in the synthetic routes of valuable complex compounds. Further advancing the technological and experimental optimization, as well as the protein engineering opportunities for this class of enzymes can provide valuable tools for the selective late-stage functionalization of compounds containing indoles or pyrroloindoles.

6. Materials

6.1 Devices

Table 15. List of devices used in this work and their producer.

Device	Producer
Pipettes	
Eppendorf Research Plus - pipette 0.5-10 µL - pipette 10-100 µL - pipette 100-1000 µL - pipette 10-100 µL - pipette 0.5-5 mL	*Eppendorf AG*, Hamburg, Germany
Eppendorf Research Plus - multichannel pipette, 12 channels, 0.5-10 µL - multichannel pipette, 12 channels, 10-100 µL - multichannel pipette, 12 channels, 30-300 µL - multichannel pipette, 12 channels, 120-1200 µL	*Eppendorf AG*, Hamburg, Germany
Mettler Toledo, Rainin - Pipet-Lite Adjustable Spacer LA8-300XLS, multichannel pipette, 8 channels, 20-300 µL - Pipet-Lite Adjustable Spacer LA8-1200XLS, multichannel pipette, 8 channels, 100-1200 µL	*Mettler Toledo,* Oakland, USA
Incubators and shakers	
- *Heidolph incubator 1000* coupled with *Heidolph unimax 1010 shaker,* Incubation and shaking of larger volumes (up to 300 mL) and 96-well plates. - *Eppendorf Thermomixer compact,* heating block with mixing for 1.5-2 mL tubes - *HLC MKR23 Cooling-ThermoMixer*, heating block with mixing for 1.5-50 mL tubes - *Eppendorf MixMate PCB-11*, plate shaker - *BioCote Stuart Rotator SB2,* rotating tube mixer, used in a room with 37 °C constant temperature - *New Brunswick Innova 42 incubator shaker,* incubator for cell cultures	*Heidolph Intruments GmbH*, Kelheim, Germany *Eppendorf AG*, Hamburg, Germany *DITABIS Digital Biomedical Imaging Systems AG*, Pforzheim, Germany *Eppendorf AG*, Hamburg, Germany *BioCote LTD*, Wolverhampton, UK *New Brunswick Scientific GmbH*, Nürtingen, Germany

Centrifuges	
- *Eppendorf Concentrator* 5301, vacuum centrifuge	*Eppendorf AG*, Hamburg, Germany
Eppendorf Centrifuge 5242R, cooling centrifuge for tubes (1.5, 2 mL)	*Eppendorf AG*, Hamburg, Germany
- *Eppendorf centrifuge 5810R*, cooling centrifuge for tubes (15-50 mL)	*Eppendorf AG*, Hamburg, Germany
- *Sorvall RC6+*, cooled centrifuge with PTI F10S-6x-500y and PTI F9S-4x1000y rotors	*Thermo Fisher Scientific*, Waltham, MA, USA
- *Hettich Rotanta 460R centrifuge*, cooled plate centrifugation	*Hettich AG*, Bäch, Switzerland
Balances	
- *Sartorius 2004MP*, analytical balance	*Sartorius AG*, Göttingen, Germany
- *Sartorius MC1*, laboratory balance	*Sartorius AG*, Göttingen, Germany
- *VWR PBA224i-1S-FC,* analytical balance	*VWR International GmbH*, Darmstadt, Germany
Photometers	
- *NanoDrop 2000c*, photometer for small volumes	*Thermo Fisher Scientific*, Waltham, MA, USA
- *NanoDrop One*, photometer for small volumes	*Thermo Fisher Scientific*, Waltham, MA, USA
- *Tecan Infinite® M1000 PRO*, plate reader	*Tecan Group AG*, Männedorf, Switzerland
Chromatography	
- *Jasco X-LC series*, used for reverse-phase HPLC	Jasco Deutschland GmbH, Pfungstadt, Germany
- *Dionex Ultimate™3000 HPLC*, used for normal phase, chiral HPLC	*Thermo Fisher Scientific*, Waltham, MA, USA
- *Äkta Pure* chromatography system, for protein purification	*Cytiva*, Marlborough, MA, USA
- *Thermo Fisher UltiMate 3000 UHPLC system*, LC-MS	*Thermo Fisher Scientific*, Waltham, MA, USA
NMR	
Advance/DRX 600 MHz NMR	Brucker, Billerica, MA, USA
Other analytics	
- *Perkin Elmer Spectrum Two FT*, IR Spectrometer	*Perkin Elmer*, Waltham, MA, USA
- *Krüss P8000-TF*, polarimeter	*Krüss optronic GmbH,* Hamburg, Germany
- *Advion exPressIon CMS*, mass spectrometer	*Advion Inc.*, Ithaka, NY, USA

Others	
- *Bandelin Sonorex RK 100 H*, ultrasonic bath	*Bandelin electronic* GmbH, Berlin, Germany
- *Biometra TProfessional Basic Gradient*, PCR-Cycler	Analytik Jena AG, Jena, Germany
- *VWR XT96 PCR thermal cycler*	*VWR International GmbH*, Darmstadt, Germany
- *Bio-Rad Mini Protean Tetra System*, SDS-Page gel electrophoresis system	*Bio-Rad Laboratories* GmbH, Münich, Germany
- *Bio-Rad PowerPac Basic*, agarose gel electrophoresis system	*Bio-Rad Laboratories* GmbH, Münich, Germany
- *Heidolph Hei-VAP Core* rotary evaporator, equipped with a G3 vertical cooler and vacuum control	*Heidolph Scientific Products GmbH*, Schwabach, Germany
- *Camag UV Cabinet 4*, UV camera for gel documentation	*Camag*, Muttenz, Switzerland
- *Canon EOS 1000D*, Digital camera for gel documentation	*Canon Deutschland* GmbH, Krefeld, Germany
- *Heidolph MR 3001 K*, Heating plate with a magnetic stirrer, combined with *EKT HeiCon* thermometer	*Heidolph Instruments* GmbH & Co.KG, Schwabach, Germany
- *Invitrogen Novex MiniCell*, electrophoresis system for pre-cast SDS-PAGE gels	*Invitrogen* GmbH, Darmstadt, Germany
- *pH-Meter Knick 766 Calimatic*	*Knick Elektronische Messgeräte* GmbH, Berlin, Germany
- *Sonopuls*, ultrasonic cell disruptor, with various tip sizes (1.5–50 mL)	*Bandelin electronic* GmbH, Berlin, Germany
- *Steinel HG3002LCD 3458*, heatgun	*Steinel Vertrieb* GmbH, Herzebrock-Clarholz, Germany
- *Vacuubrand MD 4C*, vacuum pump	*Vacuubrand* GmbH, Wertheim, Germany
- *Vacuubrand RZ 6*, vacuum pump	*Vacuubrand* GmbH, Wertheim, Germany

6.2 Software

Table 16. List of software used in this work and their publisher.

Software	Publisher
ChemBioDraw 18.0, used for chemical structure representation	*PerkinElmer Informatics*
Clone Manager 9.4, cloning aid, primer design, sequencing results visualization	*Scientific & Educational Software*
SnapGene 7.1.1, cloning aid, primer design, sequencing results visualization	*GSL Biotech LLC*
ensochemLab 7.0.5, electronic chemical lab journal	*enso Software* GmbH
MestReNova 8.0.1-10878, NMR data visualization and processing	*Mestrelab Research S.L.*

Microsoft Office 2016 (Word, Excel, Powerpoint, OneNote), data collection, processing and presentation	*Microsoft Corp.*
OriginPro 2018, data processing, non-linear regression, graph construction	*OriginLab*
DesignExpert 12, design of experiment planning and data processing	*StatEase Inc.*
COREL Photo-Paint 2018, image manipulation	*Corel Corp.*
Jalview 2.11.1, protein and gene sequence alignment visualization	*University of Dundee*
UCSF Chimera 1.14, protein 3D structure visualization and processing	*UC San Francisco*
Autodock Vina, protein-ligand docking	*Scripps research*
Endnote 21, reference manager	*Clarivate*
ChatGPT 4, language refining in written text *	*OpenAI*

* The text in this thesis was NOT generated using ChatGPT 4; artificial intelligence was strictly used as a language refining aid for better readability (i. e. identifying synonims and refining phrasing).

6.3 Consumable materials

Pipette tips were acquired in bulk from *Ratiolab* (Dreieich, Germany) and *Sarstedt AG* (Numbrecht, Germany). Single-use 1 mL plastic cuvettes were purchased from *Ratiolab*. Sterile syringe filters (FiltroPur S 0.2) and closed plastic tubes (1.5, 2, 15 and 50 mL) were purchased from *Sarstedt AG*. 0.2 µm membrane filters were purchased from *Sartorius* (Göttingen, Germany). ExcelScientific AeraSeal permeable plate sealing films were purchased from *Merck* (Darmstadt, Germany). Thin-layer chromatography plates with silica gel (Polygram®SIL G/UV_{254} with fluorescence indicator; 0.2 mm layer thickness) were purchased from *Macherey-Nagel* (Düren, Germany). Silica gel 60 (particle size 40-63 µm) for preparative column chromatography was acquired from *Macherey-Nagel* (Düren, Germany). Disposable syringes (cylinders made of polypropylene, polyethylene plunger) were purchased from *Braun Melsungen AG* (Melsungen, Germany). White microtiter plates (Nunclon®; polystyrene, white, flat bottom) were acquired from Nunc™ *Thermo Fisher Scientific* (Waltham, MA, USA) and transparent and black microtiter plates were acquired from *Greiner* (Kremsmünster, Austria). Deep-well plates (polypropylene, solvent-resistant, conical bottom) were acquired from *Eppendorf AG* (Hamburg, Germany). Vivaspin© 500 and Vivaspin© 20 (10000 MWCO, PES) centrifugal concentrators were purchased from *Sartorius* (Stonehouse, UK).

6.4 Chemicals

The commercial chemicals used in this work were purchased from *Carl Roth GmbH* (Karlsruhe, Germany), *Sigma-Aldrich* (Steinheim, Germany), *Alfa Aesar* (Karlsruhe, Germany), *VWR*

International (Radnor, PA, USA), *BLD Pharma* (Kaiserslautern, Germany) or *TCI Europe* (Zwijndrecht, Belgium).

6.5 Oligonucleotides and synthetic genes

The oligonucleotides used in this work were purchased from *Merck* (Darmstadt, Germany) in dry format and dissolved in distilled H_2O to form 100 µM stock solutions. All the oligonucleotide sequences can be found in Annex 8.4. The synthetic genes were ordered from *GenScript USA Inc.* (Piscataway, NJ, USA) in pET21a(+) or pET28a(+) vectors. The commercial DNA sequencing services were provided by *Eurofins Genomics* (Ebersberg, Germany).

6.6 Enzymes

The enzymes used in the molecular biology applications (restriction, ligation and polymerases) were purchased from *Thermo Fisher Scientific* (Waltham, MA, USA), *New England BioLabs GmbH* (Frankfurt am Main, Germany) and *Takara Bio Europe* (Saint-Germain-en-Laye, France).

6.7 Kits

Commercial kits were used for DNA purification from various sources. For plasmid purification from cell cultures, innuPREP Plasmid Mini Kit 2.0 from *IST Innuscreen GmbH* (Berlin, Germany) was used. DNA purification from agarose gels was performed using the innuPREP DOUBLEpure Kit from *IST Innuscreen GmbH*.

7. Methods

7.1 Molecular biology

The native PsmD_*Sa* synthetic gene was purchased individually and was inserted into the pET21a(+) vector by digestion with XhoI and NdeI for 20 min at 37 °C, followed by the dephosphorylation of the plasmid at the 5´-end with FastAP (*ThermoFisher Scientific*, USA). The restriction products were purified by agarose gel electrophoresis. The ligation of the vector and insert was mediated by T4 DNA Ligase (*ThermoFisher Scientific*, USA) o/n at 16 °C. The pET21a(+)_PsmD_*Sg* construct was obtained as previously described in the literature.[358] The codon harmonized PsmD_*Sa* gene and all the other genes coding the proteins described in this work were purchased from *GenScript* (USA) directly within the desired plasmid (pET21a(+) or pET28a(+)).

7.1.1 Plasmid isolation and analysis

For the amplification and isolation of plasmids, *E. coli* DH5α or *E. coli* BL21 Gold (DE3) strains containing the vector with the gene of interest were cultivated overnight in 5 mL LB medium supplemented with the corresponding antibiotic. The innuPREP Plasmid Mini Kit 2.0 from *IST Innuscreen GmbH* (Berlin, Germany) plasmid isolation kit was used according to the manufacturer's protocol. The final elution was performed with 50 µL Milli-Q pure water. The DNA concentration was determined by NanoDrop analysis, measuring the absorbance at 260 nm and the obtained samples were sequenced using the Sanger sequencing service of *Eurofins Genomics* (Ebersberg, Germany) using the T7 and/or T7term standard primers.

7.1.2 Site-specific mutagenesis

The residues for the alanine scan were selected based on the structural information from PsmD_*Sg*, as well as the generated homology model of PsmD_*Sa*. PsmD_*Sa* mutant genes were obtained by mutagenesis PCR amplification, using the PsmD_*Sa*-pET21a(+) construct as a template. The reaction mixtures contained 1x Phire buffer, 200 µM (each) dNTPs, 100 nM (each) forward and reverse primers, 0.5 ng/µL template, 5% DMSO and 0.4 µL Phire Hot Start II DNA polymerase. The initial denaturation was performed at 98 °C for 3 min, after which the program was continued with 25 cycles of denaturation (98 °C, 10 s), annealing (72 °C, 5 s) and elongation (72 °C, 1 min). The final annealing was performed at 72°C for 5 min. The PCR products were subjected to digestion with dpn1 and then used to transform chemically competent *E. coli* DH5α cells via heat shock, out of which the mutant plasmids were isolated using a plasmid isolation kit (Innuprep, *Analytik Jena*) and further used to transform via heat shock chemically competent *E. coli* BL21 Gold (DE3) for protein expression.

7.1.3 Site-saturated mutagenesis

The amino acids in the selected positions were modified by iterative saturation mutagenesis. The mutant libraries were generated using the 22c-trick. This reduces codon redundancy, leading to reduced libraries.[420] Degenerated primer mixtures were used in a whole plasmid amplification PCR approach. The codon harmonized PsmD_*Sa* gene in pET21a(+) was purchased from *Genscript* and used as a template. The reaction mixtures contained 1x PrimeStar GXL buffer, 200 µM (each) dNTPs, 300 nM (each) forward and reverse primers, 0.2 ng/µL template and 1 µL PrimeStar DNA polymerase. The initial denaturation was performed at 98 °C for 30 s, after which the program was continued with 17 cycles of denaturation (98 °C, 10 s), annealing (touchdown 72 °C to 56 °C 15 s) and elongation (68 °C, 3 min). After, 25 cycles of denaturation (98 °C, 10 s), annealing (55 °C 15 s) and elongation (68 °C, 3 min) were performed. The final annealing was performed at 68°C for 5 min. The PCR products were subjected to digestion with dpn1 and then analyzed by agarose (1%) gel electrophoresis, using Midori Green™ as a stain. After purification from the gel, the products were subjected to ligation with T4 DNA ligase in the presence of 6% (v/v) PEG 4000. After the inactivation of the ligase, 10 µL of the PCR product were used to transform chemically competent *E. coli* DH5α cells using heat shock. All the obtained colonies were collected and mixed and the plasmid mixtures were isolated using a plasmid isolation kit (Innuprep, *Analytik Jena*). The pure primer mixtures were analyzed by sequencing and used to transform via heat shock chemically competent *E. coli* BL21 Gold (DE3) for protein expression.

7.1.4 Agarose gel electrophoresis

For DNA analysis, the PCR products were mixed with 6X TriTrack DNA Loading Dye (*Thermo Scientific*, USA) and 6 µL (analytical gel) or 35 µL (preparative gel) samples were loaded into the wells of a 1% agarose gel.

Table 17. Component list for the agarose gel electrophoresis.

Solution	Components
5 x TBE buffer	89 mM TRIS 89 mM Boric acid 2.5 mM EDTA
Agarose gel solution	1x TBE buffer 1 % (w/v) agarose 0.1 % (v/v) Midori Green™

The agarose gel solution was prepared by boiling 1% (w/v) agarose in 1 X TBE buffer until the agarose was fully dissolved. After, the fluorescent dye Midori Green™ (*Nippon Genetics*, Germany) was added and the solution was stored at 60 °C to avoid polymerization. After casting, the gel polymerized at room temperature (~25 °C) for approx. 30 min. For the DNA size determination, 3 µL of the 1 kb DNA Ladder (*Thermo Scientific*, USA) were used as

standard and the electrophoresis was performed at 100 V for 35 min. The analysis and documentation were conducted using a gel documentation system (*INTAS Science Imaging Instruments GmbH*, Göttingen, Germany).

7.2 Microbiological methods

7.2.1 Bacterial strains

Table 18. Overview of the bacterial strains and description of their genotype and their application in this work.

Strain	Genotype	Supplier	Application
E. coli DH5α	F⁻ Φ80*lac*ZΔM15 Δ(*lac*ZYA-*arg*F)U169 *rec*A1 *end*A1 *hsd*R17 (r_k^-,m_k^+) *pho*A *sup*E44 *thi*-1 *gyr*A96 *rel*A1 *λ*⁻	*Merck*	Plasmid amplification, transformation
E. coli BL21(DE3) Gold	F⁻ *omp*T *hsd*S($r_B^-m_B^-$) *dcm*⁺ Tet^r *gal* λ(DE3) *end*A Hte	*Merck*	Protein expression
E. coli BL21(DE3) Gold Δmtn	F⁻, Δ(*araD-araB*)567, *pfs-773(del)* Δ*lacZ4787*(:rrnB-3), *λ*⁻, *rph*-1, Δ(*rhaD-rhaB*)568, *hsdR514*, *λ*(DE3)	*Florian Seebeck group, University of Basel* [207]	Protein expression

7.2.2 Cultivation

The bacteria cultivation was generally performed in sterile LB medium for overnight pre-cultures and TB for the expression cultures, both containing ampicillin or kanamycin in a final concentration of 100 µg/mL, depending on the plasmid and strain antibiotic resistance. In case autoinduction was required, TB was used, supplemented with 2% (v/v) autoinduction additive. In some cases, SOC medium was used for the regeneration step after the heat-shock transformation of the *E. coli* cells with mutagenesis PCR products. For cultivation on plates, LB medium was supplemented with 1.5% (w/v) agar-agar prior to autoclave sterilization.

Table 19. Bacterial growth media components.

Medium	Components
LB	0.1 % (w/v) tryptone 0.05 % (w/v) yeast extract 0.1 % (w/v) NaCl Distilled H_2O
TB	5.08 % (w/v) Commercial TB medium (*Carl Roth*, Germany) 0.4 % (v/v) glycerol Distilled H_2O
Autoinduction additive (50X)	25% (v/v) glycerol 2.5% (w/v) glucose 10% (w/v) lactose Distilled H_2O

SOC	2 % (w/v) tryptone 0.5 % (w/v) yeast extract 10 mM NaCl 2.5 mM KCl 10 mM $MgCl_2$*$6H_2O$ 10 mM $MgSO_4$ 20 mM glucose Distilled H_2O

SOC medium was sterilized by filtration through a 0.2 µm cut-off membrane filter. All other media were sterilized using an autoclave prior to use.

7.2.3 Production and transformation of chemically competent *E. coli* cells

The transformation of *E. coli* strains with plasmid DNA was performed using chemically competent cells. To prepare competent cell stocks, 5 mL preculture in LB were incubated at 37 °C overnight. After, a culture in 400 mL LB was inoculated with 2 mL pre-culture and incubated at 37 °C until the cell density (OD_{600}) reached 0.4-0.6. Then, the cells were harvested by centrifugation at 1230 rcf and 4 °C for 10 min. The cell pellet was resuspended carefully in 10 mL Buffer A and incubated 20-30 min on ice. The cells were then harvested by centrifugation at 1230 rcf and 4 °C for 10 min and resuspended in 2 mL Buffer B. 50 µL aliquots of the suspension were distributed in sterile Eppendorf plastic tubes and frozen immediately in liquid nitrogen. The competent cell stocks were stored at -80 °C for later use.

Table 20. Composition of the buffers used for the preparation of chemically competent cells.

Solution	Components
Buffer A	100 mM $MgCl_2$
Buffer B	100 mM $CaCl_2$ 15% Glycerol

The transformation of chemically competent cells was performed using heat shock. One competent cell stock tube was thawed on ice for 30 min. After, 1-2 µL (purified plasmid) or 10-15 µL (PCR/ligation product) DNA was added to the competent cells and incubated on ice for 30 min. Then, the heat shock was performed by incubating the tube at 42 °C on a water bath for 45 s, followed by immediate incubation on ice for 2 min. Then, 1 mL TB or SOC medium was added to the competent cells and the culture was incubated at 37 °C for 1 h. Finally, the cells were plated on LB-agar plates supplemented with the appropriate antibiotic and incubated overnight at 37 °C.

The capacity for plasmid incorporation of newly created competent cells was tested by comparison of the transformation of the cells with the plasmid pET21a(+) (1 µL, 42 ng/µL) and sterile dH_2O. The transformation was performed as described earlier and the cells were

incubated on LB agar plates containing ampicillin, which only allows for the growth of colonies containing the pET21a(+) plasmid. The transformation efficiency was determined using equation 3. The antibiotic sensitivity of the competent cells was also tested by cultivating the cells in 5 mL LB medium containing (separately) ampicillin, tetracycline, chloramphenicol, streptomycin and kanamycin. The cultures were incubated overnight at 37 °C.

$$total\ DNA\ concentration\ (\mu g/\mu L) = \frac{stock\ DNA\ conc.(\mu g/\mu L) * V\ DNA\ sol.used(\mu L)}{Vcompetent\ cells + Vmedia + Vvector\ (\mu L)}$$

Equation 1. Formula for the calculation of the total DNA concentration in the competent cell culture

$$final\ DNA\ amount\ (\mu g) = \frac{total\ DNA\ concentration\ (\mu g/\mu L)}{Vplated\ (\mu L)}$$

Equation 2. Formula for the calculation of the final DNA amount in the plated competent cells culture volume

$$CFU/\mu g\ DNA = \frac{no.of\ colonies}{final\ DNA\ amount\ (\mu g)}$$

Equation 3. Formula for transformation efficiency determination of competent cells. CFU=colony forming units.

7.2.4 Cryo-preservation of *E. coli* cell cultures for long-term storage

For long-term storage, 1-2 mL cell culture in LB containing the plasmid of interest were mixed with 25% (v/v) glycerol and stored at -80 °C.

7.2.5 *E. coli* cell lysis

The cell-free extracts used for the preparative biotransformations were prepared as follows: the cell pellets containing the expressed protein of interest were resuspended in reaction buffer (50 mM KP_i, pH 7.5) to a concentration of 0.2 g cells/mL of buffer. The cells were lysed using an ultrasonic probe 2 x 10 min, with a 2 min incubation on ice between the two sessions, using an ultrasonic cell disruptor (Branson Sonifier II "Modell W- 250", Heinemann) with an amplitude of 30-35%. During the procedure, the cell suspensions were kept on ice. The resulting cell

debris was then separated by centrifugation at 10000 x g and 4 °C for 1h and discarded, while the supernatant was immediately used in further experiments.

7.3 Protein methods

7.3.1 Heterologous protein expression in *E. coli*

The procedure for manually induced heterologous expression with IPTG was identical for all proteins and types of strains used in this work, and was performed as follows: pre-cultures in LB media containing ampicillin (pET21a(+)) or kanamycin (pET28a(+)) were inoculated with single cultures from agar plates or from glycerol cell stocks and incubated overnight at 37 °C. The expression was performed in TB media, supplemented with 100 µg/mL ampicillin (pET21a(+)) or kanamycin (pET28a(+)). The medium was inoculated with the overnight culture to an initial concentration of 1% (v/v) and incubated at 37 °C and 130 rpm until an OD_{600} of 0.5-0.8 was reached. Then, the expression was induced by adding IPTG to a final concentration of 100 µM. The cultures were further incubated for 16-20 h at 25°C and 130 rpm. The cells were harvested by centrifugation at 4000 rpm and 4 °C for 30 min, and the pellets were stored at -20 °C until further use.

7.3.2 Protein expression in *E. coli* BL21 Gold strain by autoinduction

The expression by auto-induction was performed for PsmD_*Sa* and its mutants. Pre-cultures in LB media containing ampicillin (pET21a(+)) or kanamycin (pET28a(+)) were inoculated with single cultures from agar plates or from glycerol cell stocks and incubated overnight at 37 °C. The expression was performed in TB media, supplemented with an additional 0.5% (w/v) glycerol, 0.05% (w/v) glucose, 0.2 (w/v) lactose and 100 µg/mL ampicillin (pET21a(+)) or kanamycin (pET28a(+)). The medium was inoculated with the overnight culture to an initial concentration of 1% (v/v) and incubated at 35 °C and 130 rpm for 24 h. The cells were harvested by centrifugation at 4000 rpm and 4 °C for 30 min, and the pellets were stored at -20 °C until further use.

7.3.3 Protein purification using affinity chromatography

Purification of all proteins and their mutants carrying a His_6-tag was performed by immobilized metal affinity chromatography. After heterologous protein expression, the cells were suspended in an equilibration buffer to the final concentration of 0.5 mg/mL. The cell disruption was carried out by sonication (Branson Sonifier II "Modell W-250", *Heinemann*). The cell debris was removed by centrifugation (10000 rpm, 4 °C, 30 min), and the supernatant was filtered through a 0.45 µm syringe filter. A 5 mL Ni-NTA column (Superflow Cartridge, *QIAGEN* GmbH, Hilden, Germany) was used for affinity binding. The column was equilibrated with 3 column volumes (CV) of equilibration buffer. Afterward, cell lysate was loaded on the column. The column was washed with 5 CV of washing buffer, after which the target protein was eluted with 3 CV of elution buffer. Eluted protein was concentrated via centrifugation in Vivaspin® 20 centrifugal concentrators (MWCO 10 kDa, *Sartorius*, Germany). The protein solution was

washed three times with 20 mL of storage buffer. The purified protein was flash-frozen in liquid nitrogen and stored at −20 °C for further use.

Table 21. Composition of the buffers used for the protein isolation by Ni-NTA affinity chromatography.

Equilibration buffer	**PsmD_*Sa* (and mutants)**: KP_i 50 mM, pH 7.5, 500 mM NaCl
	TkMAT: Tris-HCl 40 mM, pH 8.0, 100 mM NaCl
	CtHMT: KP_i 50 mM, pH 7.5, 500 mM NaCl
	AcHMT: KP_i 50 mM, pH 7.5, 500 mM NaCl
	***Ec*MTAN:** KP_i 50 mM, pH 7.5, 500 mM NaCl
Washing buffer	**PsmD_*Sa* (and mutants)**: Equilibration buffer + 50 mM imidazole
	***Tk*MAT**: Equilibration buffer + 20 mM imidazole
	***Ct*HMT**: Equilibration buffer + 100 mM imidazole
	***Ac*HMT**: Equilibration buffer + 50 mM imidazole
	***Ec*MTAN:** Equilibration buffer + 40 mM imidazole
Elution buffer	**PsmD_*Sa* (and mutants)**: Equilibration buffer + 150 mM imidazole
	***Tk*MAT**: Equilibration buffer + 250 mM imidazole
	***Ct*HMT**: Equilibration buffer + 250 mM imidazole
	***Ac*HMT**: Equilibration buffer + 250 mM imidazole
	***Ec*MTAN:** Equilibration buffer + 300 mM imidazole
Purge buffer	**PsmD_*Sa* (and mutants)**: Equilibration buffer + 1 M imidazole
	***Tk*MAT**: Equilibration buffer + 1 M imidazole
	***Ct*HMT**: Equilibration buffer + 1 M imidazole
	***Ac*HMT**: Equilibration buffer + 1 M imidazole
	***Ec*MTAN:** Equilibration buffer + 1 M imidazole
Storage buffer	**PsmD_*Sa* (and mutants)**: KP_i 50 mM, pH 7.5
	***Tk*MAT**: Tris-HCl 40 mM, pH 8.0, 100 mM NaCl
	***Ct*HMT**: KP_i 50 mM, pH 7.5, 500 mM NaCl
	***Ac*HMT**: KP_i 50 mM, pH 7.5
	***Ec*MTAN:** KP_i 50 mM, pH 7.5, 500 mM NaCl

For analytical scale activity analysis, the affinity chromatography purification method was adapted for smaller-scale simultaneous isolation of multiple proteins. In this case, the *E. coli* BL21 Gold cells obtained from 25 mL culture (approx. 0.3 g) were resuspended in 2 mL equilibration buffer. The cells were lysed by ultrasonic probes for 10 min on ice. The lysates were centrifuged at max speed (15000 rpm) for 30 min. Separately, 500 µL Ni-NTA resin (*Protino*) was added to mini-spin columns (BGB, 800 µL capacity, PTFE, 0.2 µm, with 2 mL receiver tube). The columns were centrifuged at 5000 x g and the flow-through was discarded. 600 uL equilibration buffer were added to the column and the resin was resuspended and incubated for 10 min. The columns were centrifuged for 30 s at 5000 x g, discarding the flow-through. 600 µL cell-free lysate was added to the column, resuspending the resin. The columns

were incubated for 5 min on ice, with occasional stirring. The columns were centrifuged at 5000 x g for 30 s. The flow-through was discarded. Washing buffer was added to the columns. The columns were incubated for 1 min, with occasional stirring. The washing step was repeated twice more. The collector tube was replaced with a clean tube and 300 µL elution buffer were added to the column. The columns were incubated for 1 min, with occasional stirring and centrifuged at 5000 x g for 30 s. The elution step was repeated once more, keeping the flow-through in both cases. The collector tubes with the obtained protein solution were removed and the filters were inserted back into the initial collection tubes. 600 µL purge buffer were added to each column for the removal of the residual bound proteins. The columns were incubated for 1 min, with occasional stirring, then centrifuged at 5000 x g for 30 s. The supernatant was discarded and the columns were stored in 20% ethanol in the fridge for re-use. For buffer exchange, the eluted solutions were added to mini-centricons with 10 kDa cut-out. 500 µL storage buffer was added and the mixtures were centrifuged at 12000 x g for 5 min. This step was repeated 3 times. The final protein solutions were supplemented with glycerol (20% v%) and stored at -20 °C for further use.

7.3.4 Protein purification using size exclusion chromatography

Gel filtration for PsmD_*Sa* and PsmD_*Sg* was performed using an ÄKTA Purifier device. Separation was performed on a HiLoad 16/600 Superdex™ 200 pg column (*Cytiva*, USA) at 25 °C and a flow rate of 1 mL/min. The elution was performed with a K_{Pi} 50 mM buffer containing 150 mM NaCl, with a pH of 7.5. Calibration was performed using a gel filtration markers kit for protein molecular weights 12000-200000 Da (*Sigma*). Analytical size exclusion chromatography was performed for PsmD_*Sa* using an ÄKTA Prime 25L device, and separation was performed on a 16 Superdex™ 75 Increase 3.2/300 column (*Cytiva*) at 4 °C and a flowrate of 0.03 mL/min. The elution was performed with K_{Pi} 50 mM buffer with a pH of 7.5. BSA was used as a standard.

7.3.5 Protein analysis by SDS-Page electrophoresis

For SDS-Page electrophoresis, the desired protein samples were mixed with 20 % (v/v) 5X SDS loading buffer and incubated at 95 °C for 10 min to ensure the denaturation of the proteins. 10 µL samples were loaded into the gel wells using a Hamilton syringe and the electrophoresis was performed at 120 V for 10 min, followed by 150 V for approx. 1 h, until the dye front reached the lower edge of the gel.

Usually, the gels were manually prepared and cast in two layers: a 10% acrylamide gel for protein separation (bottom) and a 4% acrylamide gel for sample concentration (top). The bottom gel was first prepared by mixing all the components in a plastic tube. The activation of the polymerization was performed by adding TEMED and APS (10%) as the last components, the mixture was poured into the casting plates immediately and incubated until the gel fully solidified (approx. 30 min). After the lower gel solidified, the same procedure was repeated with the top gel layer, adding the gel comb, to produce the sample wells. The gels were used immediately after, or stored at 4 °C for a maximum of 2 weeks. As running buffers for electrophoresis, the cathode buffer occupied the inner gel cell and the anode buffer was added to the outer tank. After the electrophoresis, the gel was removed from the glass case, rinsed with dH_2O and incubated in staining solution overnight, then in dH_2O for 24 h.

Table 22. Composition of the buffers used for the SDS-Page protein electrophoresis.

Solution	Components
5X SDS loading buffer	10% (w/v) SDS 30% (w/v) sucrose 0.1% (w/v) bromophenol blue 50 mM DTT 0.5 M Tris/HCl solution, pH 6.8 as a solvent
Cathode buffer	0.1 M TRIS 0.1 M tricine 0.1% (w/v) SDS Distilled H2O pH 8.25
Anode buffer	0.1 M TRIS 25.5 mM HCl Distilled H2O pH 8.9
3X Gel buffer	3 M TRIS 1 M HCl 0.3% (w/v) SDS pH 8.45
10% acrylamide gel	33% (v/v) acrylamide/bis-acrylamide 30% solution 33% (v/v) 3X gel buffer 8% (v/v) glycerol Distilled H2O **For polymerization activation:** 0.1% (v/v) TEMED 1% (v/v) APS 10% solution in water
4% acrylamide gel	13% (v/v) acrylamide/bis-acrylamide 30% solution 25% (v/v) 3X gel buffer Distilled H2O **For polymerization activation:** 0.1% (v/v) TEMED 1% (v/v) APS 10% solution in water

Staining solution	2 % (w/v) ortho-phosphoric acid 10% (v/v) ethanol 5% (w/v) aluminium sulphate-(14-18)-hydrate 0.02% (w/v) Coomassie Brilliant Blue© G-250 distilled H2O

In certain cases, commercial NuPAGE Bis-Tris pre-cast gels (*Invitrogen*, USA) were used in combination with the NuPAGE buffer, according to the specifications of the manufacturer. The samples were prepared as described. After electrophoresis, the gels were processed as previously described.

7.3.6 Dynamic light scattering analysis of PsmD_*Sa* and PsmD_*Sg*

DLS experiments were performed on a SpectroSize 300 device (*Xtal Concepts*, Germany), using protein solutions with concentrations of 1 mg/mL. The samples were centrifuged at 20,000 × g and 4 °C for 30 min prior to the measurements. Scattering data was recorded over 25 successive acquisitions of 10 s each. Fitting of diffusion coefficients to the intensity autocorrelation function and estimation of molecular masses based on the Stokes-Einstein equation were performed using software provided by the manufacturer (SpectroCrystal). The DLS measurements were performed in collaboration with Dr. Oliver Weiergräber (IBI-1, Forschungszentrum Jülich).

7.4 X-ray crystallography

The crystallization of the PsmD_*Sg* was performed by Dr. Oliver Weiergräber (IBI-1, Forschungszentrum Jülich) and Nadiia Pozhydaieva (IBOC, Heinrich Heine University, Düsseldorf). The X-ray diffraction and data interpretation were performed by Dr. Oliver Weiergräber and made available for this work. Vapor diffusion screening experiments were set up at 293 K in sitting-drop geometry, using a Freedom Evo robotic system (*Tecan*, Switzerland). Protein crystals were observed for a number of conditions; diffraction-quality samples of PsmD_*Sg* used in this study were obtained with a reservoir solution containing 0.2 M magnesium formate and a protein concentration of 24 mg/ml; successful conditions for the SAM complex were 30% (w/v) PEG 1000, 0.1 M Tris-HCl pH 8.5 (crystal form 1), and 10% (w/v) SOKALAN CP 42, 0.1 M Tris-HCl pH 8.5 (crystal form 2), using a sample containing 12.5 mg/ml of protein and 2 mM SAM. In the case of form 2, the crystal was incubated in a reservoir solution containing 20% (v/v) 2-methyl-2,4-pentanediol prior to cryocooling, the other samples were mounted directly from their mother liquor. Diffraction datasets were recorded at 100 K on beamline P11 at the Deutsches Elektronen-Synchrotron (DESY, Hamburg, Germany) using an X-ray wavelength of 1.033 Å and a PILATUS 6MF detector. Following data integration and scaling with XDS,[446] the structure of PsmD_*Sg* in the presence of SAM (crystal form 1) was determined by molecular replacement using MOLREP[447] with the crystal structure of the methyltransferase from *Pyrococcus horikoshii* (PDB-ID: 1WZN) as search model. Correctness of the weak initial solution was verified by automated rebuilding in phenix.autobuild,[448] and the model was iteratively improved by reciprocal space refinement in phenix.refine[449] and interactive rebuilding in COOT.[450] An early version of this model served as a template in molecular replacement for the second crystal form of the SAM complex as well as the apo structure; these solutions were further processed according to the procedure described above. As confirmed by MolProbity[451] and the wwPDB validation, all three models exhibit good geometry with no outliers in the Ramachandran plot and a proportion of rare side chain rotamers in the expected range. For full data collection and refinement statistics refer to Annex 8.8.

7.5 Biocatalytic analysis

7.5.1 PsmD analytical scale reactions using the MTase-Glo™ assay

The specific activity of the selected hits was determined using the MTase-Glo™ assay (*Promega*, Germany).[369] The reaction mixture contained 20 µM substrate, 30 µM SAM and 1 µg enzyme in 1x MTase-Glo™ buffer (20mM TRIS buffer, pH 8, 50 mM NaCl, 1 mM EDTA, 3 mM $MgCl_2$, 0.1 mg/ml BSA, 1 mM DTT) in a final volume of 20 µL. The mixtures were incubated at 40 °C for 15 min in Nunc™ flat-bottom white 96-well plates, after which the assay was performed according to the manufacturer's protocol. A SAH calibration curve was produced for the quantification of SAH final concentration. The luminescence was measured using a Tecan Infinite M1000Pro microplate reader. The measurements were performed at 23 °C, with no attenuation and an integration time of 1000 ms.

7.5.2 SAH calibration using the MTase-Glo™ assay

The SAH calibration of the MTase-Glo™ Assay was performed in the same conditions as the activity measurements, without adding any methyltransferase to the initial mixture. A 15 µM SAH stock solution was provided by the kit manufacturer. Successive dillutions in 1X MTase-Glo™ buffer (20 mM TRIS buffer, pH 8, 50 mM NaCl, 1 mM EDTA, 3 mM $MgCl_2$, 0.1 mg/ml BSA, 1 mM DTT) lead to a range of SAH concentrations between 0 and 10 µM in 20 µL final well volumes. All the concentration points were prepared in triplicate. The further steps of the assay were performed according to the kit manual, including the addition of 5 µL TFA 0.5% solution in water. A linear dependency between the SAH concentration and the final luminescence yielded the calibration equation. The SAH calibration was repeated for each newly acquired MTase-Glo™ kit.

7.5.3 General MTase-Glo™ assay procedure for PsmD activity determination

The specific activity of PsmD variants was determined using the MTase-Glo™ assay. The reaction mixture contained 20 µM substrate, 30 µM SAM and 1 µg enzyme in 1x MTase-Glo™ buffer (20 mM TRIS buffer, pH 8, 50 mM NaCl, 1 mM EDTA, 3 mM $MgCl_2$, 0.1 mg/ml BSA, 1 mM dithiothreitol) in a final volume of 20 µL. The mixtures were incubated at 35 °C or 40 °C for 15 min in Nunc™ flat-bottom white 96-well plates, after which the assay was performed according to the manufacturer's protocol. A SAH calibration curve was produced for the quantification of SAH final concentration. The luminescence was measured using a Tecan

Infinite M1000Pro microplate reader. The measurements were performed at 23 °C, with no attenuation and an integration time of 1000 ms.

7.5.4 Determination of the optimum temperature for PsmD_*Sa* activity

For every reaction, 1.5 mM substrate **10**, 2 mM SAM and 50 µg PsmD_*Sa* were mixed in reaction buffer (50 mM KP_i, pH 7.5) to a final volume of 500 µL. The mixtures were incubated at various temperatures ranging from 20 to 55 °C and 700 rpm for 3 hours. Afterwards, the reaction was quenched and the product was extracted by adding 2 x 500 µL ethyl acetate to the reaction mixture. The organic phase was collected and the solvent evaporated by vacuum centrifugation. The solvent-free samples were then prepared and measured via HPLC as described in Chapter 7.6.2.

7.5.5 Determination of the optimum pH for PsmD_*Sa* activity

1.5 mM substrate **10**, 2 mM SAM and 50 µg PsmD_*Sa* were mixed in reaction buffer (50 mM KP_i, variable pH) to a final volume of 500 µL. The mixtures were incubated at 35 °C and 700 rpm for 3 hours. Afterwards, the reaction was quenched and the product was extracted by adding 2 x 500 µL ethyl acetate to the reaction mixture. After phase separation, the organic phase was combined and the solvent evaporated using a vacuum centrifuge (Eppendorf Concentrator 5301, Eppendorf). The conversion was determined via normal phase HPLC, as described in Chapter 7.6.2.

7.5.6 Kinetic measurements using the MTase-Glo™ assay

The kinetic parameters were determined using the MTase-Glo™ Assay. The enzymatic reactions were performed in Greiner white flat-bottom 96-well plates in a final volume of 20 µL reaction mixture containing 3 µM PsmD_*Sa*, 5 µL 4X MTase-Glo™ reaction buffer (20 mM TRIS buffer, pH 8, 50 mM NaCl, 1 mM EDTA, 3 mM $MgCl_2$, 0.1 mg/mL BSA, 1 mM DTT) and various SAM and substrate **10** concentrations. The kinetic parameters were determined both for SAM and substrate **10**. In the case of the substrate kinetics, the concentration varied between 0 and 100 µM, while SAM concentration was kept constant at 40 µM. Conversely, for SAM kinetic parameters determination, the SAM concentration in the reaction mixture varied between 0 and 100 µM, while substrate concentration was kept constant at 50 µM. The reactions were performed according to the MTase-Glo™ kit and the mixtures were incubated at 45 °C in the case of PsmD_*Sa* and 35 °C for PsmD_*Sg*, and stopped after 5, 10 and 15 min

by adding 5 µL 0.5% TFA solution (v% in water). Further processing was performed according to the MTase-Glo™ kit and the SAH concentration was determined based on the standard calibration curve. Kinetic parameters were determined by non-linear regression using the standard Michaelis-Menten model.

7.5.7 Substrate scope evaluation for PsmD_*Sa*

The activity of PsmD_*Sa* towards the range of substrates was determined using the MTase-Glo™ Assay kit. The reactions were performed in Greiner white flat-bottom 96-well plates, in a total volume of 20 µL, containing 20 µM substrate, 30 µM SAM, 5 µL 4X MTase-Glo™ reaction buffer and 1 µg PsmD_*Sa*. The mixtures were incubated at 35 °C for 15 min, after which the reactions were quenched by adding 5 µL 0.5% TFA (v% in water) solution and the assay was performed further according to the MTase-Glo™ kit.

7.5.8 PsmD-HMT-coupled enzymatic reaction - Design of experiment

Design of experiment samples were prepared in reaction buffer (50 mM KP_i, pH 7.5), using 1 mM substrate **10** and variable concentrations of MeI (0.1-20.5 mM) and SAH (0-80 µM), as well as variable volumes of PsmD_*Sa* (0.05 U/mL) and *Ct*HMT (0.6 U/mL) lysates (volumes ranging from 25 to 350 µL), in a 500 µL final volume. A total of 15 µL of DMSO was present in all samples, used as solvent for MeI, SAH and substrate **10**. The samples were incubated for 16 h at 35°C and 700 rpm, after which the reaction was quenched and the product extracted with 2x 500 µL ethyl acetate. The samples were then analyzed via normal-phase HPLC, as previously described. The model used for data processing was a central composite design, from a total of 54 experiments. The validation of the model was performed using the same conditions and the predicted parameters for 10, 50 and 100% conversion. A temperature screening was performed using the predicted optimal parameters, incubating the reaction mixtures at 30, 35, 40 and 45 °C for 16 h and 700 rpm. The product was extracted with 2x 500 µL ethyl acetate and the samples were analyzed via normal phase HPLC as previously described. Experimental design and model computation were performed using Design Expert 12 (12.0.7.0). The experimental parameters can be found in Annex 8.6.

7.5.9 General procedure for PsmD-HMT coupled reactions in lysate format

E. coli BL21 (DE3) Δmtn cells containing the expressed PsmD and HMT were lysed according to the procedure described in Chapter 7.2.5. The lysate was always prepared shortly prior to

the combined enzymatic reaction. Unless specified otherwise, the reaction mixture contained 20% (v%) PsmD lysate, 14% (v%) HMT lysate, 1 mM substrate (supplemented from 200 mM stocks in DMSO) and 10 mM MeI (supplemented from 1 M stocks in DMSO) in 50 mM KP_i buffer, pH 7.5. The mixture was incubated at 35 °C and 700 rpm for 18 h. After the reaction, an extraction of the product and remaining substrate was performed with EtOAc, followed by the vacuum evaporation of the solvent. The conversion was analyzed by NP-HPLC or RP-HPLC.

7.5.10 Activity determination of lysates

7.5.10.1 PsmD_*Sa* lysate activity determination

PsmD_*Sa* lysate was prepared as previously described. 1 mL of mixture containing 200 µL PsmD_*Sa* lysate, 1 mM substrate **10** and 1 mM SAM in KP_i 50 mM, pH 7.5 buffer was incubated at 35 °C and 700 rpm. Samples were taken after 2, 5, 7 and 10 min and quenched with TFA 5% aqueous solution to a final concentration of 0.5%. The protein debris was removed by centrifugation at 15000 rpm for 10 min, and the supernatant was used directly in RP-HPLC measurements.

7.5.10.2 CtHMT lysate activity determination

*Ct*HMT lysate was prepared as previously described. 1 mL of mixture containing 100 µL *Ct*HMT lysate, 1 mM SAH and 5 mM MeI in KP_i 50 mM, pH 7.5 buffer was incubated at 35 °C and 700 rpm. Samples were taken after 2, 4, 6 and 8 min and quenched with TFA 5% aqueous solution to a final concentration of 0.5%. The protein debris was removed by centrifugation at 13000 x g for 10 min, and the supernatant was used directly in RP-HPLC measurements.

7.5.11 SAM derivative production using *Ac*HMT

The *Ac*HMT reaction for cofactor derivative production was performed in 50 mM KPi buffer, pH 7.5 containing 95 µM isolated *Ac*HMT, 7 mM SAH and 70 mM alkyl/allyl iodide (supplemented from a 7 M stock in DMSO). The mixture was incubated at 35 °C and 800 rpm for 2 h. After, the mixture was used as such as cofactor derivative supplement in reaction with PsmD. The cofactor derivatives were prepared immediately before their use in the PsmD reaction.

7.5.12 SAM derivative production using *Tk*MAT

The *Tk*MAT reaction for SAE production was performed in 100 mM TRIS buffer, pH 8 containing 20 mM $MgCl_2$, 200 mM KCl, 20 µM isolated *Tk*MAT, 7 mM ATP and 7 mM L-ethionine. The mixture was incubated at 50 °C and 800 rpm for 1 h. After, the mixture was used as such as cofactor derivative supplement in reaction with PsmD. The cofactor derivatives were prepared shortly before their use in the PsmD reaction.

7.5.13 PsmD reaction with SAM cofactor derivatives

The reaction mixture containing 20% (v%) SAE mix (either prepared using *Ac*HMT or *Tk*MAT), 30 µM isolated PsmD_*Sa* (or variant), 1 mM substrate **10** and 8 µM MTAN in 50 mM KP_i buffer, pH 7.5. The mixture was incubated at 37 °C and 1000 rpm for 17 h. After, the reaction was quenched with 5% (v%) TFA 5% solution and the samples were centrifuged at 1000 x g for 10 min. The supernatant was used directly in RP-HPLC analysis.

7.6 Analytical methods

7.6.1 Reverse-phase HPLC

Reverse phase HPLC was performed using a Jasco X-LC series device, equipped with a diode array; separation was achieved on a HyperClone 5µm ODS 120 Å (4 x 250 mm) C18 column. In the case of PsmD reactions using the natural substrate, distilled water and acetonitrile were used as eluents, using the following gradient sequence: min 0.00: 10% acetonitrile, 90% water; min 10.00: 20% acetonitrile, 80% water; min 12.00 20% acetonitrile, 80% water. For the evaluation of ethylation reactions, distilled water and acetonitrile were used as eluents, with the gradient sequence: min 0.00: 10% acetonitrile, 90% water; min 10.00: 20% acetonitrile, 80% water; min 12.00 20% acetonitrile, 80% water; min 17.00 20% acetonitrile, 80% water; min 18.00 10% acetonitrile, 90% water. The column was maintained at 40 °C during both types of measurements.

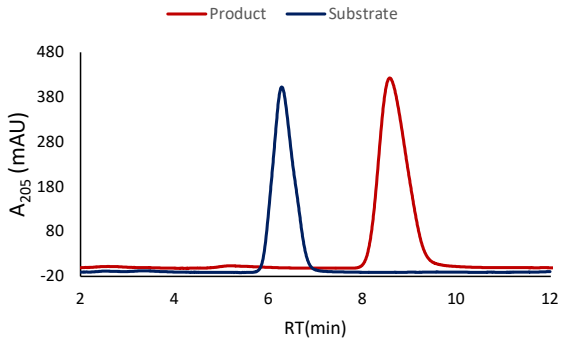

Figure 102. RP-HPLC chromatogram of PsmD substrate **10** (blue) and **P10** (red) standards. Conditions: HyperClone 5µm ODS 120A (4x250 mm) C18, water:acetonitrile gradient, 40 °C, 30 µL, 1 mL/min, UV 205 nm.

For SAM detection in HMT reactions, the mobile phase was a mix of MeOH and 50 mM NH_4CO_2H, pH 4.0, using the following gradient sequence: 0 min: 5% MeOH, 1 min: 5% MeOH, 7 min: 50% MeOH, 8 min: 100% MeOH, 10 min: 100% MeOH, 11 min: 5% MeOH at 25°C. The measurement was performed at 25 °C.

For the detection of SAE and other cofactor derivatives, the mobile phase was a mix of buffer A (10 mM NaH_2PO_4, 5 mM sodium 1-heptane sulfonate, pH 3.5, adjusted with phosphoric acid) and MeCN. The gradient sequence is: 0.00 min 95% A, 5% MeCN; 5.00 min 95% A, 5% MeCN; 20.00 min 80% A, 20% MeCN; 21.00 min 95% A, 5% MeCN; 23.00 min 95% A, 5% MeCN. The column temperature was kept at 25 °C.

In all cases, the injection volume was 30 µL and the flow rate was set at 1 mL/min.

7.6.2 Normal-phase HPLC

For the analysis of the enantioselectivity of PsmD variants, normal phase HPLC analysis was performed on a Lux Amylose-1, 250 x 4.6 mm, 5 µm column packed with a chiral stationary phase. 1 mM substrate, 2 mM SAM and 30 µg enzyme were mixed in Kp_i buffer (50 mM, pH 7.5) in a total volume of 200 µL. The reaction mixture was incubated at 40 °C and 800 rpm for 20 h. After incubation, the substrate and product were extracted with 3 x 200 µL ethyl acetate. After evaporation of the extraction solvent, the samples were solved in 200 mL elution solvent mixture (90:10 *n*-heptane:2-propanol). The samples were run through the column at a rate of 1 mL/min, using 20 µL injection volume, with detection at 205 nm for a total of 90 min per run.

7.6.3 LC-MS

LC-MS analysis was performed using a reverse phase HyperClone 5 µm ODS 120A (4x250 mM) C18 column coupled with an MS detector with electron spray ionization (ESI). The running conditions and solvent gradient sequences corresponded to the ones used in RP-HPLC analysis: water:acetonitrile gradient, 40 °C, 30 µL, 1 mL/min, UV 205 nm.

7.6.4 Mass spectrometry

High-resolution mass spectrometry (HRMS) was measured at the Heinrich Heine University in Düsseldorf using the Applied Biosystems MDS SCIEX QTrap 4000 with electron spray ionization (ESI). Low resolution mass spectrometry was performed on the Advion expression Compact Mass Spectrometer (CMS) using atmospheric pressure chemical ionization (APCI).

7.6.5 Colorimetric indole detection assay – general procedure

50 µL analyte aqueous solution was pipetted into a 96-well transparent microtiter plate. 50 µL H_2SO_4 98% was added to the analyte solution and the mixture was incubated at room temperature for 10 min. After, 50 µL DMAB solution in isopropanol (300 mM) was added to the mixture. The mixture was thoroughly mixed in a plate shaker at 800 rpm for 10 s. Thorough mixing is important in order to get homogenous mixtures – a lack of mixing leads to the formation of multiple phases, which can affect the spectrophotometric read-out. The plate was

exposed to 405 nm radiation for 10 min, using an LED lamp. After 10 min, the absorbance was measured using a Tecan® plate reader.

7.6.6 NMR spectroscopy/quantitative NMR

The NMR measurements were performed using an Advance/DRX 600 NMR Spectrometer (*Brucker Corp.*, USA). The measurements were performed at 297 K using samples solved in $CDCl_3$ or CD_3OD at 600 or 151 MHz. Quantitative NMR was performed to determine compound purity using trimethoxybenzene (TraceCERT, >99% purity, *Merck*) as an internal standard. The characteristic peaks of the standard were used as references and normalized to 100% and the purity of the target compound was calculated using the following formula:

$$Purity\ (\%) = \frac{I_a}{I_{std}} \cdot \frac{H_{std}}{H_a} \cdot \frac{M_a}{M_{std}} \cdot \frac{m_{std}}{m_a} \cdot P_{std}$$

I_a - Intensity of the analyte peak
I_{std} - Intensity of the analyte peak
H_{std} - number of protons in the standard signal
H_a - number of protons in the analyte signal
M_a - molecular mass of the analyte
M_{std} - molecular mass of the standard
m_{std} - weighted mass of standard
m_a - weighted mass of analyte
P_{std} - standard purity

7.6.7 Optical rotation analysis

The specific rotation of the enzymatically synthesized compounds was measured using a PerkinElmer 341 polarimeter using the sodium D-line at 589 nm in a 10 mm measuring cell. The compounds were solved in $CHCl_3$ to a final concentration of 10 mg/mL. 5 measurements were performed and the average value was determined. The average optical rotation was calculated using the following formula:

$$[\alpha]_\lambda^T = \frac{\alpha}{d \cdot c}$$

α – average measured optical rotation (degrees)
d – cuvette length (dm)
c – sample concentration (mg/mL)
T – temperature (°C)
λ – wavelength (nm)

7.6.8 Mass photometry

Mass photometry for the determination of the oligomeric state of PsmD proteins was performed by Nadiia Pozhydaeva (MPI Marburg), using a OneMP mass photometer (*Refeyn Ltd.*, Oxford, UK). The data acquisition was performed with AcquireMP (*Refeyn Ltd*. v.2.3). The movies were recorded at 1 kHz. The calibration of the instrument occurred directly before measurement using NativeMark Protein Standard (*ThermoFisher Scientific*, USA). The concentration of measured protein was adjusted to 100 nM in PBS buffer. The analysis of the data was performed using DiscoverMP software.

7.7 Colorimetric assay development

7.7.1 Time evolution of absorbance

50 µL solution of compound **10** or melatonin (**25**) 1 mM in KP_i buffer (50 mM, pH 7.5) was pipetted into a 96-well transparent microtiter plate. 50 µL H_2SO_4 98% was added to the analyte solution and the mixture was incubated at room temperature for 10 min. After, 50 µL DMAB solution in isopropanol (300 mM) was added to the mixture. The mixture was thoroughly mixed in a plate shaker at 800 rpm for 10 s. Afterward, the plate was exposed to 405 or 365 nm radiation for various amounts of time, using a LED or mercury UV lamp. After 10 min, the absorbance was measured using a Tecan® plate reader.

7.7.2 Light source analysis

50 µL solution of melatonin (**25**) 1 mM in KP_i buffer (50 mM, pH 7.5) was pipetted into a 96-well transparent microtiter plate. 50 µL H_2SO_4 98% was added to the analyte solution and the mixture was incubated at room temperature for 10 min. Then, 50 µL DMAB solution in isopropanol (300 mM) was added to the mixture. The mixture was thoroughly mixed in a plate shaker at 800 rpm for 10 s. Afterward, the plate was exposed to various radiation sources for 10 min, using either LED or UV lamps. A control mixture was incubated in the dark. After 10 min, the absorbance was measured using a Tecan® plate reader.

7.7.3 Acid and alcohol influence

To assess the influence of the acid type, the assay was performed with compound **10** and melatonin (**25**) according to the procedure described above, using different types of acids at their maximum possible concentration, with isopropanol as the solvent for DMAB. In the case of the alcohol screening, the optimized assay procedure was used with various pure alcohols as solvents for DMAB. The concentration of DMAB was 300 mM in all cases, and the acid used was H_2SO_4 98%. The negative controls contained all the components, except for the analyte.

7.7.4 DMAB concentration influence

To assess the influence of DMAB concentrations, the assay was performed according to the optimized procedure, using melatonin as a model analyte and various DMAB concentrations in isopropanol.

7.7.5 Buffer pH influence

Melatonin (**25**) was solved in different buffers to 1 mM final concentration and the assay was performed using the previously described procedure. For pH 5, sodium acetate 100 mM was used as buffer. KP_i 100 mM was used for pH 6, 7 and 8, and sodium bicarbonate for pH 9 and 10. Strong background coloration occurred when using TRIS buffer, after the DMAB supplementation. As such, TRIS buffer should be avoided for this analysis method, as it interferes with the assay.

7.7.6 Methyltransferase activity evaluation using the colorimetric assay

A reaction mixture containing 1 mM **10**, 2 mM *S*-adenosyl methionine (SAM) and 100 µg/mL isolated PsmD from *S. albulus* in Kp_i buffer (50 mM, pH 7.5) was incubated at 35 °C and 700 rpm. At different time points, samples were taken and the reaction was quenched with TFA (final concentration 0.5% v/v). Each sample was then analyzed using each of the optimized assay procedures. The substrate concentration was plotted against time and the slope was used to calculate enzymatic activity.

7.7.7 Methyltransferase mutant screening in whole cells

E. coli cells expressing PsmD WT, R85A and E35A as well as cells containing the empty pET21a(+) vector were resuspended in 500 µL reaction mixture containing 1 mM **10** and 2 mM SAM in KP_i buffer (50 mM, pH 7.5). A final OD_{600} of 6 was used in all cases. The mixtures were incubated at 35 °C and 700 rpm for 16 h. Afterward, the cells were separated from the mixture by centrifugation at 15000 rpm for 15 min. 50 µL (indole assay) or 200 µL (pyrroloindole assay) supernatants were then used in the respective optimized assay procedure. 200 µL of the supernatant were filtered and analyzed using RP-HPLC.

7.8 Substrate synthesis

7.8.1 Synthesis of the natural substrate (10)

7.8.1.1 Synthesis of N-(2-(5-(benzyloxy)-1H-indol-3-yl)ethyl)acetamide (14)

This synthesis step was performed by Lisa Guo, as part of her bachelor thesis project.
5 g (19.6 mmol) 2-(5-(benzyloxy)-1*H*-indol-3-yl) acetonitrile (**39**) were solved in 200 mL methanol at 0 °C on an ice bath. After, 3.6 mL (38.12 mmol) acetic anhydride and 3.95 g (30.5 mmol) $NiCl_2$ were added. Finally, 2.52 g (66.72 mmol) $NaBH_4$ was added carefully to the mixture. The reaction was incubated at 0 °C for 30 min. After, the mix was incubated overnight at room temperature. The reaction was monitored by thin layer chromatography (TLC) using EtOAc as solvent. After the completion of the reaction, the solvent was evaporated, the remaining solid was solved in 20 mL EtOAc, and the mixture was filtered. The filtrate was washed with 2 x10 mL saturated $NaHCO_3$ solution and brine. The two phases were separated and the organic phase was dried with $MgSO_4$. After filtration, the solvent was evaporated, and the product was isolated by column chromatography, using ethyl acetate as elution solvent. 1957 mg of product were obtained, corresponding to 33% yield.

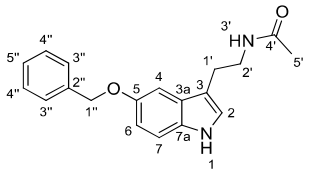

^{1}H-NMR (600 MHz; methanol-d4): δ [ppm] = 7.49 (d, $^3J_{3'', 4''}$ = 7.5 Hz, 2H, 3″-H), 7.38 (t, $^3J_{4'', 5''}$ = 7.5 Hz, $^3J_{4'', 3''}$ = 7.5 Hz, 2H, 4″-H), 7.31 (t, $^3J_{5'', 4''}$ = 7.4 Hz, 1H, 5″-H), 7.25 (d, $^3J_{7, 6}$ = 8.7 Hz, 1H, 7-H), 7.17 (d, $^4J_{4, 6}$ = 2.4 Hz, 1H, 4-H), 7.06 (s, 1H, 2-H), 6.85 (dd, $^3J_{6, 7}$ = 8.8, $^4J_{6, 4}$ = 2.4 Hz, 1H, 6-H), 5.11 (s, 2H, 1″-H), 3.45 (t, $^3J_{2',1'}$ = 7.4 Hz, 2H, 2′-H), 2.91 (t, $^3J_{1',2'}$ = 7.4 Hz, 2H, 1′-H), 1.93 (s, 3H, 5′-H).
^{13}C-NMR (151 MHz; methanol-d4) δ [ppm] = 173.26 (C-4′), 154.01 (C-5), 139.45 (C-2″), 133.66 (C-7a), 129.41 (C-4″), 129.12 (C-3a), 128.74 (C-5″), 128.70 (C-3″), 124.25 (C-2), 113.33 (C-6), 113.12 (C-3), 112.88 (C-7), 103.25 (C-4), 72.16 (C-1″), 41.47 (C-2′), 26.26 (C-1′), 22.62 (C-5′).
MS (APCI): m/z calculated for $C_{19}H_{20}N_2O_2$: 308.15 $[M]^+$ found: 308.9

7.8.1.2 Synthesis of N-(2-(5-hydroxy-1H-indol-3-yl)ethyl)acetamide (9)

This synthesis step was performed by Lisa Guo, as part of her bachelor thesis project.
1.92 g (30.47 mmol) ammonium formate and 414 mg (10% w/w) Pd/C were mixed in a round bottom flask. **41** was solved in 120 mL ethanol and added to the mixture. The reaction mix was stirred for 30 min at 120 °C, at reflux. After, the mixture was cooled down and filtered, and the

filtrate was washed with EtOAc. The solvent was then removed by evaporation. 1.658 mg crude product were obtained.

***N*-(2-(5-Hydroxy-1*H*-indol-3-yl)ethyl)acetamide (*N*-acetylserotonin) (9)**

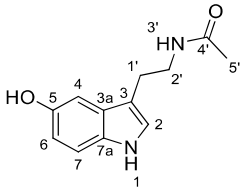

^{1}H-NMR (600 MHz; methanol-d4): δ [ppm] = 8.00 (s, 1H, 1-H), 7.17 (d, $^{3}J_{7,6}$ = 8.6 Hz, 1H, 7-H), 7.02 (s, 1H, 2-H), 6.94 (d, $^{4}J_{4,6}$ = 2.4 Hz, 1H, 4-H), 6.68 (dd, $^{3}J_{6,7}$ = 8.6, $^{4}J_{6,4}$ = 2.4 Hz, 1H, 6-H), 3.45 (t, $^{3}J_{2',1'}$ = 7.3 Hz, 2H, 2′-H), 2.87 (t, $^{3}J_{1',2'}$ = 7.3 Hz, 2H, 1′-H), 1.93 (s, 3H, 5′-H).
^{13}C-NMR (151 MHz; methanol-d4) δ [ppm] = 173.26 (C-4′), 151.13 (C-5), 133.11 (C-7a), 129.48 (C-3a), 124.19 (C-2), 112.64 (C-7), 112.52 (C-3), 112.36 (C-6), 103.48 (C-4), 41.45 (C-2′), 26.26 (C-1′), 22.59 (C-5′).
MS (APCI): m/z calculated for $C_{17}H_{23}N_3O_3$+H$^+$: 219.105 [M+H]$^+$; found: 219.2.

7.8.1.3 Synthesis of 3-(2-acetamidoethyl)-1H-indol-5-yl methylcarbamate (10)

All steps were performed under inert conditions. 500 mg **9** were solved in 20 mL dry THF under N_2 atmosphere. 1.59 mL (11.45 mmol) triethylamine were added to the mixture and stirred at room temperature for 30 min. 28 mg (0.23 mol) DMAP were then added, followed by 428 mg (4.58 mmol) methylcarbamoyl chloride. The reaction mixture was incubated at 45 °C under inert atmosphere, overnight. The reaction progress was analyzed via TLC, using petrol ether:EtOAc (1:1) as elution system. Afterwards, the reaction was quenched with KP_i buffer (50 mM, pH 7.5) until the mixture clarified. The product was extracted 3 times with EtOAc and dried on $MgSO_4$. The solid was filtered, and the solvent evaporated. The product was isolated using flash chromatography with EtOAc containing 2.5 % (v%) MeOH as elution system. The product was obtained as a white solid. Multiple batches of compound **10** were synthesized, with overall yields ranging between 38 and 47%.

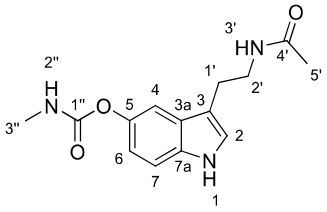

^{1}H-NMR (600 MHz; MeOD): δ [ppm] = 7.31 (d, $^{3}J_{7,6}$ = 8.7 Hz, 1H, 7-H), 7.27 (d, $^{4}J_{4,6}$ = 2.3 Hz, 1H, 4-H), 7.13 (s, 1H, 2-H), 6.85 (dd, $^{3}J_{6,7}$ = 8.6, $^{4}J_{6,4}$ = 2.3 Hz, 1H, 6-H), 3.45 (t, $^{3}J_{2',1'}$ = 7.3 Hz, 2H, 2′-H), 2.92 (t, $^{3}J_{1',2'}$ = 7.3 Hz, 2H, 1′-H), 2.81 (s, 3H, 3″-H), 1.92 (s, 3H, 5′-H).
^{13}C-NMR (151 MHz; MeOD) δ [ppm] = 173.30 (C-4′), 159.09 (C-1″), 145.55 (C-5), 135.80 (C-7a), 129.00 (C-3a), 124.95 (C-2), 116.87 (C-6), 113.66 (C-3), 112.44 (C-7), 111.67 (C-4), 41.54 (C-2′), 27.62 (C-3″), 26.12 (C-1′), 22.59 (C-5′)
HRMS (ESI): m/z calculated for $C_{14}H_{17}N_3O_3$+H^+: 276.1343 [M+H]$^+$; found: 276.1350

The ^{1}H and ^{13}C NMR data are in accordance with the data previously described in the literature.[358]

7.8.2 Synthesis of *t*-Bu amide PsmD substrate (23)

7.8.2.1 Synthesis of N-(2-(5-(benzyloxy)-1*H*-indol-3-yl)ethyl)pivalamide (41)

500 mg (1.9 mmol) 2-(5-(benzyloxy)-1*H*-indol-3-yl) acetonitrile (**39**) were solved in 20 mL methanol at 0 °C on an ice bath. 816 µL (3.8 mmol) di-tert-butyl dicarbonate, and 395 mg (3.05 mmol) $NiCl_2$ were added followed by 505 mg (13.3 mmol) $NaBH_4$. The reaction was incubated with stirring at 0 °C for 30 min. After, the reaction mix was incubated for 4 h at room temperature. The reaction was monitored by TLC (eluent: EtOAc). After, the solvent was removed by evaporation and the remaining solid was solved in 20 mL EtOAc followed by filtration. The filtrate was washed twice with 10 mL saturated $NaHCO_3$ solution and 10 mL brine. The two phases were separated and the organic phase was dried with $MgSO_4$. After filtration, the solvent was evaporated. The product was separated by flash column chromatography (solvent: EtOAc). 298 mg (0.85 mmol) product were obtained as a white powder, corresponding to a 44% yield.

***N*-(2-(5-(Benzyloxy)-1*H*-indol-3-yl)ethyl)pivalamide (41)**

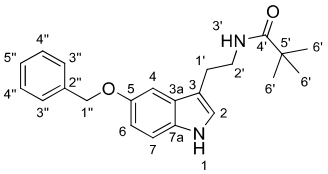

^{1}H-NMR (600 MHz, methanol-d4): δ[ppm] = 7.48 (d, $^{3}J_{3'',4''}$ = 7.3 Hz, 2H, 3''-H), 7.37 (t, $^{3}J_{4'',3''}$ = 7.6 Hz, $^{3}J_{4'',5''}$ = 7.6 Hz, 2H, 4''-H), 7.30 (t, $^{3}J_{5'',4''}$ = 8.0 Hz, 1H, 5''-H), 7.22 (d, $^{3}J_{7,6}$= 8.7 Hz, 1H, 7-H), 7.17 (s, 1H, 4-H), 7.03 (s, 1H, 2-H), 6.83 (d, $^{3}J_{6,7}$= 11.2 Hz, 1H, 6-H), 5.10 (s, 2H, 1''-H), 3.29 (t, $^{3}J_{2',1'}$ = 7.5 Hz, 2H, 2'-H), 2.85 (t,$^{3}J_{1',2'}$= 7.4 Hz, 2H, 1'-H), 1.43 (s, 9H, 6'-H).
^{13}C NMR (151 MHz, methanol-d4): δ[ppm] = 158.54 (C-4'), 154.00 (C-5), 139.46 (C-2''), 133.63 (C-7a), 129.41 (C-4''), 129.16 (C-5''), 128.77 (C-3a), 128.70 (C-3''), 124.24 (C-2), 113.26 (C-

6), 112.82 (C-7), 103.33 (C-4), 79.89(C-5'), 72.16 (C-1''), 42.45 (C-2'), 28.80 (C-6'), 26.94 (C-1').
MS (ESI): m/z calculated for $C_{17}H_{23}N_3O_3$+K^+: 389.163, $[M+K]^+$ found: 389.3.

7.8.2.2 Synthesis of N-(2-(5-hydroxy-1*H*-indol-3-yl)ethyl)pivalamide (42)

252 mg (3.99 mmol) ammonium formate and 85 mg (10% w/w) Pd/C were mixed in a round bottom flask. 280 mg (0.8 mmol) **41** was solved in 20 mL ethanol and added to the mixture. The reaction mix was incubated for 30 min at 120 °C, at reflux. After cooling, the mixture was filtered, and the filtrate was washed with EtOAc. The solvent was then removed by evaporation, obtaining 174 mg crude product. The crude mixture was used in the following step.

7.8.2.3 Synthesis of 3-(2-pivalamidoethyl)-1*H*-indol-5-yl methylcarbamate (23)

All steps were performed under inert conditions. The crude **42** was solved in 15 mL dry THF under N_2 atmosphere. 461 µL (3.31 mmol) triethylamine were added to the mixture and stirred at room temperature for 30 min. 8.16 mg (0.07 mmol) DMAP was then added, followed by 247 mg (2.65 mmol) methylcarbamoyl chloride. The reaction mixture was incubated at 45 °C under inert atmosphere overnight. The reaction progress was analyzed via TLC, using petrol ether:EtOAc (1:1) as elution system. Afterwards, the reaction was quenched with KP_i buffer (50 mM, pH 7.5) until the mixture clarified. The product was extracted 3 times with EtOAc and dried on $MgSO_4$. The solid was filtered, and the solvent evaporated. The product was isolated via flash chromatography using EtOAc containing 2.5 % (v%) MeOH as elution system. 105 mg of product **23** were obtained as a white solid, corresponding to 50% yield.

3-(2-pivalamidoethyl)-1*H*-indol-5-yl methylcarbamate (23)

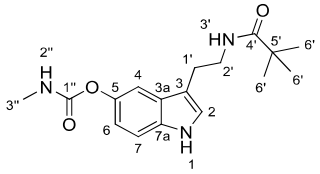

^{1}H-NMR (600 MHz, methanol-d4): δ[ppm] = 7.31 – 7.24 (m, 2H, 7-H, 4-H), 7.09 (s, 1H, 2-H), 6.83 (d, $^3J_{6,7}$ = 8.7 Hz, 1H, 6-H), 3.29 (t, $^3J_{2',1'}$ = 6.8 Hz, 2H, 2'-H), 2.86 (t, $^3J_{1',2'}$ = 7.3 Hz, 2H, 1'-H), 2.79 (s, 3H, 3''-H), 1.43 (s, 9H, 6'-H).
^{13}C NMR (151 MHz,methanol-d4): δ[ppm] = 158.96 (C-1''), 158.37 (C-4'), 145.34 (C-5), 135.64 (C-7a), 128.89 (C-3a), 124.82 (C-2), 116.69 (C-6), 113.67 (C-3), 112.24(C-7), 111.67 (C-4), 79.75 (C-5'), 42.35 (C-2'), 28.64(C-6'), 27.49 (C-3''), 26.63 (C-1').
MS (ESI): m/z calculated for $C_{17}H_{23}N_3O_3$+K^+: 356.137 $[M+K]^+$; found: 356.3.

The ^{1}H and ^{13}C NMR data are in accordance with the data previously described in the literature.[358]

7.8.3 Synthesis of Phe-carbamate PsmD substrate (19)

7.8.3.1 Synthesis of *N*-(2-(5-(benzyloxy)-1*H*-indol-3-yl)ethyl)acetamide (14)

500 mg 2-(5-(benzyloxy)-1*H*-indol-3-yl) acetonitrile (**39**) were solved in 20 mL methanol at 0 °C on an ice bath. After, 511 mg (3.81 mmol) acetic anhydride and 395 mg (3.05 mmol) $NiCl_2$ were added. Finally, 505 mg (13.3 mmol) $NaBH_4$ were added carefully. The reaction was incubated at 0 °C for 30 min. After, the reaction mix was incubated overnight at room temperature. The reaction was monitored by TLC (solvent: EtOAc). After, the solvent was evaporated, the remaining solid was solved in 20 mL EtOAc, and the mixture was filtered. The filtrate was washed with 2 x 10 mL saturated $NaHCO_3$ solution and brine. The two phases were separated and the organic phase was dried with $MgSO_4$. After filtration, the solvent was evaporated, obtaining 573 mg of a brown oil. The crude product was used directly in the next step.

7.8.3.2 Synthesis of *N*-(2-(5-hydroxy-1*H*-indol-3-yl)ethyl)acetamide (9)

511 mg (8.11 mmol) ammonium formate and 172 mg (10% w/w) Pd/C were mixed in a round bottom flask. 500 mg crude **41** was solved in 20 mL ethanol and added to the mixture. The reaction mix was stirred for 30 min at 120 °C, at reflux. After, the mixture was cooled down and filtered, and the filtrate was washed with EtOAc. The solvent was then removed by evaporation. The product was purified by flash chromatography, using EtOAc with 7% (v%) MeOH for elution. 205 mg of product were obtained as a white powder, corresponding to a 57% yield.

***N*-(2-(5-Hydroxy-1*H*-indol-3-yl)ethyl)acetamide (*N*-acetylserotonin) (9)**

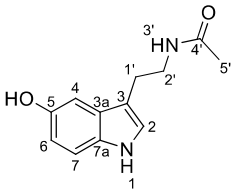

^{1}H-NMR (600 MHz, methanol-d4): δ[ppm] = 7.15 (d, $^{3}J_{7,6}$ = 8.6 Hz, 1H, 7-H), 6.99 (s, 1H, 2-H), 6.93 (d, $^{4}J_{4,6}$= 2.4 Hz, 1H, 4-H), 6.67 (dd, $^{3}J_{6,7}$ = 8.6, $^{3}J_{6,4}$ =2.5 Hz, 1H, 6-H), 3.42 (t, $^{3}J_{2',1'}$ = 7.4 Hz, 2H, 2'-H), 2.85 (t, $^{3}J_{1',2'}$ = 7.4 Hz, 2H, 1'-H), 1.91 (s, 3H, 5'-H).

^{13}C NMR (151 MHz, methanol-d4): δ[ppm] = 173.26 (C-4'), 151.09 (C-5), 133.07 (C-7a), 129.48 (C-3a), 124.20 (C-2), 112.66 (C-3), 112.49 (C-4), 112.35 (C-6), 103.47 (C-7), 41.43 (C-2'), 26.22 (C-1'), 22.59 (C-5').
MS (ESI): m/z calculated for $C_{17}H_{23}N_3O_3$+H$^+$: 219.1055 [M+H]$^+$; found: 219.2.

7.8.3.3 Synthesis of 3-(2-acetamidoethyl)-1*H*-indol-5-yl phenylcarbamate (19)

All steps were performed under inert conditions. 213 mg (2.11 mmol) triethylamine and 163 mg (0.7 mmol) **9** were solved in 4 mL dry THF and stirred under N_2 atmosphere for 15 min. 92 mg (0.77 mmol) phenyl isocyanate was added dropwise over 5 s and then 17 mg (0.14 mmol) DMAP was added. After stirring for 30 min at 23 °C, the reaction was quenched with saturated aqueous ammonium chloride solution (20 mL). The product was extracted with EtOAc (3 × 15 mL). The combined organic layers were washed with brine, dried over Na_2SO_4 and concentrated under reduced pressure. The resulting residue was purified by flash chromatography (9:1 DCM/MeOH). 151 mg **17** were obtained as a white powder, corresponding to a 61% yield.

3-(2-acetamidoethyl)-1H-indol-5-yl phenylcarbamate (19)

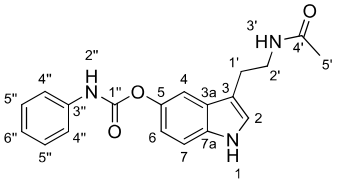

^{1}H-NMR (600 MHz, methanol-d4): δ[ppm] = 7.50 (d, $^3J_{4'',5''}$ = 7.7 Hz, 2H, 4''-H), 7.37 – 7.27 (m, 4H, 7-H, 4-H, 5''-H), 7.14 (s, 1H, 2-H), 7.05 (t, $^3J_{6'',5''}$ = 7.4 Hz, 1H, 6''-H), 6.92 (dd, $^3J_{6,7}$ = 8.6 Hz, $^3J_{6,4}$ = 2.3 Hz, 1H, 6-H), 3.45 (t, $^3J_{2',1'}$ = 7.3 Hz, 2H, 2'-H), 2.92 (t, $^3J_{1',2'}$ = 7.3 Hz, 2H, 1'-H), 1.91 (s, 3H, 5'-H).
^{13}C NMR (151 MHz, methanol-d4): δ[ppm] = 173.34 (C-4'), 155.55 (C-1''), 145.14 (C-5), 140.07 (C-6''), 135.92 (C-7a), 129.90 (C-4''), 129.07 (C-3a), 125.05 (C-2), 124.31 (C-3''), 119.94 (C-5''), 116.87 (C-6), 113.73 (C-3), 112.5 (C-4), 111.8 (C-7), 41.5 (C-2'), 26.1 (C-1'), 22.6 (C-5').
MS (ESI): m/z calculated for $C_{19}H_{19}N_3O_3$+H$^+$: 338.1426 [M+H]$^+$; found: 338.3.

The ^{1}H and ^{13}C NMR data are in accordance with the data previously described in the literature.[358]

7.9 Automated mutant library screening

The protein expression module and enzymatic reaction module were run on an automated platform using a SpiNNaker2 BT (*Thermo Scientific*, Canada) for all material transfer between devices and the process was orchestrated by the Momentum Software (*Thermo Scientific*, Canada). The activity assay module was performed using an OT-2 liquid handler (*Opentrons*, USA).

7.9.1 Expression module

Per library, 66 colonies resulting from the mutant library transformation were picked using a liquid handler (Tecan Fluent, *Tecan*, Switzerland) with integrated colony picker (Pickolo, *SciRobotics*, Israel) and used to inoculate 900 µL of LB media in a square well deep well plate (sqDWP). Additionally, controls were carried on each plate. Cells transformed with WT PsmD_*Sa* were used as positive and cells transformed with the empty pET21a(+) vector as negative control. After incubation for 16 hours at 800 rpm and 37°C in an automated incubator (Cytomat2, Thermo Scientific, Germany), 10 µL of the precultures were transferred to fresh a sqDWP to inoculate 900 µL TB-autoinduction media and were incubated for another 24 hours before being passed down to the enzymatic reaction module. The TB media contained additionally 0.5% (w/v) glycerol, 0.05% (w/v) glucose and 0.2 (w/v) lactose for auto-induction.

7.9.2 Enzymatic reaction module

After cultivation, the cells were separated by centrifugation for 5 minutes at 3500 rpm (Rotanda 450R, *Hettich*, Germany) and the TB medium was removed using the liquid handler. The cells were resuspended in 200 µL freshly prepared reaction mixture containing 1 mM substrate (100 mM stocks in DMSO were used, leading to 1% v/v DMSO content in the final mixture) and 2 mM SAM in KP_i buffer (50 mM, pH 7.5). The reaction was performed in sqDWP at 40°C for 24, 7 or 3 hours in an automated incubator (Cytomat 10, *Thermo Scientific*, Germany). After the reaction, the cells were quenched by addition of 20 µL 5% TFA and separated via centrifugation. 100 µL of the supernatant was transferred to a fresh microtiter plate (MTP) and stored at -20 °C until further use.

7.9.3 Activity assay module

For the activity assay, 50 µL of the supernatant resulting from the enzymatic reaction module were mixed with 50 µL H_2S0_4 98% and incubated for 30 minutes at room temperature. After, 50 µL DMAB solution (300 mM in isopropanol) were added to each well, mixing thoroughly.

After another 1 h incubation step at room temperature, the absorbance at 580 nm was measured using a plate reader. Heat maps were generated based on absorbance values and the cells providing the lowest absorbance at 580 nm were subjected to plasmid isolation and sequencing.

7.10 Computational methods

7.10.1 Structure visualization and analysis

The visualization and analysis of 3D protein structures, as well as the analysis of the molecular docking results was performed using UCSF Chimera.[421]

7.10.2 Homology model generation and structure editing

The homology model of WT PsmD_*Sa* was generated by Dr. Benoit David (IBG-4, Forschungszentrum Jülich) using Modeller and the crystal structure of PsmD_*Sg* in the closed conformation as template.[2, 372] The mutant models were generated by the author by replacing residue W166 using the rotamer function in UCSF Chimera. The conformation of the new residue was chosen from the Dunbrack 2010 library, based on the highest probability.[422]

7.10.3 Molecular docking

For the docking of the natural substrate in the catalytic sites of PsmD_*Sg* and PsmD_*Sa*, the docking predictions were performed using the Schrödinger software suite (2021-4). Before docking, the modeled protein structures in open and closed conformations were prepared using the prepwizard module and the substrate was prepared using the ligprep module (version 57156) at pH 7.4. The Glide module (version 90156) with the OPLS_2005 force field and the SP docking precision mode were used. To keep the C3 atom of the substrate close to the methyl group (C9 atom) of the SAM cofactor, a distance restraint was enforced within a radius of 3 Å from the center of mass calculated between the two atoms. This experiment was performed by Dr. Benoit David (IBG-4, Forschungszentrum Jülich) and made available for this work.

An extensive docking within the active site of PsmD_*Sa* wt, W166P, and W166C has been performed by docking the substrates **21** and **17** using *AutoDock Vina* (V1.2.3), employing the *Vinardo* scoring function.[452] The configuration parameters were:

```
center_x = 38.45; center_y = 41.65; center_z = 43.62; size_x = 20.90;
size_y = 25.30; size_z = 32.27; scoring = vinardo; energy_range = 3;
exhaustiveness = 8; num_modes = 50; cpu = 11
```

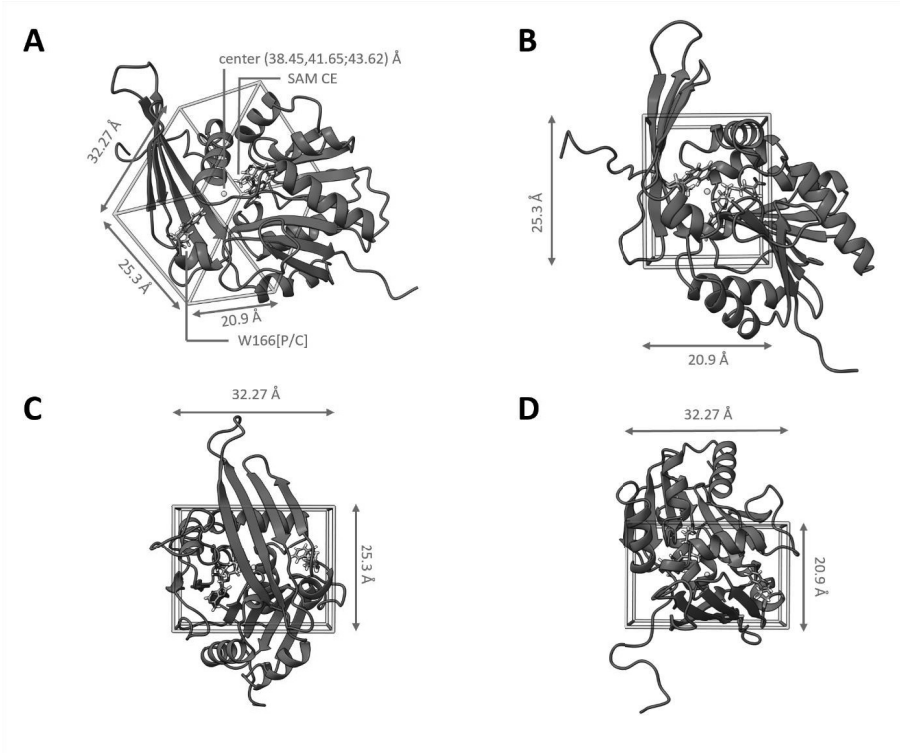

Figure 103. Docking box size and position within the structure of PsmD_*Sa*. A. Perspective overview. The center of the box is shown as a grey sphere juxtaposed with the reactive methyl group of SAM. W166 is shown explicitly superimposing tryptophan, proline, and cysteine. **B-C –** Orthogonal, axial perspectives. The figure was produced for [3] and used without modifications according to the CC licensing of the Royal Society of Chemistry.

The energy range has been set to be restrictive (3 kcal/mol). Each docking could yield 50 poses. To probe the conformational space allowing for quantitative analysis, each docking combination ([**2a**,**3a**]x[wt,W166C,W166P]) has been repeated 40 times. Scripting/coding in bash, python, Windows PowerShell, and UCSF Chimera were supported by ChatGPT, as implemented in the search engine Ecosia. The molecular docking in Autodock Vina and post-processing were performed by Dr. Thomas Classen (Institute of Bioorganic Chemistry, Heinrich Heine University Düsseldorf) and made available for this work.

7.10.4 Docking post-processing

For the comparative analysis, the dimensionality of the data set has been reduced by selecting pivotal atoms only representing the entire degree of freedom of the conformation. In total, the conformation could be represented by 11 atoms for substrates **17** and **21** together, leading to a 33-dimensional data set. This reduced data set of 11567 poses was subjected to principal component analysis, independent of substrate type or enzyme docked into, extracting three principal components resembling 67% (PC1), 9% (PC2), and 6% (PC3) of the entire variance. This was done to make the data set readable, representing the conformational space in a 3D manner.

The three-dimensional conformational data set (principal component) has been clustered by distance into 10 clusters. These clusters represent different types of binding poses. The putative productive binding pose was selected based on the structural and mechanistic information previously acquired for the homolog PsmD_*Sg*.[1] Within the obtained data set, the productive binding pose corresponds to cluster 6. Various information such as substrate membership, enzyme environment, binding energy, distance between nucleophile and electrophile could be projected onto the data set.

The molecular docking in Autodock Vina and post-processing were performed by Dr. Thomas Classen (Institute of Bioorganic Chemistry, HHU Düsseldorf) and made available for this work. The interpretation of the obtained data was performed by the author, in collaboration with Dr. Thomas Classen.

7.10.5 Molecular dynamics simulations

MD simulations of the dimeric structure of the selected PsmD_*Sa* models in complex with both the SAM cofactor and the docked substrate poses were performed using the pmemd.MPI (minimizations) and pmemd.cuda[12] (solvent relaxation and MD productions) modules of the AMBER20 package.[13] The ff14SB[14] and gaff2[15] force fields were used to describe the protein and the ligand respectively. The TIP3P water model[16] was used and 18 sodium ions were added to the solvent to neutralize the net charge of the protein. The protonation states of histidine and acidic residues were assigned using PROPKA 3.0.[17] The resulting system was minimized in four stages of 15000 steps each, including 5000 steepest-descent iterations and 10000 conjugate-gradient iterations. Positional restraints applied on the protein were gradually decreased at each stage from 10 to 5, 2.5 and 0 kcal/mol/Å^2 respectively, while keeping water, ions and ligands unrestrained. The Particle Mesh Ewald algorithm[18] was used to treat long-range electrostatic interactions defined beyond a 9 Å inter-atomic distance cutoff.

The system was thermalized (NVT) for 500 ps at 300K and pressurized (NPT) for 10 ns at 1 bar using a positional restraint of 10 kcal/mol/Å^2 on all protein and ligands atoms. Unrestrained MD production runs were performed using a 2 fs time step. All subsequent analyses were conducted using the CPPTRAJ program[19]. MD snapshots were saved every 40 ps and the first 12 ns of production were excluded from all analyses. The MD simulations were performed by Dr. Benoit David (IBG-4, Forschugszentrum Jülich) and made available for this work.

7.10.6 Residue conservation analysis

The conservation scores were derived using the WebLogo server[22] taking as input a multiple sequence alignment (MSA) of 39 sequences built using the MAFFT-L-INS-i algorithm[23] implemented in the ConSurf server[24,25]. Homologous sequences to PsmD_*Sa* were searched in the UniRef90 database[26] using psi-BLAST[27] and only those presenting a pair-wise sequence identity between 40% and 90% were considered. The residue conservation analysis was performed by Dr. Benoit David (IBG-4, Forschugszentrum Jülich) and made available for this work.

7.11 Preparative scale enzymatic methylation

7.11.1 Preparative methylation using the PsmD-HMT system – 50-100 mg scale

*Ct*HMT (0.3 U/mL) and PsmD_Sa (0.1 U/mL) lysates were freshly prepared according to the previously described procedure and used immediately. 49 mL of HMT lysate and 73 mL PsmD lysate were combined and diluted with 239 mL buffer (50 mM KP_i, pH 7.5). Compound **10** was added (1.82 mL of 200 mM stock solution in DMSO) to a final concentration of 1 mM. MeI was then added (10 M stock in DMSO) to a final concentration of 10 mM. When using 2 mM substrate, the MeI concentration was increased to 20 mM and the final volume was 182 mL, containing 14% (v%) HMT lysate and 20% (v%) PsmD volume. The reactions were performed in closed glass bottles (*Schott Duran*) at 35 °C and 300 rpm for 16 h. The reactions were quenched by adding 150 mL of saturated aqueous ammonium chloride solution. The precipitated protein debris was separated from the mixture by vacuum filtration on Celite. The product was then extracted from the filtrate with 3 x 500 mL ethyl acetate. The reunited organic fractions were washed with brine, dried over $MgSO_4$ and filtered in vacuum. The solvent was evaporated and purification of the product was performed via flash chromatography, using a mixture of ethyl acetate:methanol (95:5) for elution. After solvent evaporation, 52-57 mg of product in the form of a white solid was obtained (90% qNMR purity).

(3a*S*)-1-acetyl-3a-methyl-1,2,3,3a,8,8a-hexahydropyrrolo[2,3-b]indol-5-yl methylcarbamate (P10)

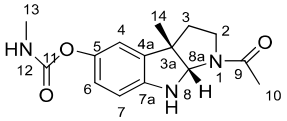

1H-NMR (600 MHz, chloroform-d): δ[ppm] = 6.85 (s, 1H, 4-H), 6.80-6.76 (m, 1H, 6-H), 6.52 (d, $^3J_{7,6}$= 8.3 Hz, 1H, 7-H), 5.17 (s, 1H, 8a-H), 3.57 (t, 1H, $^3J_{2,3}$ = 8.3 Hz, 1H, 2-H), 3.28-3.23 (m, 1H, 2-H), 2.88 (d, $^3J_{13,12}$ = 5.0 Hz, 3H, 13-H), 2.29 (dd, $^3J_{3,2}$=12.9, $^4J_{3,14}$= 5.7 Hz, 1H, 3-H), 2.14-2.05 (m, 1H, 3-H), 2.00 (s, 3H, 10-H),1.40 (s, 3H, 14-H).

13C NMR (151 MHz, chloroform-d): δ[ppm] = 170.58 (C-9), 156.36 (C-11), 146.51 (C-7a), 144.18 (C-5), 134.31 (C-4a), 121.57 (C-6), 116.68 (C-4), 109.74 (C-7), 82.82 (C-8a), 52.82 (C-3a), 47.72 (C-2), 37.46 (C-3), 28.08 (C-13), 24.46 (C-14), 22.98 (C-10).
MS (APCI): m/z calculated for $C_{15}H_{19}N_3O_3$+H^+: 290.1 $[M+H]^+$; found: 290.0.

The ^{1}H and ^{13}C NMR data are in accordance with the data previously described in the literature.[1,37]

7.11.2 Preparative methylation using the PsmD-HMT system – 1 g scale

1.05 g substrate **10** (1 equiv. final concentration 2 mM), 2.38 mL MeI (10 equiv. final concentration 20 mM) and 559 mg EDTA (final concentration 1 mM) were mixed with 1.87 L KP_i buffer (50 mM, pH 7.5) in a 2 L Shott Duran closed glass bottle. 15 g *E. coli* BL21 Δmtn cells containing the expressed *Ct*HMT and 30 g *E. coli* BL21 Δmtn cells containing the expressed PsmD_*Sa* were sealed together in a dialysis bag. The bag containing the cells was suspended in the liquid reaction mixture using straw rope, avoiding contact with the bottom of the flask. The flask was incubated in an orbital shaker for 21 h at 30 °C and 100 rpm. In an attempt to improve conversion, after 21 h a fresh identical cell-containing dialysis bag was added to the mixture and the flask was placed on a water bath at 35 °C with magnetic stirring. The reaction progression was monitored by TLC, using DCM with 10% MeOH as elution system and cerium molybdate stain for visualization. After another 19 h of incubation, the remaining MeI was quenched by adding 20 equiv. ammonium thiosulfate and incubating the mixture under magnetic stirring for 1.5 h. The dialysis bags were removed from the mixture and incubated in EtOAc for 48 h. The product was extracted from the remaining reaction volume two times with 2 L EtOAc the organic phases were mixed with the solvent in which the dialysis bags were incubated, dried with $MgSO_4$, then filtered under vacuum. The solvent was removed by rotary evaporation and the product was purified using flash chromatography. Due to poor separation, two separate column purifications were performed. The first used DCM with 2.5% (v%) MeOH as elution system, while the second purification was performed using EtOAc as eluent. In the end, 496 mg of white solid product were obtained with 74% purity (qNMR). The gram scale enzymatic methylation was performed by Lisa Guo (HHU, Düsseldorf), as part of her bachelor thesis project.

7.11.3 Immobilization of PsmD_*Sa* and *Ct*HMT on Ni-NTA resin

After protein expression, lysates were prepared using 0.2 g *E. coli* BL21 Gold (DE3) cells containing W166C mutant/mL buffer (Kp_i 50 mM, pH 7.5). 10% (v/v) Ni-NTA agarose resin (*Protino*, Germany) slurry was added to the lysate and the mixture was incubated on ice for 1 h, mixing gently by rotation. The mixture was then centrifuged for 2 min at 3000 rpm, the supernatant removed and the resin was resuspended in washing buffer (KP_i 50 mM, 50 mM imidazole, pH 7.5) and incubated on ice for 5 min. The mixture was centrifuged 2 min at 3000 rpm and the previous washing step was repeated. The resin was then washed once with reaction buffer (KP_i 50 mM, pH 7.5) and was separated by centrifugation to be used in the preparative reaction. The immobilization of *Ct*HMT was performed using the same procedure.

7.11.4 Preparative methylation using immobilized PsmD(W166C)-HMT

The preparative enzymatic methylation of substrate **21** was performed using the mutant W166C and *Ct*HMT immobilized on Ni-NTA resin. 3.2 mL resin slurry containing immobilized W166C and 2.2 mL resin slurry containing *Ct*HMT were mixed and resuspended in 79 mL reaction mixture containing 50 mg substrate **21** (2 mM final concentration, added from 200 mM stock in DMSO), 0.2 mM SAH, 10 mM MeI (added from a 10 M stock in DMSO) in KP_i buffer (50 mM, pH 7.5). The mixture was incubated at 35 °C and 300 rpm for 15 h. After, the Ni-NTA resin was separated by centrifugation and the product was extracted from the supernatant with 3 x 100 mL ethyl acetate. The organic phase was then washed with brine and dried with $MgSO_4$. After filtration and solvent evaporation, the product was isolated by column chromatography using a DCM:MeOH (9:1) mixture for elution. The product was obtained as a white powder, with 60% yield.

(3a*S*,8a*S*)-3a-methyl-1-pivaloyl-1,2,3,3a,8,8a-hexahydropyrrolo[2,3-*b*]indol-5-yl methylcarbamate (P23)

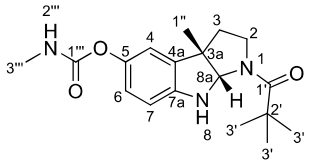

^{1}H-NMR (600 MHz, methanol-d4): δ[ppm] = 6.83 (s, 1H, 6-H), 6.73 (d, $^3J_{7,6}$ = 8.3 Hz, 1H, 7-H), 6.65 – 6.55 (m, 1H, 4-H), 5.02 (s, 1H, 8a-H), 3.65 – 3.56 (m, 1H, 2-H), 3.05 – 2.97 (m, 1H, 2-H), 2.76 (s, 3H, 3'''-H), 2.20 (q, $^4J_{3,1''}$ = 6.1 Hz, 1H, 3-H), 2.08 – 1.99 (m, 1H, 3-H), 1.53 (s, 5H, 3'-H), 1.46 (s, 4H, 3'-H), 1.39 (s, 3H, 1''-H).
^{13}C NMR (151 MHz,methanol-d4): δ[ppm] = 158.63 (C-1'''), 156.20 - 155.67 (C-1'), 147.72 (C-7a), 145.49 (C-5), 136.14 - 136.06 (C-4a), 122.28 (C-7), 117.50 (C-6), 110.44 (C-4), 83.84 (C-8a), 81.65 – 81.19 (C-2'), 55.20-54.32 (C-3a), 47.16 - 46.56 (C-2), 38.17 - 37.93 (C-3), 28.72 (C-3'), 27.73 (C-3'''), 24.92 - 24.65 (C-1'').
MS (ESI): m/z calculated for $C_{18}H_{25}N_3O_3$+K^+: 370.153 $[M+K]^+$; found: 370.3.

The ^{1}H and ^{13}C NMR data are in accordance with the data previously described in the literature.[358]

7.11.5 Preparative enzymatic methylation of the 7-halogenated substrates

The preparative enzymatic methylation of the 7-chlorinated substrate **29** was performed using WT PsmD_*Sa* and and *Ct*HMT in lysate format. 20 mL PsmD_Sa lysate 14 mL CtHMT lysate were prepared shortly before the reaction, according to the procedure described in Chapter

7.2.5. They were added to the reaction mixture containing 30 mg **29** (1 mM, from a 200 mM stock in DMSO) and 10 mM MeI (from a 10 M stock in DMSO) in KP_i buffer (50 mM, pH 7.5) to a final volume of 100 mL. The mixture was incubated at 35 °C and 300 rpm for 18 h, when full conversion was observed (using TLC). The MeI was quenched by adding 20 equiv. ammonium thiosulfate and incubating for 1 h, then the product was extracted with EtOAc, dried on $MgSO_4$ and purified using column chromatography. After purification, 15.5 mg product were obtained (50% yield).

The preparative enzymatic methylation of the 7-brominated substrate **30** was performed using WT PsmD_*Sa* and and *Ct*HMT immobilized on Ni-NTA resin. 900 µL resin slurry containing immobilized WT PsmD_*Sa* and 630 µL resin slurry containing *Ct*HMT were mixed and resuspended in 45 mL reaction mixture containing 16 mg substrate **30** (1 mM final concentration, added from 200 mM stock in DMSO), 0.5 mM SAH, 10 mM MeI (added from a 10 M stock in DMSO) in KP_i buffer (50 mM, pH 7.5). The mixture was incubated at 35 °C and 300 rpm for 20 h. After, the Ni-NTA resin was separated by centrifugation and the product was extracted from the supernatant with ethyl acetate. The organic phase was then washed with brine and dried with $MgSO_4$. After filtration and solvent evaporation, the product was isolated by column chromatography. The conversion to product was determined at 57% (NMR). 2.7 mg product were isolated, with a 17% yield.

The synthesis of the halogenated PsmD substrates **29** and **30**, as well as the purification of the products after the enzymatic reactions were performed by Marchel Schatton (Institute of Bioorganic Chemistry, Heinrich Heine University, Düsseldorf), as part of his doctoral thesis project.

7.11.6 Evaluation of the methyl iodide quenching methods

Solutions were prepared containing 100, 500 or 1000 mM ammonium thiosulfate, 10 mM MeI and 1% (v%) DMSO in KP_i buffer (50 mM, pH 7.5) to a final volume of 1.5 mL. A negative control was prepared without MeI. After 10 min incubation at room temperature, the mixtures were extracted with 600 µL $CDCl_3$ and the organic phase was used for ^1H NMR analysis. The relative peak intensity between the specific MeI peak (2.16 ppm) and the $CDCl_3$ solvent peak was calculated and used for comparison. The MeI quenching experiment was performed by Lisa Guo (Heinrich Heine University, Düsseldorf), as part of her bachelor thesis project.

7.12 Protein sequences

Chloracidobacterium thermophilum* halide methyltransferase *(CtHMT)

MGHHHHHHAENLYFQGSGLGMDADTASFWEEKYRADLTAWDRGGVSPALEHWLAEGAL
KPGRILIPGCGYGHEVLALARRGFEVWGLDIALTPVRRLQEKLAQAGLTAHVVEGDVRTWQ
PEQPFDAVYEQTCLCALSPEDWPRYEAQLCRWLRPGGRLFALWMQTDRPGGPPYHCGLE
AMRVLFALERWRWVEPPQRTVPHPTGFFEYAAILERLV*

GenBank: AEP12557.1
Molecular weight: 24617.03 kDa
Extinction coefficient (280 nm): 65680 $M^{-1}cm^{-1}$

***Streptomyces griseofuscus* PsmD methyltransferase (PsmD_*Sg*)**

MMQGQPHQDAGMPEPYAATADVYDRLVDYAIAEWGECPRPQMADFVEQAWAARGHRVR
RVLELCCGTGLMTEQLVRRGYEVTAVDRSETMLALAKQRVGGAADFHQIELPAPLPDGADA
VVCTAAAFNYQASARSLGETLRAVATVLPAGATFVFDIETAALLKGHWGNRVWAADEGDLA
FIWDFTSEPDTTYCDVHYTQFTRHEAGADAYTGVREVHRLYAFDHDTVRAQARAAGFAQA
EVFDNYTERPATDTTRYETWVLTRDERHHHHHH*

GenBank: AHL44342.15
Molecular weight: 30497.87 Da
Extinction coefficient (280 nm): 49640 $M^{-1}cm^{-1}$

***Streptomyces albulus** * PsmD methyltransferase (PsmD_*Sa*)**

MQGQPHQDAGMPEPYAATADVYDRLVAYAIAQWGESPRPRMADFIEQAWKARGQRVRRV
LELCCGTGLMTEELVRRGYEVTAVDRSETMLALAKKRVGGAADFRQIELPAPLPGDTDAVV
CTAAAFNYQSSAHSLGETLHAVATVLPAGATFVFDIETAALLKGHWGNRMWAADEGDLAFI
WNFTSQPDTTYCDVHYTQFTRSEAGPDTYTGTREVHRLYAFDHDTVRAQARAAGFARAEV
FDNYTERPATDATHYETWFLTRDESLEHHHHHH*

*Recently reclassified in databases as *Streptomyces noursei*

GenBank: AIA00691.1
Molecular weight: 30662.06 Da
Extinction coefficient (280 nm): 49640 $M^{-1}cm^{-1}$

***Aspergillus clavatus* halide methyltransferase (*Ac*HMT)**

MGSTPSLIPSGVHEVLAKYKDGNYVDGWAELWDKSKGDRLPWDRGFPNPALEDTLIQKRAI
IGGPLGQDAQGKTYRKKALVPGCGRGVDVLLLASFGYDAYGLEYSATAVDVCQEEQAKNG
DQYPVRDAEIGQGKITFVQGDFFEDTWLEKLNLTRNCFDVIYDYTFFCALNPSMRPQWALR
HTQLLADSPRGHLICLEFPRHKDPSVQGPPWGSASEAYRAHLSHPGEEIPYDASRQCQFDS
SKAPSAQGLERVAYWQPERTHEVGKNEKGEVQDRVSIWQRPPQSSLLEHHHHHH*

GenBank: EAW10780
Molecular weight: 33453.36 Da
Extinction coefficient (280 nm): 62255 $M^{-1}cm^{-1}$

***Thermococcus kodakarensis* methionine adenosyl transferase (*Tk*MAT)**

MAGKVRNIVVEELVRTPVEMQKVELVERKGIGHPDSIADGIAEAVSRALSREYVKRYGIILHH
NTDQVEVVGGRAYPQFGGGEVIKPIYILLSGRAVEMVDREFFPVHEIALKAAKDYLRKAVRH
LDLEHHVIIDSRIGQGSVDLVGVFNKAKKNPIPLANDTSFGVGYAPLSETEKIVLETEKYLNSD

EFKKKYPAVGEDIKVMGLRKGDEIDLTIAAAIVDSEVDNPDDYMAVKEAIYEAAKGIVESHTE
RPTNIYVNTADDPKEGIYYITVTGTSAEAGDDGSVGRGNRVNGLITPNRHMSMEAAAGKNP
VSHVGKIYNILSMLIANDIAEQVEGVEEVYVRILSQIGKPIDEPLVASVQIIPKKGYSIDVLQKPA
YEIADEWLANITKIQKMILEDKVNVFLEHHHHHH*

GenBank: Q5JF22
Molecular weight: 45680.16 Da
Extinction coefficient (280 nm): 30830 $M^{-1}cm^{-1}$

***Escherichia coli* methylthioadenosine/*S*-adenosylhomocysteine nucleosidase (*Ec*MTAN)**

MGSSHHHHHHSSGLVPRGSHMKIGIIGAMEEEVTLLRDKIENRQTISLGGCEIYTGQLNGTE
VALLKSGIGKVAAALGATLLLEHCKPDVIINTGSAGGLAPTLKVGDIVVSDEARYHDADVTAF
GYEYGQLPGCPAGFKADDKLIAAAEACIAELNLNAVRGLIVSGDAFINGSVGLAKIRHNFPQA
IAVEMEATAIAHVCHNFNVPFVVVRAISDVADQQSHLSFDEFLAVAAKQSSLMVESLVQKLA
HG*

GenBank: KIH35059
Molecular weight: 26517.29 Da
Extinction coefficient (280 nm): 6210 $M^{-1}cm^{-1}$

***Streptacidiphilus griseoplanus (Peterkaempfera griseoplana)* PsmD homolog methyltransferase (PsmD_*Gp*)**

MKGQPITAGIPEPYEAISDTYDRLAVWACEHWGESPRYKMAAFLEKVWSDHPAPVHSVLEV
CCGTGLMLEQLVRRGYAVSGLDRSGPMLARARTRLGSDVPLVRSELPEIPGDQQYDAVICA
AAALNYMPDEQTLQRTFEAVARTVRPGGSFVFDILAHRMVADRFGTSVWADDLGDLAFIWK
FQNHPGQSHTDLDYTQFLRDGDGPDTYTVVRETHRLFALDRETVRELARRAGFTDIAVYDN
YSFEPADGATDYETWTLTRGQATDPPRHHHHHH*

GenBank: WP_055591319
Molecular weight: 31215.89 Da
Extinction coefficient (280 nm): 49640 $M^{-1}cm^{-1}$

***Streptomyces cattleya (Streptantibioticus cattleyicolor* NRRL 8057) PsmD homolog methyltransferase (PsmD_*Cat*)**

MTTTTEPYAHLAPAYDRLVDWVVTERGECPRGRIADFLAEYWGGRPRPVRTVLEVCCGTG
LTLAELAGRGYAVTGLDRSAAMLEQAARRLGPDVPLVQAQLPSIPLRPGFDAVISAAAGLNY
LPDETALTETLAAVARVLAPGGTFVFDLLSTTLLERSFDPAAPRVQGAELEDVSYLWTFETP
PSRAHFDLTYVQFLRRPDAPGQTYVKTREVHRMYPVPQEAVRRAADRAGFTDVAVHDNYG
PHRAGPETLYETWTLALPAAPAAGEHGHHHHHH*

GenBank: AEW99339.1
Molecular weight: 30351.26 Da
Extinction coefficient (280 nm): 38515 $M^{-1}cm^{-1}$

7.13 Gene sequences

PsmD_*Sa* - native gene sequence:

ATGATGCAGGGACAGCCGCACCAGGATGCGGGCATGCCCGAGCCGTACGCCGCGACC
GCCGACGTGTACGACCGGCTCGTCGCGTACGCCATCGCCCAGTGGGGAGAGTCTCCC
CGGCCGCGGATGGCCGACTTCATCGAGCAGGCATGGAAGGCTCGCGGGCAGCGCGTG
CGCCGGGTGCTGGAGCTGTGTTGCGGCACCGGGCTGATGACCGAGGAACTGGTGCGG
CGCGGTTACGAGGTGACCGCCGTCGACCGTTCCGAGACCATGTTGGCCCTGGCGAAG
AAGCGGGTCGGCGGTGCAGCCGACTTCCGACAGATCGAACTCCCCGCCCCGCTGCCC
GGCGACACGGACGCCGTGGTGTGCACCGCAGCCGCGTTCAACTACCAGTCCAGCGCG
CACTCGCTGGGAGAAACCCTGCACGCCGTGGCCACGGTGCTGCCGGCCGGTGCGACG
TTCGTCTTCGACATCGAGACTGCCGCGCTCCTCAAGGGACACTGGGGCAACCGCATGT
GGGCCGCCGACGAGGGCGACCTGGCGTTCATCTGGAACTTCACCAGTCAGCCGGACA
CCACCTACTGCGACGTGCACTACACCCAGTTCACGCGCTCCGAAGCGGGACCGGACAC
CTACACCGGCACCCGCGAGGTGCACCGGCTGTACGCCTTCGACCACGACACCGTCCG
CGCCCAGGCACGCGCCGCCGGATTCGCACGGGCGGAAGTGTTCGACAACTACACCGA
ACGCCCCGCCACCGACGCCACCCACTACGAGACGTGGTTCCTCACCCGGGACGAGAG
CTGA

PsmD_*Sa* - codon harmonized:

ATGCAGGGACAGCCGCACCAGGATGCGGGTATGCCCGAGCCATACGCCGCGACGGCC
GATGTGTACGACCGGCTCGTCGCGTATGCCATAGCCCAATGGGGAGAGTCTCCGCGGC
CTCGGATGGCCGACTTCATCGAGCAGGCATGGAAGGCTCGTGGGCAGCGCGTGGCCG
GGTGCTGGAGCTGTGTTGCGGCACCGGTCTGATGACTGAGGAACTGGTGCGGCGCGG
TTACGAGGTGACAGCTGTAGACCGTTCCGAGACCATGTTGGCCCTCGCGAAGAAGCGG
GTCGGCGGTGCAGCCGACTTCCGACAGATCGAGCTCCCCGCCCCGCTGCCCGGCGAC
ACGGACGCAGTGGTATGCACCGCAGCCGCGTTCAACTACCAGTCCAGTGCACACTCAC
TGGGAGAAACCCTACACGCCGTAGCCACGGTGCTGCCAGCCGGTGCAACGTTCGTCTT
CGACATCGAGACTGCAGCGCTCCTCAAGGGACATTGGGGCAATCGCATGTGGGCCGC
CGACGAGGGCGACCTGGCGTTCATCTGGAACTTCACTAGTCAGCCGGACACCACCTAC
TGCGACGTGCATTACACACAGTTCACGCGCTCTGAAGCGGGACCGGACACCTACACCG
GCACCCGCGAGGTACACCGGCTGTACGCGTTCGACCACGACACCGTCCGCGCCCAGG
CACGCGCCGCCGGATTCGCACGTGCGGAAGTGTTCGACAACTACACCGAACGCCCCG
CCACCGACGCCACCCACTACGAGACGTGGTTCCTCACCCGGGACGAGAGC

8. Bibliography

[1] D. A. Amariei, N. Pozhydaieva, B. David, P. Schneider, T. Classen, H. Gohlke, O. H. Weiergräber, J. Pietruszka, *ACS Catal.* **2022**, *12*, 14130-14139; 'Enzymatic C3-Methylation of Indoles Using Methyltransferase PsmD─Crystal Structure, Catalytic Mechanism, and Preparative Applications'; https://doi.org/10.1021/acscatal.2c04240

[2] D. A. Amariei, M. Haase, M. K. T. Klischan, M. Wäscher, J. Pietruszka, *ChemCatChem* **2024**, *16*, e202400052; 'High-throughput colorimetric detection and quantification of indoles and pyrroloindoles for enzymatic activity determination'; https://doi.org/10.1002/cctc.202400052

[3] D. A. Amariei, J. Tenhaef, T. Classen, B. David, T. M. Rosch, H. Gohlke, S. Noack, J. Pietruszka, *Catal. Sci. Technol.* **2024**, *14*, 6298-6306; 'Directed evolution of C-methyltransferase PsmD for enantioselective pyrroloindole derivative production'; https://doi.org/10.1039/d4cy00657g

[4] UN, *United Nations: New York, NY, USA* **2015**; 'Transforming our world: the 2030 Agenda for Sustainable Development';

[5] H. Hermann, L. Emele, *WWF Deutschland* **2024**; 'Dirty dozen: chemical industry - Emissions from the 12 largest chemical parks in Germany';

[6] U. T. Bornscheuer, K. Buchholz, *Eng. Life Sci.* **2005**, *5*, 309-323; 'Highlights in Biocatalysis - Historical Landmarks and Current Trends'; https://doi.org/10.1002/elsc.200520089

[7] A. Fryszkowska, P. N. Devine, *Curr. Opin. Chem. Biol.* **2020**, *55*, 151-160; 'Biocatalysis in drug discovery and development'; https://doi.org/10.1016/j.cbpa.2020.01.012

[8] D. J. Newman, G. M. Cragg, *J. Nat. Prod.* **2020**, *83*, 770-803; 'Natural Products as Sources of New Drugs over the Nearly Four Decades from 01/1981 to 09/2019'; https://doi.org/10.1021/acs.jnatprod.9b01285

[9] E. J. Barreiro, A. E. Kummerle, C. A. Fraga, *Chem. Rev.* **2011**, *111*, 5215-5246; 'The methylation effect in medicinal chemistry'; https://doi.org/10.1021/cr200060g

[10] D. Aynetdinova, M. C. Callens, H. B. Hicks, C. Y. X. Poh, B. D. A. Shennan, A. M. Boyd, Z. H. Lim, J. A. Leitch, D. J. Dixon, *Chem. Soc. Rev.* **2021**, *50*, 5517-5563; 'Installing the "magic methyl"- C-H methylation in synthesis'; https://doi.org/10.1039/d0cs00973c

[11] M. R. Bennett, S. A. Shepherd, V. A. Cronin, J. Micklefield, *Curr. Opin. Chem. Biol.* **2017**, *37*, 97-106; 'Recent advances in methyltransferase biocatalysis'; https://doi.org/10.1016/j.cbpa.2017.01.020

[12] A.-W. Struck, M. L. Thompson, L. S. Wong, J. Micklefield, *ChemBioChem* **2012**, *13*, 2642–2655; 'S -Adenosyl-Methionine-Dependent Methyltransferases: Highly Versatile Enzymes in Biocatalysis, Biosynthesis and Other Biotechnological Applications'; https://doi.org/10.1002/cbic.201200556

[13] J. G. Mahdi, A. J. Mahdi, A. J. Mahdi, I. D. Bowen, *Cell Prolif.* **2006**, *39*, 147-155; 'The historical analysis of aspirin discovery, its relation to the willow tree and antiproliferative and anticancer potential'; https://doi.org/10.1111/j.1365-2184.2006.00377.x

[14] J. F. Nunn, 'Ancient egyptian medicine', University of Oklahoma Press, **2002**.

[15] E. Patridge, P. Gareiss, M. S. Kinch, D. Hoyer, *Drug Discov. Today* **2016**, *21*, 204-207; 'An analysis of FDA-approved drugs: natural products and their derivatives'; https://doi.org/10.1016/j.drudis.2015.01.009

[16] P. L. Schiff, *Am. J. Pharm. Educ.* **2002**, *66*, 188-196; 'Opium and its alkaloids';

[17] M. Wainwright, *Mycologist* **1989**, *3*, 21-23; 'Moulds in ancient and more recent medicine'; https://doi.org/10.1016/S0269-915X(89)80010-2

[18] H. Hatcher, R. Planalp, J. Cho, F. M. Torti, S. V. Torti, *Cell. Mol. Life Sci.* **2008**, *65*, 1631-1652; 'Curcumin: from ancient medicine to current clinical trials'; https://doi.org/10.1007/s00018-008-7452-4

[19] E. J. Bassett, M. S. Keith, G. J. Armelagos, D. L. Martin, A. R. Villanueva, *Science* **1980**, *209*, 1532-1534; 'Tetracycline-labeled human bone from ancient Sudanese Nubia (A.D. 350)'; https://doi.org/10.1126/science.7001623

[20] A. Bauer, M. Bronstrup, *Nat. Prod. Rep.* **2014**, *31*, 35-60; 'Industrial natural product chemistry for drug discovery and development'; https://doi.org/10.1039/c3np70058e

[21] D. G. Brown, T. Lister, T. L. May-Dracka, *Bioorg. Med. Chem. Lett.* **2014**, *24*, 413-418; 'New natural products as new leads for antibacterial drug discovery'; https://doi.org/10.1016/j.bmcl.2013.12.059

[22] H. van Hattum, H. Waldmann, *J. Am. Chem. Soc.* **2014**, *136*, 11853-11859; 'Biology-oriented synthesis: harnessing the power of evolution'; https://doi.org/10.1021/ja505861d

[23] K. C. Morrison, P. J. Hergenrother, *Nat. Prod. Rep.* **2014**, *31*, 6-14; 'Natural products as starting points for the synthesis of complex and diverse compounds'; https://doi.org/10.1039/c3np70063a

[24] F. E. Koehn, G. T. Carter, *Nat. Rev. Drug. Discov.* **2005**, *4*, 206-220; 'The evolving role of natural products in drug discovery'; https://doi.org/10.1038/nrd1657

[25] S. J. Projan, *Curr. Opin. Microbiol.* **2003**, *6*, 427-430; 'Why is big Pharma getting out of antibacterial drug discovery?'; https://doi.org/10.1016/j.mib.2003.08.003

[26] B. E. Kirsop, *J. Ind. Microbiol. Biotech.* **1996**, *17*, 505–511; 'The convention on Biological Diversity: Some implications for microbiology and microbial culture collections.'; https://doi.org/10.1007/BF01574782

[27] J. W. Li, J. C. Vederas, *Science* **2009**, *325*, 161-165; 'Drug discovery and natural products: end of an era or an endless frontier?'; https://doi.org/10.1126/science.1168243

[28] T. Rodrigues, D. Reker, P. Schneider, G. Schneider, *Nat. Chem.* **2016**, *8*, 531-541; 'Counting on natural products for drug design'; https://doi.org/10.1038/nchem.2479

[29] A. L. Harvey, R. Edrada-Ebel, R. J. Quinn, *Nat. Rev. Drug Discov.* **2015**, *14*, 111-129; 'The re-emergence of natural products for drug discovery in the genomics era'; https://doi.org/10.1038/nrd4510

[30] D. Reker, A. M. Perna, T. Rodrigues, P. Schneider, M. Reutlinger, B. Monch, A. Koeberle, C. Lamers, M. Gabler, H. Steinmetz, R. Muller, M. Schubert-Zsilavecz, O. Werz, G. Schneider, *Nat. Chem.* **2014**, *6*, 1072-1078; 'Revealing the macromolecular targets of complex natural products'; https://doi.org/10.1038/nchem.2095

[31] J. Larsson, J. Gottfries, S. Muresan, A. Backlund, *J. Nat. Prod.* **2007**, *70*, 789-794; 'ChemGPS-NP: tuned for navigation in biologically relevant chemical space'; https://doi.org/10.1021/np070002y

[32] K. Blin, S. Shaw, A. M. Kloosterman, Z. Charlop-Powers, G. P. van Wezel, M. H. Medema, T. Weber, *Nucleic Acids Res.* **2021**, *49*, W29-W35; 'antiSMASH 6.0: improving cluster detection and comparison capabilities'; https://doi.org/10.1093/nar/gkab335

[33] M. A. Skinnider, C. W. Johnston, M. Gunabalasingam, N. J. Merwin, A. M. Kieliszek, R. J. MacLellan, H. Li, M. R. Ranieri, A. L. Webster, M. P. Cao, A. Pfeifle, N. Spencer, H. Q. To, D. P. Wallace, C. A. Dejong, N. A. Magarvey, *Nat. Commun.* **2020**, *11*, 6058; 'Comprehensive prediction of secondary metabolite structure and biological activity from microbial genome sequences'; https://doi.org/10.1038/s41467-020-19986-1

[34] P. Cimermancic, M. H. Medema, J. Claesen, K. Kurita, L. C. W. Brown, K. Mavrommatis, A. Pati, P. A. Godfrey, M. Koehrsen, J. Clardy, B. W. Birren, E. Takano, A. Sali, R. G. Linington, M. A. Fischbach, *Cell* **2014**, *158*, 412-421; 'Insights into secondary metabolism from a global analysis of prokaryotic biosynthetic gene clusters'; https://doi.org/10.1016/j.cell.2014.06.034

[35] G. D. Hannigan, D. Prihoda, A. Palicka, J. Soukup, O. Klempir, L. Rampula, J. Durcak, M. Wurst, J. Kotowski, D. Chang, R. Wang, G. Piizzi, G. Temesi, D. J. Hazuda, C. H. Woelk, D. A. Bitton, *Nucleic Acids Res.* **2019**, *47*, e110; 'A deep learning genome-mining strategy for biosynthetic gene cluster prediction'; https://doi.org/10.1093/nar/gkz654

[36] L. M. Carroll, M. Larralde, J. S. Fleck, R. Ponnudurai, A. Milanese, E. Cappio, G. Zeller, *bioRxiv* **2021**, 2021.2005.2003.442509; 'Accurate de novo identification of biosynthetic gene clusters with GECCO'; https://doi.org/10.1101/2021.05.03.442509

[37] R. Reher, H. W. Kim, C. Zhang, H. H. Mao, M. Wang, L.-F. Nothias, A. M. Caraballo-Rodriguez, E. Glukhov, B. Teke, T. Leao, K. L. Alexander, B. M. Duggan, E. L. Van Everbroeck, P. C. Dorrestein, G. W. Cottrell, W. H. Gewick, *J. Am. Chem. Soc.* **2020**, *142*, 4114-4120; 'A convolutional neural network-based approach for the rapid annotation of molecularly diverse natural products'; https://doi.org/10.1021/jacs.9b13786

[38] H. W. Kim, C. Zhang, G. W. Cottrell, W. H. Gerwick, *Magn. Reson. Chem.* **2022**, *60*, 1070-1075; 'SMART-Miner: a convolutional neural network-based metabolite identification from 1H-13C HSQC spectra'; https://doi.org/10.1002/mrc.5240

[39] C. Wang, I. n. Timári, B. Zhang, D.-W. Li, A. Leggett, A. O. Amer, L. Bruschweiler-Li, R. E. Kopec, R. Brüschweiler, *J. Proteome Res.* **2020**, *19*, 1674-1683; 'COLMAR lipids web server and ultrahigh-resolution methods for two-dimensional nuclear magnetic resonance-and mass spectrometry-based lipidomics'; https://doi.org/10.1021/acs.jproteome.9b00845

[40] D. Reker, A. M. Perna, T. Rodrigues, P. Schneider, M. Reutlinger, B. Mönch, A. Koeberle, C. Lamers, M. Gabler, H. Steinmetz, R. Müller, M. Schubert-Zsilavecz, O. Werz, G. Schneider, *Nat. Chem.* **2014**, *6*, 1072-1078; 'Revealing the macromolecular targets of complex natural products'; https://doi.org/10.1038/nchem.2095

[41] V. Bortolaia, R. S. Kaas, E. Ruppe, M. C. Roberts, S. Schwarz, V. Cattoir, A. Philippon, R. L. Allesoe, A. R. Rebelo, A. F. Florensa, L. Fagelhauer, T. Chakraborty, B. Neumann, G. Werner, J. K. Bender, K. Stingl, M. Nguyen, J. Coppens, B. B. Xavier, S. Mahlhotra-Kumar, H. Westh, M. Pinholt, M. F. Anjum, N. A. Duggett, I. Kempf, S. Nykäsenoja, S. Olkkola, K. Wieczorek, A. Amaro, L. Clemente, J. Mossong, S. Losch, C. Ragimbeau, O. Lund, F. M. Aarestrup, *J. Antimicrob. Chemother.* **2020**, *75*, 3491-3500; 'ResFinder 4.0 for predictions of phenotypes from genotypes'; https://doi.org/10.1093/jac/dkaa345

[42] M. W. Mullowney, K. R. Duncan, S. S. Elsayed, N. Garg, J. J. J. van der Hooft, N. I. Martin, D. Meijer, B. R. Terlouw, F. Biermann, K. Blin, J. Durairaj, M. Gorostiola Gonzalez, E. J. N. Helfrich, F. Huber, S. Leopold-Messer, K. Rajan, T. de Rond, J. A. van Santen, M. Sorokina, M. J. Balunas, M. A. Beniddir, D. A. van Bergeijk, L. M. Carroll, C. M. Clark, D. A. Clevert, C. A. Dejong, C. Du, S. Ferrinho, F. Grisoni, A. Hofstetter, W. Jespers, O. V. Kalinina, S. A. Kautsar, H. Kim, T. F. Leao, J. Masschelein, E. R. Rees, R. Reher, D. Reker, P. Schwaller, M. Segler, M. A. Skinnider, A. S. Walker, E. L. Willighagen, B. Zdrazil, N. Ziemert, R. J. M. Goss, P. Guyomard, A. Volkamer, W. H. Gerwick, H. U. Kim, R. Muller, G. P. van Wezel, G. J. P. van Westen, A. K. H. Hirsch, R. G. Linington, S. L. Robinson, M. H. Medema, *Nat. Rev. Drug. Discov.* **2023**, *22*, 895-916; 'Artificial intelligence for natural product drug discovery'; https://doi.org/10.1038/s41573-023-00774-7

[43] F. I. Saldivar-Gonzalez, V. D. Aldas-Bulos, J. L. Medina-Franco, F. Plisson, *Chem. Sci.* **2022**, *13*, 1526-1546; 'Natural product drug discovery in the artificial intelligence era'; https://doi.org/10.1039/d1sc04471k

[44] M. H. Medema, M. A. Fischbach, *Nat. Chem. Biol.* **2015**, *11*, 639-648; 'Computational approaches to natural product discovery'; https://doi.org/10.1038/nchembio.1884

[45] S. Barelier, O. Eidam, I. Fish, J. Hollander, F. Figaroa, R. Nachane, J. J. Irwin, B. K. Shoichet, G. Siegal, *ACS Chem. Biol.* **2014**, *9*, 1528-1535; 'Increasing chemical space coverage by combining empirical and computational fragment screens'; https://doi.org/10.1021/cb5001636

[46] C. W. Murray, D. C. Rees, *Nat. Chem.* **2009**, *1*, 187-192; 'The rise of fragment-based drug discovery'; https://doi.org/10.1038/nchem.217

[47] D. Schuster, C. Laggner, T. Langer, *Curr. Pharm. Des.* **2005**, *11*, 3545-3559; 'Why drugs fail--a study on side effects in new chemical entities'; https://doi.org/10.2174/138161205774414510

[48] C. A. Lipinski, *J. Pharmacol. Toxicol. Methods* **2000**, *44*, 235-249; 'Drug-like properties and the causes of poor solubility and poor permeability'; https://doi.org/10.1016/s1056-8719(00)00107-6

[49] M. Congreve, R. Carr, C. Murray, H. Jhoti, *Drug Discov. Today* **2003**, *8*, 876-877; 'A 'rule of three' for fragment-based lead discovery?'; https://doi.org/10.1016/s1359-6446(03)02831-9

[50] D. F. Veber, S. R. Johnson, H. Y. Cheng, B. R. Smith, K. W. Ward, K. D. Kopple, *J. Med. Chem.* **2002**, *45*, 2615-2623; 'Molecular properties that influence the oral bioavailability of drug candidates'; https://doi.org/10.1021/jm020017n

[51] F. Ntie-Kang, L. L. Lifongo, P. N. Judson, W. Sippl, S. M. Efange, *J. Mol. Model.* **2014**, *20*, 2069; 'How "drug-like" are naturally occurring anti-cancer compounds?'; https://doi.org/10.1007/s00894-014-2069-z

[52] M.-Q. Zhang, B. Wilkinson, *Curr. Opin. Biotechnol.* **2007**, *18*, 478-488; 'Drug discovery beyond the 'rule-of-five''; https://doi.org/10.1016/j.copbio.2007.10.005

[53] C. A. Lipinski, *Adv. Drug Deliv. Rev.* **2016**, *101*, 34-41; 'Rule of five in 2015 and beyond: Target and ligand structural limitations, ligand chemistry structure and drug discovery project decisions'; https://doi.org/10.1016/j.addr.2016.04.029

[54] B. Over, S. Wetzel, C. Grütter, Y. Nakai, S. Renner, D. Rauh, H. Waldmann, *Nat. Chem.* **2013**, *5*, 21-28; 'Natural-product-derived fragments for fragment-based ligand discovery'; https://doi.org/10.1038/nchem.1506

[55] P. Schneider, G. Schneider, *Angew. Chem. Int. Ed.* **2017**, *56*, 7971-7974; 'Privileged Structures Revisited'; (*Angew. Chem.*, *129*, 8079-8083) https://doi.org/10.1002/anie.201702816

[56] L. Costantino, D. Barlocco, *Curr. Med. Chem.* **2006**, *13*, 65-85; 'Privileged structures as leads in medicinal chemistry'; https://doi.org/10.2174/092986706775197999

[57] H. Kubinyi, *Privileged structures and analogue-based drug discovery,* in *Analogue-based Drug Discovery* (Eds.: J. Fischer, R. Ganellin), Wiley, **2006**, pp. 53-68.

[58] Y. Hu, J. Bajorath, *J. Chem. Inf. Model.* **2010**, *50*, 500-510; 'Molecular scaffolds with high propensity to form multi-target activity cliffs'; https://doi.org/10.1021/ci100059q

[59] J. B. Baell, G. A. Holloway, *J. Med. Chem.* **2010**, *53*, 2719-2740; 'New substructure filters for removal of pan assay interference compounds (PAINS) from screening libraries and for their exclusion in bioassays'; https://doi.org/10.1021/jm901137j

[60] J. B. Baell, *J. Nat. Prod.* **2016**, *79*, 616-628; 'Feeling Nature's PAINS: Natural Products, Natural Product Drugs, and Pan Assay Interference Compounds (PAINS)'; https://doi.org/10.1021/acs.jnatprod.5b00947

[61] M. E. Welsch, S. A. Snyder, B. R. Stockwell, *Curr. Opin. Chem. Biol.* **2010**, *14*, 347-361; 'Privileged scaffolds for library design and drug discovery'; https://doi.org/10.1016/j.cbpa.2010.02.018

[62] Y. Chen, C. Rosenkranz, S. Hirte, J. Kirchmair, *Nat. Prod. Rep.* **2022**, *39*, 1544-1556; 'Ring systems in natural products: structural diversity, physicochemical properties, and coverage by synthetic compounds'; https://doi.org/10.1039/d2np00001f

[63] T. Henkel, R. M. Brunne, H. Müller, F. Reichel, *Angew. Chem. Int. Ed.* **1999**, *38*, 643-647; 'Statistical Investigation into the Structural Complementarity of Natural Products and Synthetic Compounds'; (*Angew. Chem.*, *111*, 688-691) https://doi.org/10.1002/(SICI)1521-3773(19990301)38:5<643::AID-ANIE643>3.0.CO;2-G

[64] M. L. Lee, G. Schneider, *J. Comb. Chem.* **2001**, *3*, 284-289; 'Scaffold architecture and pharmacophoric properties of natural products and trade drugs: application in the design of natural product-based combinatorial libraries'; https://doi.org/10.1021/cc000097l

[65] P. Ertl, S. Jelfs, J. Muhlbacher, A. Schuffenhauer, P. Selzer, *J. Med. Chem.* **2006**, *49*, 4568-4573; 'Quest for the rings. In silico exploration of ring universe to identify novel bioactive heteroaromatic scaffolds'; https://doi.org/10.1021/jm060217p

[66] K. Grabowski, K. H. Baringhaus, G. Schneider, *Nat. Prod. Rep.* **2008**, *25*, 892-904; 'Scaffold diversity of natural products: inspiration for combinatorial library design'; https://doi.org/10.1039/b715668p

[67] N. K. Kaushik, N. Kaushik, P. Attri, N. Kumar, C. H. Kim, A. K. Verma, E. H. Choi, *Molecules* **2013**, *18*, 6620–6662; 'Biomedical Importance of Indoles'; https://doi.org/10.3390/molecules18066620.

[68] T. V. Sravanthi, S. L. Manju, *Eur. J. Pharm. Sci.* **2016**, *91*, 1-10; 'Indoles - A promising scaffold for drug development'; https://doi.org/10.1016/j.ejps.2016.05.025

[69] N. Teraiya, K. Agrawal, T. M. Patel, A. Patel, S. Patel, U. Shah, S. Shah, K. Rathod, K. Patel, *Curr. Drug. Discov. Technol.* **2023**, *20*, 9-37; 'A Review of the Therapeutic Importance of Indole Scaffold in Drug Discovery'; https://doi.org/10.2174/1570163820666230505120553

[70] A. I. Scott, *Acc. Chem. Res.* **1970**, *3*, 151-157; 'Biosynthesis of the indole alkaloids'; https://doi.org/10.1021/ar50029a002

[71] W. Xu, D. J. Gavia, Y. Tang, *Nat. Prod. Rep.* **2014**, *31*, 1474-1487; 'Biosynthesis of fungal indole alkaloids'; https://doi.org/10.1039/c4np00073k

[72] E. R. Radwanski, R. L. Last, *Plant Cell* **1995**, *7*, 921-934; 'Tryptophan biosynthesis and metabolism: biochemical and molecular genetics'; https://doi.org/10.1105/tpc.7.7.921

[73] S. Xiao, Z. Wang, B. Wang, B. Hou, J. Cheng, T. Bai, Y. Zhang, W. Wang, L. Yan, J. Zhang, *Front. Microbiol.* **2023**, *14*, 1099098; 'Expanding the application of tryptophan: Industrial biomanufacturing of tryptophan derivatives'; https://doi.org/10.3389/fmicb.2023.1099098

[74] S. Liu, J.-Z. Xu, W.-G. Zhang, *World J. Microbiol. Biotechnol.* **2022**, *38*, 22; 'Advances and prospects in metabolic engineering of *Escherichia coli* for L-tryptophan production'; https://doi.org/10.1007/s11274-021-03212-1

[75] E. Fischer, F. Jourdan, *Ber. Dtsch. Chem. Ges.* **1883**, *16*, 2241-2245; 'Ueber die hydrazine der brenztraubensäure'; https://doi.org/10.1002/cber.188301602141

[76] B. Robinson, *Chem. Rev.* **1963**, *63*, 373-401; 'The Fischer indole synthesis'; https://doi.org/10.1021/cr60224a003

[77] Majid M. Heravi, S. Rohani, V. Zadsirjan, N. Zahedi, *RSC Adv.* **2017**, *7*, 52852-52887; 'Fischer indole synthesis applied to the total synthesis of natural products'; https://doi.org/10.1039/c7ra10716a

[78] K. Hu, Y. Zhang, Z. Zhou, Y. Yang, Z. Zha, Z. Wang, *Org. Lett.* **2020**, *22*, 5773-5777; 'Iodine-mediated electrochemical C (sp2)–H amination: switchable synthesis of indolines and indoles'; https://doi.org/10.1021/acs.orglett.0c01821

[79] J. H. Kim, S. A. Lee, T. S. Jeon, J. K. Cha, Y. G. Kim, *Synlett* **2023**, *34*, 1719-1722; 'A unified approach to mono-and 2, 3-disubstituted N–H indoles'; https://doi.org/10.1055/s-0042-1752656

[80] K. Maeda, R. Matsubara, M. Hayashi, *Org. Lett.* **2021**, *23*, 1530-1534; 'Synthesis of substituted anilines from cyclohexanones using Pd/C–ethylene system and its application to indole Synthesis'; https://doi.org/10.1021/acs.orglett.0c04056

[81] C. Zeng, S. Fang, S. Guo, H. Jiang, S. Yang, W. Wu, *Org. Lett.* **2023**, *25*, 1409-1414; 'Palladium-Catalyzed Tandem Nucleophilic Addition/C–H Functionalization of Anilines and Bromoalkynes for the Synthesis of 2-Phenylindoles'; https://doi.org/10.1021/acs.orglett.3c00137

[82] F. Chassagne, G. Cabanac, G. Hubert, B. David, G. Marti, *Phytochem. Rev.* **2019**, *18*, 601-622; 'The landscape of natural product diversity and their pharmacological relevance from a focus on the Dictionary of Natural Products®'; https://doi.org/10.1007/s11101-019-09606-2

[83] P. F. Rosales, G. S. Bordin, A. E. Gower, S. Moura, *Fitoterapia* **2020**, *143*, 104558; 'Indole alkaloids: 2012 until now, highlighting the new chemical structures and biological activities'; https://doi.org/10.1016/j.fitote.2020.104558

[84] M. Naughton, J. B. Mulrooney, B. E. Leonard, *Hum. Psychopharmacol.* **2000**, *15*, 397-415; 'A review of the role of serotonin receptors in psychiatric disorders'; https://doi.org/10.1002/1099-1077(200008)15:6<397::AID-HUP212>3.0.CO;2-L

[85] A. Lee, H. Choo, B. Jeon, *Int. J. Mol. Sci.* **2022**, *23*, 6515; 'Serotonin receptors as therapeutic targets for autism spectrum disorder treatment'; https://doi.org/10.3390/ijms23126515

[86] J. Sourbron, L. Lagae, *Epilepsia Open* **2022**, *7*, 231-246; 'Serotonin receptors in epilepsy: Novel treatment targets?'; https://doi.org/10.1002/epi4.12580

[87] D. V. Eremin, E. M. Kondaurova, A. Y. Rodnyy, C. A. Molobekova, D. A. Kudlay, V. S. Naumenko, *Biochem. (Mosc.)* **2023**, *88*, 2023-2042; 'Serotonin Receptors as a

Potential Target in the Treatment of Alzheimer's Disease'; https://doi.org/10.1134/S0006297923120064

[88] F. R. de Sa Alves, E. J. Barreiro, C. A. Fraga, *Mini. Rev. Med. Chem.* **2009**, *9*, 782-793; 'From nature to drug discovery: the indole scaffold as a 'privileged structure''; https://doi.org/10.2174/138955709788452649

[89] S. S. Jhee, T. Shiovitz, A. W. Crawford, N. R. Cutler, *Clin. Pharmacokinet.* **2001**, *40*, 189-205; 'Pharmacokinetics and pharmacodynamics of the triptan antimigraine agents: a comparative review'; https://doi.org/10.2165/00003088-200140030-00004

[90] S. D. Silberstei, *Headache* **1994**, *34*, 408-417; 'Serotonin (5-HT) and migraine'; https://doi.org/10.1111/j.1526-4610.1994.hed3407408.x

[91] P. Plenge, D. Yang, K. Salomon, L. Laursen, I. E. Kalenderoglou, A. H. Newman, E. Gouaux, J. A. Coleman, C. J. Loland, *Nat. Commun.* **2021**, *12*, 5063; 'The antidepressant drug vilazodone is an allosteric inhibitor of the serotonin transporter'; https://doi.org/10.1038/s41467-021-25363-3

[92] W. Aellig, *Am. Heart J.* **1982**, *104*, 346-356; 'Clinical pharmacology of pindolol'; https://doi.org/10.1016/0002-8703(82)90125-9

[93] J. Parkes, M. Schachter, C. Marsden, B. Smith, A. Wilson, *Ann. Neurol.* **1981**, *9*, 48-52; 'Lisuride in parkinsonism'; https://doi.org/10.1002/ana.410090109

[94] L. A. Houghton, J. M. Foster, P. J. Whorwell, *Aliment. Pharmacol. Ther.* **2000**, *14*, 775-782; 'Alosetron, a 5-HT_3 receptor antagonist, delays colonic transit in patients with irritable bowel syndrome and healthy volunteers'; https://doi.org/10.1046/j.1365-2036.2000.00762.x

[95] J. H. Ye, R. Ponnudurai, R. Schaefer, *CNS Drug Rev.* **2001**, *7*, 199-213; 'Ondansetron: a selective 5-HT_3 receptor antagonist and its applications in CNS-related disorders'; https://doi.org/10.1111/j.1527-3458.2001.tb00195.x

[96] K. Andersen, T. Liljefors, J. Hyttel, J. Perregaard, *J. Med. Chem.* **1996**, *39*, 3723-3738; 'Serotonin 5-HT_2 receptor, dopamine D2 receptor, and α1 adrenoceptor antagonists. Conformationally flexible analogues of the atypical antipsychotic sertindole'; https://doi.org/10.1021/jm960159f

[97] F. Artigas, P. Celada, M. Laruelle, A. Adell, *Trends Pharmacol. Sci.* **2001**, *22*, 224-228; 'How does pindolol improve antidepressant action?'; https://doi.org/10.1016/S0165-6147(00)01682-5

[98] P. Ruiz-Sanchis, S. A. Savina, F. Albericio, M. Alvarez, *Chem. Eur. J.* **2011**, 1388-1408; 'Structure, Bioactivity and Synthesis of Natural Products with Hexahydropyrrolo[2,3-b]indole'; https://doi.org/10.1002/chem.201001451

[99] C. Sun, W. Tian, Z. Lin, X. Qu, *Nat. Prod. Rep.* **2022**, *39*, 1721-1765; 'Biosynthesis of pyrroloindoline-containing natural products'; https://doi.org/10.1039/D2NP00030J

[100] S. Li, J. M. Finefield, J. D. Sunderhaus, T. J. McAfoos, R. M. Williams, D. H. Sherman, *J. Am. Chem. Soc.* **2012**, *134*, 788-791; 'Biochemical characterization of NotB as an FAD-dependent oxidase in the biosynthesis of notoamide indole alkaloids'; https://doi.org/10.1021/ja2093212

[101] C. Y. Lai, I. W. Lo, R. T. Hewage, Y. C. Chen, C. T. Chen, C. F. Lee, S. Lin, M. C. Tang, H. C. Lin, *Angew. Chem. Int. Ed.* **2017**, *56*, 9478-9482; 'Biosynthesis of complex indole alkaloids: elucidation of the concise pathway of okaramines'; (*Angew. Chem.*, *129*, 9606-9610) https://doi.org/10.1002/ange.201705501

[102] S. W. Haynes, X. Gao, Y. Tang, C. T. Walsh, *J. Am. Chem. Soc.* **2012**, *134*, 17444-17447; 'Assembly of asperlicin peptidyl alkaloids from anthranilate and tryptophan: a two-enzyme pathway generates heptacyclic scaffold complexity in asperlicin E'; https://doi.org/10.1021/ja308371z

[103] D. J. Janzen, H. Wang, S.-M. Li, *J. Nat. Prod.* **2023**, *86*, 1779-1785; 'A flavin-dependent oxygenase catalyzes hydroxylation and simultaneous pyrrolidine ring formation in protubonine biosynthesis in *Aspergillus ustus*'; https://doi.org/10.1021/acs.jnatprod.3c00274

[104] J. Ma, Z. Wang, H. Huang, M. Luo, D. Zuo, B. Wang, A. Sun, Y.-Q. Cheng, C. Zhang, J. Ju, *Angew. Chem. Int. Ed.* **2011**, *50*, 7797-7802; 'Biosynthesis of Himastatin: Assembly Line and Characterization of Three Cytochrome P450 Enzymes Involved in

the Post-tailoring Oxidative Steps'; (*Angew. Chem.*, *123*, 7943-7948) https://doi.org/10.1002/anie.201102305

[105] J. Liu, T. Ng, Z. Rui, O. Ad, W. Zhang, *Angew. Chem. Int. Ed.* **2014**, 136-139; 'Unusual Acetylation-Dependent Reaction Cascade in the Biosynthesis of the Pyrroloindole Drug Physostigmine'; (*Angew. Chem.*, *126*, 140-143) https://doi.org/10.1002/anie.201308069

[106] N. Alqahtani, S. K. Porwal, E. D. James, D. M. Bis, J. A. Karty, A. L. Lane, R. Viswanathan, *Org. Biomol. Chem.* **2015**, *13*, 7177-7192; 'Synergism between genome sequencing, tandem mass spectrometry and bio-inspired synthesis reveals insights into nocardioazine B biogenesis'; https://doi.org/10.1039/C5OB00537J

[107] S. W. Haynes, X. Gao, Y. Tang, C. T. Walsh, *ACS Chem. Biol.* **2013**, *8*, 741-748; 'Complexity generation in fungal peptidyl alkaloid biosynthesis: a two-enzyme pathway to the hexacyclic MDR export pump inhibitor ardeemin'; https://doi.org/10.1021/cb3006787

[108] H. Ali, M. I. Ries, J. G. Nijland, P. P. Lankhorst, T. Hankemeier, R. A. Bovenberg, R. J. Vreeken, A. J. Driessen, *PloS one* **2013**, *8*, e65328; 'A branched biosynthetic pathway is involved in production of roquefortine and related compounds in *Penicillium chrysogenum*'; https://doi.org/10.1371/journal.pone.0065328

[109] J. Liu, Y. Yang, L. Harken, S.-M. Li, *J. Nat. Prod.* **2021**, *84*, 3100-3109; 'Elucidation of the streptoazine biosynthetic pathway in *Streptomyces aurantiacus* reveals the presence of a promiscuous prenyltransferase/cyclase'; https://doi.org/10.1021/acs.jnatprod.1c00844

[110] M. Pfaffenbach, T. Gaich, *Chem. -Eur. J.* **2016**, *22*, 3600-3610; 'The diaza [5.5. 6.6] fenestrane skeleton—Synthesis of leuconoxine alkaloids'; https://doi.org/10.1002/chem.201502228

[111] K. Viehrig, F. Surup, C. Volz, J. Herrmann, A. Abou Fayad, S. Adam, J. Köhnke, D. Trauner, R. Müller, *Angew. Chem. Int. Ed.* **2017**, *56*, 7407-7410; 'Structure and Biosynthesis of Crocagins: Polycyclic Posttranslationally Modified Ribosomal Peptides from *Chondromyces crocatus*'; (*Angew. Chem.*, *129*, 7513-7517) https://doi.org/10.1002/anie.201612640

[112] S. Adam, D. Zheng, A. Klein, C. Volz, W. Mullen, S. L. Shirran, B. O. Smith, O. V. Kalinina, R. Muller, J. Koehnke, *Nat. Chem.* **2023**, *15*, 560-568; 'Unusual peptide-binding proteins guide pyrroloindoline alkaloid formation in crocagin biosynthesis'; https://doi.org/10.1038/s41557-023-01153-w

[113] C. Y. Lai, I. W. Lo, R. T. Hewage, Y. C. Chen, C. T. Chen, C. F. Lee, S. Lin, M. C. Tang, H. C. Lin, *Angew. Chem. Int. Ed.* **2017**, *56*, 9478-9482; 'Biosynthesis of Complex Indole Alkaloids: Elucidation of the Concise Pathway of Okaramines'; (*Angew. Chem.*, *129*, 9606-9610) https://doi.org/10.1002/anie.201705501

[114] S. W. Haynes, X. Gao, Y. Tang, C. T. Walsh, *J. Am. Chem. Soc.* **2012**, *134*, 17444-17447; 'Assembly of asperlicin peptidyl alkaloids from anthranilate and tryptophan: a two-enzyme pathway generates heptacyclic scaffold complexity in asperlicin E'; https://doi.org/10.1021/ja308371z

[115] H. Li, Y. Qiu, C. Guo, M. Han, Y. Zhou, Y. Feng, S. Luo, Y. Tong, G. Zheng, S. Zhu, *Chem. Commun.* **2019**, *55*, 8390–8393; 'Pyrroloindoline Cyclization in Tryptophan-Containing Cyclodipeptides Mediated by an Unprecedented Indole C3 Methyltransferase from *Streptomyces* Sp. HPH0547'; https://doi.org/10.1039/c9cc03745d.

[116] W.-B. Yin, A. Grundmann, J. Cheng, S.-M. Li, *J. Biol. Chem.* **2009**, *284*, 100-109; 'Acetylaszonalenin biosynthesis in *Neosartorya fischeri*: Identification of the biosynthetic gene cluster by genomic mining and functional proof of the genes by biochemical investigation'; https://doi.org/10.1074/jbc.M807606200

[117] T. Yao, J. Liu, Z. Liu, T. Li, H. Li, Q. Che, T. Zhu, D. Li, Q. Gu, W. Li, *Nat. Commun.* **2018**, *9*, 4091; 'Genome mining of cyclodipeptide synthases unravels unusual tRNA-dependent diketopiperazine-terpene biosynthetic machinery'; https://doi.org/10.1038/s41467-018-06411-x

[118] W. Tian, C. Sun, M. Zheng, J. R. Harmer, M. Yu, Y. Zhang, H. Peng, D. Zhu, Z. Deng, S.-L. Chen, *Nat. Commun.* **2018**, *9*, 4428; 'Efficient biosynthesis of heterodimeric C3-aryl pyrroloindoline alkaloids'; https://doi.org/10.1038/s41467-018-06528-z

[119] J. Liu, X. Xie, S.-M. Li, *Chem. Commun.* **2020**, *56*, 11042-11045; 'Increasing cytochrome P450 enzyme diversity by identification of two distinct cyclodipeptide dimerases'; https://doi.org/10.1039/D0CC04772D

[120] T. Saruwatari, F. Yagishita, T. Mino, H. Noguchi, K. Hotta, K. Watanabe, *ChemBioChem* **2014**, *15*, 656-659; 'Cytochrome P450 as dimerization catalyst in diketopiperazine alkaloid biosynthesis'; https://doi.org/10.1002/cbic.201300751

[121] G.-J. Mei, W. L. Koay, C. X. A. Tan, Y. Lu, *Chem. Soc. Rev.* **2021**, *50*, 5985-6012; 'Catalytic asymmetric preparation of pyrroloindolines: strategies and applications to total synthesis'; https://doi.org/10.1039/D0CS00530D

[122] J. F. Austin, S.-G. Kim, C. J. Sinz, W.-J. Xiao, D. W. MacMillan, *Proc. Natl. Acad. Sci. U. S. A.* **2004**, *101*, 5482-5487; 'Enantioselective organocatalytic construction of pyrroloindolines by a cascade addition–cyclization strategy: synthesis of (–)-flustramine B'; https://doi.org/10.1073/pnas.0308177101

[123] R. Jiang, L. Ding, C. Zheng, S.-L. You, *Science* **2021**, *371*, 380-386; 'Iridium-catalyzed Z-retentive asymmetric allylic substitution reactions'; https://doi.org/10.1126/science.abd6095

[124] M. E. Kieffer, L. M. Repka, S. E. Reisman, *J. Am. Chem. Soc.* **2012**, *134*, 5131-5137; 'Enantioselective synthesis of tryptophan derivatives by a tandem Friedel–Crafts conjugate addition/asymmetric protonation reaction'; https://doi.org/10.1021/ja209390d

[125] J. R. Wolstenhulme, A. Cavell, M. Gredičak, R. W. Driver, M. D. Smith, *Chem. Commun.* **2014**, *50*, 13585-13588; 'A cation-directed two-component cascade approach to enantioenriched pyrroloindolines'; https://doi.org/10.1039/C4CC06683A

[126] M. Pallavicini, E. Valoti, L. Villa, I. Resta, *Tetrahedron: Asymmetry* **1994**, *5*, 363-370; 'New asymmetric synthesis of (−)-esermethole'; https://doi.org/10.1016/S0957-4166(00)86207-2

[127] W. Kong, Q. Wang, J. Zhu, *Angew. Chem. Int. Ed.* **2016**, *55*, 9714-9718; 'Synthesis of Diversely Functionalized Oxindoles Enabled by Migratory Insertion of Isocyanide to a Transient σ-Alkylpalladium (II) Complex'; (*Angew. Chem.*, *128*, 9866-9870) https://doi.org/10.1002/anie.201603950

[128] H. Tian, F. Peng, P. Zhang, H. Yang, H. Fu, *Org. Lett.* **2019**, *21*, 8501-8505; 'Highly enantioselective iridium-catalyzed cascade double allylation strategy: synthesis of pyrrolidinoindolines with an all-carbon quaternary stereocenter'; https://doi.org/10.1021/acs.orglett.9b03382

[129] L. M. Repka, S. E. Reisman, *J. Org. Chem.* **2013**, *78*, 12314-12320; 'Recent developments in the catalytic, asymmetric construction of pyrroloindolines bearing all-carbon quaternary stereocenters'; https://doi.org/10.1021/jo4017953

[130] I. Silman, J. L. Sussman, *Curr. Opin. Pharmacol.* **2005**, *5*, 293-302; 'Acetylcholinesterase: 'classical' and 'non-classical' functions and pharmacology'; https://doi.org/10.1016/j.coph.2005.01.014

[131] M. Jokanović, *Toxicol. Lett.* **2009**, *190*, 107-115; 'Medical treatment of acute poisoning with organophosphorus and carbamate pesticides'; https://doi.org/10.1016/j.toxlet.2009.07.025

[132] L. Santarpia, I. Grandone, F. Contaldo, F. Pasanisi, *J. Cachexia Sarcopenia Muscle* **2013**, *4*, 31-39; 'Butyrylcholinesterase as a prognostic marker: a review of the literature'; https://doi.org/10.1007/s13539-012-0083-5

[133] P. Masson, O. Lockridge, *Arch. Biochem. Biophys.* **2010**, *494*, 107-120; 'Butyrylcholinesterase for protection from organophosphorus poisons: catalytic complexities and hysteretic behavior'; https://doi.org/10.1016/j.abb.2009.12.005

[134] S. Xing, Q. Li, B. Xiong, Y. Chen, F. Feng, W. Liu, H. Sun, *Med. Res. Rev.* **2021**, *41*, 858-901; 'Structure and therapeutic uses of butyrylcholinesterase: application in detoxification, Alzheimer's disease, and fat metabolism'; https://doi.org/10.1002/med.21745

[135] H. Soreq, S. Seidman, *Nat. Rev. Neurosci.* **2001**, *2*, 294-302; 'Acetylcholinesterase--new roles for an old actor'; https://doi.org/10.1038/35067589
[136] Ł. J. Walczak-Nowicka, M. Herbet, *Int. J. Mol. Sci.* **2021**, *22*, 9290; 'Acetylcholinesterase inhibitors in the treatment of neurodegenerative diseases and the role of acetylcholinesterase in their pathogenesis'; https://doi.org/10.3390/ijms22179290
[137] I. Silman, J. L. Sussman, *Chem.-Biol. Interact.* **2008**, *175*, 3-10; 'Acetylcholinesterase: how is structure related to function?'; https://doi.org/10.1016/j.cbi.2008.05.035
[138] H. Dvir, I. Silman, M. Harel, T. L. Rosenberry, J. L. Sussman, *Chem.-Biol. Interact.* **2010**, *187*, 10-22; 'Acetylcholinesterase: from 3D structure to function'; https://doi.org/10.1016/j.cbi.2010.01.042
[139] P. Taylor, S. Camp, Z. Radić, *Acetylcholinesterase,* in *Encyclopedia of Neuroscience* (Ed.: L. R. Squire), Academic Press, Oxford, **2009**, pp. 5-7.
[140] C. E. Felder, S. A. Botti, S. Lifson, I. Silman, J. L. Sussman, *J. Mol. Graphics Modell.* **1997**, *15*, 318-327; 'External and internal electrostatic potentials of cholinesterase models'; https://doi.org/10.1016/S1093-3263(98)00005-9
[141] G. Marucci, M. Buccioni, D. D. Ben, C. Lambertucci, R. Volpini, F. Amenta, *Neuropharmacology* **2021**, *190*, 108352; 'Efficacy of acetylcholinesterase inhibitors in Alzheimer's disease'; https://doi.org/10.1016/j.neuropharm.2020.108352
[142] B. David, P. Schneider, P. Schäfer, J. Pietruszka, H. Gohlke, *J. Enzyme Inhib. Med. Chem.* **2021**, *36*, 491-496; 'Discovery of new acetylcholinesterase inhibitors for Alzheimer's disease: virtual screening and in vitro characterisation'; https://doi.org/10.1080/14756366.2021.1876685
[143] B. Dworacek, J. Rupreht, *Int. Congr. Ser.* **2002**, *1242*, 87-93; 'Physostigmine: short history and its impact on anaesthesiology of present days'; https://doi.org/10.1016/S0531-5131(02)00705-7
[144] D. J. Triggle, J. M. Mitchell, R. Filler, *CNS Drug Rev.* **1998**, *4*, 87–136; 'The Pharmacology of Physostigmine'; https://doi.org/10.1111/j.1527-3458.1998.tb00059.x
[145] A. Kadir, N. Andreasen, O. Almkvist, A. Wall, A. Forsberg, H. Engler, G. Hagman, M. Lärksäter, B. Winblad, H. Zetterberg, K. Blennow, B. Långström, A. Nordberg, *Ann. Neurol.* **2008**, *63*, 621-631; 'Effect of phenserine treatment on brain functional activity and amyloid in Alzheimer's disease'; https://doi.org/10.1002/ana.21345
[146] J. Klein, *Expert Opin. Invest. Drugs* **2007**, *16*, 1087-1097; 'Phenserine'; https://doi.org/10.1517/13543784.16.7.1087
[147] D. K. Lahiri, D. Chen, B. Maloney, H. W. Holloway, Q.-s. Yu, T. Utsuki, T. Giordano, K. Sambamurti, N. H. Greig, *J. Pharmacol. Exp. Ther.* **2007**, *320*, 386-396; 'The experimental Alzheimer's disease drug posiphen [(+)-phenserine] lowers amyloid-β peptide levels in cell culture and mice'; https://doi.org/10.1124/jpet.106.112102
[148] F. Dale, B. Robinson, *J. Pharm. Pharmacol.* **1970**, *22*, 889-896; 'The synthesis and anti-acetylcholinesterase activities of (+)-physostigmine and (+)-physovenine'; https://doi.org/10.1111/j.2042-7158.1970.tb08469.x
[149] B. Robinson, 'The Calabar Bean and Its Alkaloids: From Magic, Via Miracle, to Memory', Springer, **2023**.
[150] Q.-s. Yu, X. Zhu, H. W. Holloway, N. F. Whittaker, A. Brossi, N. H. Greig, *J. Med. Chem.* **2002**, *45*, 3684-3691; 'Anticholinesterase activity of compounds related to geneserine tautomers. N-Oxides and 1, 2-oxazines'; https://doi.org/10.1021/jm010491d
[151] A. Shafferman, D. Barak, D. Stein, C. Kronman, B. Velan, N. H. Greig, A. Ordentlich, *Chem. Biol. Interact.* **2008**, *175*, 166-172; 'Flexibility versus "rigidity" of the functional architecture of AChE active center'; https://doi.org/10.1016/j.cbi.2008.03.013
[152] H. Zhang, Y. Wang, Y. Wang, X. Li, S. Wang, Z. Wang, *Eur. J. Med. Chem.* **2022**, *240*, 114606; 'Recent advance on carbamate-based cholinesterase inhibitors as potential multifunctional agents against Alzheimer's disease'; https://doi.org/10.1016/j.ejmech.2022.114606
[153] L. Winand, P. Schneider, S. Kruth, N. J. Greven, W. Hiller, M. Kaiser, J. Pietruszka, M. Nett, *Org. Lett.* **2021**, *23*, 6563-6567; 'Mutasynthesis of Physostigmines in *Myxococcus xanthus*'; https://doi.org/10.1021/acs.orglett.1c02374

[154] E. Romero, B. S. Jones, B. N. Hogg, A. Rué Casamajo, M. A. Hayes, S. L. Flitsch, N. J. Turner, C. Schnepel, *Angew. Chem. Int. Ed.* **2021**, *60*, 16824-16855; 'Enzymatic late-stage modifications: better late than never'; (*Angew. Chem.*, *133*, 16962-16993) https://doi.org/10.1002/anie.202014931

[155] N. A. McGrath, M. Brichacek, J. T. Njardarson, *J. Chem. Educ.* **2010**, *87*, 1348-1349; 'A Graphical Journey of Innovative Organic Architectures That Have Improved Our Lives'; https://doi.org/10.1021/ed1003806

[156] H. Schönherr, T. Cernak, *Angew. Chem. Int. Ed.* **2013**, *52*, 12256-12267; 'Profound Methyl Effects in Drug Discovery and a Call for New C-H Methylation Reactions'; https://doi.org/10.1002/anie.201303207.

[157] B. G. Vértessy, J. Tóth, *Acc. Chem. Res.* **2009**, *42*, 97-106; 'Keeping uracil out of DNA: physiological role, structure and catalytic mechanism of dUTPases'; https://doi.org/10.1021/ar800114w

[158] D. L. Nelson, A. L. Lehninger, M. M. Cox, 'Lehninger principles of biochemistry', Macmillan, **2008**.

[159] P. S. M. Pinheiro, L. S. Franco, C. A. M. Fraga, *Pharmaceuticals (Basel)* **2023**, *16*, 1157; 'The Magic Methyl and Its Tricks in Drug Discovery and Development'; https://doi.org/10.3390/ph16081157

[160] C. S. Leung, S. S. F. Leung, J. Tirado-Rives, W. L. Jorgensen, *J. Med. Chem.* **2012**, *55*, 4489–4500; 'Methyl Effects on Protein − Ligand Binding'; https://doi.org/10.1021/jm3003697

[161] K. W. Kuntz, J. E. Campbell, H. Keilhack, R. M. Pollock, S. K. Knutson, M. Porter-Scott, V. M. Richon, C. J. Sneeringer, T. J. Wigle, C. J. Allain, C. R. Majer, M. P. Moyer, R. A. Copeland, R. Chesworth, *J. Med. Chem.* **2016**, *59*, 1556-1564; 'The importance of being me: magic methyls, methyltransferase inhibitors, and the discovery of tazemetostat'; https://doi.org/10.1021/acs.jmedchem.5b01501

[162] P. W. Ondachi, C. M. Kormos, S. P. Runyon, J. B. Thomas, S. W. Mascarella, A. M. Decker, H. A. Navarro, T. R. Fennell, R. W. Snyder, F. I. Carroll, *J. Med. Chem.* **2018**, *61*, 7525-7545; 'Potent and Selective Tetrahydroisoquinoline Kappa Opioid Receptor Antagonists of Lead Compound (3 R)-7-Hydroxy-N-[(1 S)-2-Methyl-1-(Piperidin-1-Ylmethyl) Propyl]-1, 2, 3, 4-Tetrahydroisoquinoline-3-Carboxamide (PDTic)'; https://doi.org/10.1021/acs.jmedchem.8b00673

[163] D. A. Rodrigues, G. À. Ferreira-Silva, A. C. Ferreira, R. A. Fernandes, J. K. Kwee, C. M. Sant'Anna, M. Ionta, C. A. Fraga, *J. Med. Chem.* **2016**, *59*, 655-670; 'Design, synthesis, and pharmacological evaluation of novel N-acylhydrazone derivatives as potent histone deacetylase 6/8 dual inhibitors'; https://doi.org/10.1021/acs.jmedchem.5b01525

[164] K. Liu, D. Li, W. Zheng, M. Shi, Y. Chen, M. Tang, T. Yang, M. Zhao, D. Deng, C. Zhang, J. Liu, X. Yuan, Z. Yang, L. Chen, *J. Med. Chem.* **2021**, *64*, 8951-8970; 'Discovery, optimization, and evaluation of quinazolinone derivatives with novel linkers as orally efficacious phosphoinositide-3-kinase delta inhibitors for treatment of inflammatory diseases'; https://doi.org/10.1021/acs.jmedchem.1c00004

[165] R. Angell, N. M. Aston, P. Bamborough, J. B. Buckton, S. Cockerill, S. J. deBoeck, C. D. Edwards, D. S. Holmes, K. L. Jones, D. I. Laine, S. Patel, P. A. Smee, K. J. Smith, D. O. Somers, A. L. Walker, *Bioorg. Med. Chem. Lett.* **2008**, *18*, 4428-4432; 'Biphenyl amide p38 kinase inhibitors 3: Improvement of cellular and in vivo activity'; https://doi.org/10.1016/j.bmcl.2008.06.048

[166] T. W. Lyons, M. S. Sanford, *Chem. Rev.* **2010**, *110*, 1147-1169; 'Palladium-catalyzed ligand-directed C− H functionalization reactions'; https://doi.org/10.1021/cr900184e

[167] T.-Z. Wang, Y.-Q. Guan, T.-Y. Zhang, Y.-F. Liang, *Advanced Science* **2024**, *11*, 2306923; 'Ligand Relay for Nickel-Catalyzed Decarbonylative Alkylation of Aroyl Chlorides'; https://doi.org/10.1002/advs.202306923

[168] A. I. Frolov, E. N. Ostapchuk, A. E. Pashenko, Y. O. Chuchvera, E. B. Rusanov, D. M. Volochnyuk, S. V. Ryabukhin, *J. Org. Chem.* **2021**, *86*, 7333-7346; 'Selective α-Methylation of Ketones'; https://doi.org.10.1021/acs.joc.1c00148

[169] F. Minisci, R. Bernardi, F. Bertini, R. Galli, M. Perchinummo, *Tetrahedron* **1971**, *27*, 3575-3579; 'Nucleophilic character of alkyl radicals—VI: A new convenient selective alkylation of heteroaromatic bases'; https://doi.org/10.1016/S0040-4020(01)97768-3

[170] J. Jin, D. W. MacMillan, *Nature* **2015**, *525*, 87-90; 'Alcohols as alkylating agents in heteroarene C–H functionalization'; https://doi.org/10.1038/nature14885

[171] F. Zhang, X.-F. Duan, *Org. Lett.* **2011**, *13*, 6102-6105; 'Facile one-pot direct arylation and alkylation of nitropyridine N-oxides with Grignard reagents'; https://doi.org/10.1021/ol202597b

[172] X.-C. Wang, W. Gong, L.-Z. Fang, R.-Y. Zhu, S. Li, K. M. Engle, J.-Q. Yu, *Nature* **2015**, *519*, 334-338; 'Ligand-enabled meta-C–H activation using a transient mediator'; https://doi.org/10.1038/nature14214

[173] Z.-T. He, H. Li, A. M. Haydl, G. T. Whiteker, J. F. Hartwig, *J. Am. Chem. Soc.* **2018**, *140*, 17197-17202; 'Trimethylphosphate as a methylating agent for cross coupling: a slow-release mechanism for the methylation of arylboronic esters'; https://doi.org/10.1021/jacs.8b10076

[174] C. Le, Y. Liang, R. W. Evans, X. Li, D. W. C. MacMillan, *Nature* **2017**, *547*, 79-83; 'Selective sp^3 C–H alkylation via polarity-match-based cross-coupling'; https://doi.org/10.1038/nature22813

[175] M. Liu, Z. Qiu, L. Tan, R. T. Rashid, S. Chu, Y. Cen, Z. Luo, R. Z. Khaliullin, Z. Mi, C.-J. Li, *ACS Catal.* **2020**, *10*, 6248-6253; 'Photocatalytic methylation of nonactivated Sp^3 and Sp^2 C–H Bonds using methanol on GaN'; https://doi.org/10.1021/acscatal.0c00881

[176] Y. Chen, *Chemistry – A European Journal* **2019**, *25*, 3405-3439; 'Recent Advances in Methylation: A Guide for Selecting Methylation Reagents'; https://doi.org/10.1002/chem.201803642

[177] R. Cano, A. Zakarian, G. P. McGlacken, *Angew. Chem. Int. Ed.* **2017**, *56*, 9278-9290; 'Direct Asymmetric Alkylation of Ketones: Still Unconquered'; https://doi.org/10.1002/anie.201703079

[178] T. B. Wright, P. A. Evans, *Chem. Rev.* **2021**, *121*, 9196-9242; 'Catalytic enantioselective alkylation of prochiral enolates'; https://doi.org/10.1021/acs.chemrev.0c00564

[179] D. J. Pollard, J. M. Woodley, *Trends Biotechnol.* **2007**, *25*, 66-73; 'Biocatalysis for pharmaceutical intermediates: the future is now'; https://doi.org/10.1016/j.tibtech.2006.12.005

[180] H. Yamada, M. Kobayashi, *Biosci. Biotechnol. Biochem.* **1996**, *60*, 1391-1400; 'Nitrile hydratase and its application to industrial production of acrylamide'; https://doi.org/10.1271/bbb.60.1391

[181] O. Kirk, T. V. Borchert, C. C. Fuglsang, *Curr. Opin. Biotechnol.* **2002**, *13*, 345-351; 'Industrial enzyme applications'; https://doi.org/10.1016/s0958-1669(02)00328-2

[182] J. M. Woodley, *ChemSusChem* **2022**, *15*, e202102683; 'Ensuring the Sustainability of Biocatalysis'; https://doi.org/10.1002/cssc.202102683

[183] D. Yi, T. Bayer, C. P. S. Badenhorst, S. Wu, M. Doerr, M. Hohne, U. T. Bornscheuer, *Chem. Soc. Rev.* **2021**, *50*, 8003-8049; 'Recent trends in biocatalysis'; https://doi.org/10.1039/d0cs01575j

[184] F. Guo, P. Berglund, *Green Chem.* **2017**, *19*, 333-360; 'Transaminase biocatalysis: optimization and application'; https://doi.org/10.1039/C6GC02328B

[185] Y. Deng, Q. Zhou, Y. Wu, X. Chen, F. Zhong, *Int. J. Mol. Sci.* **2022**, *23*, 2622; 'Properties and Mechanisms of Flavin-Dependent Monooxygenases and Their Applications in Natural Product Synthesis'; https://doi.org/10.3390/ijms23052622

[186] Z. Li, H. Yang, J. Liu, Z. Huang, F. Chen, *Chem. Rec.* **2021**, *21*, 1611-1630; 'Application of Ketoreductase in Asymmetric Synthesis of Pharmaceuticals and Bioactive Molecules: An Update (2018-2020)'; https://doi.org/10.1002/tcr.202100062

[187] S. Verma, R. N. Choudhary, A. P. Kanadje, U. C. Banerjee, *Catalysts* **2021**, *11*, 1328; 'Diversifying arena of drug synthesis: In the realm of lipase mediated waves of biocatalysis'; https://doi.org/10.3390/catal11111328

[188] N. J. Turner, *Curr. Opin. Chem. Biol.* **2011**, *15*, 234-240; 'Ammonia lyases and aminomutases as biocatalysts for the synthesis of α-amino and β-amino acids'; https://doi.org/10.1016/j.cbpa.2010.11.009

[189] L. Guillemard, N. Kaplaneris, L. Ackermann, M. J. Johansson, *Nat. Rev. Chem.* **2021**, *5*, 522-545; 'Late-stage C-H functionalization offers new opportunities in drug discovery'; https://doi.org/10.1038/s41570-021-00300-6

[190] V. Tournier, C. M. Topham, A. Gilles, B. David, C. Folgoas, E. Moya-Leclair, E. Kamionka, M. L. Desrousseaux, H. Texier, S. Gavalda, M. Cot, E. Guemard, M. Dalibey, J. Nomme, G. Cioci, S. Barbe, M. Chateau, I. Andre, S. Duquesne, A. Marty, *Nature* **2020**, *580*, 216-219; 'An engineered PET depolymerase to break down and recycle plastic bottles'; https://doi.org/10.1038/s41586-020-2149-4

[191] A. Nivina, K. P. Yuet, J. Hsu, C. Khosla, *Chem. Rev.* **2019**, *119*, 12524-12547; 'Evolution and diversity of assembly-line polyketide synthases: Focus review'; https://doi.org/10.1021/acs.chemrev.9b00525

[192] E. L. Bell, W. Finnigan, S. P. France, A. P. Green, M. A. Hayes, L. J. Hepworth, S. L. Lovelock, H. Niikura, S. Osuna, E. Romero, *Nat. Rev. Methods Primers* **2021**, *1*, 1-21; 'Biocatalysis'; https://doi.org/10.1038/s43586-021-00044-z

[193] S. Wu, R. Snajdrova, J. C. Moore, K. Baldenius, U. T. Bornscheuer, *Angew. Chem. Int. Ed.* **2021**, *60*, 88-119; 'Biocatalysis: Enzymatic Synthesis for Industrial Applications'; (*Angew. Chem.*, *133*, 89-123) https://doi.org/10.1002/anie.202006648

[194] M. A. Huffman, A. Fryszkowska, O. Alvizo, M. Borra-Garske, K. R. Campos, K. A. Canada, P. N. Devine, D. Duan, J. H. Forstater, S. T. Grosser, H. M. Halsey, G. J. Hughes, J. Jo, L. A. Joyce, J. N. Kolev, J. Liang, K. M. Maloney, B. F. Mann, N. M. Marshall, M. McLaughlin, J. C. Moore, G. S. Murphy, C. C. Nawrat, J. Nazor, S. Novick, N. R. Patel, A. Rodriguez-Granillo, S. A. Robaire, E. C. Sherer, M. D. Truppo, A. M. Whittaker, D. Verma, L. Xiao, Y. Xu, H. Yang, *Science* **2019**, *366*, 1255-1259; 'Design of an in vitro biocatalytic cascade for the manufacture of islatravir'; https://doi.org/10.1126/science.aay8484

[195] M. A. Valliere, T. P. Korman, M. A. Arbing, J. U. Bowie, *Nat. Chem. Biol.* **2020**, *16*, 1427-1433; 'A bio-inspired cell-free system for cannabinoid production from inexpensive inputs'; https://doi.org/10.1038/s41589-020-0631-9

[196] C. Greunke, A. Glockle, J. Antosch, T. A. Gulder, *Angew. Chem. Int. Ed.* **2017**, *56*, 4351-4355; 'Biocatalytic Total Synthesis of Ikarugamycin'; (*Angew. Chem.*, *129*, 4416-4420) https://doi.org/10.1002/anie.201611063

[197] Q. Cheng, L. Xiang, M. Izumikawa, D. Meluzzi, B. S. Moore, *Nat. Chem. Biol.* **2007**, *3*, 557-558; 'Enzymatic total synthesis of enterocin polyketides'; https://doi.org/10.1038/nchembio.2007.22

[198] P. Srinivasan, C. D. Smolke, *Nature* **2020**, *585*, 614-619; 'Biosynthesis of medicinal tropane alkaloids in yeast'; https://doi.org/10.1038/s41586-020-2650-9

[199] S. Szymkuć, E. P. Gajewska, T. Klucznik, K. Molga, P. Dittwald, M. Startek, M. Bajczyk, B. A. Grzybowski, *Angew. Chem. Int. Ed.* **2016**, *55*, 5904-5937; 'Computer-Assisted Synthetic Planning: The End of the Beginning'; https://doi.org/10.1002/anie.201506101

[200] M. Koch, T. Duigou, J.-L. Faulon, *ACS Synth. Biol.* **2020**, *9*, 157-168; 'Reinforcement Learning for Bioretrosynthesis'; https://doi.org.10.1021/acssynbio.9b00447

[201] W. Finnigan, L. J. Hepworth, S. L. Flitsch, N. J. Turner, *Nat. Catal.* **2021**, *4*, 98-104; 'RetroBioCat as a computer-aided synthesis planning tool for biocatalytic reactions and cascades'; https://doi.org/10.1038/s41929-020-00556-z

[202] V. K. Sharma, J. M. Hutchison, A. M. Allgeier, *ChemSusChem* **2022**, *15*, e202200888; 'Redox Biocatalysis: Quantitative Comparisons of Nicotinamide Cofactor Regeneration Methods'; https://doi.org/10.1002/cssc.202200888

[203] K. Bachosz, J. Zdarta, M. Bilal, A. S. Meyer, T. Jesionowski, *Sci. Total Environ.* **2023**, *868*, 161630; 'Enzymatic cofactor regeneration systems: A new perspective on efficiency assessment'; https://doi.org/10.1016/j.scitotenv.2023.161630

[204] H. Chen, Y. P. J. Zhang, *Crit. Rev. Biotechnol.* **2021**, *41*, 16-33; 'Enzymatic regeneration and conservation of ATP: challenges and opportunities'; https://doi.org/10.1080/07388551.2020.1826403

[205] M. Frese, N. Sewald, *Angew. Chem. Int. Ed.* **2015**, *54*, 298-301; 'Enzymatic halogenation of tryptophan on a gram scale'; (*Angew. Chem.*, *127*, 302-305) https://doi.org/10.1002/anie.201408561

[206] J. T. Payne, M. C. Andorfer, J. C. Lewis, *Angew. Chem. Int. Ed.* **2013**, *52*, 5271-5274; 'Regioselective arene halogenation using the FAD-dependent halogenase RebH'; (*Angew. Chem.*, *125*, 5379-5382) https://doi.org/10.1002/anie.201300762

[207] C. Liao, F. P. Seebeck, *Nat. Catal.* **2019**, *2*, 696–701; '*S*-Adenosylhomocysteine as a Methyl Transfer Catalyst in Biocatalytic Methylation Reactions'; https://doi.org/10.1038/s41929-019-0300-0.

[208] C. Wandrey, A. Liese, D. Kihumbu, *Org. Process Res. Dev.* **2000**, *4*, 286-290; 'Industrial biocatalysis: past, present, and future'; https://doi.org/10.1021/op990101l

[209] K. Vedha-Peters, M. Gunawardana, J. D. Rozzell, S. J. Novick, *J. Am. Chem. Soc.* **2006**, *128*, 10923-10929; 'Creation of a broad-range and highly stereoselective D-amino acid dehydrogenase for the one-step synthesis of D-amino acids'; https://doi.org/10.1021/ja0603960

[210] K. H. Nam, *Appl. Sci.* **2022**, *12*, 428; 'Glucose isomerase: functions, structures, and applications'; https://doi.org/10.3390/app12010428

[211] S. V. Nilsson, G. Magnusson, *Nucleic Acids Res.* **1982**, *10*, 1425-1437; 'Sealing of gaps in duplex DNA by T4 DNA ligase'; https://doi.org/10.1093/nar/10.5.1425

[212] E. Jockmann, F. Subrizi, M. K. F. Mohr, E. M. Carter, P. M. Hebecker, D. Popadić, H. C. Hailes, J. N. Andexer, *ChemCatChem* **2023**, *15*, e202300930; 'Expanding the Substrate Scope of N- and O-Methyltransferases from Plants for Chemoselective Alkylation'; https://doi.org/10.1002/cctc.202300930

[213] I. Drienovská, G. Roelfes, *Nat. Catal.* **2020**, *3*, 193-202; 'Expanding the enzyme universe with genetically encoded unnatural amino acids'; https://doi.org/10.1038/s41929-019-0410-8

[214] Z. Birch-Price, F. J. Hardy, T. M. Lister, A. R. Kohn, A. P. Green, *Chem. Rev.* **2024**, *124*, 8740-8786; 'Noncanonical Amino Acids in Biocatalysis'; https://doi.org/10.1021/acs.chemrev.4c00120

[215] I. Drienovska, C. Mayer, C. Dulson, G. Roelfes, *Nat. Chem.* **2018**, *10*, 946-952; 'A designer enzyme for hydrazone and oxime formation featuring an unnatural catalytic aniline residue'; https://doi.org/10.1038/s41557-018-0082-z

[216] Y. Pan, G. Li, R. Liu, J. Guo, Y. Liu, M. Liu, X. Zhang, L. Chi, K. Xu, R. Wu, Y. Zhang, Y. Li, X. Gao, S. Li, *Nat. Commun.* **2023**, *14*, 1669; 'Unnatural activities and mechanistic insights of cytochrome P450 PikC gained from site-specific mutagenesis by non-canonical amino acids'; https://doi.org/10.1038/s41467-023-37288-0

[217] W. Harrison, X. Huang, H. Zhao, *Acc. Chem. Res.* **2022**, *55*, 1087-1096; 'Photobiocatalysis for Abiological Transformations'; https://doi.org/10.1021/acs.accounts.1c00719

[218] Y. Peng, Z. Chen, J. Xu, Q. Wu, *Org. Process Res. Dev.* **2022**, *26*, 1900-1913; 'Recent advances in photobiocatalysis for selective organic synthesis'; https://doi.org/10.1021/acs.oprd.1c00413

[219] X. Huang, B. Wang, Y. Wang, G. Jiang, J. Feng, H. Zhao, *Nature* **2020**, *584*, 69-74; 'Photoenzymatic enantioselective intermolecular radical hydroalkylation'; https://doi.org/10.1038/s41586-020-2406-6

[220] K. F. Biegasiewicz, S. J. Cooper, X. Gao, D. G. Oblinsky, J. H. Kim, S. E. Garfinkle, L. A. Joyce, B. A. Sandoval, G. D. Scholes, T. K. Hyster, *Science* **2019**, *364*, 1166-1169; 'Photoexcitation of flavoenzymes enables a stereoselective radical cyclization'; https://doi.org/10.1126/science.aaw1143

[221] M. A. Emmanuel, N. R. Greenberg, D. G. Oblinsky, T. K. Hyster, *Nature* **2016**, *540*, 414-417; 'Accessing non-natural reactivity by irradiating nicotinamide-dependent enzymes with light'; https://doi.org/10.1038/nature20569

[222] A. S. Klein, F. Leiss-Maier, R. Muhlhofer, B. Boesen, G. Mustafa, H. Kugler, C. Zeymer, *J. Am. Chem. Soc.* **2024**, *146*, 25976-25985; 'A *De Novo* Metalloenzyme for Cerium Photoredox Catalysis'; https://doi.org/10.1021/jacs.4c04618
[223] H. Naess-Schmidt, S., S. R. Vejgaard, M. M. Hansen, J. Lutz, *Copenhagen Economics* **2022**; 'The potentials of biosolutions ';
[224] C. Fetting, *ESDN Report, December* **2020**, *2*; 'The European green deal';
[225] M. Braun, C. C. Gruber, A. Krassnigg, A. Kummer, S. Lutz, G. Oberdorfer, E. Siirola, R. Snajdrova, *ACS Catal.* **2023**, *13*, 14454-14469; 'Accelerating Biocatalysis Discovery with Machine Learning: A Paradigm Shift in Enzyme Engineering, Discovery, and Design'; https://doi.org/10.1021/acscatal.3c03417
[226] U. T. Bornscheuer, G. W. Huisman, R. J. Kazlauskas, S. Lutz, J. C. Moore, K. Robins, *Nature* **2012**, *485*, 185-194; 'Engineering the third wave of biocatalysis'; https://doi.org/10.1038/nature11117
[227] E. E. Drufva, N. R. Spengler, E. G. Hix, C. B. Bailey, *ChemBioChem* **2021**, *22*, 1122-1150; 'Site-Directed Mutagenesis of Modular Polyketide Synthase Ketoreductase Domains for Altered Stereochemical Control'; https://doi.org/10.1002/cbic.202000613
[228] L. Tong, J. Zheng, X. Wang, X. Wang, H. Huang, H. Yang, T. Tu, Y. Wang, Y. Bai, B. Yao, H. Luo, X. Qin, *Biotechnol. Biofuels* **2021**, *14*, 202; 'Improvement of thermostability and catalytic efficiency of glucoamylase from *Talaromyces leycettanus* JCM12802 via site-directed mutagenesis to enhance industrial saccharification applications'; https://doi.org/10.1186/s13068-021-02052-3
[229] W. P. Stemmer, *Nature* **1994**, *370*, 389-391; 'Rapid evolution of a protein in vitro by DNA shuffling'; https://doi.org/10.1038/370389a0
[230] R. C. Cadwell, G. F. Joyce, *PCR Methods Appl.* **1992**, *2*, 28-33; 'Randomization of genes by PCR mutagenesis'; https://doi.org/10.1101/gr.2.1.28
[231] Y. Wang, P. Xue, M. Cao, T. Yu, S. T. Lane, H. Zhao, *Chem. Rev.* **2021**, *121*, 12384-12444; 'Directed Evolution: Methodologies and Applications'; https://doi.org/10.1021/acs.chemrev.1c00260
[232] R. Carr, M. Alexeeva, A. Enright, T. S. Eve, M. J. Dawson, N. J. Turner, *Angew. Chem. Int. Ed.* **2003**, *42*, 4807-4810; 'Directed evolution of an amine oxidase possessing both broad substrate specificity and high enantioselectivity'; (*Angew. Chem.*, *155*, 4955-4958) https://doi.org/10.1002/anie.200352100
[233] L. Shi, P. Liu, Z. Tan, W. Zhao, J. Gao, Q. Gu, H. Ma, H. Liu, L. Zhu, *Angew. Chem. Int. Ed.* **2023**, *62*, e202218390; 'Complete depolymerization of PET wastes by an evolved PET hydrolase from directed evolution'; (*Angew. Chem.*, *135*, e202218390) https://doi.org/10.1002/anie.202218390
[234] S. K. Ma, J. Gruber, C. Davis, L. Newman, D. Gray, A. Wang, J. Grate, G. W. Huisman, R. A. Sheldon, *Green Chem.* **2010**, *12*, 81-86; 'A green-by-design biocatalytic process for atorvastatin intermediate'; https://doi.org/10.1039/B919115C
[235] M. T. Reetz, S. Wu, *Chem. Commun.* **2008**, 5499-5501; 'Greatly reduced amino acid alphabets in directed evolution: making the right choice for saturation mutagenesis at homologous enzyme positions'; https://doi.org/10.1039/b813388c
[236] M. T. Reetz, J. D. Carballeira, *Nat. Protoc.* **2007**, *2*, 891-903; 'Iterative saturation mutagenesis (ISM) for rapid directed evolution of functional enzymes'; https://doi.org/10.1038/nprot.2007.72
[237] K. Wu, H. Wang, L. Chen, H. Fan, Z. Zhao, D. Wei, *Appl. Microbiol. Biotechnol.* **2016**, *100*, 8757-8767; 'Practical two-step synthesis of enantiopure styrene oxide through an optimized chemoenzymatic approach'; https://doi.org/10.1007/s00253-016-7631-4
[238] Y. P. Xue, C. C. Shi, Z. Xu, B. Jiao, Z. Q. Liu, J. F. Huang, Y. G. Zheng, Y. C. Shen, *Adv. Synth. Catal.* **2015**, *357*, 1741-1750; 'Design of nitrilases with superior activity and enantioselectivity towards sterically hindered nitrile by protein engineering'; https://doi.org/10.1002/adsc.201500039
[239] R. J. Fox, S. C. Davis, E. C. Mundorff, L. M. Newman, V. Gavrilovic, S. K. Ma, L. M. Chung, C. Ching, S. Tam, S. Muley, J. Grate, J. Gruber, J. C. Whitman, R. A. Sheldon, G. W. Huisman, *Nat. Biotechnol.* **2007**, *25*, 338-344; 'Improving catalytic function by ProSAR-driven enzyme evolution'; https://doi.org/10.1038/nbt1286

[240] F. Cheng, L. Zhu, U. Schwaneberg, *Chem. Commun.* **2015**, *51*, 9760-9772; 'Directed evolution 2.0: improving and deciphering enzyme properties'; 10.1039/C5CC01594D

[241] S. Brands, H. U. C. Brass, A. S. Klein, J. G. Sikkens, M. D. Davari, J. Pietruszka, A. J. Ruff, U. Schwaneberg, *Catal. Sci. Technol.* **2021**, *11*, 2805-2815; 'KnowVolution of prodigiosin ligase PigC towards condensation of short-chain prodiginines'; https://doi.org/10.1039/D0CY02297G

[242] F. Contreras, M. J. Thiele, S. Pramanik, A. M. Rozhkova, A. S. Dotsenko, I. N. Zorov, A. P. Sinitsyn, M. D. Davari, U. Schwaneberg, *ACS Sustainable Chemistry & Engineering* **2020**, *8*, 12388-12399; 'KnowVolution of a GH5 Cellulase from Penicillium verruculosum to Improve Thermal Stability for Biomass Degradation'; https://doi.org/10.1021/acssuschemeng.0c02465

[243] C. Novoa, G. V. Dhoke, D. M. Mate, R. Martínez, T. Haarmann, M. Schreiter, J. Eidner, R. Schwerdtfeger, P. Lorenz, M. D. Davari, F. Jakob, U. Schwaneberg, *ChemBioChem* **2019**, *20*, 1458-1466; 'KnowVolution of a Fungal Laccase toward Alkaline pH'; https://doi.org/10.1002/cbic.201800807

[244] M. A. Reiter, T. Bradley, L. A. Buchel, P. Keller, E. Hegedis, T. Gassler, J. A. Vorholt, *Nat. Catal.* **2024**, *7*, 560-573; 'A synthetic methylotrophic *Escherichia coli* as a chassis for bioproduction from methanol'; https://doi.org/10.1038/s41929-024-01137-0

[245] J. Ru, Y. Huo, Y. Yang, *Front. Microbiol.* **2020**, *11*, 442; 'Microbial Degradation and Valorization of Plastic Wastes'; https://doi.org/10.3389/fmicb.2020.00442

[246] Y. Dehouck, J. M. Kwasigroch, D. Gilis, M. Rooman, *BMC Bioinf.* **2011**, *12*, 151; 'PoPMuSiC 2.1: a web server for the estimation of protein stability changes upon mutation and sequence optimality'; https://doi.org/10.1186/1471-2105-12-151

[247] Y. Choi, A. P. Chan, *Bioinformatics* **2015**, *31*, 2745-2747; 'PROVEAN web server: a tool to predict the functional effect of amino acid substitutions and indels'; https://doi.org/10.1093/bioinformatics/btv195

[248] E. Chovancova, A. Pavelka, P. Benes, O. Strnad, J. Brezovsky, B. Kozlikova, A. Gora, V. Sustr, M. Klvana, P. Medek, L. Biedermannova, J. Sochor, J. Damborsky, *PLoS Comput. Biol.* **2012**, *8*, e1002708; 'CAVER 3.0: a tool for the analysis of transport pathways in dynamic protein structures'; https://doi.org/10.1371/journal.pcbi.1002708

[249] O. Khersonsky, R. Lipsh, Z. Avizemer, Y. Ashani, M. Goldsmith, H. Leader, O. Dym, S. Rogotner, D. L. Trudeau, J. Prilusky, P. Amengual-Rigo, V. Guallar, D. S. Tawfik, S. J. Fleishman, *Mol. Cell* **2018**, *72*, 178-186.E175; 'Automated Design of Efficient and Functionally Diverse Enzyme Repertoires'; https://doi.org/10.1016/j.molcel.2018.08.033

[250] L. Sumbalova, J. Stourac, T. Martinek, D. Bednar, J. Damborsky, *Nucleic Acids Res.* **2018**, *46*, W356-W362; 'HotSpot Wizard 3.0: web server for automated design of mutations and smart libraries based on sequence input information'; https://doi.org/10.1093/nar/gky417

[251] D. A. Case, H. M. Aktulga, K. Belfon, D. S. Cerutti, G. A. Cisneros, V. W. D. Cruzeiro, N. Forouzesh, T. J. Giese, A. W. Gotz, H. Gohlke, S. Izadi, K. Kasavajhala, M. C. Kaymak, E. King, T. Kurtzman, T. S. Lee, P. Li, J. Liu, T. Luchko, R. Luo, M. Manathunga, M. R. Machado, H. M. Nguyen, K. A. O'Hearn, A. V. Onufriev, F. Pan, S. Pantano, R. Qi, A. Rahnamoun, A. Risheh, S. Schott-Verdugo, A. Shajan, J. Swails, J. Wang, H. Wei, X. Wu, Y. Wu, S. Zhang, S. Zhao, Q. Zhu, T. E. Cheatham, 3rd, D. R. Roe, A. Roitberg, C. Simmerling, D. M. York, M. C. Nagan, K. M. Merz, Jr., *J. Chem. Inf. Model.* **2023**, *63*, 6183-6191; 'AmberTools'; https://doi.org/10.1021/acs.jcim.3c01153

[252] H. Lu, D. J. Diaz, N. J. Czarnecki, C. Zhu, W. Kim, R. Shroff, D. J. Acosta, B. R. Alexander, H. O. Cole, Y. Zhang, N. A. Lynd, A. D. Ellington, H. S. Alper, *Nature* **2022**, *604*, 662-667; 'Machine learning-aided engineering of hydrolases for PET depolymerization'; https://doi.org/10.1038/s41586-022-04599-z

[253] Y. F. Ao, S. Pei, C. Xiang, M. J. Menke, L. Shen, C. Sun, M. Dorr, S. Born, M. Hohne, U. T. Bornscheuer, *Angew. Chem. Int. Ed.* **2023**, *62*, e202301660; 'Structure- and Data-Driven Protein Engineering of Transaminases for Improving Activity and

Stereoselectivity'; (*Angew. Chem.*, *135*, e202301660) https://doi.org/10.1002/anie.202301660

[254] J. Jumper, R. Evans, A. Pritzel, T. Green, M. Figurnov, O. Ronneberger, K. Tunyasuvunakool, R. Bates, A. Zidek, A. Potapenko, A. Bridgland, C. Meyer, S. A. A. Kohl, A. J. Ballard, A. Cowie, B. Romera-Paredes, S. Nikolov, R. Jain, J. Adler, T. Back, S. Petersen, D. Reiman, E. Clancy, M. Zielinski, M. Steinegger, M. Pacholska, T. Berghammer, S. Bodenstein, D. Silver, O. Vinyals, A. W. Senior, K. Kavukcuoglu, P. Kohli, D. Hassabis, *Nature* **2021**, *596*, 583-589; 'Highly accurate protein structure prediction with AlphaFold'; https://doi.org/10.1038/s41586-021-03819-2

[255] G. Valentini, D. Malchiodi, J. Gliozzo, M. Mesiti, M. Soto-Gomez, A. Cabri, J. Reese, E. Casiraghi, P. N. Robinson, *Front. Bioinform.* **2023**, *3*, 1304099; 'The promises of large language models for protein design and modeling'; https://doi.org/10.3389/fbinf.2023.1304099

[256] W. Zeng, L. Guo, S. Xu, J. Chen, J. Zhou, *Trends Biotechnol.* **2020**, *38*, 888-906; 'High-Throughput Screening Technology in Industrial Biotechnology'; https://doi.org/10.1016/j.tibtech.2020.01.001

[257] L. Li, X. Liu, Y. Bai, B. Yao, H. Luo, T. Tu, *Journal of Agricultural and Food Chemistry* **2024**, *72*, 3833-3845; 'High-Throughput Screening Techniques for the Selection of Thermostable Enzymes'; https://doi.org.10.1021/acs.jafc.3c07554

[258] M. Dörr, M. P. C. Fibinger, D. Last, S. Schmidt, J. Santos-Aberturas, D. Böttcher, A. Hummel, C. Vickers, M. Voss, U. T. Bornscheuer, *Biotechnology and Bioengineering* **2016**, *113*, 1421-1432; 'Fully automatized high-throughput enzyme library screening using a robotic platform'; https://doi.org/10.1002/bit.25925

[259] G. Du, Q. Fang, J. M. J. den Toonder, *Analytica Chimica Acta* **2016**, *903*, 36-50; 'Microfluidics for cell-based high throughput screening platforms—A review'; https://doi.org/10.1016/j.aca.2015.11.023

[260] N. Jankowski, K. Koschorreck, *Journal of Biotechnology* **2022**, *346*, 47-51; 'Agar plate assay for rapid screening of aryl-alcohol oxidase mutant libraries in Pichia pastoris'; https://doi.org/10.1016/j.jbiotec.2022.01.006

[261] M. S. Weiß, U. T. Bornscheuer, M. Höhne, *Solid-Phase Agar Plate Assay for Screening Amine Transaminases,* in *Protein Engineering: Methods and Protocols* (Eds.: U. T. Bornscheuer, M. Höhne), Springer New York, New York, NY, **2018**, pp. 283-296.

[262] A. O'Connell, A. Barry, A. J. Burke, A. E. Hutton, E. L. Bell, A. P. Green, E. O'Reilly, *Chem. Soc. Rev.* **2024**, *53*, 2828-2850; 'Biocatalysis: landmark discoveries and applications in chemical synthesis'; https://doi.org.10.1039/D3CS00689A

[263] K. H. Schülke, J. S. Fröse, A. Klein, M. Garcia-Borràs, S. C. Hammer, *ChemBioChem* **2024**, *25*, e202400079; 'Efficient Transferase Engineering for SAM Analog Synthesis from Iodoalkanes'; https://doi.org/10.1002/cbic.202400079

[264] S. Tian, X. Ge, Q. Yan, M. Li, Q. Huang, X. Zhang, M. Ma, B. Chen, J.-b. Wang, *Green Synthesis and Catalysis* **2024**; 'Directed evolution of stereoselective enzymes meets click reactions: Asymmetric synthesis of chiral triazoles using a Cu(I)-compatible halohydrin dehalogenase'; https://doi.org/10.1016/j.gresc.2024.01.001

[265] L. M. Mayr, D. Bojanic, *Curr. Opin. Pharmacol.* **2009**, *9*, 580-588; 'Novel trends in high-throughput screening'; https://doi.org/10.1016/j.coph.2009.08.004

[266] C. Pitzler, G. Wirtz, L. Vojcic, S. Hiltl, A. Boker, R. Martinez, U. Schwaneberg, *Chem. Biol.* **2014**, *21*, 1733-1742; 'A fluorescent hydrogel-based flow cytometry high-throughput screening platform for hydrolytic enzymes'; https://doi.org/10.1016/j.chembiol.2014.10.018

[267] E. Fernandez-Alvaro, R. Snajdrova, H. Jochens, T. Davids, D. Bottcher, U. T. Bornscheuer, *Angew. Chem. Int. Ed.* **2011**, *50*, 8584-8587; 'A combination of in vivo selection and cell sorting for the identification of enantioselective biocatalysts'; (*Angew. Chem.*, *123*, 8742-8746) https://doi.org/10.1002/anie.201102360

[268] T. H. Yoo, M. Pogson, B. L. Iverson, G. Georgiou, *ChemBioChem* **2012**, *13*, 649-653; 'Directed evolution of highly selective proteases by using a novel FACS-based screen that capitalizes on the p53 regulator MDM2'; https://doi.org/10.1002/cbic.201100718

[269] P. Jacques, M. Bechet, M. Bigan, D. Caly, G. Chataigne, F. Coutte, C. Flahaut, E. Heuson, V. Leclere, D. Lecouturier, V. Phalip, R. Ravallec, P. Dhulster, R. Froidevaux, *Bioprocess Biosyst. Eng.* **2017**, *40*, 161-180; 'High-throughput strategies for the discovery and engineering of enzymes for biocatalysis'; https://doi.org/10.1007/s00449-016-1690-x

[270] J. J. Agresti, E. Antipov, A. R. Abate, K. Ahn, A. C. Rowat, J. C. Baret, M. Marquez, A. M. Klibanov, A. D. Griffiths, D. A. Weitz, *Proc. Natl. Acad. Sci. U.S.A.* **2010**, *107*, 4004-4009; 'Ultrahigh-throughput screening in drop-based microfluidics for directed evolution'; https://doi.org/10.1073/pnas.0910781107

[271] M. Gantz, S. Neun, E. J. Medcalf, L. D. van Vliet, F. Hollfelder, *Chem. Rev.* **2023**, *123*, 5571-5611; 'Ultrahigh-Throughput Enzyme Engineering and Discovery in *In Vitro* Compartments'; https://doi.org/10.1021/acs.chemrev.2c00910

[272] A. B. Theberge, F. Courtois, Y. Schaerli, M. Fischlechner, C. Abell, F. Hollfelder, W. T. Huck, *Angew. Chem. Int. Ed.* **2010**, *49*, 5846-5868; 'Microdroplets in microfluidics: an evolving platform for discoveries in chemistry and biology'; (*Angew. Chem.*, *122*, 5982-6005) https://doi.org/10.1002/anie.200906653

[273] R. A. Scheele, Y. Weber, F. E. H. Nintzel, M. Herger, T. S. Kaminski, F. Hollfelder, *ACS Catal.* **2024**, *14*, 6259-6271; 'Ultrahigh Throughput Evolution of Tryptophan Synthase in Droplets via an Aptamer Sensor'; https://doi.org/10.1021/acscatal.4c00230

[274] M. Gantz, S. Mathis, F. Nintzel, P. J. Zurek, T. Knaus, E. Patel, D. Boros, F.-M. Weberling, M. R. Kenneth, O. J. Klein, E. J. Medcalf, J. Moss, M. Herger, T. S. Kaminski, F. G. Mutti, P. Lio, F. Hollfelder, *bioRxiv* **2024**, 2024.2004.2008.588565; 'Microdroplet screening rapidly profiles a biocatalyst to enable its AI-assisted engineering'; https://doi.org/10.1101/2024.04.08.588565

[275] P. Tufvesson, J. Lima-Ramos, M. Nordblad, J. M. Woodley, *Org. Process Res. Dev.* **2011**, *15*, 266-274; 'Guidelines and cost analysis for catalyst production in biocatalytic processes'; https://doi.org/10.1021/op1002165

[276] A. J. Straathof, S. Panke, A. Schmid, *Curr. Opin. Biotechnol.* **2002**, *13*, 548-556; 'The production of fine chemicals by biotransformations'; https://doi.org/10.1016/s0958-1669(02)00360-9

[277] K. R. Choi, W. D. Jang, D. Yang, J. S. Cho, D. Park, S. Y. Lee, *Trends Biotechnol.* **2019**, *37*, 817-837; 'Systems metabolic engineering strategies: integrating systems and synthetic biology with metabolic engineering'; https://doi.org/10.1016/j.tibtech.2019.01.003

[278] J. A. Lee, H. U. Kim, J. G. Na, Y. S. Ko, J. S. Cho, S. Y. Lee, *Trends Biotechnol.* **2023**, *41*, 798-816; 'Factors affecting the competitiveness of bacterial fermentation'; https://doi.org/10.1016/j.tibtech.2022.10.005

[279] J. Wachtmeister, D. Rother, *Curr. Opin. Biotechnol.* **2016**, *42*, 169-177; 'Recent advances in whole cell biocatalysis techniques bridging from investigative to industrial scale'; https://doi.org/10.1016/j.copbio.2016.05.005

[280] T. B. Madavi, S. Chauhan, A. Keshri, H. Alavilli, K. Y. Choi, S. D. Pamidimarri, *Biofuels, Bioprod. Biorefin.* **2022**, *16*, 859-876; 'Whole-cell biocatalysis: Advancements toward the biosynthesis of fuels'; https://doi.org/10.1002/bbb.2331

[281] A. Alissandratos, *Biophys. Rev.* **2020**, *12*, 175-182; 'In vitro multi-enzymatic cascades using recombinant lysates of *E. coli*: an emerging biocatalysis platform'; https://doi.org/10.1007/s12551-020-00618-3

[282] Z. Pourhassan, S. H. Smits, J. H. Ahn, L. Schmitt, *Biotechnol. Adv.* **2021**, *53*, 107864; 'Biotechnological applications of type 1 secretion systems'; https://doi.org/10.1016/j.biotechadv.2021.107864

[283] P. Lenz, P. J. Bakkes, C. Muller, M. Malek, R. Freudl, M. Oldiges, T. Drepper, K. E. Jaeger, A. Knapp, *Microb. Cell. Fact.* **2023**, *22*, 203; 'Analysis of protein secretion in *Bacillus subtilis* by combining a secretion stress biosensor strain with an in vivo split GFP assay'; https://doi.org/10.1186/s12934-023-02199-8

[284] M. Hoarau, S. Badieyan, E. N. G. Marsh, *Org. Biomol. Chem.* **2017**, *15*, 9539-9551; 'Immobilized enzymes: understanding enzyme - surface interactions at the molecular level'; https://doi.org/10.1039/c7ob01880k

[285] R. A. Sheldon, D. Brady, *ChemSusChem* **2019**, *12*, 2859-2881; 'Broadening the Scope of Biocatalysis in Sustainable Organic Synthesis'; https://doi.org/10.1002/cssc.201900351

[286] European Commission, Joint Research Centre, A. Korosuo, M. Borzacchiello, J. Giuntoli, J. Lasarte Lopez, R. M'barek, S. Mubareka, A. Camia, 'Trends in the EU bioeconomy – Update 2024', Publications Office of the European Union, **2024**.

[287] E. Abdelraheem, B. Thair, R. F. Varela, E. Jockmann, D. Popadic, H. C. Hailes, J. M. Ward, A. M. Iribarren, E. S. Lewkowicz, J. N. Andexer, P. L. Hagedoorn, U. Hanefeld, *ChemBioChem* **2022**, *23*, e202200212; 'Methyltransferases: Functions and Applications'; https://doi.org/10.1002/cbic.202200212

[288] R. A. Copeland, M. E. Solomon, V. M. Richon, *Nat. Rev. Drug. Discov.* **2009**, *8*, 724-732; 'Protein methyltransferases as a target class for drug discovery'; https://doi.org/10.1038/nrd2974

[289] V. M. Del Castillo Falconi, K. Torres-Arciga, G. Matus-Ortega, J. Diaz-Chavez, L. A. Herrera, *Int. J. Mol. Sci.* **2022**, *23*, 8994; 'DNA Methyltransferases: From Evolution to Clinical Applications'; https://doi.org/10.3390/ijms23168994

[290] J. M. Foulks, K. M. Parnell, R. N. Nix, S. Chau, K. Swierczek, M. Saunders, K. Wright, T. F. Hendrickson, K. K. Ho, M. V. McCullar, S. B. Kanner, *J. Biomol. Screen.* **2012**, *17*, 2-17; 'Epigenetic drug discovery: targeting DNA methyltransferases'; https://doi.org/10.1177/1087057111421212

[291] B. J. C. Law, A. W. Struck, M. R. Bennett, B. Wilkinson, J. Micklefield, *Chem. Sci.* **2015**, *6*, 2885-2892; 'Site-specific bioalkylation of rapamycin by the RapM 16-O-methyltransferase'; https://doi.org/10.1039/c5sc00164a

[292] M. Haase, B. David, B. Paschold, T. Classen, P. Schneider, N. Pozhydaieva, H. Gohlke, J. Pietruszka, *ACS Catal.* **2024**, *14*, 227-236; 'Application of the C3-Methyltransferase StspM1 for the Synthesis of the Natural Pyrroloindole Motif'; https://doi.org/10.1021/acscatal.3c04952

[293] A. Gutmann, M. Schiller, M. Gruber-Khadjawi, B. Nidetzky, *Org. Biomol. Chem.* **2017**, *15*, 7917-7924; 'An ortho C-methylation/O-glycosylation motif on a hydroxy-coumarin scaffold, selectively installed by biocatalysis'; https://doi.org/10.1039/c7ob01513e

[294] E. Abdelraheem, E. Jockmann, J. Li, S. Günther, J. N. Andexer, P. L. Hagedoorn, U. Hanefeld, *ChemCatChem* **2023**, *16*, e202301217; 'Enzymatic S-Methylation of Thiols Catalyzed by Different O-Methyltransferases'; https://doi.org/10.1002/cctc.202301217

[295] R. Roddan, F. Subrizi, J. Broomfield, J. M. Ward, N. H. Keep, H. C. Hailes, *Org. Lett.* **2021**, *23*, 6342-6347; 'Chemoenzymatic Cascades toward Methylated Tetrahydroprotoberberine and Protoberberine Alkaloids'; https://doi.org/10.1021/acs.orglett.1c02110

[296] J. Fricke, A. Sherwood, R. Kargbo, A. Orry, F. Blei, A. Naschberger, B. Rupp, D. Hoffmeister, *ChemBioChem* **2019**, *20*, 2824-2829; 'Enzymatic Route toward 6-Methylated Baeocystin and Psilocybin'; https://doi.org/10.1002/cbic.201900358

[297] H. Stecher, M. Tengg, B. J. Ueberbacher, P. Remler, H. Schwab, H. Griengl, M. Gruber-Khadjawi, *Angew. Chem. Int. Ed.* **2009**, *48*, 9546-9548; 'Biocatalytic Friedel-Crafts alkylation using non-natural cofactors'; (*Angew. Chem.*, *121*, 9710-9712) https://doi.org/10.1002/anie.200905095

[298] F. Subrizi, Y. Wang, B. Thair, D. Méndez-Sánchez, R. Roddan, M. Cárdenas-Fernández, J. Siegrist, M. Richter, J. N. Andexer, J. M. Ward, H. C. Hailes, *Angew. Chem. Int. Ed.* **2021**, *60*, 18673-18679; 'Multienzyme One-Pot Cascades Incorporating Methyltransferases for the Strategic Diversification of Tetrahydroisoquinoline Alkaloids'; (*Angew. Chem.*, *133*, 18821-18827) https://doi.org/10.1002/anie.202104476

[299] H. L. Schubert, R. M. Blumenthal, X. Cheng, *Trends Biochem. Sci.* **2003**, *28*, 329-335; 'Many paths to methyltransfer: a chronicle of convergence'; https://doi.org/10.1016/S0968-0004(03)00090-2

[300] J. Vidgren, L. A. Svensson, A. Liljas, *Nature* **1994**, *368*, 354-358; 'Crystal structure of catechol O-methyltransferase'; https://doi.org/10.1038/368354a0

[301] M. M. Dixon, S. Huang, R. G. Matthews, M. Ludwig, *Structure* **1996**, *4*, 1263-1275; 'The structure of the C-terminal domain of methionine synthase: presenting *S*-adenosylmethionine for reductive methylation of B12'; https://doi.org/10.1016/s0969-2126(96)00135-9

[302] V. Anantharaman, E. V. Koonin, L. Aravind, *J. Mol. Microbiol. Biotechnol.* **2002**, *4*, 71-75; 'SPOUT: a class of methyltransferases that includes spoU and trmD RNA methylase superfamilies, and novel superfamilies of predicted prokaryotic RNA methylases';

[303] T. O. Yeates, *Cell* **2002**, *111*, 5-7; 'Structures of SET domain proteins: protein lysine methyltransferases make their mark'; https://doi.org/10.1016/s0092-8674(02)01010-3

[304] D. K. Liscombe, G. V. Louie, J. P. Noel, *Nat. Prod. Rep.* **2012**, *29*, 1238-1250; 'Architectures, mechanisms and molecular evolution of natural product methyltransferases'; https://doi.org/10.1039/c2np20029e

[305] K. Swiderek, I. Tunon, I. H. Williams, V. Moliner, *J. Am. Chem. Soc.* **2018**, *140*, 4327-4334; 'Insights on the Origin of Catalysis on Glycine N-Methyltransferase from Computational Modeling'; https://doi.org/10.1021/jacs.7b13655

[306] R. J. Boyd, C. K. Kim, Z. Shi, N. Weinberg, S. Wolfe, *J. Am. Chem. Soc.* **2002**, *115*, 10147-10152; 'Secondary H/D isotope effects and transition state looseness in nonidentity methyl transfer reactions. Implications for the concept of enzymic catalysis via transition state compression'; https://doi.org/10.1021/ja00075a033

[307] J. Zhang, H. J. Kulik, T. J. Martinez, J. P. Klinman, *Proc. Natl. Acad. Sci. U.S.A.* **2015**, *112*, 7954-7959; 'Mediation of donor-acceptor distance in an enzymatic methyl transfer reaction'; https://doi.org/10.1073/pnas.1506792112

[308] J. Zhang, J. P. Klinman, *J. Am. Chem. Soc.* **2016**, *138*, 9158-9165; 'Convergent Mechanistic Features between the Structurally Diverse N- and O-Methyltransferases: Glycine N-Methyltransferase and Catechol O-Methyltransferase'; https://doi.org/10.1021/jacs.6b03462

[309] Y. Peng, D. Sartini, V. Pozzi, D. Wilk, M. Emanuelli, V. C. Yee, *Biochem.* **2011**, *50*, 7800-7808; 'Structural basis of substrate recognition in human nicotinamide N-methyltransferase'; https://doi.org/10.1021/bi2007614

[310] C. Zubieta, X. Z. He, R. A. Dixon, J. P. Noel, *Nat. Struct. Biol.* **2001**, *8*, 271-279; 'Structures of two natural product methyltransferases reveal the basis for substrate specificity in plant O-methyltransferases'; https://doi.org/10.1038/85029

[311] D. E. Lang, J. S. Morris, M. Rowley, M. A. Torres, V. A. Maksimovich, P. J. Facchini, K. K. S. Ng, *J. Biol. Chem.* **2019**, *294*, 14482-14498; 'Structure-function studies of tetrahydroprotoberberine N-methyltransferase reveal the molecular basis of stereoselective substrate recognition'; https://doi.org/10.1074/jbc.RA119.009214

[312] F. Yan, J. M. LaMarre, R. Rohrich, J. Wiesner, H. Jomaa, A. S. Mankin, D. G. Fujimori, *J. Am. Chem. Soc.* **2010**, *132*, 3953-3964; 'RlmN and Cfr are radical SAM enzymes involved in methylation of ribosomal RNA'; https://doi.org/10.1021/ja910850y

[313] A. G. Chew, D. A. Bryant, *Annu. Rev. Microbiol.* **2007**, *61*, 113-129; 'Chlorophyll biosynthesis in bacteria: the origins of structural and functional diversity'; https://doi.org/10.1146/annurev.micro.61.080706.093242

[314] M. Tao, L. Wang, E. Wendt-Pienkowski, N. P. George, U. Galm, G. Zhang, J. M. Coughlin, B. Shen, *Mol. BioSyst.* **2007**, *3*, 60-74; 'The tallysomycin biosynthetic gene cluster from *Streptoalloteichus hindustanus* E465-94 ATCC 31158 unveiling new insights into the biosynthesis of the bleomycin family of antitumor antibiotics'; https://doi.org/10.1039/b615284h

[315] Q. Zhang, W. A. van der Donk, W. Liu, *Acc. Chem. Res.* **2012**, *45*, 555-564; 'Radical-mediated enzymatic methylation: a tale of two SAMs'; https://doi.org/10.1021/ar200202c

[316] R. Liao, L. Duan, C. Lei, H. Pan, Y. Ding, Q. Zhang, D. Chen, B. Shen, Y. Yu, W. Liu, *Chem. Biol.* **2009**, *16*, 141-147; 'Thiopeptide biosynthesis featuring ribosomally synthesized precursor peptides and conserved posttranslational modifications'; https://doi.org/10.1016/j.chembiol.2009.01.007

[317] C. Zhang, S. A. Sultan, X. Chen, *Bioresour. Bioprocess.* **2021**, *8*, 72; 'Biotechnological applications of *S*-adenosyl-methionine-dependent methyltransferases for natural products biosynthesis and diversification'; https://doi.org/10.1186/s40643-021-00425-y

[318] J. Zhang, Y. G. Zheng, *ACS Chem. Biol.* **2016**, *11*, 583-597; 'SAM/SAH Analogs as Versatile Tools for SAM-Dependent Methyltransferases'; https://doi.org/10.1021/acschembio.5b00812

[319] A. W. Struck, M. R. Bennett, S. A. Shepherd, B. J. Law, Y. Zhuo, L. S. Wong, J. Micklefield, *J. Am. Chem. Soc.* **2016**, *138*, 3038-3045; 'An Enzyme Cascade for Selective Modification of Tyrosine Residues in Structurally Diverse Peptides and Proteins'; https://doi.org/10.1021/jacs.5b10928

[320] J. C. Sadler, L. D. Humphreys, R. Snajdrova, G. A. Burley, *ChemBioChem* **2017**, *18*, 992-995; 'A Tandem Enzymatic sp^2-C-Methylation Process: Coupling in Situ *S*-Adenosyl-L-Methionine Formation with Methyl Transfer'; https://doi.org/10.1002/cbic.201700115

[321] C. Zhang, R. L. Weller, J. S. Thorson, S. R. Rajski, *J. Am. Chem. Soc.* **2006**, *128*, 2760-2761; 'Natural product diversification using a non-natural cofactor analogue of *S*-adenosyl-L-methionine'; https://doi.org/10.1021/ja056231t

[322] M. J. van Haren, J. Sastre Torano, D. Sartini, M. Emanuelli, R. B. Parsons, N. I. Martin, *Biochem.* **2016**, *55*, 5307-5315; 'A Rapid and Efficient Assay for the Characterization of Substrates and Inhibitors of Nicotinamide N-Methyltransferase'; https://doi.org/10.1021/acs.biochem.6b00733

[323] F. Ospina, K. H. Schulke, J. Soler, A. Klein, B. Prosenc, M. Garcia-Borras, S. C. Hammer, *Angew. Chem. Int. Ed.* **2022**, *61*, e202213056; 'Selective Biocatalytic N-Methylation of Unsaturated Heterocycles'; (*Angew. Chem.*, *134*, e202213056) https://doi.org/10.1002/anie.202213056

[324] F. Soualmia, A. Guillot, N. Sabat, C. Brewee, X. Kubiak, M. Haumann, X. Guinchard, A. Benjdia, O. Berteau, *Chem. -Eur. J.* **2022**, *28*, e202200627; 'Exploring the Biosynthetic Potential of TsrM, a B12-dependent Radical SAM Methyltransferase Catalyzing Non-radical Reactions'; https://doi.org/10.1002/chem.202200627

[325] R. Wu, W. Ding, Q. Zhang, *Chin. J. Chem.* **2022**, *40*, 1693-1698; 'Consecutive Methylation catalyzed by TsrM, an atypical Class B radical SAM methylase'; https://doi.org/10.1002/cjoc.202200174

[326] C. Sommer-Kamann, J. Breiltgens, Z. Zou, S. Gerhardt, R. Saleem-Batcha, F. Kemper, O. Einsle, J. N. Andexer, M. Müller, *ChemBioChem* **2024**, e202400258; 'Structures and Protein Engineering of the α-Keto Acid C-Methyltransferases SgvM and MrsA for Rational Substrate Transfer'; https://doi.org/10.1002/cbic.202400258

[327] S. Ju, K. P. Kuzelka, R. Guo, B. Krohn-Hansen, J. Wu, S. K. Nair, Y. Yang, *Nat. Commun.* **2023**, *14*, 5704; 'A biocatalytic platform for asymmetric alkylation of α-keto acids by mining and engineering of methyltransferases'; https://doi.org/10.1038/s41467-023-40980-w

[328] C. Liao, F. P. Seebeck, *Angew. Chem. Int. Ed.* **2020**, *59*, 7184-7187; 'Asymmetric β-Methylation of L-and D-α-Amino Acids by a Self-Contained Enzyme Cascade'; (*Angew. Chem.*, *132*, 7251-7254) https://doi.org/10.1002/anie.201916025

[329] J. R. Matos, C.-H. Wong, *Bioorg. Chem.* **1987**, *15*, 71-80; '*S*-adenosylmethionine: Stability and stabilization'; https://doi.org/10.1016/0045-2068(87)90008-3

[330] M. Richter, *Nat. Prod. Rep.* **2013**, *30*, 1324-1345; 'Functional diversity of organic molecule enzyme cofactors'; https://doi.org/10.1039/c3np70045c

[331] M. Fontecave, M. Atta, E. Mulliez, *Trends Biochem. Sci.* **2004**, *29*, 243-249; '*S*-adenosylmethionine: nothing goes to waste'; https://doi.org/10.1016/j.tibs.2004.03.007

[332] J. M. Lipson, M. Thomsen, B. S. Moore, R. P. Clausen, J. J. La Clair, M. D. Burkart, *ChemBioChem* **2013**, *14*, 950; 'A Tandem Chemoenzymatic Methylation via *S*-Adenosyl-L-methionine'; https://doi.org/10.1002/cbic.201300221

[333] J. Siegrist, S. Aschwanden, S. Mordhorst, L. Thony-Meyer, M. Richter, J. N. Andexer, *ChemBioChem* **2015**, *16*, 2576-2579; 'Regiocomplementary O-Methylation of

Catechols by Using Three-Enzyme Cascades'; https://doi.org/10.1002/cbic.201500410

[334] S. Singh, J. Zhang, T. D. Huber, M. Sunkara, K. Hurley, R. D. Goff, G. Wang, W. Zhang, C. Liu, J. Rohr, S. G. Van Lanen, A. J. Morris, J. S. Thorson, *Angew. Chem. Int. Ed.* **2014**, *53*, 3965-3969; 'Facile chemoenzymatic strategies for the synthesis and utilization of *S*-adenosyl-(L)-methionine analogues'; (*Angew. Chem.*, *126*, 4046-4050) https://doi.org/10.1002/anie.201308272

[335] S. Mordhorst, J. Siegrist, M. Muller, M. Richter, J. N. Andexer, *Angew. Chem. Int. Ed.* **2017**, *56*, 4037-4041; 'Catalytic Alkylation Using a Cyclic *S*-Adenosylmethionine Regeneration System'; (*Angew. Chem.*, 129, 4095-4099) https://doi.org/10.1002/anie.201611038

[336] D. Popadic, D. Mhaindarkar, M. H. N. Dang Thai, H. C. Hailes, S. Mordhorst, J. N. Andexer, *RSC Chem. Biol.* **2021**, *2*, 883-891; 'A bicyclic *S*-adenosylmethionine regeneration system applicable with different nucleosides or nucleotides as cofactor building blocks'; https://doi.org/10.1039/d1cb00033k

[337] Q. Tang, I. V. Pavlidis, C. P. S. Badenhorst, U. T. Bornscheuer, *ChemBioChem* **2021**, *22*, 2584-2590; 'From Natural Methylation to Versatile Alkylations Using Halide Methyltransferases'; https://doi.org/10.1002/cbic.202100153

[338] N. C. f. B. Information*, Vol. accessed 4 October 2024*, PubChem, **2024**.

[339] X. Wen, F. Leisinger, V. Leopold, F. P. Seebeck, *Angew. Chem. Int. Ed.* **2022**, *61*, e202208746; 'Synthetic Reagents for Enzyme-Catalyzed Methylation'; (*Angew. Chem.*, *134*, e202208746) https://doi.org/10.1002/anie.202208746

[340] M. A. Avila, E. R. Garcia-Trevijano, S. C. Lu, F. J. Corrales, J. M. Mato, *Int. J. Biochem. Cell. Biol.* **2004**, *36*, 2125-2130; 'Methylthioadenosine'; https://doi.org/10.1016/j.biocel.2003.11.016

[341] M. Thomsen, S. B. Vogensen, J. Buchardt, M. D. Burkart, R. P. Clausen, *Org. Biomol. Chem.* **2013**, *11*, 7606-7610; 'Chemoenzymatic synthesis and in situ application of *S*-adenosyl-L-methionine analogs'; https://doi.org/10.1039/c3ob41702f

[342] I. J. W. McKean, P. A. Hoskisson, G. A. Burley, *ChemBioChem* **2020**, *21*, 2890-2897; 'Biocatalytic Alkylation Cascades: Recent Advances and Future Opportunities for Late-Stage Functionalization'; https://doi.org/10.1002/cbic.202000187

[343] I. J. W. McKean, J. C. Sadler, A. Cuetos, A. Frese, L. D. Humphreys, G. Grogan, P. A. Hoskisson, G. A. Burley, *Angew. Chem. Int. Ed.* **2019**, *58*, 17583-17588; '*S*-Adenosyl Methionine Cofactor Modifications Enhance the Biocatalytic Repertoire of Small Molecule C-Alkylation'; (*Angew. Chem.*, *131,* 17747-17752) https://doi.org/10.1002/anie.201908681

[344] Z. J. Lu, G. D. Markham, *J. Biol. Chem.* **2002**, *277*, 16624-16631; 'Enzymatic properties of *S*-adenosylmethionine synthetase from the archaeon *Methanococcus jannaschii*'; https://doi.org/10.1074/jbc.M110456200

[345] G. D. Markham, E. W. Hafner, C. W. Tabor, H. Tabor, *J. Biol. Chem.* **1980**, *255*, 9082-9092; '*S*-Adenosylmethionine synthetase from *Escherichia coli*'; https://doi.org/10.1016/S0021-9258(19)70530-4

[346] R. Wang, K. Islam, Y. Liu, W. Zheng, H. Tang, N. Lailler, G. Blum, H. Deng, M. Luo, *J. Am. Chem. Soc.* **2013**, *135*, 1048-1056; 'Profiling genome-wide chromatin methylation with engineered posttranslation apparatus within living cells'; https://doi.org/10.1021/ja309412s

[347] G. L. Cantoni, *J. Biol. Chem.* **1953**, *204*, 403-416; '*S*-Adenosylmethionine; a new intermediate formed enzymatically from L-methionine and adenosinetriphosphate'; https://doi.org/10.1016/S0021-9258(18)66148-4

[348] M. K. F. Mohr, R. Saleem-Batcha, N. V. Cornelissen, J. N. Andexer, *Chemistry* **2023**, *29*, e202301503; 'Enzymatic Synthesis of L-Methionine Analogues and Application in a Methyltransferase Catalysed Alkylation Cascade'; https://doi.org/10.1002/chem.202301503

[349] F. Michailidou, N. Klocker, N. V. Cornelissen, R. K. Singh, A. Peters, A. Ovcharenko, D. Kummel, A. Rentmeister, *Angew. Chem. Int. Ed.* **2021**, *60*, 480-485; 'Engineered SAM Synthetases for Enzymatic Generation of AdoMet Analogs with Photocaging

Groups and Reversible DNA Modification in Cascade Reactions'; (*Angew. Chem.*, *133*, 484-489) https://doi.org/10.1002/anie.202012623

[350] K. H. Schulke, F. Ospina, K. Hornschemeyer, S. Gergel, S. C. Hammer, *ChemBioChem* **2022**, *23*, e202100632; 'Substrate Profiling of Anion Methyltransferases for Promiscuous Synthesis of *S*-Adenosylmethionine Analogs from Haloalkanes'; https://doi.org/10.1002/cbic.202100632

[351] J. Peng, C. Liao, C. Bauer, F. P. Seebeck, *Angew. Chem. Int. Ed.* **2021**, *60*, 27178-27183; 'Fluorinated *S*-Adenosylmethionine as a Reagent for Enzyme-Catalyzed Fluoromethylation'; (*Angew. Chem.*, *133*, 27384-27389) https://doi.org/10.1002/anie.202108802

[352] Q. Tang, C. W. Grathwol, A. S. Aslan-Uzel, S. Wu, A. Link, I. V. Pavlidis, C. P. S. Badenhorst, U. T. Bornscheuer, *Angew. Chem. Int. Ed.* **2021**, *60*, 1524-1527; 'Directed Evolution of a Halide Methyltransferase Enables Biocatalytic Synthesis of Diverse SAM Analogs'; (*Angew. Chem.*, *133*, 1547-1551) https://doi.org/10.1002/anie.202013871

[353] G.-Y. Yang, G.-W. Zheng, B.-B. Zeng, J.-H. Xu, Q. Chen, *Mol. Catal.* **2023**, *550*, 113533; 'Engineering of halide methyltransferases for synthesis of SAE and its application in biosynthesis of ethyl vanillin'; https://doi.org/10.1016/j.mcat.2023.113533

[354] A. Hoffmann, K. H. Schulke, S. C. Hammer, A. Rentmeister, N. V. Cornelissen, *Chem. Commun.* **2023**, *59*, 5463-5466; 'Comparative *S*-adenosyl-L-methionine analogue generation for selective biocatalytic Friedel-Crafts alkylation'; https://doi.org/10.1039/d3cc01036h

[355] C. Sommer-Kamann, A. Fries, S. Mordhorst, J. N. Andexer, M. Müller, *Angew. Chem. Int. Ed.* **2017**, *56*, 4033-4036; 'Asymmetric C-Alkylation by the *S*-Adenosylmethionine-Dependent Methyltransferase SgvM'; (*Angew. Chem., 129*, 4091-4094) https://doi.org/10.1002/anie.201609375

[356] L. L. Bengel, B. Aberle, A. N. Egler-Kemmerer, S. Kienzle, B. Hauer, S. C. Hammer, *Angew. Chem. Int. Ed.* **2021**, *60*, 5554-5560; 'Engineered Enzymes Enable Selective N-Alkylation of Pyrazoles With Simple Haloalkanes'; (*Angew. Chem.*, *133*, 5614-5620) https://doi.org/10.1002/anie.202014239

[357] S. Murao, H. Hayashi, *Agric. Biol. Chem.* **1986**, *50*, 523-524; 'Physostigmine and N8-norphysostigmine, insecticidal compounds, from *Streptomyces* sp'; https://doi.org/10.1080/00021369.1986.10867419

[358] P. Schneider, B. Henssen, B. Paschold, B. P. Chapple, M. Schatton, F. P. Seebeck, T. Classen, J. Pietruszka, *Angew. Chem. Int. Ed.* **2021**, *60*, 23412-23418; 'Biocatalytic C3-Indole Methylation-A Useful Tool for the Natural-Product-Inspired Stereoselective Synthesis of Pyrroloindoles'; (*Angew. Chem.*, *133*, 23600-23606) https://doi.org/10.1002/anie.202107619

[359] N. Pozhydaieva, Master thesis, Heinrich Heine University, Düsseldorf **2020**. 'C-methyltransferases as a powerful tool for organic synthesis – characterisation, optimisation and application for the stereoselective formation of indole alkaloids'.

[360] W. Butdee, S. Muangham, D. Chonudomkul, K. Duangmal, *Int. J. Syst. Evol. Microbiol.* **2023**, *73*, 005639; '*Streptomyces rhizoryzae* sp. nov., isolated from paddy rhizosphere soil and formal proposal to reclassify *Streptomyces albulus* as a later heterotypic synonym of *Streptomyces noursei*'; https://doi.org/10.1099/ijsem.0.005639

[361] F. W. Studier, B. A. Moffatt, *J. Mol. Biol.* **1986**, *189*, 113-130; 'Use of bacteriophage T7 RNA polymerase to direct selective high-level expression of cloned genes'; https://doi.org/10.1016/0022-2836(86)90385-2

[362] J. Grodberg, J. J. Dunn, *J. Bacteriol.* **1988**, *170*, 1245-1253; 'ompT encodes the *Escherichia coli* outer membrane protease that cleaves T7 RNA polymerase during purification'; https://doi.org/10.1128/jb.170.3.1245-1253.1988

[363] J. N. Phue, S. J. Lee, L. Trinh, J. Shiloach, *Biotechnol. Bioeng.* **2008**, *101*, 831-836; 'Modified *Escherichia coli* B (BL21), a superior producer of plasmid DNA compared with *Escherichia coli* K (DH5alpha)'; https://doi.org/10.1002/bit.21973

[364] S. Y. Yau, E. Keshavarz-Moore, J. Ward, *Biotechnol. Bioeng.* **2008**, *101*, 529-544; 'Host strain influences on supercoiled plasmid DNA production in *Escherichia coli*:

Implications for efficient design of large-scale processes'; https://doi.org/10.1002/bit.21915
[365] B. Jia, C. O. Jeon, *Open Biol.* **2016**, *6*; 'High-throughput recombinant protein expression in *Escherichia coli*: current status and future perspectives'; https://doi.org/10.1098/rsob.160196
[366] M. Griffith, R. D. Gietz, *Biotechniques* **2003**, *35*, 272-278; '*Escherichia coli* endA deletion strain for use in two-hybrid shuttle vector selection'; https://doi.org/10.2144/03352bm05
[367] M. Jekel, W. Wackernagel, *J. Bacteriol.* **1994**, *176*, 1550-1551; 'Location of the endA gene coding for endonuclease I on the physical map of the *Escherichia coli* K-12 chromosome'; https://doi.org/10.1128/jb.176.5.1550-1551.1994
[368] J. Zhang, C. Marcin, M. A. Shifflet, P. Salmon, T. Brix, R. Greasham, B. Buckland, M. Chartrain, *Appl. Microbiol. Biotechnol.* **1996**, *44*, 568-575; 'Development of a defined medium fermentation process for physostigmine production by *Streptomyces griseofuscus*'; https://doi.org/10.1007/BF00172487
[369] K. Hsiao, H. Zegzouti, S. A. Goueli, *Epigenomics* **2016**, *8*, 321-339; 'Methyltransferase-Glo: a universal, bioluminescent and homogenous assay for monitoring all classes of methyltransferases'; https://doi.org/10.2217/epi.15.113
[370] B. P. S. Chouhan, S. Maimaiti, M. Gade, P. Laurino, *Biochem.* **2019**, *58*, 166-170; 'Rossmann-Fold Methyltransferases: Taking a "beta-Turn" around Their Cofactor, *S*-Adenosylmethionine'; https://doi.org/10.1021/acs.biochem.8b00994
[371] S. Barik, *Int. J. Mol. Sci.* **2020**, *21*; 'The Uniqueness of Tryptophan in Biology: Properties, Metabolism, Interactions and Localization in Proteins'; https://doi.org/10.3390/ijms21228776
[372] B. Webb, A. Sali, *Curr. Protoc. Bioinformatics.* **2016**, *54*, 5.6.1-5.6.37; 'Comparative Protein Structure Modeling Using MODELLER'; https://doi.org/10.1002/cpbi.3
[373] Y. Xia, W. Chu, Q. Qi, L. Xun, *Nucleic Acids Res.* **2015**, *43*, e12; 'New insights into the QuikChange process guide the use of Phusion DNA polymerase for site-directed mutagenesis'; https://doi.org/10.1093/nar/gku1189
[374] D. Silva, G. Santos, M. Barroca, D. Costa, T. Collins, *Methods Mol. Biol.* **2023**, *2967*, 223-238; 'Inverse PCR for Site-Directed Mutagenesis'; https://doi.org/10.1007/978-1-0716-3358-8_18
[375] C. N. Dominy, D. W. Andrews, *Site-Directed Mutagenesis by Inverse PCR. ,* in *E. coli Plasmid Vectors. Methods in Molecular Biology, Vol. 235* (Eds.: N. Casali, A. Preston), Humana Press., **2003**, pp. 209-223.
[376] R. Garcia-Meseguer, K. Zinovjev, M. Roca, J. J. Ruiz-Pernia, I. Tunon, *J. Phys. Chem. B.* **2015**, *119*, 873-882; 'Linking electrostatic effects and protein motions in enzymatic catalysis. A theoretical analysis of catechol o-methyltransferase'; https://doi.org/10.1021/jp505746x
[377] P. A. Del Rizzo, J. F. Couture, L. M. Dirk, B. S. Strunk, M. S. Roiko, J. S. Brunzelle, R. L. Houtz, R. C. Trievel, *J. Biol. Chem.* **2010**, *285*, 31849-31858; 'SET7/9 catalytic mutants reveal the role of active site water molecules in lysine multiple methylation'; https://doi.org/10.1074/jbc.M110.114587
[378] X. Zhang, L. Zhou, X. Cheng, *EMBO J.* **2000**, *19*, 3509-3519; 'Crystal structure of the conserved core of protein arginine methyltransferase PRMT3'; https://doi.org/10.1093/emboj/19.14.3509
[379] S. G. Lee, Y. Kim, T. D. Alpert, A. Nagata, J. M. Jez, *J. Biol. Chem.* **2012**, *287*, 1426-1434; 'Structure and reaction mechanism of phosphoethanolamine methyltransferase from the malaria parasite *Plasmodium falciparum*: an antiparasitic drug target'; https://doi.org/10.1074/jbc.M111.315267
[380] Y. Takata, Y. Huang, J. Komoto, T. Yamada, K. Konishi, H. Ogawa, T. Gomi, M. Fujioka, F. Takusagawa, *Biochem.* **2003**, *42*, 8394-8402; 'Catalytic mechanism of glycine N-methyltransferase'; https://doi.org/10.1021/bi034245a
[381] M. C. Lemfack, W. Brandt, K. Kruger, A. Gurowietz, J. Djifack, J. P. Jung, M. Hopf, H. Noack, B. Junker, S. von Reuss, B. Piechulla, *Sci. Rep.* **2021**, *11*, 3182; 'Reaction mechanism of the farnesyl pyrophosphate C-methyltransferase towards the

biosynthesis of pre-sodorifen pyrophosphate by *Serratia plymuthica* 4Rx13'; https://doi.org/10.1038/s41598-021-82521-9

[382] J. C. Yi, C. Liu, L. X. Dai, S. L. You, *Chem. Asian J.* **2017**, *12*, 2975-2979; 'Synthesis of C3-Methyl-Substituted Pyrroloindolines and Furoindolines via Cascade Dearomatization of Indole Derivatives with Methyl Iodide'; https://doi.org/10.1002/asia.201701151

[383] J. M. Schuller, G. Zocher, M. Liebhold, X. Xie, M. Stahl, S. M. Li, T. Stehle, *J. Mol. Biol.* **2012**, *422*, 87-99; 'Structure and catalytic mechanism of a cyclic dipeptide prenyltransferase with broad substrate promiscuity'; https://doi.org/10.1016/j.jmb.2012.05.033

[384] C. D. Poulter, H. C. Rilling, *Biochem.* **1976**, *15*, 1079-1083; 'Prenyltransferase: the mechanism of the reaction'; https://doi.org/10.1021/bi00650a019

[385] D. D. Boehr, R. Nussinov, P. E. Wright, *Nat. Chem. Biol.* **2009**, *5*, 789-796; 'The role of dynamic conformational ensembles in biomolecular recognition'; https://doi.org/10.1038/nchembio.232

[386] K. A. Henzler-Wildman, V. Thai, M. Lei, M. Ott, M. Wolf-Watz, T. Fenn, E. Pozharski, M. A. Wilson, G. A. Petsko, M. Karplus, C. G. Hubner, D. Kern, *Nature* **2007**, *450*, 838-844; 'Intrinsic motions along an enzymatic reaction trajectory'; https://doi.org/10.1038/nature06410

[387] D. Kern, E. R. Zuiderweg, *Curr. Opin. Struct. Biol.* **2003**, *13*, 748-757; 'The role of dynamics in allosteric regulation'; https://doi.org/10.1016/j.sbi.2003.10.008

[388] A. P. Perlinska, M. Kalek, T. Christian, Y. M. Hou, J. I. Sulkowska, *ACS Catal.* **2020**, *10*, 8058-8068; 'Mg^{2+}-Dependent Methyl Transfer by a Knotted Protein: A Molecular Dynamics Simulation and Quantum Mechanics Study'; https://doi.org/10.1021/acscatal.0c00059

[389] I. Gomez Garcia, C. E. Stevenson, I. Uson, C. L. Freel Meyers, C. T. Walsh, D. M. Lawson, *J. Mol. Biol.* **2010**, *395*, 390-407; 'The crystal structure of the novobiocin biosynthetic enzyme NovP: the first representative structure for the TylF O-methyltransferase superfamily'; https://doi.org/10.1016/j.jmb.2009.10.045

[390] E. Cundliffe, N. Bate, A. Butler, S. Fish, A. Gandecha, L. Merson-Davies, *Antonie Van Leeuwenhoek* **2001**, *79*, 229-234; 'The tylosin-biosynthetic genes of *Streptomyces fradiae*'; https://doi.org/10.1023/a:1012065300116

[391] S. M. Bernard, D. L. Akey, A. Tripathi, S. R. Park, J. R. Konwerski, Y. Anzai, S. Li, F. Kato, D. H. Sherman, J. L. Smith, *ACS Chem. Biol.* **2015**, *10*, 1340-1351; 'Structural basis of substrate specificity and regiochemistry in the MycF/TylF family of sugar O-methyltransferases'; https://doi.org/10.1021/cb5009348

[392] J. C. Sadler, C. H. Chung, J. E. Mosley, G. A. Burley, L. D. Humphreys, *ACS Chem. Biol.* **2017**, *12*, 374-379; 'Structural and Functional Basis of C-Methylation of Coumarin Scaffolds by NovO'; https://doi.org/10.1021/acschembio.6b01053

[393] C. F. Stratton, M. B. Poulin, Q. Du, V. L. Schramm, *ACS Chem. Biol.* **2017**, *12*, 342-346; 'Kinetic Isotope Effects and Transition State Structure for Human Phenylethanolamine N-Methyltransferase'; https://doi.org/10.1021/acschembio.6b00922

[394] M. F. Hegazi, R. T. Borchardt, R. L. Schowen, *J. Am. Chem. Soc.* **2002**, *101*, 4359-4365; 'α-Deuterium and carbon-13 isotope effects for methyl transfer catalyzed by catechol O-methyltransferase. S_N2-like transition state'; https://doi.org/10.1021/ja00509a052

[395] A. Soriano, R. Castillo, C. Christov, J. Andres, V. Moliner, I. Tunon, *Biochem.* **2006**, *45*, 14917-14925; 'Catalysis in glycine N-methyltransferase: testing the electrostatic stabilization and compression hypothesis'; https://doi.org/10.1021/bi061319k

[396] N. A. Bruender, J. B. Thoden, M. Kaur, M. K. Avey, H. M. Holden, *Biochem.* **2010**, *49*, 5891-5898; 'Molecular architecture of a C-3'-methyltransferase involved in the biosynthesis of D-tetronitrose'; https://doi.org/10.1021/bi100782b

[397] A. E. Carney, H. M. Holden, *Biochem.* **2011**, *50*, 780-787; 'Molecular architecture of TylM1 from *Streptomyces fradiae*: an N,N-dimethyltransferase involved in the production of dTDP-D-mycaminose'; https://doi.org/10.1021/bi101733y

[398] S. Horowitz, L. M. Dirk, J. D. Yesselman, J. S. Nimtz, U. Adhikari, R. A. Mehl, S. Scheiner, R. L. Houtz, H. M. Al-Hashimi, R. C. Trievel, *J. Am. Chem. Soc.* **2013**, *135*, 15536-15548; 'Conservation and functional importance of carbon-oxygen hydrogen bonding in AdoMet-dependent methyltransferases'; https://doi.org/10.1021/ja407140k

[399] Y. Gu, T. Kar, S. Scheiner, *J. Am. Chem. Soc.* **1999**, *121*, 9411-9422; 'Fundamental Properties of the CH···O Interaction: Is It a True Hydrogen Bond?'; https://doi.org/10.1021/ja991795g

[400] G. E. Crooks, G. Hon, J. M. Chandonia, S. E. Brenner, *Genome Res.* **2004**, *14*, 1188-1190; 'WebLogo: a sequence logo generator'; https://doi.org/10.1101/gr.849004

[401] F. Glaser, T. Pupko, I. Paz, R. E. Bell, D. Bechor-Shental, E. Martz, N. Ben-Tal, *Bioinformatics* **2003**, *19*, 163-164; 'ConSurf: identification of functional regions in proteins by surface-mapping of phylogenetic information'; https://doi.org/10.1093/bioinformatics/19.1.163

[402] M. Landau, I. Mayrose, Y. Rosenberg, F. Glaser, E. Martz, T. Pupko, N. Ben-Tal, *Nucleic Acids Res.* **2005**, *33*, W299-302; 'ConSurf 2005: the projection of evolutionary conservation scores of residues on protein structures'; https://doi.org/10.1093/nar/gki370

[403] P. Ehrlich, *Die Med. Woche und Balneol. Cent.* **1901**, 151; 'Über die dimethylaminobenzaldehydreaction';

[404] H. L. Bonkovsky, G. F. Barnard, *Semin. Liver Dis.* **1998**, *18*, 57-65; 'Diagnosis of porphyric syndromes: a practical approach in the era of molecular biology'; https://doi.org/10.1055/s-2007-1007141

[405] M. A. El-Guindi, H. H. El-Said, M. H. Hussein, S. Nassar Rel, A. M. Sira, *Hepatol. Res.* **2016**, *46*, 174-182; 'Urinary urobilinogen in biliary atresia: A missed, simple and cheap diagnostic test'; https://doi.org/10.1111/hepr.12558

[406] D. W. Nixon, *Cancer* **1973**, *31*, 596-599; 'Colorimetric response to Ehrlich's reagent in plasma from patients with and without cancer'; https://doi.org/10.1002/1097-0142(197303)31:3<596::aid-cncr2820310315>3.0.co;2-g

[407] H. D. Isenberg, L. H. Sundheim, *J. Bacteriol.* **1958**, *75*, 682-690; 'Indole reactions in bacteria'; https://doi.org/10.1128/jb.75.6.682-690.1958

[408] P. Fildes, *Microbiology* **1956**, *15*, 636-642; 'Production of Tryptophan by *Salmonella typhi* and *Escherichia coli*'; https://doi.org/10.1099/00221287-15-3-636

[409] F. C. Happold, L. Hoyle, *Biochem. J.* **1934**, *28*, 1171-1173; 'The quantitative determination of indole in bacterial cultures'; https://doi.org/10.1042/bj0281171

[410] M. Philp, S. Fu, *Drug Test. Anal.* **2018**, *10*, 95-108; 'A review of chemical 'spot' tests: A presumptive illicit drug identification technique'; https://doi.org/10.1002/dta.2300

[411] K. R. Scott, J. D. Power, S. D. McDermott, J. E. O'Brien, B. N. Talbot, M. G. Barry, P. V. Kavanagh, *Drug Test. Anal.* **2014**, *6*, 598-606; 'Identification of (2-aminopropyl)indole positional isomers in forensic samples'; https://doi.org/10.1002/dta.1508

[412] F. J. Hidalgo, M. Alaiz, R. Zamora, *Anal. Biochem.* **1998**, *262*, 129-136; 'A spectrophotometric method for the determination of proteins damaged by oxidized lipids'; https://doi.org/10.1006/abio.1998.2758

[413] H. Durmus, S. Durmazel, A. Uzer, B. Gokdere, E. Ercag, R. Apak, *Anal. Sci.* **2018**, *34*, 1419-1425; 'Colorimetric Determination of (Aminoalkyl)indole-containing Synthetic Cannabimimetics'; https://doi.org/10.2116/analsci.18P305

[414] M. Knowlton, F. C. Dohan, H. Sprince, *Anal. Chem.* **2002**, *32*, 666-668; 'Use of Modified Ehrlich's Reagent for Measurement of Indolic Compounds'; https://doi.org/10.1021/ac60162a029

[415] A. Ehmann, *J. Chromatogr.* **1977**, *132*, 267-276; 'The van urk-Salkowski reagent-a sensitive and specific chromogenic reagent for silica gel thin-layer chromatographic detection and identification of indole derivatives'; https://doi.org/10.1016/s0021-9673(00)89300-0

[416] R. Cairns, A. Gomm, C. Peel, M. Sharkey, E. O'Reilly, *ChemCatChem* **2019**, *11*, 4738-4743; 'A Comprehensive Quantitative Assay for Amine Transaminases'; https://doi.org/10.1002/cctc.201901430

[417] A. C. Lamb, R. A. Federico-Perez, Z. L. Xue, *Anal .Biochem.* **2015**, *484*, 21-23; 'Product in indole detection by Ehrlich's reagent'; https://doi.org/10.1016/j.ab.2015.04.033
[418] R. J. Goldacre, J. N. Phillips, *J. Chem. Soc.* **1949**, 1724; 'The ionization of basic triphenylmethane dyes'; https://doi.org/10.1039/jr9490001724
[419] D. F. Duxbury, *Chem. Rev.* **2002**, *93*, 381-433; 'The photochemistry and photophysics of triphenylmethane dyes in solid and liquid media'; https://doi.org/10.1021/cr00017a018
[420] S. Kille, C. G. Acevedo-Rocha, L. P. Parra, Z. G. Zhang, D. J. Opperman, M. T. Reetz, J. P. Acevedo, *ACS Synth. Biol.* **2013**, *2*, 83-92; 'Reducing codon redundancy and screening effort of combinatorial protein libraries created by saturation mutagenesis'; https://doi.org/10.1021/sb300037w
[421] E. F. Pettersen, T. D. Goddard, C. C. Huang, G. S. Couch, D. M. Greenblatt, E. C. Meng, T. E. Ferrin, *J. Comput. Chem.* **2004**, *25*, 1605-1612; 'UCSF Chimera - a visualization system for exploratory research and analysis'; https://doi.org/10.1002/jcc.20084
[422] M. V. Shapovalov, R. L. Dunbrack, Jr., *Structure* **2011**, *19*, 844-858; 'A smoothed backbone-dependent rotamer library for proteins derived from adaptive kernel density estimates and regressions'; https://doi.org/10.1016/j.str.2011.03.019
[423] J. Schlesier, J. Siegrist, S. Gerhardt, A. Erb, S. Blaesi, M. Richter, O. Einsle, J. N. Andexer, *BMC Struct. Biol.* **2013**, *13*, 22; 'Structural and functional characterisation of the methionine adenosyltransferase from *Thermococcus kodakarensis*'; https://doi.org/10.1186/1472-6807-13-22
[424] B. P. Chapple, Master thesis, Heinrich Heine University, Düsseldorf **2021**. 'Enzymatic alkyl-derivatization of a physostigmine pre-cursor using two different SAM-supply systems'.
[425] A. Suzuki, *Angew. Chem. Int. Ed.* **2011**, *50*, 6722-6737; 'Cross-coupling reactions of organoboranes: an easy way to construct C-C bonds (Nobel Lecture)'; (*Angew. Chem.*, *123*, 6854-6869) https://doi.org/10.1002/anie.201101379
[426] H. Doucet, *Eur. J. Org. Chem.* **2008**, *2008*, 2013-2030; 'Suzuki–Miyaura Cross-Coupling Reactions of Alkylboronic Acid Derivatives or Alkyltrifluoroborates with Aryl, Alkenyl or Alkyl Halides and Triflates'; https://doi.org/10.1002/ejoc.200700984
[427] S. L. Buchwald, 'Cross-coupling reactions: a practical guide', *Vol. 219*, Springer Science & Business Media, **2002**.
[428] J. Buchler, S. H. Malca, D. Patsch, M. Voss, N. J. Turner, U. T. Bornscheuer, O. Allemann, C. Le Chapelain, A. Lumbroso, O. Loiseleur, R. Buller, *Nat. Commun.* **2022**, *13*, 371; 'Algorithm-aided engineering of aliphatic halogenase WelO5* for the asymmetric late-stage functionalization of soraphens'; https://doi.org/10.1038/s41467-022-27999-1
[429] J. R. Horton, K. Sawada, M. Nishibori, X. Zhang, X. Cheng, *Structure* **2001**, *9*, 837-849; 'Two polymorphic forms of human histamine methyltransferase: structural, thermal, and kinetic comparisons'; https://doi.org/10.1016/s0969-2126(01)00643-8
[430] R. M. Thompson, F. M. Strong, *Biochem. Biophys. Res. Commun.* **1971**, *43*, 213-216; 'Identification of erythromycin A in cultures of *Streptomyces griseoplanus*'; https://doi.org/10.1016/s0006-291x(71)80109-2
[431] L. D. Boeck, K. L. Christy, R. Shah, *Appl. Microbiol.* **1971**, *21*, 1075-1079; 'Production of anticapsin by *Streptomyces griseoplanus*'; https://doi.org/10.1128/am.21.6.1075-1079.1971
[432] M. van Kempen, S. S. Kim, C. Tumescheit, M. Mirdita, J. Lee, C. L. M. Gilchrist, J. Soding, M. Steinegger, *Nat. Biotechnol.* **2024**, *42*, 243-246; 'Fast and accurate protein structure search with Foldseek'; https://doi.org/10.1038/s41587-023-01773-0
[433] A. M. Lilja, Y. Luo, Q. S. Yu, J. Rojdner, Y. Li, A. M. Marini, A. Marutle, A. Nordberg, N. H. Greig, *PLoS One* **2013**, *8*, e54887; 'Neurotrophic and neuroprotective actions of (-)- and (+)-phenserine, candidate drugs for Alzheimer's disease'; https://doi.org/10.1371/journal.pone.0054887

[434] A. Huang, J. J. Kodanko, L. E. Overman, *J. Am. Chem. Soc.* **2004**, *126*, 14043-14053; 'Asymmetric synthesis of pyrrolidinoindolines. Application for the practical total synthesis of (-)-phenserine'; https://doi.org/10.1021/ja046690e

[435] K. J. Padiya, S. Gavade, B. Kardile, M. Tiwari, S. Bajare, M. Mane, V. Gaware, S. Varghese, D. Harel, S. Kurhade, *Org. Lett.* **2012**, *14*, 2814-2817; 'Unprecedented "in water" imidazole carbonylation: paradigm shift for preparation of urea and carbamate'; https://doi.org/10.1021/ol301009d

[436] Y. Ren, S. A. Rousseaux, *J. Org. Chem.* **2018**, *83*, 913-920; 'Metal-free synthesis of unsymmetrical ureas and carbamates from CO_2 and amines via isocyanate intermediates';

[437] E. Watkins-Dulaney, S. Straathof, F. Arnold, *ChemBioChem* **2021**, *22*, 5-16; 'Tryptophan synthase: biocatalyst extraordinaire'; https://doi.org/10.1002/cbic.202000379

[438] A. D. McDonald, S. K. Bruffy, A. T. Kasat, A. R. Buller, *Angew. Chem. Int. Ed.* **2022**, *61*, e202212637; 'Engineering enzyme substrate scope complementarity for promiscuous cascade synthesis of 1,2-amino alcohols'; (*Angew. Chem.*, *134*, e202212637) https://doi.org/10.1002/anie.202212637

[439] Q. Wang, C. Li, B. Yuan, A. Yu, G. Qu, Z. Sun, *ChemBioChem* **2024**, *25*, e202400069; 'Engineering the activity of a newly identified arylalkylamine N-acetyltransferase in the acetylation of 5-hydroxytryptamine'; https://doi.org/10.1002/cbic.202400069

[440] M. Musil, A. Jezik, J. Horackova, S. Borko, P. Kabourek, J. Damborsky, D. Bednar, *Briefings Bioinf.* **2024**, *25*, bbad425; 'FireProt 2.0: web-based platform for the fully automated design of thermostable proteins'; https://doi.org/10.1093/bib/bbad425

[441] J. Schymkowitz, J. Borg, F. Stricher, R. Nys, F. Rousseau, L. Serrano, *Nucleic Acids Res.* **2005**, *33*, W382-388; 'The FoldX web server: an online force field'; https://doi.org/10.1093/nar/gki387

[442] F. Pucci, R. Bourgeas, M. Rooman, *Sci. Rep.* **2016**, *6*, 23257; 'Predicting protein thermal stability changes upon point mutations using statistical potentials: Introducing HoTMuSiC'; https://doi.org/10.1038/srep23257

[443] H. Cao, J. Wang, L. He, Y. Qi, J. Z. Zhang, *J. Chem. Inf. Model.* **2019**, *59*, 1508-1514; 'DeepDDG: Predicting the Stability Change of Protein Point Mutations Using Neural Networks'; https://doi.org/10.1021/acs.jcim.8b00697

[444] T. M. Rosch, J. Tenhaef, T. Stoltmann, T. Redeker, D. Kosters, N. Hollmann, K. Krumbach, W. Wiechert, M. Bott, S. Matamouros, J. Marienhagen, S. Noack, *ACS Synth. Biol.* **2024**, *13*, 2227-2237; 'AutoBioTech - A versatile biofoundry for automated strain engineering'; https://doi.org/10.1021/acssynbio.4c00298

[445] M. J. Menke, P. Schneider, C. P. S. Badenhorst, A. Kunzendorf, F. Heinz, M. Dorr, M. A. Hayes, U. T. Bornscheuer, *Angew. Chem. Int. Ed.* **2023**, *62*, e202313912; 'A universal, continuous assay for SAM-dependent methyltransferases'; (*Angew. Chem.*, *135*, e202313912) https://doi.org/10.1002/anie.202313912

[446] W. Kabsch, *Acta Crystallogr., Sect. D: Biol. Crystallogr.* **2010**, *66*, 125-132; 'Xds'; https://doi.org/10.1107/S0907444909047337

[447] A. Vagin, A. Teplyakov, *Acta Crystallogr., Sect. D: Biol. Crystallogr.* **2010**, *66*, 22-25; 'Molecular replacement with MOLREP'; https://doi.org/10.1107/S0907444909042589

[448] T. C. Terwilliger, R. W. Grosse-Kunstleve, P. V. Afonine, N. W. Moriarty, P. H. Zwart, L. W. Hung, R. J. Read, P. D. Adams, *Acta Crystallogr., Sect. D: Biol. Crystallogr.* **2008**, *64*, 61-69; 'Iterative model building, structure refinement and density modification with the PHENIX AutoBuild wizard'; https://doi.org/10.1107/S090744490705024X

[449] D. Liebschner, P. V. Afonine, M. L. Baker, G. Bunkoczi, V. B. Chen, T. I. Croll, B. Hintze, L. W. Hung, S. Jain, A. J. McCoy, N. W. Moriarty, R. D. Oeffner, B. K. Poon, M. G. Prisant, R. J. Read, J. S. Richardson, D. C. Richardson, M. D. Sammito, O. V. Sobolev, D. H. Stockwell, T. C. Terwilliger, A. G. Urzhumtsev, L. L. Videau, C. J. Williams, P. D. Adams, *Acta Crystallogr., Sect. D: Struct. Biol.* **2019**, *75*, 861-877; 'Macromolecular structure determination using X-rays, neutrons and electrons: recent developments in Phenix'; https://doi.org/10.1107/S2059798319011471

[450] P. Emsley, B. Lohkamp, W. G. Scott, K. Cowtan, *Acta Crystallogr., Sect. D: Biol. Crystallogr.* **2010**, *66*, 486-501; 'Features and development of Coot'; https://doi.org/10.1107/S0907444910007493

[451] C. J. Williams, J. J. Headd, N. W. Moriarty, M. G. Prisant, L. L. Videau, L. N. Deis, V. Verma, D. A. Keedy, B. J. Hintze, V. B. Chen, S. Jain, S. M. Lewis, W. B. Arendall, 3rd, J. Snoeyink, P. D. Adams, S. C. Lovell, J. S. Richardson, D. C. Richardson, *Protein Sci.* **2018**, *27*, 293-315; 'MolProbity: More and better reference data for improved all-atom structure validation'; https://doi.org/10.1002/pro.3330

[452] J. Eberhardt, D. Santos-Martins, A. F. Tillack, S. Forli, *J. Chem. Inf. Model.* **2021**, *61*, 3891-3898; 'AutoDock Vina 1.2. 0: New docking methods, expanded force field, and python bindings'; https://doi.org/10.1021/acs.jcim.1c00203

9. Annexes

9.1 Plasmids

Table 23. List of plasmids used in this work.

Plasmid	Genotype	Origin
pET21a(+)	*lacI*, Ampr, T7 promoter, T7 terminator, f1 ori, pBR322 ori	Novagen
pET28a(+)	*lac*I, Kanr, T7 promoter, T7 terminator, f1 ori, pBR322 ori	Novagen
pET21a(+)-mat_*Tk*	pET21a(+); *Tk*MAT (*C*-His6)	B. Chapple[a]
pET21a(+)_psmd_Sa	pET21a(+); *Psmd_Sa* (*C*-His6)	P. Schneider[b]
pET21a(+)_psmd_Sa opt	pET21a(+); *Psmd_Sa* optimized (*C*-His6)	This work
pET21a(+)_psmd_Sg	pET21a(+); *Psmd_Sg* (*C*-His6)	P. Schneider[b]
pET28a_CtHMT	pET28a(+); *CtHMT* (*C*-His6)	P. Schneider[b]
pET28a(+)_AcHMT	pET28a(+); *Psmd_Sa* (*C*-His6)	B. Chapple[a]
pET28a(+)_EcMTAN	pET28a(+); EcMTAN	B. Chapple[a]
pET21a(+)_Sa_Mut(X)	pET21a(+); *Psmd_Sa* mutant no. (X) (*C*-His6)	This work
pET21a(+)_Sa_opt_Mut(X)	pET21a(+); *Psmd_Sa* optimized gene mutant no. (X) (*C*-His6)	This work
pET21a(+)_Sa_opt_Lib(X)	pET21a(+); *Psmd_Sa* optimized gene saturation library mix no. (X) (*C*-His6)	This work
pET21a(+)_psmd_GP	pET21a(+)-PsmD_Gp (*C*-His6)	This work
pET21a(+)_psmd_CAT	pET21a(+)-PsmD_Cat (*C*-His6)	This work

[a] Benjamin Chapple, Institute of Bioorganic Chemistry, Heinrich Heine University, Düsseldorf
[b] Pascal Schneider, Institute of Bioorganic Chemistry, Heinrich Heine University, Düsseldorf

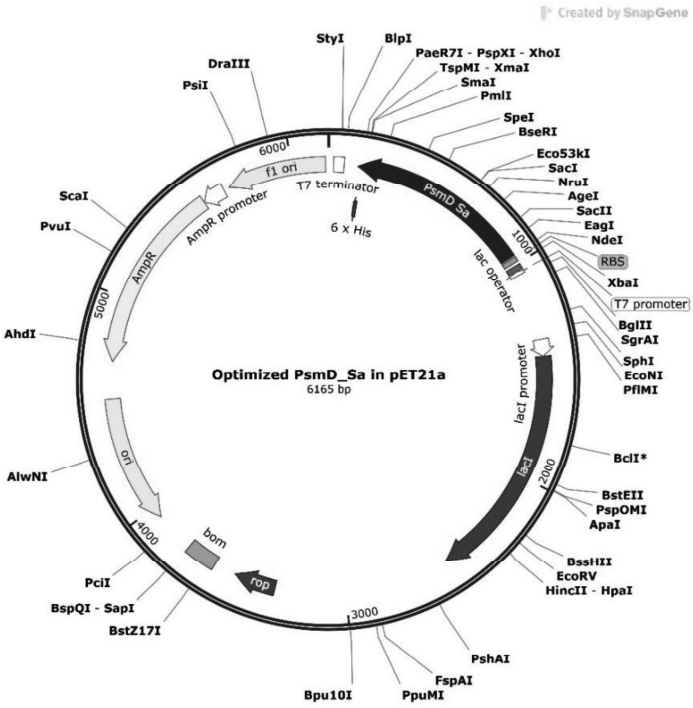

Figure 104. Plasmid map of the codon harmonized PsmD_*Sa* gene in the pET21a(+) vector. Single-cutter restriction enzyme sites are represented.

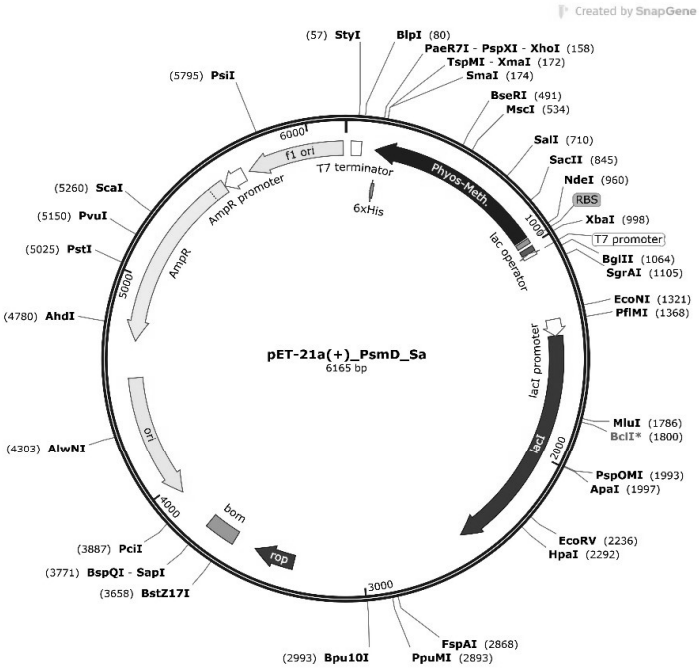

Figure 105. Plasmid map of the native PsmD_*Sa* gene in the pET21a(+) vector. Single-cutter restriction enzyme sites are represented.

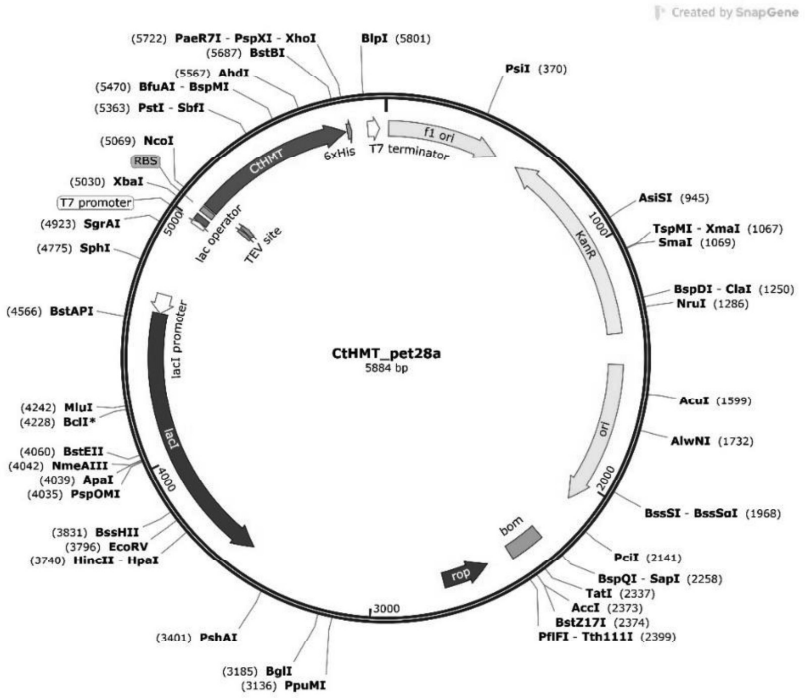

Figure 106. Plasmid map of the codon harmonized *Ct*HMT gene in the pET28a(+) vector. Single-cutter restriction enzyme sites are represented.

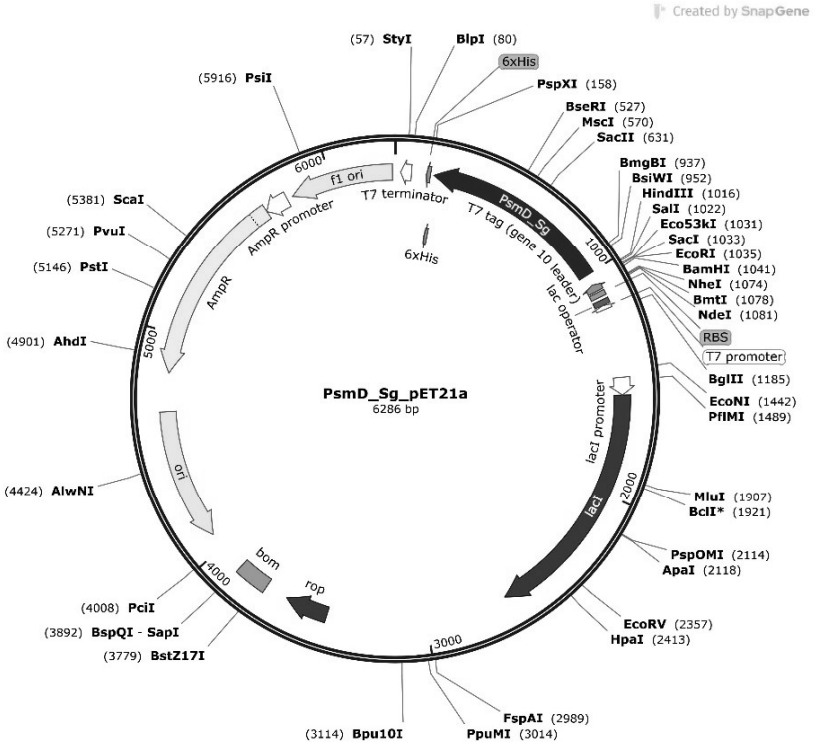

Figure 107. Plasmid map of the PsmD_*Sg* gene in the pET21a(+) vector. Single-cutter restriction enzyme sites are represented.

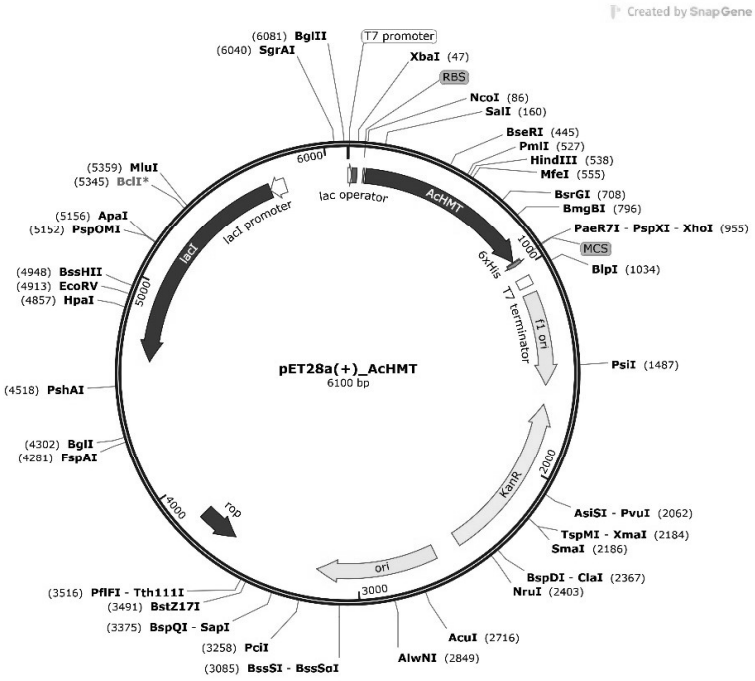

Figure 108. Plasmid map of the AcHMT gene in the pET28a(+) vector. Single-cutter restriction enzyme sites are represented.

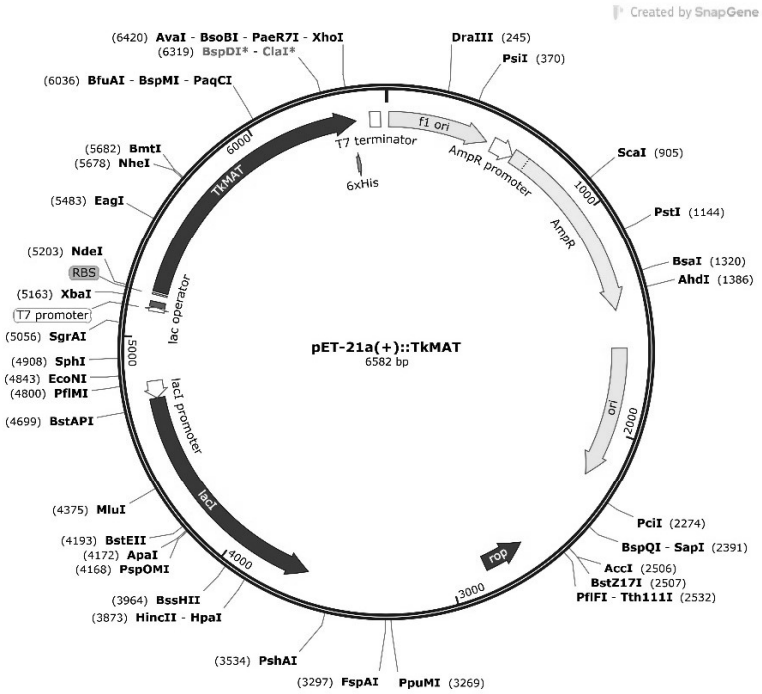

Figure 109. Plasmid map of the *Tk*MAT gene in the pET21a(+) vector. Single-cutter restriction enzyme sites are represented.

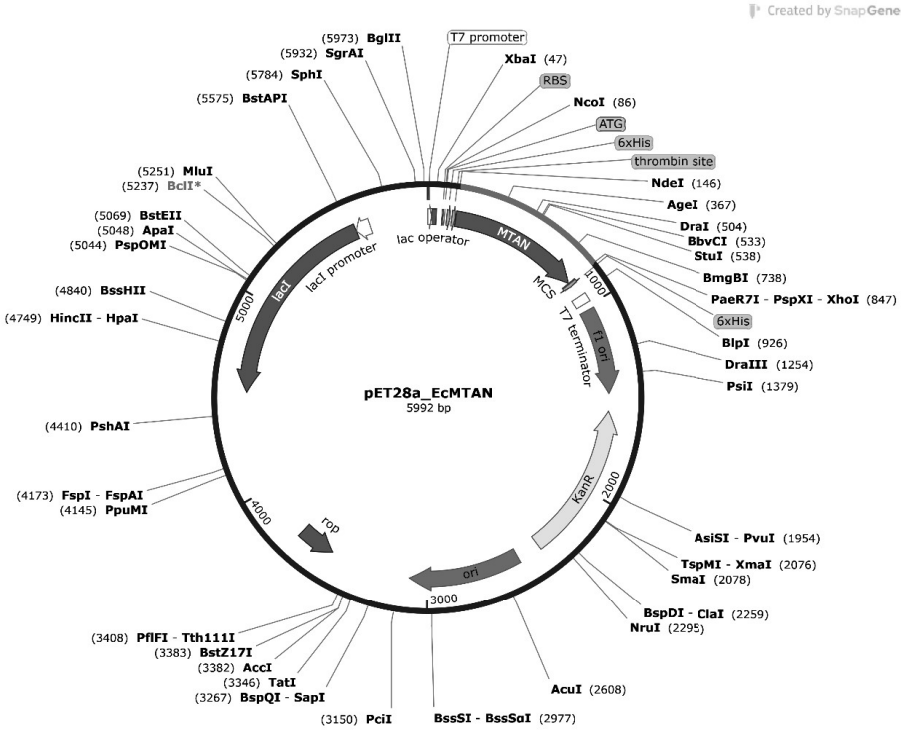

Figure 110. Plasmid map of the *Ec*MTAN gene in the pET28a(+) vector. Single-cutter restriction enzyme sites are represented.

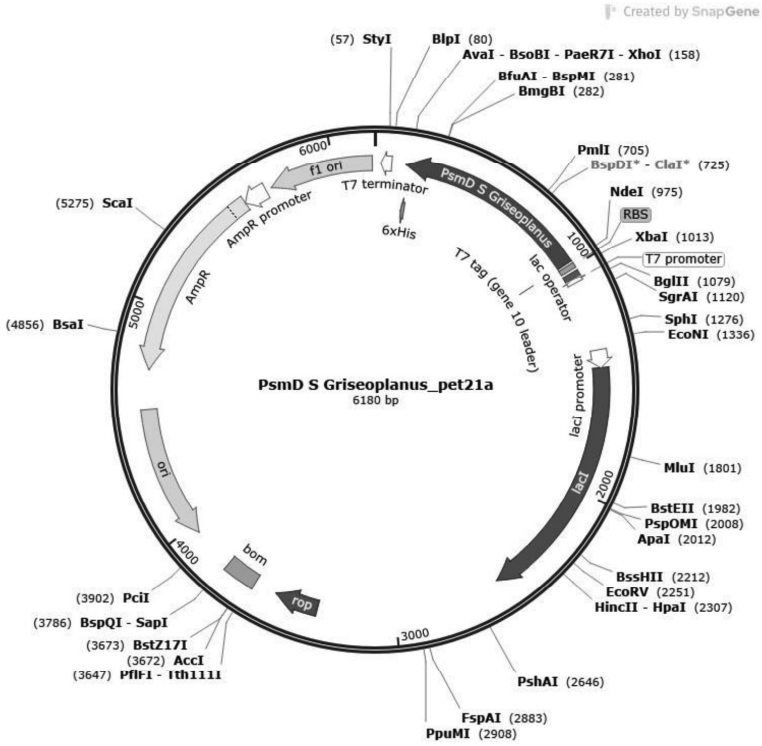

Figure 111. Plasmid map of the PsmD_GP gene in the pET21a(+) vector. Single-cutter restriction enzyme sites are represented.

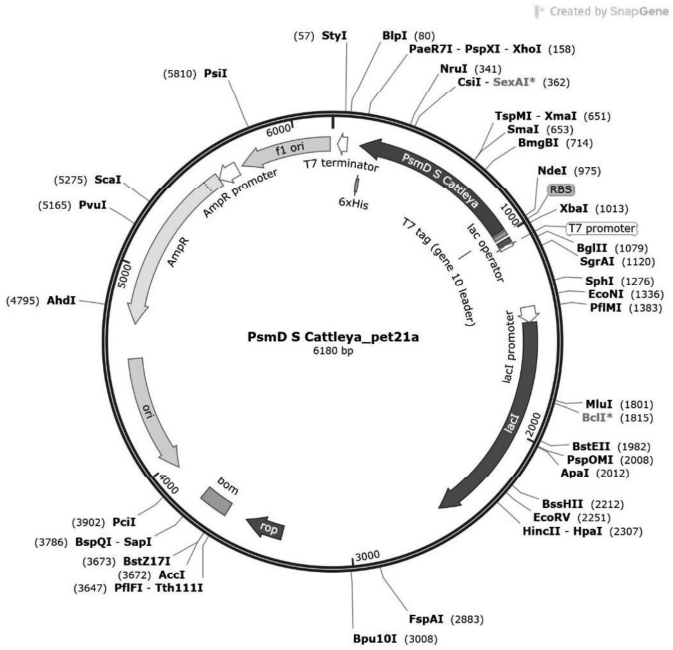

Figure 112. Plasmid map of the PsmD_Cat gene in the pET21a(+) vector. Single-cutter restriction enzyme sites are represented.

9.2 Primers

Table 24. Primers used for mutant generation through site-directed mutagenesis.

Identifier	PsmD_Sa variant	Primer sequence (5'-3')
M1	Y15A	ATGCCCGAGCCGGCCGCCGCGACCGC
		GCGGTCGCGGCGGCCGGCTCGGGCAT
M2	Y22A	GACCGCCGACGTGGCCGACCGGCTCGTC
		GACGAGCCGGTCGGCCACGTCGGCGGTC
M3	R38A	GGAGAGTCTCCCGCGCCGCGGATGGCC
		GGCCATCCGCGGCGCGGGAGACTCTCC
M4	D84A	GGTGACCGCCGTCGCCCGTTCCGAGACC
		GGTCTCGGAACGGGCGACGGCGGTCACC
M5	R85A	TGACCGCCGTCGACGCTTCCGAGACCATGTTG
		CAACATGGTCTCGGAAGCGTCGACGGCGGTCA
M6	M89A	CCGTTCCGAGACCGCGTTGGCCCTGGCG
		CGCCAGGGCCAACGCGGTCTCGGAACGG
M7	Y128A	GCCGCGTTCAACGCCCAGTCCAGCGCG
		CGCGCTGGACTGGGCGTTGAACGCGGC
M8	E157A	CGTCTTCGACATCGCGACTGCCGCGCTCC
		GGAGCGCGGCAGTCGCGATGTCGAAGACG
M9	E215A	GGCACCCGCGCGGTGCACCGGCTG
		CAGCCGGTGCACCGCGCGGGTGCC
M10	H217A	CCGCGAGGTGGCCCGGCTGTACGCCTTC
		GAAGGCGTACAGCCGGGCCACCTCGCGG
M11	Y128S	CGTTCAACTCCCAGTCCAGCGCGCACTCGCTG
		GACTGGGAGTTGAACGCGGCTGCGGTGCACAC
M12	Y128E	GTTCAACGAGCAGTCCAGCGCGCACTCG
		GGACTGCTCGTTGAACGCGGCTGCGGTGCAC
M13	E35D	GGGAGACTCTCCCCGGCCGCGGATGGCC
		GGGGAGAGTCTCCCCACTGGGCGATGGCGTAC
M14	W33A	CCCAGGCGGGAGAGTCTCCCCGGCCG
		CTCCCGCCTGGGCGATGGCGTACGCGAC
M15	L25A	CCGGGCCGTCGCGTACGCCATCGCCCAG
		CGACGGCCCGGTCGTACACGTCGGCGG
M18	W182A	GTTCATCGCGAACTTCACCAGTCAGCCGGACACCACC
		GTGAAGTTCGCGATGAACGCCAGGTCGCCCTCGTCG
M19	Y22S	CGTGTCCGACCGGCTCGTCGCGTACGC
		CGGTCGGACACGTCGGCGGTCGCGG
M21	E35A	GCCGGGGAGACGCTCCCCACTGGG
		CCCAGTGGGGAGCGTCTCCCCGGC
M22	Q199A	GGAGCGCGTGAACGCGGTGTAGTGCACGTC
		GACGTGCACTACACCGCGTTCACGCGCTCC
M23	Y197A	CTACTGCGACGTGCACGCCACCCAGTTCACGCG
		CGCGTGAACTGGGTGGCGTGCACGTCGCAGTAG
M24	W166A	CTCCTCAAGGGACACGCGGGCAACCGCATG
		CATGCGGTTGCCCGCGTGTCCCTTGAGGAG
M25	Y22D	*gene ordered from Genscript
M26	Y22E	*gene ordered from Genscript
M27	Y128E	* gene ordered from Genscript
M28	Y128S	* gene ordered from Genscript
M29	W166F	* gene ordered from Genscript
M30	W182F	* gene ordered from Genscript
M31	Y197A	* gene ordered from Genscript
M32	T18A	CCATACGCCGCGGCGGCCGATGTG

		CACATCGGCCGCCGCGGCGTATGG
M33	E13A	GGTATGCCCGCGCCATACGCCGC
		GCGGCGTATGGCGCGGGCATACC
M34	T88A	CCGTTCCGAGGCCATGTTGGCCC
		GGGCCAACATGGCCTCGGAACGG
M35	A123G	GGTATGCACCGGAGCCGCGTTC
		GAACGCGGCTCCGGTGCATACC
M36	A124G	GTATGCACCGCAGGCGCGTTCAAC
		GTTGAACGCGCCTGCGGTGCATAC
M37	W33F	CCATAGCCCAATTCGGAGAGTCTCCG
		CGGAGACTCTCCGAATTGGGCTATGG
M38	Y15F	CCCGAGCCATTCGCCGCGACG
		CGTCGCGGCGAATGGCTCGGG
M39	Y22F	GCCGATGTGTTCGACCGGCTCG
		CGAGCCGGTCGAACACATCGGC
M40	Y128F	GCGTTCAACTTCCAGTCCAGTGC
		GCACTGGACTGGAAGTTGAACGC
M41	E215D	GCACCCGCGACGTACACCGGC
		GCCGGTGTACGTCGCGGGTGC
M42	A125G	GCACCGCAGCCGGGTTCAACTACCAG
		CTGGTAGTTGAACCCGGCTGCGGTGC
M43	T18H	CCATACGCCGCGCACGCCGATGTGTACG
		CGTACACATCGGCGTGCGCGGCGTATGG
M44	F126L	Phos*CGCAGCCGCGCTCAACTACCAGTCCAG
		Phos* GTGCATACCACTGCGTCCGTGTCG
M45	F126C	Phos* CGCAGCCGCGTGCAACTACCAGTCCAG
		Phos* GTGCATACCACTGCGTCCGTGTCG
M46	T138A	Phos*CACTGGGAGAAGCCCTACACGCCGTAG
		Phos*AGTGTGCACTGGACTGGTAGTTGAACG
M47	F154V	Phos*CAACGTTCGTCTTGGACATCGAGACTGC
		Phos*CACCGGCTGGCAGCAC
M48	E157V	Phos*CGACATCGTGACTGCAGCGCTCC
		Phos*AAGACGAACGTTGCACCGG
M49	V227A	Phos*CACGACACCGCCCGCGCCC
		Phos*GTCGAACGCGTACAGCCGG
M18/15	W182A/L25A	M18 primers
M37/29	W33F/W166F	M37 primers
M18/31	W182A/Y197A	M18 primers

Table 25. Primers used for mutant library generation in site-saturation mutagenesis.

Identifier	**PsmD_*Sa* variant**	**Primer sequence (5'-3')**
S1	Y197X	**Fw:** Phos*NDTACACAGTTCACGCGCTCTGAAGCGG
		Fw: Phos*VHGACACAGTTCACGCGCTCTGAAGCGG
		Fw: Phos*TGGACACAGTTCACGCGCTCTGAAGCGG
		Rev: Phos*ATGCACGTCGCAGTAGGTGGTGTCCGG
S2	Y15X	**Fw 1:** Phos*CCCGAGCCANDTGCCGCGACGGCCG
		Fw2: Phos*CCCGAGCCAVHGGCCGCGACGGCCG
		Fw3: Phos*CCCGAGCCATGGGCCGCGACGGCCG
		Rev: Phos*CATACCCGCATCCTGGTGCGGCTG

S3	W33X	**Fw 1:** Phos* CATAGCCCAANDTGGAGAGTCTCCGC
		Fw2: Phos* CATAGCCCAAVHGGGAGAGTCTCCGC
		Rev: Phos* GCATACGCGACGAGCCGG
S4	W166X	**Fw:** Phos*GGGACATNDTGGCAATCGCATGTGG
		Fw: Phos*GGGACATVHGGGCAATCGCATGTGG
		Rev: Phos*TTGAGGAGCGCTGCAGTCTCGATG
S5	W166C/Y15X	Primer mix from S2
S6	W166C/W33X	Primer mix from S3
S7	W166C/Y197X	Primer mix from S1
S8	W166P/W33X	Primer mix from S3
S9	Y256X	**Fw1:** Phos* GCCACCCACNDTGAGACGTGGTTCCTC
		Fw2: Phos* GCCACCCACVHGGAGACGTGGTTCCTC
		Fw3: Phos* GCCACCCACTGGGAGACGTGGTTCCTC
		Rev: Phos* GTCGGTGGCGGGGCGTTC
S10	W166C/Y256X	Primer mix from S1
S11	W166C/Y197H/Y15X	Primer mix from S2
S12	W166C/Y197H/W33X	Primer mix from S3
S13	W166C/Y197H/Y15F/W33X	Primer mix from S3

9.3 SDS Gels

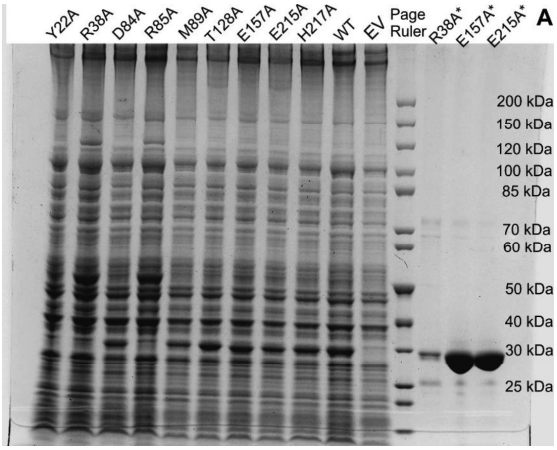

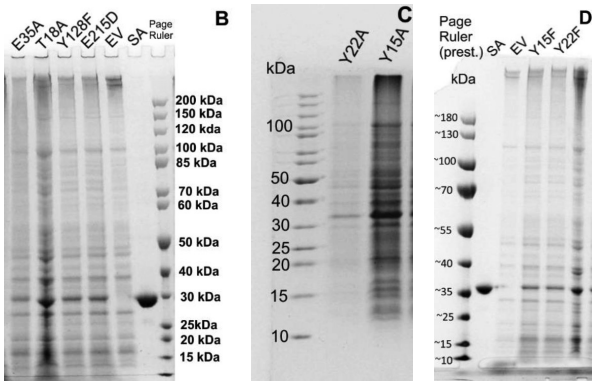

Figure 113. A,B,C,D: SDS Page displaying the expression of PsmD_*Sa* mutants in *E.coli* BL21 Gold (DE3), and the mutants isolated via Ni^{2+} affinity chromatography (marked with "*"). "WT" stands for wild type PsmD_*Sa*, and "EV" refers to *E. coli* BL21 (DE3) cells containing the empty pET21a vector**.** "SA" refers to isolated wild type PsmD_*Sa*. PsmD_*Sa* band is found at approx. 30 kDa (band at approx. 35 kDa in the case of prestained Page ruler).

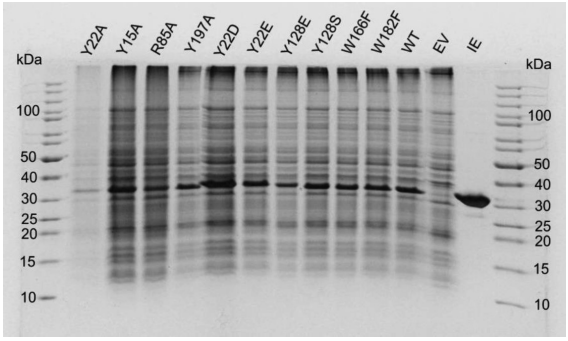

Figure 114. SDS gel showing the expression of various PsmD_Sa mutants in E. coli BL21 Gold (DE3). The PsmD protein band is expected at 30 kDa. WT-wild type; EV – empty vector; IE – isolated enzyme.

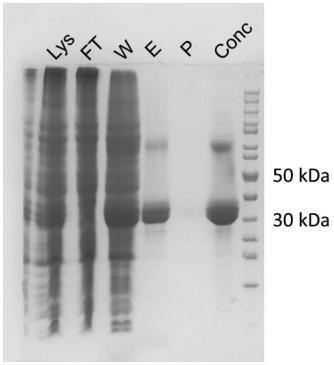

Figure 115. SDS gel of the purification steps for *Ac*HMT. Lys=lysate; FT=flow through; W=wash; E=elution; P=purge; Conc = final concentrated protein solution. PageRuler unstained was used as standard protein ladder.

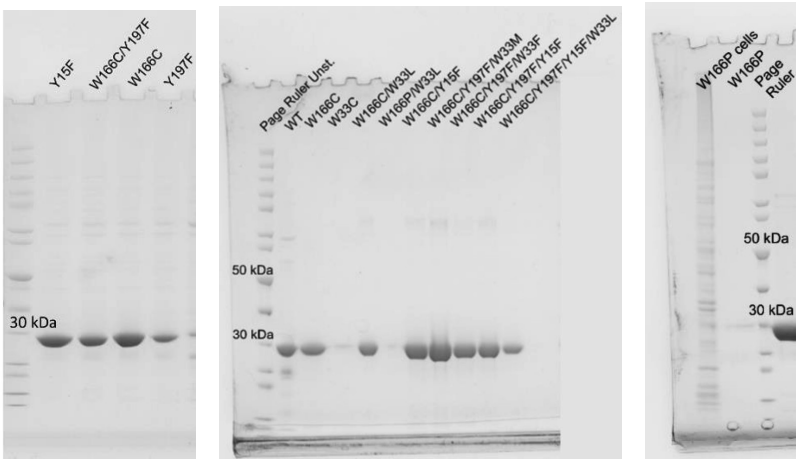

Figure 116. SDS Page gels of the isolated PsmD_*Sa* mutants from the saturation mutagenesis libraries. The expected protein band is at 30 kDa.

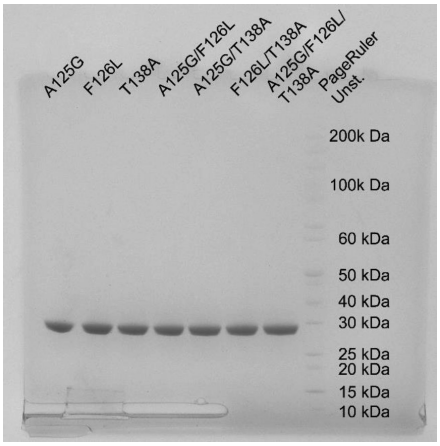

Figure 117. SDS Page gel of the isolated PsmD_*Sa* ethylation mutants. The expected protein band is at 30 kDa.

9.4 Design of experiment

Table 26. Design of experiment parameters tested for the PsmD_*Sa*/*Ct*HMT coupled reaction. The reactions were performed at 500 µL scale

		Factor 1	Factor 2	Factor 3	Factor 4	Response
Sample	**Run**	**C(Mel) (mM)**	**C(SAH) (µM)**	**Vol. HMT lysate (µL)**	**Vol. PsmD_*Sa* lysate (µL)**	**Conversion (%)**
2	1	3.6	11.7	72.6	72.6	13.5
25	2	3.6	11.7	302.4	302.4	87.9
15	3	20.5	68.3	302.4	72.6	29.9
1	4	3.6	11.7	72.6	72.6	31.7
18	5	3.6	11.7	72.6	302.4	73.8
39	6	12.1	80.0	187.5	187.5	100.0
14	7	3.6	68.3	302.4	72.6	44.3
38	8	12.1	0.0	187.5	187.5	100.0
8	9	20.5	68.3	72.6	72.6	32.7
16	10	20.5	68.3	302.4	72.6	30.4
3	11	20.5	11.7	72.6	72.6	33.9
12	12	20.5	11.7	302.4	72.6	35.6
45	13	12.1	40.0	187.5	25.0	9.4
41	14	12.1	40.0	25.0	187.5	72.0
34	15	0.1	40.0	187.5	187.5	100.0
44	16	12.1	40.0	350.0	187.5	100.0
43	17	12.1	40.0	350.0	187.5	100.0
42	18	12.1	40.0	25.0	187.5	81.1
6	19	3.6	68.3	72.6	72.6	39.7
7	20	20.5	68.3	72.6	72.6	35.9
50	21	12.1	40.0	187.5	187.5	100.0
52	22	12.1	40.0	187.5	187.5	100.0
40	23	12.1	80.0	187.5	187.5	100.0

53	24	12.1	40.0	187.5	187.5	100.0
19	25	20.5	11.7	72.6	302.4	100.0
35	26	24.0	40.0	187.5	187.5	89.6
10	27	3.6	11.7	302.4	72.6	34.1
29	28	3.6	68.3	302.4	302.4	64.2
5	29	3.6	68.3	72.6	72.6	29.2
11	30	20.5	11.7	302.4	72.6	31.1
20	31	20.5	11.7	72.6	302.4	100.0
28	32	20.5	11.7	302.4	302.4	100.0
9	33	3.6	11.7	302.4	72.6	33.7
31	34	20.5	68.3	302.4	302.4	100.0
37	35	12.1	0.0	187.5	187.5	100.0
30	36	3.6	68.3	302.4	302.4	56.0
33	37	0.1	40.0	187.5	187.5	100.0
22	38	3.6	68.3	72.6	302.4	23.9
49	39	12.1	40.0	187.5	187.5	100.0
24	40	20.5	68.3	72.6	302.4	100.0
4	41	20.5	11.7	72.6	72.6	37.7
17	42	3.6	11.7	72.6	302.4	34.3
54	43	12.1	40.0	187.5	187.5	100.0
23	44	20.5	68.3	72.6	302.4	100.0
48	45	12.1	40.0	187.5	350.0	100.0
27	46	20.5	11.7	302.4	302.4	100.0
36	47	24.0	40.0	187.5	187.5	100.0
13	48	3.6	68.3	302.4	72.6	24.1
32	49	20.5	68.3	302.4	302.4	100.0
21	50	3.6	68.3	72.6	302.4	21.6
51	51	12.1	40.0	187.5	187.5	100.0
26	52	3.6	11.7	302.4	302.4	24.6
47	53	12.1	40.0	187.5	350.0	83.9
46	54	12.1	40.0	187.5	25.0	10.0

The fit function used for the design of experiment is:

$$Conversion = -59.1323 + 4.8035 * A - 0.0357 * B + 0.5788 * C + 1.5785 * D - 0.0074 * A * C + 0.0259 * A * D - 0.2043 * A^2 - 0.0022 * C^2 - 0.0079 * D^2$$

Where:
A = Mel concentration (mM)
B = SAH concentration (µM)
C = HMT lysate volume (µL)
D = PsmD_Sa lysate volume (µL)
Fit parameters: R^2: 0.9097; Adj. R^2: 0.8913 Adeq. precision: 17.9788.

Table 27. Design of experiment parameters tested for the PsmD_*Sa*/*Ac*HMT coupled ethylation in the presence of MTAN. The reactions were performed at 50 µL scale.

		Factor 1	Factor 2	Factor 3	Response
Sample	**Run**	**Conc. PsmD (µM)**	**Vol AcHMT mix (µL)**	**Conc. MTAN (µM)**	**Conversion (%)**
3	1	82	12	9	49.4
7	2	82	33	9	33.8
33	3	55	23	17	24.7
10	4	28	12	26	16.2

8	5	82	33	9	27.4
1	6	28	12	9	14.9
4	7	82	12	9	37.0
14	8	28	33	26	11.3
11	9	82	12	26	33.3
22	10	55	5	17	26.7
26	11	55	23	3	22.4
27	12	55	23	32	21.0
5	13	28	33	9	11.6
24	14	55	40	17	21.7
17	15	10	23	17	4.0
25	16	55	23	3	24.5
19	17	100	23	17	36.1
18	18	10	23	17	4.1
9	19	28	12	26	12.6
23	20	55	40	17	23.1
34	21	55	23	17	20.6
21	22	55	5	17	27.5
15	23	82	33	26	31.3
16	24	82	33	26	36.2
29	25	55	23	17	23.2
13	26	28	33	26	8.8
30	27	55	23	17	22.5
32	28	55	23	17	21.9
12	29	82	12	26	34.9
28	30	55	23	32	20.5
20	31	100	23	17	34.4
6	32	28	33	9	11.3
31	33	55	23	17	22.2
2	34	28	12	9	15.4

The fit function used for the design of experiment is:

$$Conversion = 13.65614 + 0.429366 * A - 0.736865 * B - 0.32589 * C + 0.001232 * A * B + 0.002074 * A * C + 0.005685 * A * C - 0.001113 * A^2$$

Where:
A = Conc. PsmD (µM)
B = Vol. AcHMT mix (µL)
C = Conc. MTAN (µM)

Fit parameters: R^2: 0.9686; Adj. R^2: 0.9563 Adeq. precision: 31.1785.

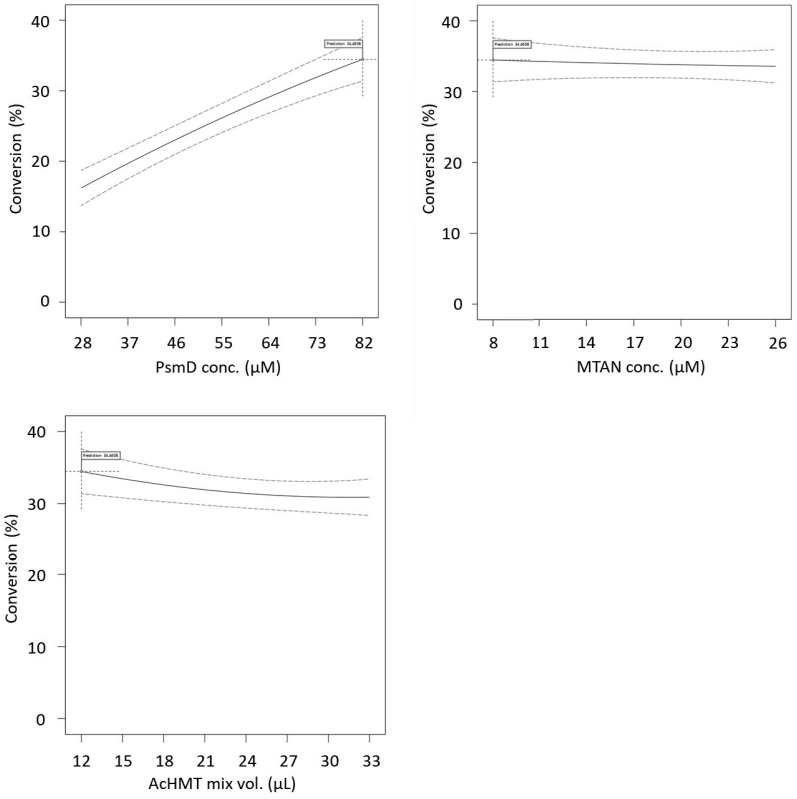

Figure 118. Influence of parameters in the ethylation reaction using PsmD_*Sa* and SAE produced by *Ac*HMT in the presence of MTAN, determined by a central composite design of experiment. The reactions were performed on a 50 µL scale.

9.5 Calibrations

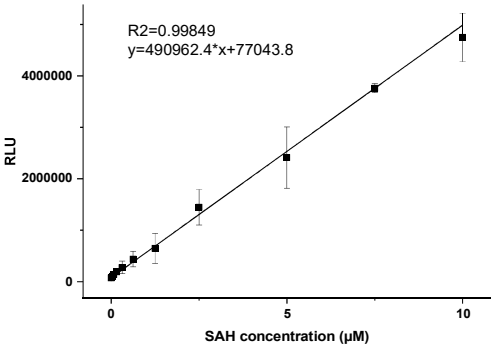

Figure 119. Example of SAH calibration for the calculation of methyltransferase activity using the MTase-Glo™ Assay. A stock solution of 15 µM SAH was provided by the kit and was used for the sample preparation. A new calibration was performed and used for each newly acquired MTase-Glo™ kit.

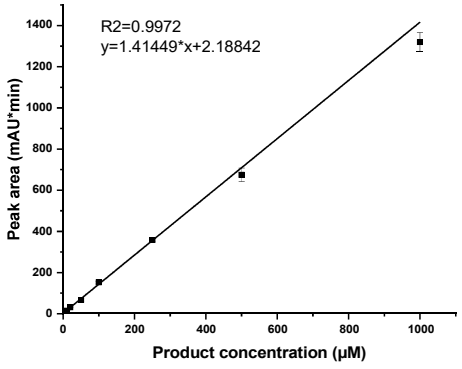

Figure 120. NP-HPLC calibration of product **P10.**

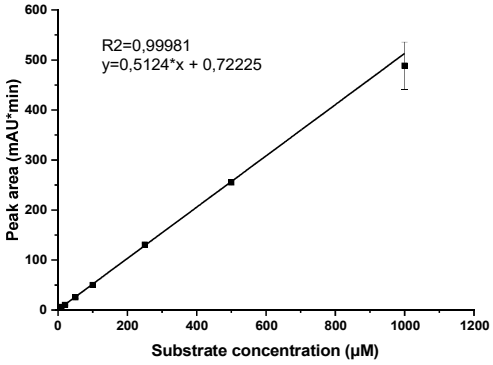

Figure 121. NP-HPLC calibration for substrate **10.**

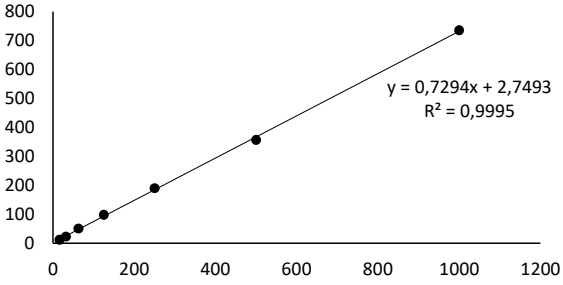

Figure 122. NP-HPLC calibration for the double methylated **N10.**

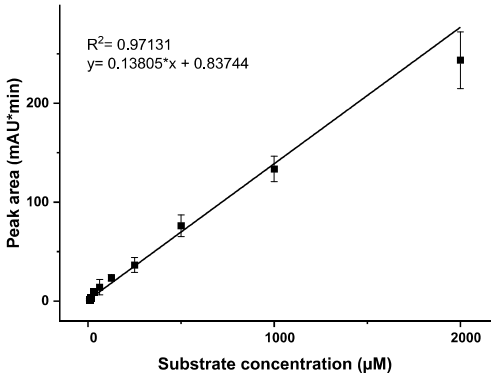

Figure 123. RP-HPLC calibration for substrate **10.**

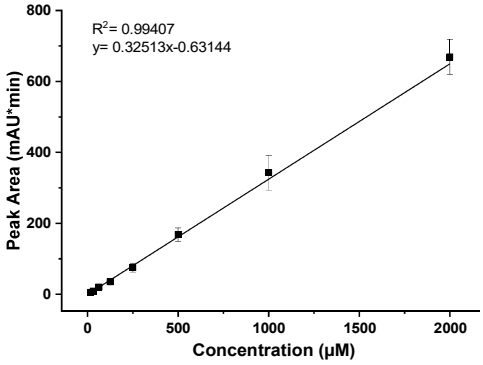

Figure 124. RP-HPLC calibration for product **P10.**

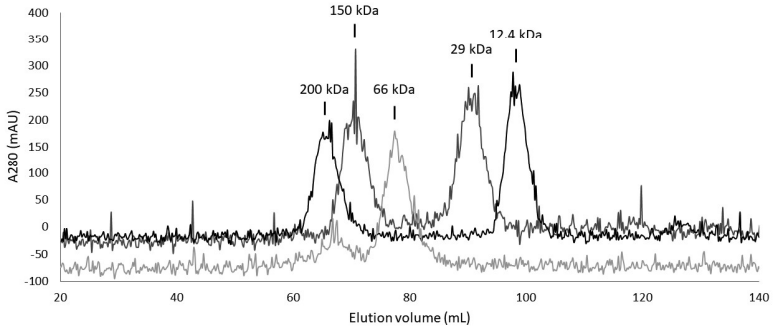

Figure 125. Size-exclusion chromatograms of standard calibration proteins from the gel filtration markers kit for protein molecular weights 12000-200000 Da (*Sigma*), and their molecular weight.

9.6 X-ray data collection and refinement statistics

Table 28. X-ray data collection and refinement statistics. Values in parentheses refer to the highest-resolution shell. The X-ray data collection and refinement were performed by Dr. Oliver Weiergräber (IBI-7, Forschungszentrum Jülich).

Specimen	**PsmD_*Sg***	**PsmD_*Sg* + SAH (crystal form 1)**	**PsmD_*Sg* + SAH (crystal form 2)**
PDB code	**7ZGT**	**7ZKH**	**7ZKG**
Data collection statistics			
Beamline	DESY P11	DESY P11	DESY P11
Detector	PILATUS 6MF	PILATUS 6MF	PILATUS 6MF
Wavelength [Å]	1.033	1.033	1.033
Space group	P 2_1 2_1 2_1	P 2_1 2_1 2	P 6_1 2 2
Unit cell parameters			
a, b, c [Å]	71.1, 87.5, 89.0	64.2, 96.0, 40.4	138.7, 138.7, 162.1
α, β, γ [°]	90, 90, 90	90, 90, 90	90, 90, 120
Resolution	46.88–2.05 (2.10–2.05)	53.36–1.40 (1.44–1.40)	56.32–2.30 (2.36–2.30)
No. reflections	35,369 (2572)	49,285 (3292)	41,427 (3019)
Completeness [%]	99.6 (99.3)	98.6 (89.7)	100.0 (100.0)
Multiplicity	13.1 (13.5)	8.2 (5.9)	39.3 (40.7)
Mean **I**/σ(**I**)	17.2 (0.8)	22.7 (0.9)	28.6 (1.1)
$CC_{1/2}$ [%]	100.0 (35.4)	100.0 (40.2)	100.0 (54.0)
Refinement statistics			
No. of reflections used	35,318	49,284	41,408
R_{work}	0.215	0.158	0.189
R_{free}	0.252	0.185	0.216
RMSD from ideal values			
Bonds [Å]	0.002	0.008	0.002
Angles [°]	0.415	0.990	0.481
Mean B [$Å^2$] (no. of atoms)			
Protein	60.6 (4023)	29.6 (2303)	76.3 (3963)
Ligands	72.8 (29)	24.0 (50)	91.2 (114)
Water	55.6 (155)	38.8 (296)	67.5 (86)
Ramachandran outliers [%]	0.0	0.0	0.0
Unusual rotamers [%]	0.5	0.0	0.0

9.7 NMR spectra

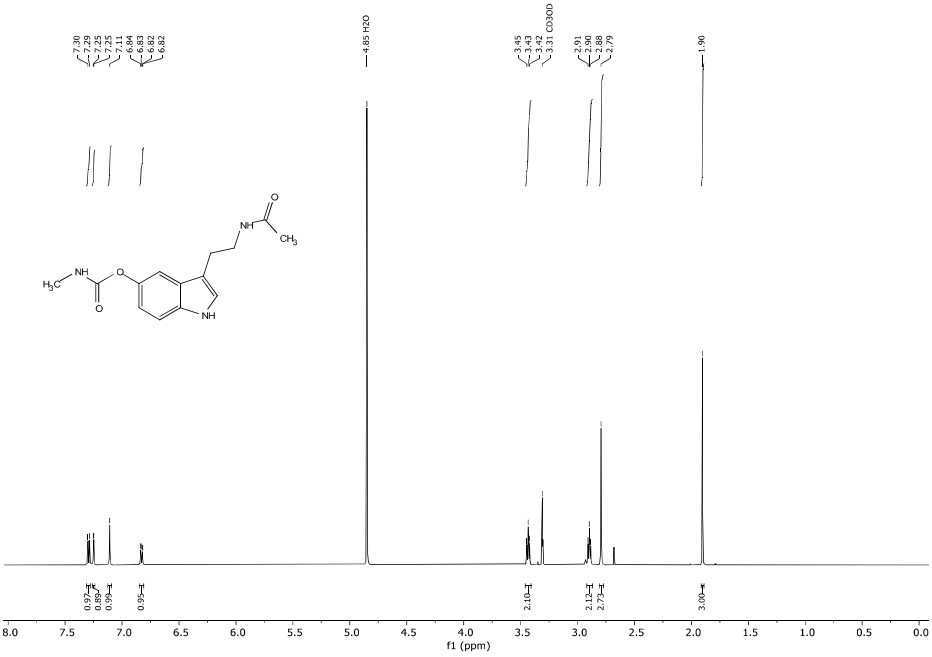

Figure 126. ^{1}H NMR spectrum of **10** (CD_3OD, 600 MHz).

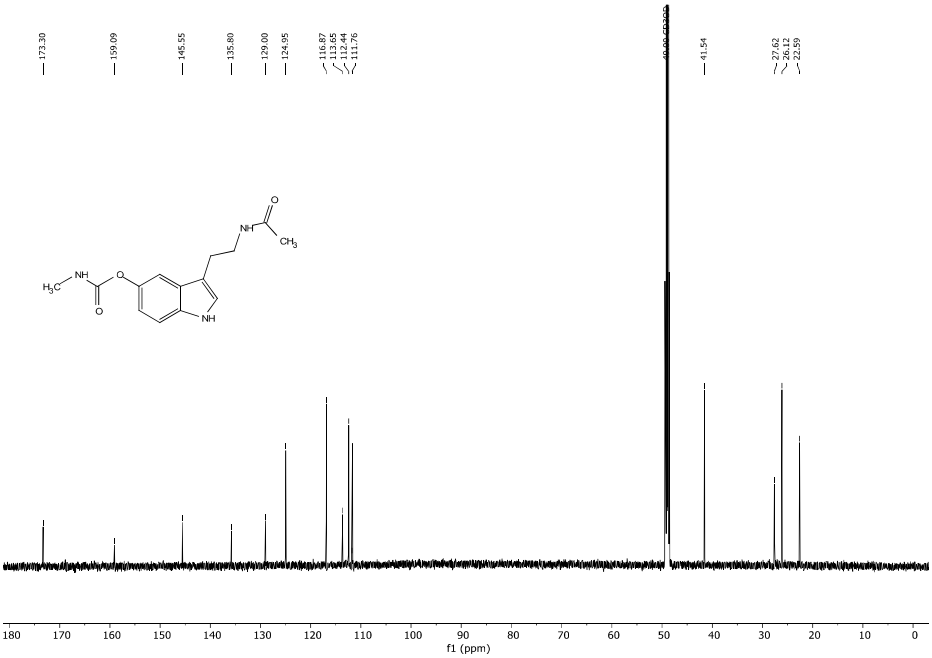

Figure 127. ^{13}C NMR spectrum of **10** (CD_3OD, 151 MHz).

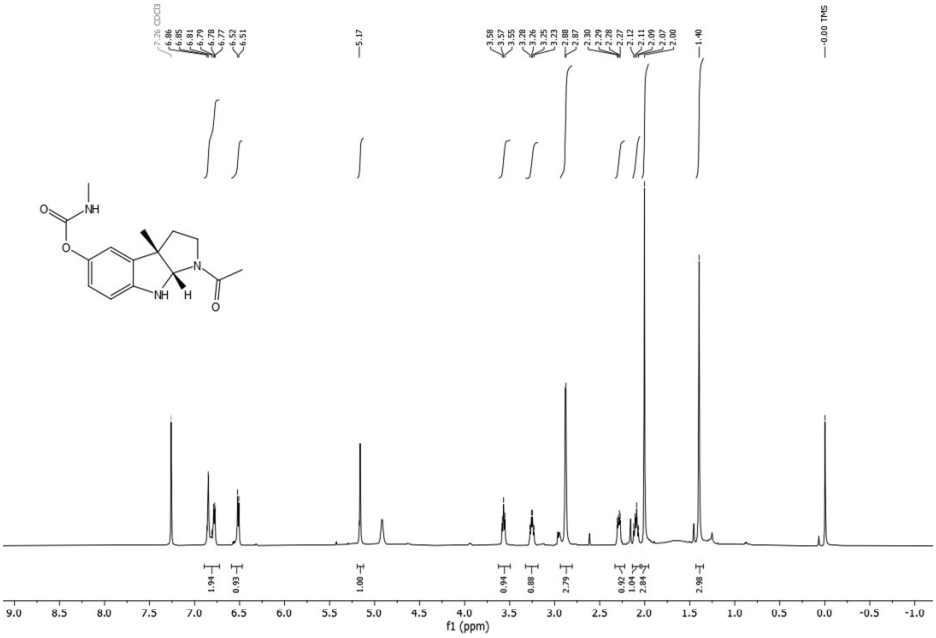

Figure 128. ^{1}H NMR spectrum of **P10** (CD_3OD, 600 MHz).

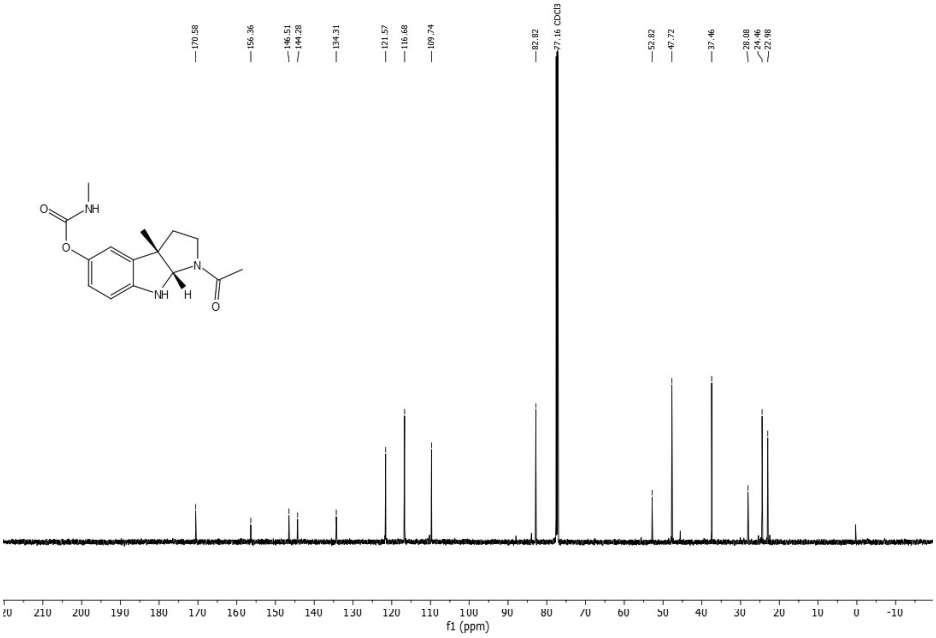

Figure 129. ^{13}C NMR spectrum of **P10** (CD_3OD, 151 MHz).

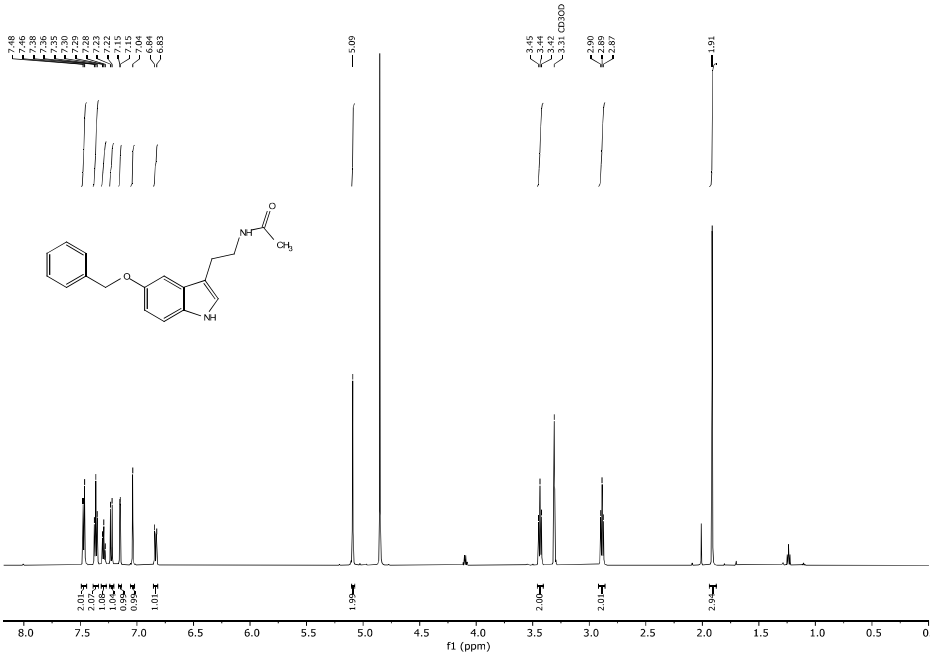

Figure 130. ^{1}H NMR spectrum of **14** (CD_3OD, 600 MHz).

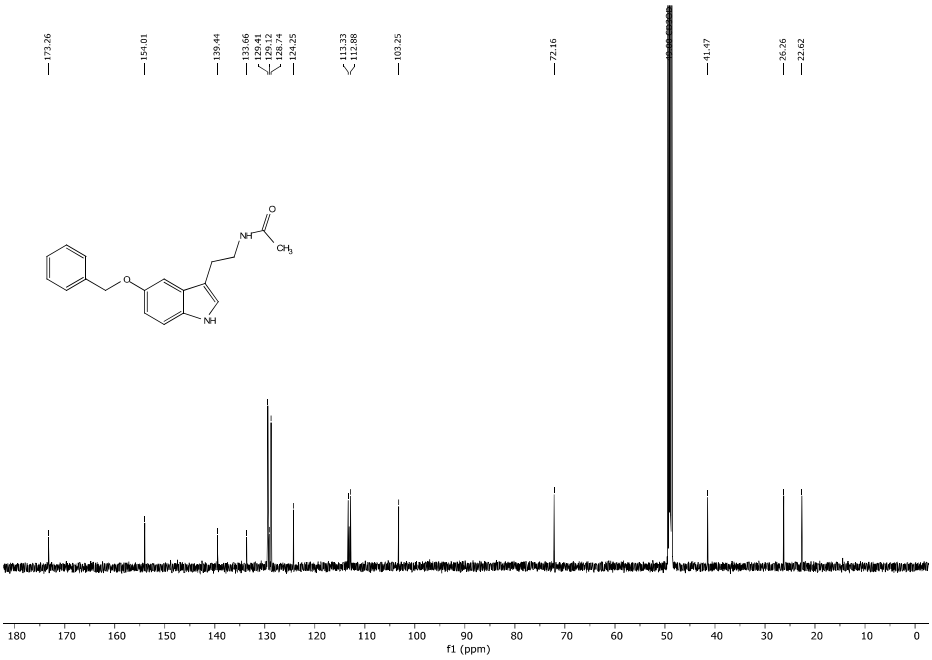

Figure 131. ^{13}C NMR spectrum of **14** (CD_3OD, 151 MHz).

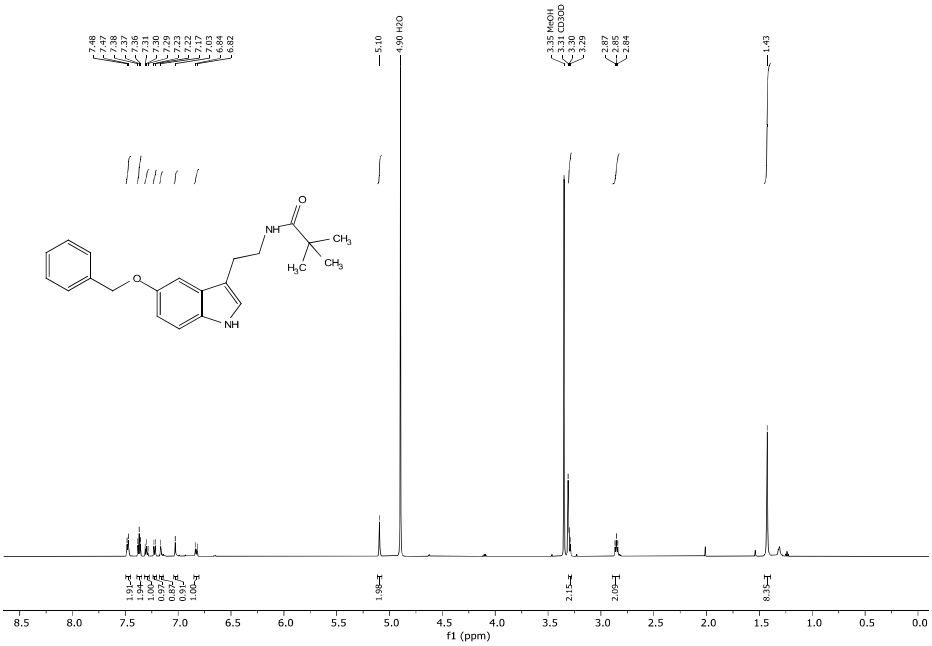

Figure 132. ^{1}H NMR spectrum of **41** (CD_3OD, 600 MHz).

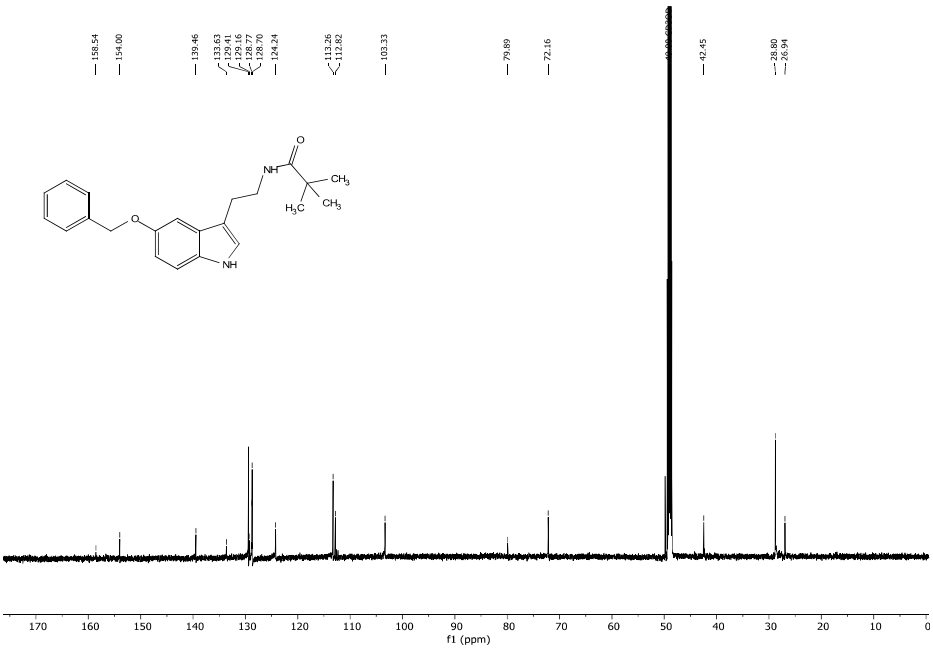

Figure 133. ^{13}C NMR spectrum of **41** (CD_3OD, 151 MHz).

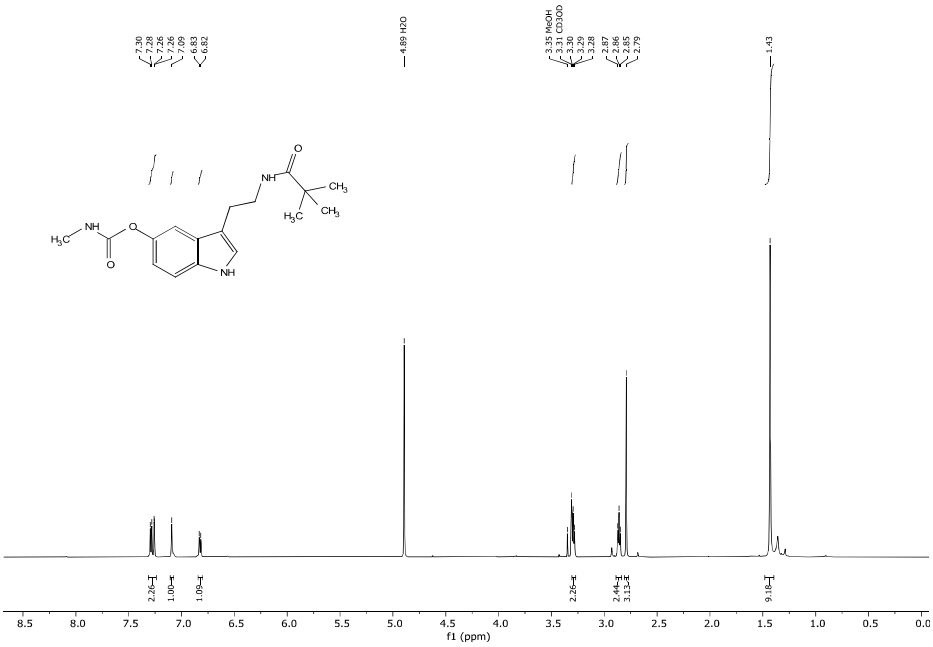

Figure 134. ^{1}H NMR spectrum of **23** (CD_3OD, 600 MHz).

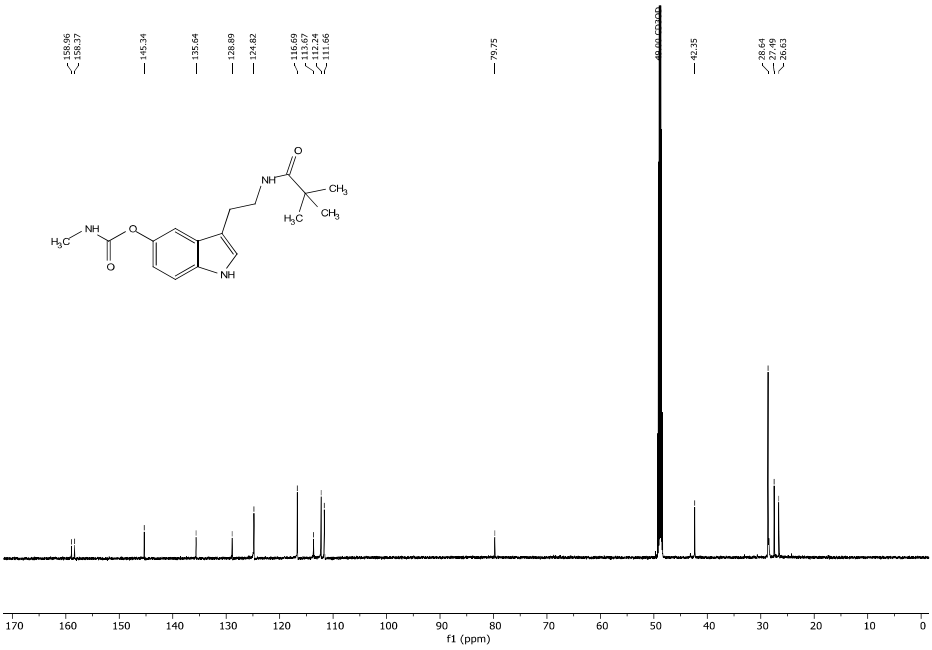

Figure 135. ^{13}C NMR spectrum of **23** (CD_3OD, 151 MHz).

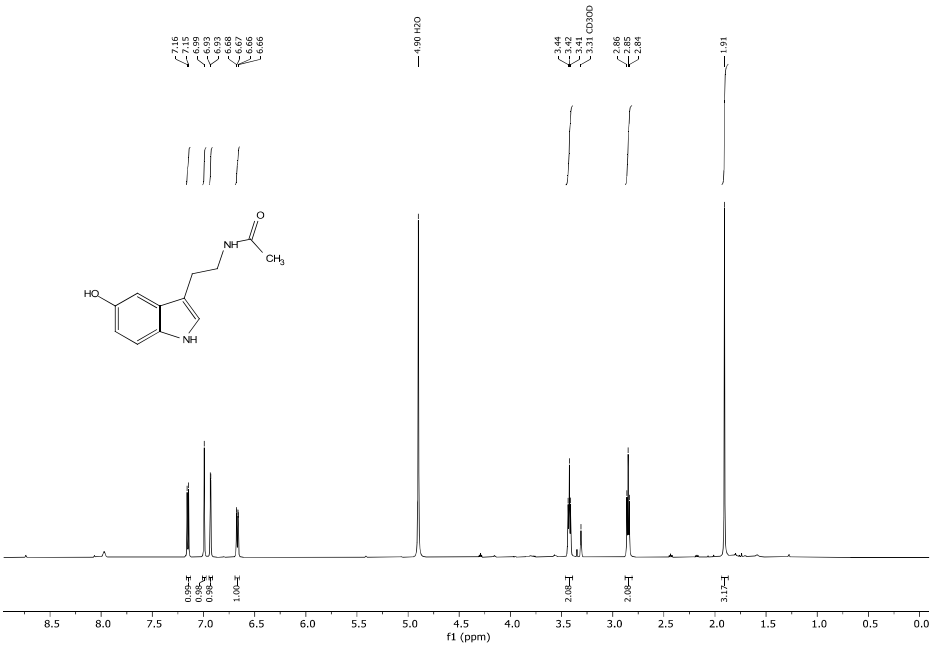

Figure 136. ^{1}H NMR spectrum of **9** (CD_3OD, 600 MHz).

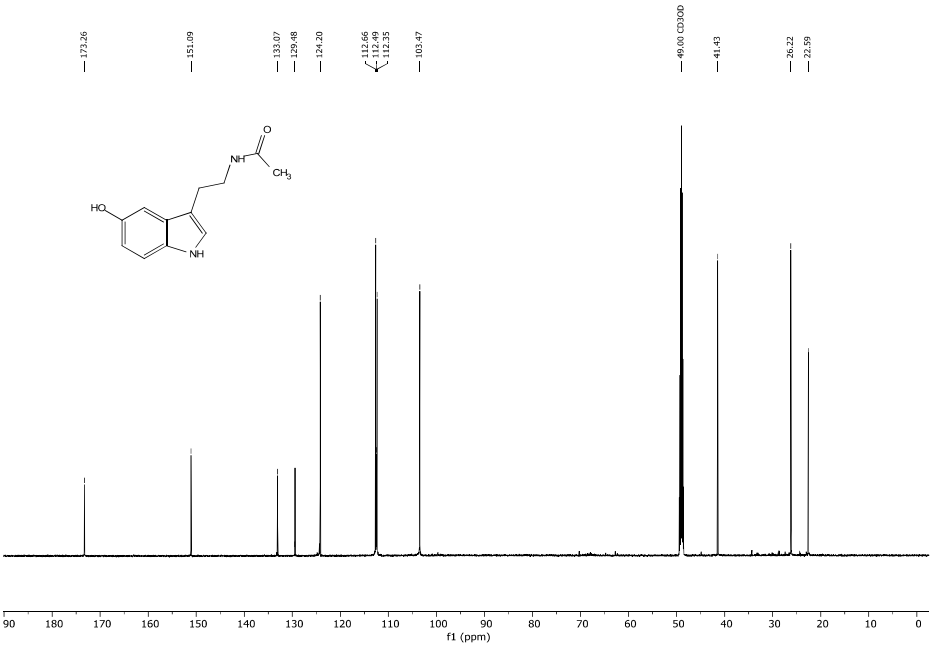

Figure 137. ^{13}C NMR of **9** (CD_3OD, 151 MHz).

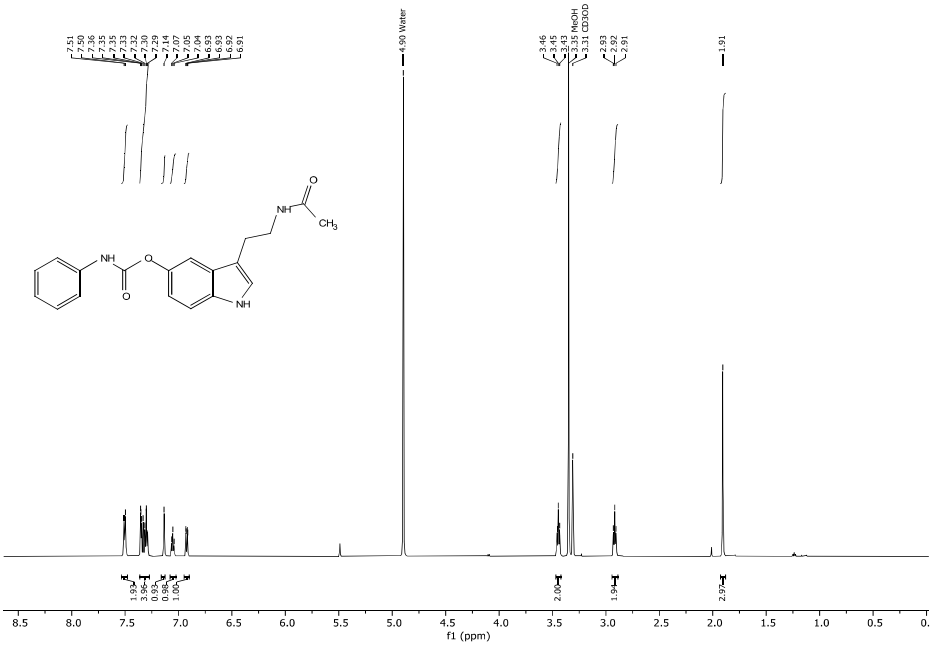

Figure 138. ^{1}H NMR spectrum of **19** (CD_3OD, 600 MHz).

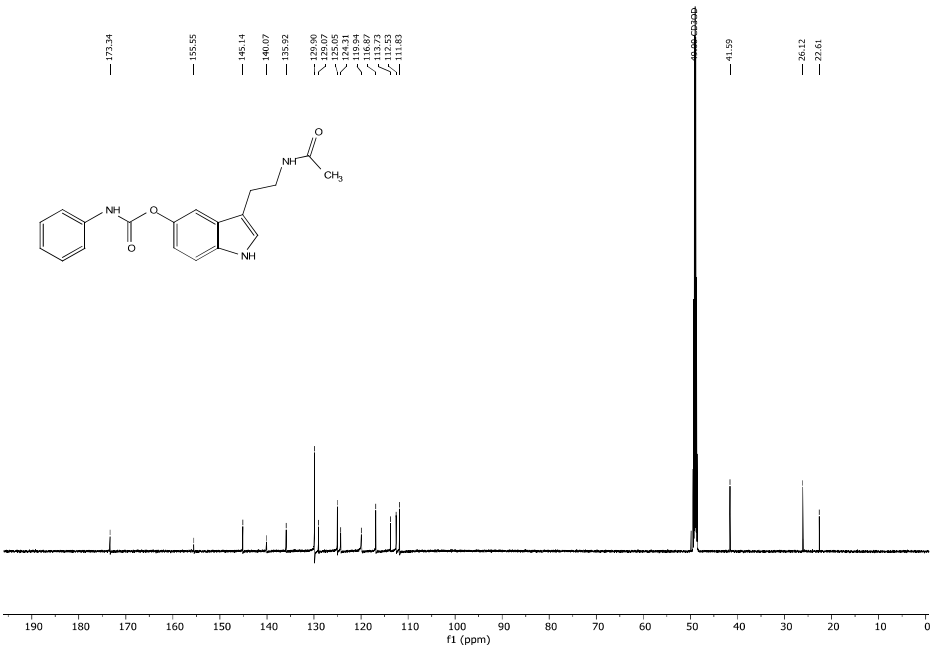

Figure 139. ^{13}C NMR spectrum of **19** (CD_3OD, 151 MHz).

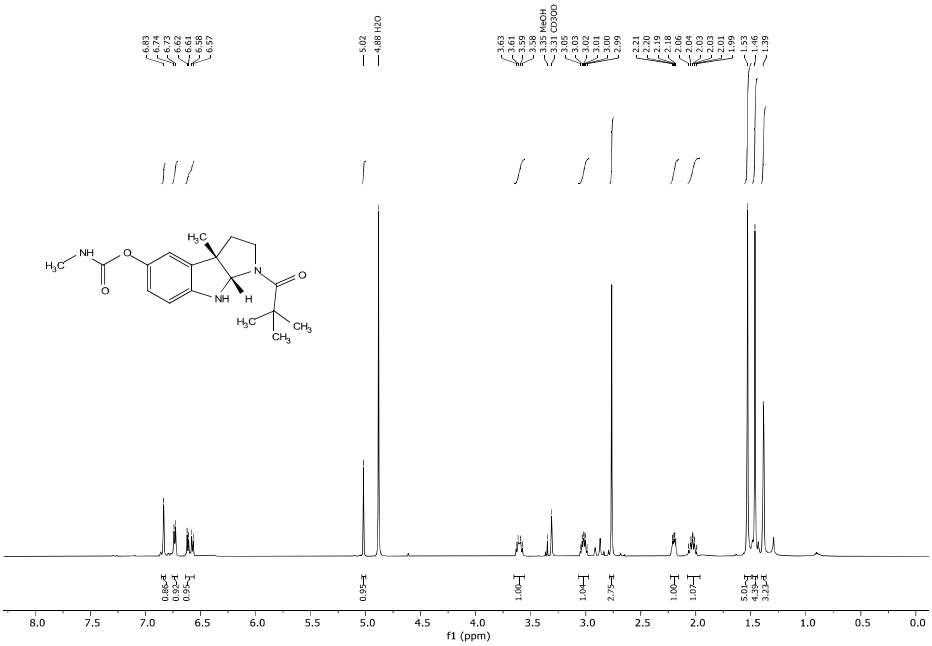

Figure 140. ^{1}H NMR spectrum of **P23** (CD_3OD, 600 MHz).

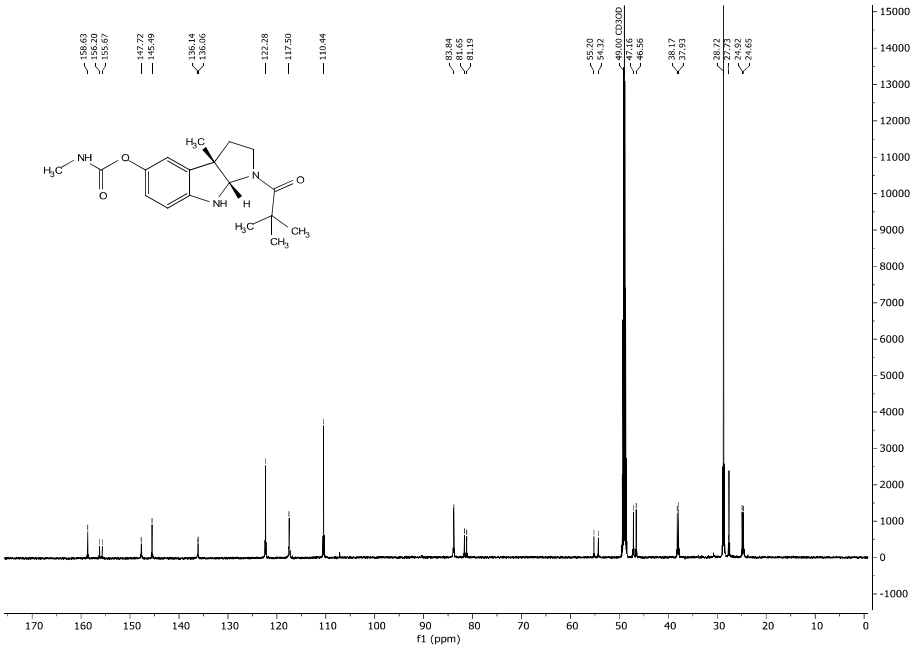

Figure 141. ^{13}C NMR spectrum of **P23** (CD_3OD, 151 MHz).

9.8 LC-MS spectra

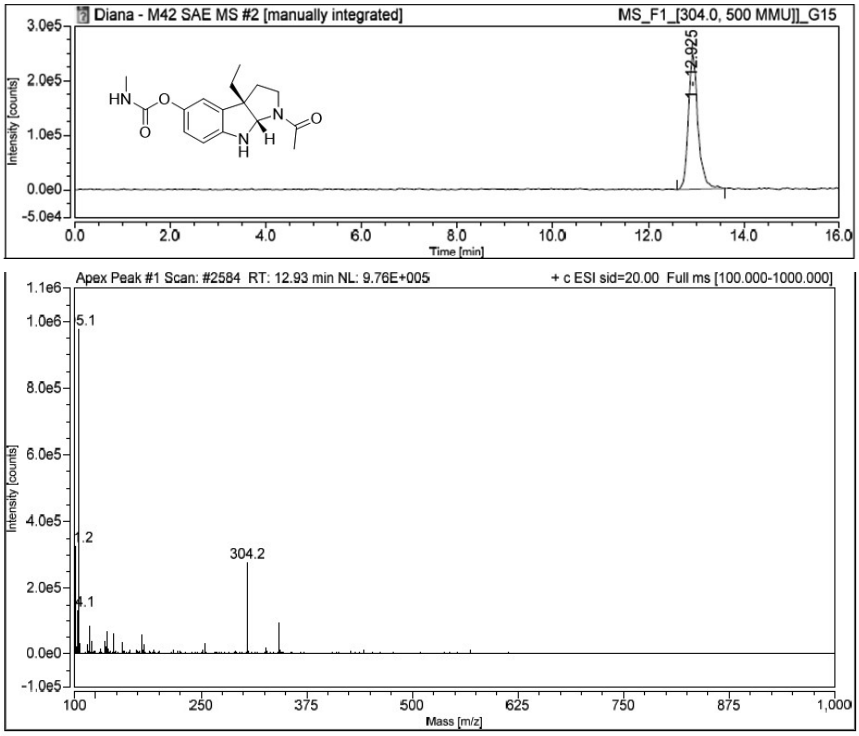

Figure 142. LC-MS chromatogram and mass spectrum of the ethylated PsmD product **Et10** (Reverse phase C-18 column, retention time: 13 min, calculated $[M+H]^+$: 304.15).

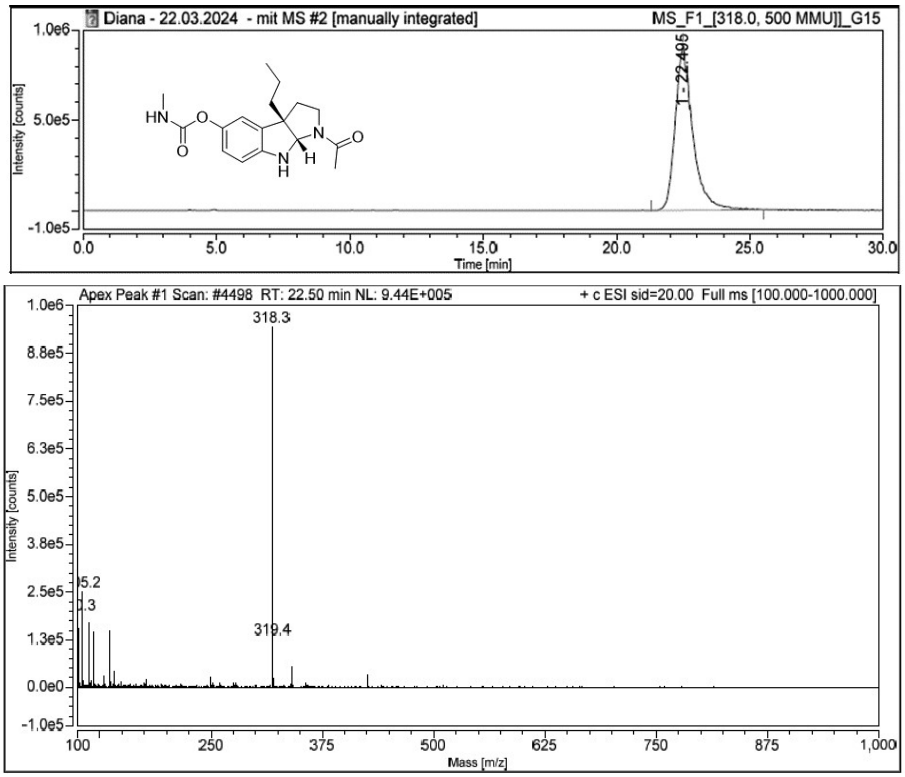

Figure 143. LC-MS chromatogram and mass spectrum of the propylated PsmD product (Reverse phase C-18 column, retention time: 22 min, calculated $[M+H]^+$: 318.17).

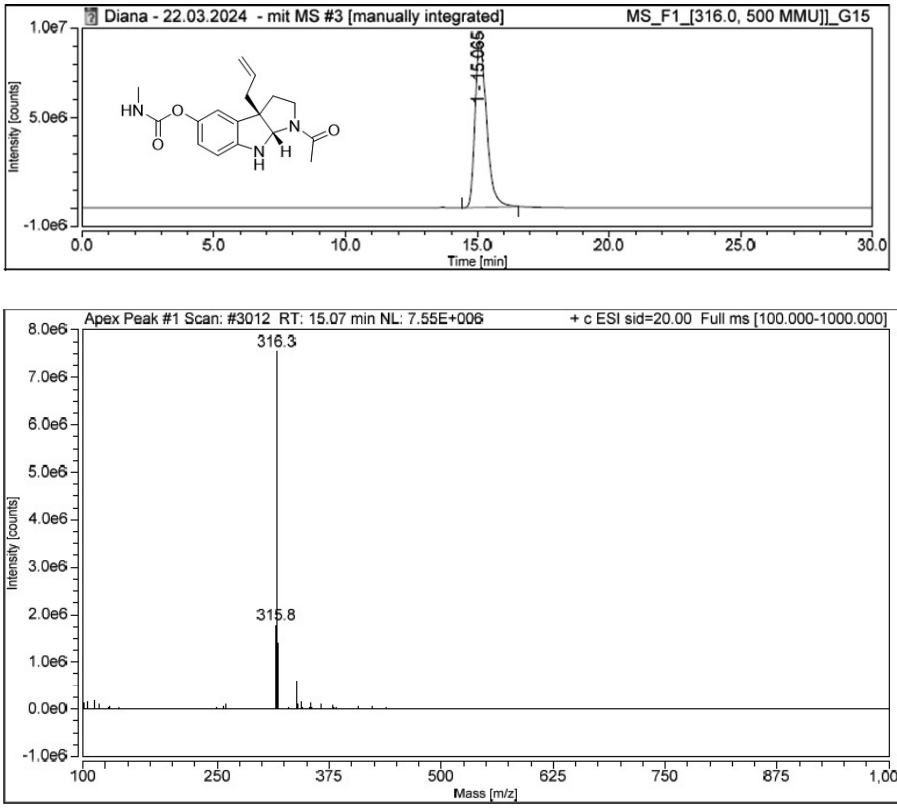

Figure 144. LC-MS chromatogram and mass spectrum of the propylated PsmD product (Reverse phase C-18 column, retention time: 15 min, calculated $[M+H]^+$: 316.15).

10. Acknowledgements

I would like to thank Prof. Jörg Pietruszka, my doctoral supervisor, for taking a chance with an unknown Erasmus student, back in 2019. I am very grateful for his continuous support ever since, and for being available with good advice – scientific and otherwise, whenever I needed. I was very happy with the direction the doctoral project developed, and I am grateful for the freedom to explore the unexpected paths my research took over the PhD years. I admire his enthusiasm and positive outlook and I enjoyed the scientific conversations we had – especially when tackling difficult questions. I learned a lot – scientifically, and about myself during my time at IBOC, and I am grateful for the opportunity to do so.

Many of the results and insights acquired during this project were only possible thanks to the great collaborations I had during my PhD time. Many thanks to Dr. Benoit David and Prof. Holger Gohlke from IBG-4 for our fruitful collaborations over the years. Besides the important results of our collaboration –present in two publications, I appreciated having the chance to "steal some trade" and learn more about computational biochemistry. I am also very grateful to Prof. Oliver Weiergräber for his dedication and hard work towards the crystallization and X-ray structure determination for the PsmD variants. I had a great time working together and I am grateful for everything I learned from our discussions and times in the crystallization lab. I would also like to thank Dr. Julia Tenhaef and Tobias Rosch for their support, and Prof. Stephan Noack for the chance to include the PsmD mutant screening in the early AutoBioTech experiments. I had a lot of fun working on this project.

I am very grateful to the entire team at IBOC, for all the interesting discussions, their continuous help and all the good times we had together. In particular, I would like to thank the (early) methyltransferase team: Lisa Böhmer, Mona Haase and Benjamin Chapple. I am happy for the time we spent together in the lab and outside of it, and very grateful for all of our interesting discussions and the projects we shared. Many thanks to Dr. Thomas Classen for all the good advice and scientific support, and for our very interesting molecular docking cooperations. Also, special thanks to Birgit Henßen for allways being kind and supportive with all of my administrative and analytical questions. In addition, I am very grateful to Lisa Böhmer and Dr. Moritz Klischan for their help in the correction of this thesis. Also, many thanks to Martin Wäscher, Mona Haase, Marcel Schatton, Nadiia Pozhydaieva and Lisa Guo for their valuable contributions to this work.

I am grateful to my partner, Stefan Hank, for his love, kindness and support during these years, for his optimism and positive worldview, even through the most difficult of times.

10. Acknowledgements

Finally, I am most of all grateful to my family. None of this would have been possible without their unrelenting love and support. They gave me the courage to go for my dreams and the safety to be able to fail and try again. They shaped the person I am today.

11. List of synthesized molecules

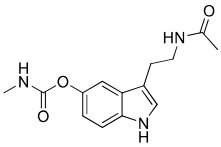

DAM003V023

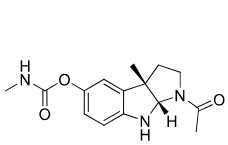

DAM003V025

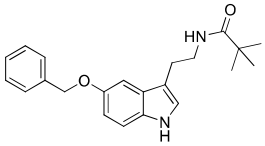

DAM004V026

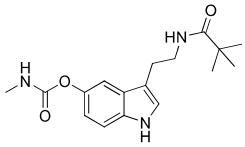

DAM004V030 t-bu amide

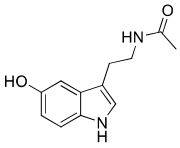

DAM004V045

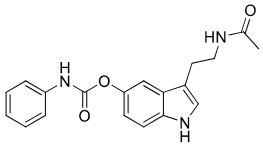

DAM004V046 phe car

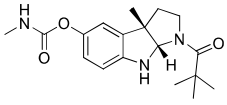

DAM004V048

12. Declaration

I declare under oath that I have produced my thesis independently and without any undue assistance by third parties under consideration of the ‘Principles for the Safeguarding of Good Scientific Practice at Heinrich Heine University Düsseldorf. This dissertation was submitted exclusively to the Faculty of Mathematics and Natural Sciences at Heinrich Heine University Düsseldorf. No other doctoral attempt was undertaken.

Diana-Alexandra Amariei

Düsseldorf, 05.02.2025

Band 40
Die farbenfrohe Welt der Prodiginine – Neue Enzyme für die Synthese bioaktiver Naturstoffderivate
H. U. C. Braß (2021), IX, 349 pp
ISBN: 978-3-95806-523-9

Band 41
Oxidoreduktasen: Von neuen Biokatalysatoren bis zum fertigen Naturstoff
D. Dickmann (2021), 274 pp
ISBN: 978-3-95806-573-4

Band 42
Chemie ohne Grenzen – Biokatalysatoren und Bororganyle als wertvolle Hilfsmittel für die zielmolekülorientierte, enantioselektive Synthese
M. R. Mantel (2021), 487 pp
ISBN: 978-3-95806-585-7

Band 43
Über tetraolbasierte Allylboronsäureester und deren Potential in der stereoselektiven Synthese
P. Ullrich (2022), xii, 324 pp
ISBN: 978-3-95806-618-2

Band 44
Design, Synthese und Charakterisierung neuartiger *photocaged compounds* – Optimierte Werkzeuge zur Etablierung wellenlängenselektiver Genexpression
F. Hogenkamp (2022), V, 456 pp
ISBN: 978-3-95806-637-3

Band 45
Charakterisierung von Methyltransferasen zur enantioselektiven Synthese von Hexahydropyrrolo[2,3-*b*]indol basierten Naturstoffen
P. Schneider (2023), x, 315 pp
ISBN: 978-3-95806-690-8

Band 46
Untersuchungen zu enzymatischen Halogenierungsreaktionen in der organischen Synthese
A. V. Fejzagić (2023), XI, 264 pp
ISBN: 978-3-95806-728-8

Band 47
Biochemische Charakterisierung von modularen dirigierenden Proteinen
N. Huwa (2024), X, 235 pp
ISBN: 978-3-95806-745-5

Band 48
Immobilisierte Enzyme und Kofaktor-Regenerierung in der kontinuierlichen Durchflusssynthese
B. Baumer (2024), XVIII, 231 pp
ISBN: 978-3-95806-783-7

Band 49
Biaryl-based natural products as structural motif for pharmaceutically relevant compounds
M. K. T. Klischan (2025), V, 657 pp
ISBN: 978-3-95806-801-8

Band 50
Flavin-abhängige Halogenasen zur Derivatisierung von Naturstoffen
J. Gebauer (2025), XXIV, 321 pp
ISBN: 978-3-95806-850-6

Band 51
Lipase-catalyzed kinetic resolution: Synthesis and application of axially chiral biphenols
R. C. Ganardi (2025), 423 pp
ISBN: 978-3-95806-854-4

Band 52
Application of *C3*-methyltransferases for natural product synthesis
M. Haase (2025), 432 pp
ISBN: 978-3-95806-862-9

Band 53
Optimierende Untersuchung von Acetaldehydabhängigen Aldolasen und deren Anwendung in der organischen Synthese
J. Hindges (2025), 211 pp
ISBN: 978-3-95806-865-0

Band 54
Indole *C*-methyltransferases – creating an efficient platform for the enantioselective methylation of bioactive compounds
D.-A. Amariei (2026), 339 pp
ISBN: 978-3-95806-881-0

Bioorganische Chemie an der Heinrich-Heine-Universität Düsseldorf
im Forschungszentrum Jülich

Herausgegeben von Jörg Pietruszka

The biosynthesis of the acetylcholinesterase inhibitor physostigmine includes a stereoselective methylation step catalyzed by the SAM-dependent *C*-methyltransferase PsmD. A new indole *C*-methyltransferase was identified, originating from *Streptomyces albulus* (PsmD_*Sa*). The structure, mechanism, and biochemical properties of the enzyme were analyzed. This revealed the high stability of the enzyme and excellent stereoselectivity of the methylation. The crystal structure of PsmD was determined using X-ray spectroscopy. Site-directed mutagenesis was used to map the catalytic site and, together with *in silico* docking and molecular dynamics simulations, to clarify the mechanism of action and provide an overview of PsmD catalysis.

Semi-rational engineering of PsmD_*Sa* enhanced its activity toward bulky indole-containing substrates. To generate and screen the resulting mutant libraries, a modular strategy was designed to automate the enzyme expression, methylation reactions and activity screening. For activity screening, a high-throughput colorimetric assay was developed to detect and quantify indoles in the presence of isolated enzymes and whole-cell biocatalysts. The alkylation capacity of PsmD_*Sa* was also expanded through reaction optimization and site-directed mutagenesis, using SAM cofactor derivatives, leading to a 7-fold improvement of ethylation activity. Finally, preparative enzymatic methylation by PsmD_*Sa* was successfully performed using lysates, whole cells, and immobilized enzymes with cofactor recycling, reaching scales of hundreds of milligrams.

Overall, the study offers practical insights into methyltransferase biocatalysis and showcases PsmD_*Sa* as a promising tool for stereoselective methylation.

Band 54
ISBN 978-3-95806-881-0